# First-principles Statistical Mechanics Approach to Step Decoration at Solid Surfaces

**von**
**M. Sc.**
**Yongsheng Zhang**

**im Fachbereich Physik der Freien Universität Berlin eingereichte Dissertation zur Erlangung des akademischen Grades**

**DOCTOR RERUM NATURALIUM**

**Berlin 2008**

**Erstgutachter: PD Dr. Karsten Reuter**
**Zweitgutachter: Prof. Eberhard K. U. Gross**
**Disputationstermin: 14. May 2008**

# Abstract

As prominent defects at solid surfaces atomic steps are commonly perceived as playing some kind of special, if not decisive role for the surface properties or functions in materials science applications. When aiming to qualify this role at the atomic scale an important first task is to identify the structure and composition at the step edge under realistic gas-phase conditions that are representative for the targeted application. From the modeling side, this requires two ingredients: A reliable description of the energetics at the surface, in other words of the chemical bonds that are formed there. And on the other side a proper treatment of the manifold of processes that can occur, in particular also due to the contact with the gaseous environment at finite temperatures.

In this thesis this problem is addressed with a first-principles statistical mechanics approach, *i.e.* with an approach that is based entirely on a reliable first-principles energetics. Since the evaluations of the partition functions required to at least thermodynamically account for the statistical interplay at finite temperatures would necessitate on unfeasible amount of first-principles total energy calculations, the approach relies on parameterizing as intermediate between the electronic and mesoscopic regime a coarse-grained lattice model, which is then employed in the statistical simulations. The approach is illustrated using the interaction of an oxygen atmosphere with a close-packed (111) step at Pd(100) as example. Apart from the methodological advances that are achieved the major result for this application is then that the specific way how oxygen atoms decorate the step even in environments with pressures of the order atmospheres and elevated temperatures around 1000 K is obtained. Since such gas phase conditions are representative for an important catalytic application like the high-temperatures combustion of methane, this work thus provides first first-principles insight into the structure and composition at a prominent defect at the surface of a working model catalyst.

*For Yuanyuan*
*and my parents*

# Contents

# List of Figures

# List of Tables

# Chapter 1

# Introduction

Modern multi-scale modeling approaches reflect the realization that for the understanding of a large number of materials science applications a treatment over a wide range of length and time scales is required. At the lowest scale are electronic interactions that lead to the formation and breaking of chemical bonds between atoms over length and time scales of the order of Angstroms and picoseconds. At the largest scale one has arrived at macroscopic dimensions where then a resolution of the atomic structure may no longer play a role. Somewhere in between one has what one could call a mesoscopic regime, where as a most important factor the statistics between the manifold of atomic scale processes sets in. While nowadays there are typically well established theories at each individual length and time scale, the links between the different methodologies are only just emerging. What is most prominently still lacking are robust links that enable a control of the error propagation from one scale to the other. Within this context first-principles statistical mechanics approaches try to establish such links between electronic structure theories and concepts that come from thermodynamics and statistical mechanics. The prior are the methods of choice when it comes to a reliable quantum mechanical description of the fundamental binding interactions between the atomic constituents, while the latter are obviously designed to handle the statistical interplay that emerges among the manifold of molecular processes at mesoscopic scales [67].

The description of a solid surface exposed to a realistic gaseous environment is a typical example where such first-principles statistical mechanics approaches are indispensably required. On the one hand side, the complex bonding in particular at transition metal surfaces requires the use of first-principles electronic structure theories if a theoretical description with predictive character is aspired. Such theories, in particular modern density-functional theory [2], have provided tremendous insight into the energetics and electronic structure of solid surfaces and of adsorbates at them. On the other hand, the interplay with the gaseous environment is not that easily grasped. An explicit modeling of even just a very finite chunk of surrounding gas phase over the solid surface would already yield system sizes that are beyond the scope of present-day computing resources. Furthermore, the statistics (or entropy in

a thermodynamic language) is playing a key role. At atmospheric pressures and room temperature on the order of $10^8$ gas phase molecules hit every single surface atom per surface. Evaluating this bombardment and its effect on the surface structure and composition can only be handled by resorting to methods from statistical mechanics. This in particular, if the effect of temperature on the structure, composition and order at the surface is to be tackled.

Correspondingly, first-principles statistical mechanics approaches have been increasingly employed to address such issues. Assuming the surface to be in equilibrium with the surrounding gas phase, so-called first-principles atomistic thermodynamics approaches couple the solid surface to a gas phase reservoir. In their prevalent form the effect of configurational entropy at the surface is neglected and the approach is employed to compare the stability of a variety of surface structural models under given environmental conditions. The evaluation of the partition function required to explicitly account for the effect of configurational entropy at finite temperatures necessitates unfortunately an amount of first-principles total energy calculations that still far exceeds present-day supercomputing resources. As one remedy first-principles lattice-gas Hamiltonian approaches first parameterize a coarse-grained lattice model of the surface with the first-principles data and then base the partition function evaluation entirely on the resulting computationally much less demanding model Hamiltonian. Issues in the aforementioned robustness of the link between the theories are then obviously the reliability range of the employed lattice model, as well as its parameterization details.

Despite the achievement in being able to study solid surfaces in contact with technologically relevant environments with pressures of the order atmospheres and elevated temperatures at all, one still has to recognize that such first-principles statistical mechanics studies are at the edge of what is feasible with current computing resources. Correspondingly, existing studies almost exclusively focused on simple model surfaces in the sense of low Miller index surfaces of single crystals. While one can argue that these surfaces represent the dominant facets of real solid surfaces, there are still essential features missing: defects and facet edges. One prominent group of defects are atomic steps, and there in particular close-packed steps due to their low formation energies. Due to the undercoordinated atoms exposed at the step edge, these defects are frequently perceived to play some special, if not decisive role for the surface properties or function in materials science applications. Theoretical studies that quantitatively pinpoint this special role while also accounting for the effect of a realistic (reactive) environment are, however, virtually not existent, not least due to the just described challenges for a first-principles based modeling.

The aim of this thesis is thus precisely to establish a methodological framework that is able to describe with predictive character what happens at an atomic step at a surface, when the latter is exposed (say in a catalytic application) to a gaseous environment. More precisely (and cautiously) the focus is on an important first step in this direction, namely on identifying the structure and composition at the atomic step when the surface is in equilibrium with the surrounding gas phase. As will

become clear in the course of this thesis, already this is a daunting task, in particular when aiming to establish a theory based on robust links between the scales and with predictive character. The modeling will be developed using a Pd(100) surface in contact with an oxygen gas phase as example. Pd is a frequently employed material in a wide range of applications, oxygen is an ubiquitous gas dominating our earths atmosphere and the (100) facet is one of the most stable and thus dominating facets of fcc structured palladium. After introducing the different methodologies underlying the employed first-principles statistical mechanics part in Part I, the robustness of the link between the electronic structure calculations and the statistical techniques in form of the lattice-gas Hamiltonian parameterization will first be critically assessed in Part II by still focusing on the ideal Pd(100) facet. Part III then addresses the step itself, by first discussing the energetic data collected from various Pd vicinal surfaces exposing (111) steps and (100) terraces, and then explaining how this data is considered in the first-principles lattice-gas Hamiltonian that is finally used to address the decoration of the step in finite environments.

# Part I

# Theoretical Background

# Chapter 2

# Density-functional Theory

The Schrödinger equation provides a theoretical way to investigate the quantum-mechanical properties of systems like atoms, molecules *etc.* Unfortunately, for most systems of practical interest the Schrödinger equation cannot be solved exactly anymore and approximations must be applied. In this respect, Density-functional theory (DFT) has become a most popular and powerful tool in studying physics and chemistry topics, and Walter Kohn was awarded by Nobel Prize in 1998 [1] for his marvelous contribution on DFT. As Isaac Newton said:" *If I have seen further it is by standing on ye shoulders of giants*". Before heading on to the modern DFT, we are going to retrace the history of this theory.

## 2.1 The Many-electron Problem

In order to understand or predict properties of materials including $N$ electrons and $M$ nuclei from *ab initio* calculations, the Schrödinger equation for time-independent nonrelativistic cases can be written as,

$$\hat{H}\Psi(\mathbf{r_i}, \mathbf{R_j}) = E\Psi(\mathbf{r_i}, \mathbf{R_j}) \quad , \tag{2.1}$$

where $\hat{H}$ is the Hamiltonian operator, and $E$ is the eigenvalue of the operator. $\Psi$ is the corresponding wave function, and $\mathbf{r_i}$ and $\mathbf{R_i}$ are the coordinates of electron $i$ and nucleus $j$, respectively. The Hamiltonian contains several contributions: Kinetic energies of electrons ($T_\mathrm{e}$) and nuclei ($T_\mathrm{n}$); interaction potentials between particles, in form of repulsive potentials between nuclei ($V_\mathrm{nn}$), attractive potentials between nuclei and electrons ($V_\mathrm{ne}$) and repulsive potentials between electrons ($V_\mathrm{ee}$). Then, the Hamiltonian operator $\hat{H}$ is rewritten as,

$$\hat{H} = T_\mathrm{n} + T_\mathrm{e} + V_\mathrm{nn} + V_\mathrm{ne} + V_\mathrm{ee} \quad . \tag{2.2}$$

Applying atomic units, *i.e.* $m_\mathrm{e} = \hbar = e = 1$, these components of the Hamiltonian

operator are written as,

$$T_{\mathrm{n}} = -\frac{1}{2}\sum_{j=1}^{M}\frac{1}{m_j}\nabla_j^2 \quad , \tag{2.3}$$

$$T_{\mathrm{e}} = -\frac{1}{2}\sum_{i=1}^{N}\nabla_i^2, \tag{2.4}$$

$$V_{\mathrm{nn}} = \sum_{i=1}^{M}\sum_{j>i}^{M}\frac{Z_i Z_j}{|\mathbf{R_i}-\mathbf{R_j}|} \quad , \tag{2.5}$$

$$V_{\mathrm{ne}} = \sum_{i=1}^{N}\sum_{j=1}^{M}\frac{-Z_j}{|\mathbf{r_i}-\mathbf{R_j}|} \quad , \tag{2.6}$$

$$V_{\mathrm{ee}} = \sum_{i=1}^{N}\sum_{j>i}^{N}\frac{1}{|\mathbf{r_i}-\mathbf{r_j}|} \quad , \tag{2.7}$$

where $m_j$, $Z_j$ and $\nabla_j$ are the mass of nucleus $j$, its atomic number and Laplacian operator, respectively.

Although Eq. 2.1 is the most accurate way to obtain the properties of materials, it is too complex to solve due to the large number of variables that the wave function depends on. For a system with $M$ nuclei and $N$ electrons, we have $3M+3N$ variables, *i.e.* 3 coordinates and 3 momenta for each particle, respectively. In order to solve Eq. 2.1 in practice for many-electron systems, approximations have to be applied. The first important approximation is the Born-Oppenheimer ($BO$) nonrelativistic approximation: Loosely stated, it assumes that the movement of the electrons is so fast that they can catch up the movement of the nuclei instantaneously and relax to the corresponding ground state instantaneously, because the mass of an electron is so much smaller than that of a nucleus. (In the worst case of a H atom, 1 electron $\approx 1/1800$ of the mass of nucleus) Then, nuclei can be viewed as static, enabling a splitting of the full Hamiltonian ($\hat{H}$) in Eq. 2.1 into two parts: Nuclear part ($\hat{H}_{\mathrm{N}}$) and electronic part ($\hat{H}_{\mathrm{e}}$). Correspondingly, the total wave function ($\Psi$) is split into the following form:

$$\Psi(\mathbf{r_i},\mathbf{R_j}) = \Psi_e^{\mathbf{R}}(\mathbf{r_i})\Psi(\mathbf{R_j}) \quad , \tag{2.8}$$

where $\Psi_e^{\mathbf{R}}(\mathbf{r_i})$ is the wave function of electrons with current nuclei positons, and $\Psi(\mathbf{R_j})$ is the wave function of nuclei. The total energy of a system then equals the sum of the nuclear energy ($E_{\mathrm{N}}$) and electronic energy ($E_{\mathrm{e}}$), $E = E_{\mathrm{N}} + E_{\mathrm{e}}$. For fixed atomic coordinates $E_N$ is a constant and we can focus on the electron Schrödinger equation,

$$\hat{H}_{\mathrm{e}}\Psi_{\mathrm{e}}(\mathbf{r_i}) = E_{\mathrm{e}}\Psi_{\mathrm{e}}(\mathbf{r_i}) \quad , \tag{2.9}$$

where

$$\hat{H}_{\mathrm{e}} = -\frac{1}{2}\sum_{i=1}^{N}\nabla_i^2 + \sum_{i=1}^{N}\sum_{j=1}^{M}\frac{-Z_j}{|\mathbf{r_i}-\mathbf{R_j}|} + \sum_{i=1}^{N}\sum_{j>i}^{N}\frac{1}{|\mathbf{r_i}-\mathbf{r_j}|} \quad . \tag{2.10}$$

It is clear that the *BO* approximation decreases the number of variables in Eq. 2.1 from $3N+3M$ to $3N$, but this computational burden still requires further approximations for most practical systems. One fundamental approach to solve the electronic Schrödinger equation (Eq. 2.9) numerically is the Hartree-Fock approximation, which transfers the many-body problem into a single particle problem through approximating the electronic wave function $\Psi_{\mathrm{e}}(\mathbf{r_i})$ by a Slater-determinant of single particle wave functions. This ensures the antisymmetry of the wave function, required to fulfill to Pauli principle, and thereby accounts for a quantum mechanical contribution to the potential, termed exchange potential ($V_{\mathrm{x}}$). On the other hand, this approximation does not account for the quantum mechanical interaction between electrons of like spin. Compared to the full potential ($V_{\mathrm{ee}}$), the Hartree-Fock potential thus includes the classical Coulomb potential ($V_{\mathrm{ee}}^{\mathrm{c}}$) and the exchange potential ($V_{\mathrm{x}}$), but misses a part termed correlation potential ($V_{\mathrm{c}}$).

Although this term is smaller than the other two, it is significant to obtain accurate results. In order to improve the original Hartree-Fock approximation, there are thus further advanced approaches to account for the correlation energy. The most popular are second or fourth order perturbation theory by Møller and Plesset (MP2 or MP4) [3], configuration interaction (CI) [4], multiconfiguration self-consistent field (MCSCF) [5], and coupled cluster approaches (CC) [6]. These methods are quite accurate, but are computationally very intense.

Alternatively, density-functional theory (DFT) is a remarkable theory that replaces the complicated $N$-electron wave function and the associated Schrödinger equation by a formulation based on the simpler electron density ($\rho$).

## 2.2 Density-functional Theory

### 2.2.1 Original Idea: Thomas-Fermi Model

In 1927 Thomas and Fermi realized that statistical considerations can be used to approximate the distribution of electrons in an atom. *Electrons are distributed uniformly in the six-dimensional phase space for the motion of an electron at the rate of two for each $h^3$ of volume,* and there is an effective potential field that "is itself determined by the nuclear charge and this distribution of electrons." Based on this realization the Thomas-Fermi formula for the electron density can be derived [7], and finally, the famous Thomas-Fermi kinetic energy functional is,

$$T_{\mathrm{TF}}(\rho) = C_F \int \rho^{5/3}(\mathbf{r}) d\mathbf{r}, \quad C_F = \tfrac{3}{10}(3\pi^2)^{2/3} = 2.871 \quad . \tag{2.11}$$

Additionally, the *electron density* $[\rho(\mathbf{r})]$ is defined as the number of electrons per unit volume in a given state. The electron density at point $\mathbf{r_1}$ means that the probability to find an electron at this point, is (without spin),

$$\rho(\mathbf{r_1}) = N \int ... \int |\Psi(\mathbf{r_1}, \mathbf{r_2}...\mathbf{r_N})|^2 d\mathbf{r_2}...d\mathbf{r_N} \quad . \tag{2.12}$$

If we integrate Eq. 2.12 over space, we will get the total number of electrons,

$$\int \rho(\mathbf{r}) d\mathbf{r} = N \quad . \tag{2.13}$$

Applying this definition on Eq. 2.10, the electron-nucleus attractive energy and classical electron-electron repulsive energy can be written as a function of $\rho(\mathbf{r})$,

$$V_{\mathrm{ne}} = Z \int \frac{\rho(\mathbf{r})}{\mathbf{r}} d\mathbf{r} \quad , \tag{2.14}$$

$$V_{\mathrm{ee}}^{\mathrm{c}} = \frac{1}{2} \int \int \frac{\rho(\mathbf{r_1})\rho(\mathbf{r_2})}{|\mathbf{r_1} - \mathbf{r_2}|} d\mathbf{r_1} d\mathbf{r_2} \quad . \tag{2.15}$$

For simplicity, we here neglect the exchange-correlation energy in the expectation value of Eq. 2.10 ($\langle \Psi_e | \hat{H}_e | \Psi_e \rangle$) for the moment. Together with the kinetic energy functional, Eq. 2.11 we then reach the energy functional of the Thomas-Fermi theory of atoms in terms of the electron density,

$$E_{\mathrm{TF}}[\rho(\mathbf{r})] = C_F \int \rho^{5/3}(\mathbf{r}) d\mathbf{r} + Z \int \frac{\rho(\mathbf{r})}{\mathbf{r}} d\mathbf{r} + \frac{1}{2} \int \int \frac{\rho(\mathbf{r_1})\rho(\mathbf{r_2})}{|\mathbf{r_1} - \mathbf{r_2}|} d\mathbf{r_1} d\mathbf{r_2} \quad . \tag{2.16}$$

Under the constraint of Eq. 2.13, the electron density is used to minimize the energy functional $E_{\mathrm{TF}}[\rho(\mathbf{r})]$, and to obtain the ground state energy. Unfortunately, while the Thomas-Fermi formula is quite simple and decrease the variables from $3N$ to 3, the approximations behind it (neglected $V_{\mathrm{xc}}$ and kinetic energy functional based on a non-interacting, homogenous electron gas) are too bold to make it of any practical use for actual calculations.

### 2.2.2 Hohenberg-Kohn Theorems

While the Thomas-Fermi model already casts the electronic energy into a functional of electron density, it did not become popular because of its low accuracy. The situation changed with the landmark paper published by Hohenberg and Kohn [8] in 1964, which demonstrates that the Thomas-Fermi formula is only an approximation to an exact theory, the *density-functional theory*. For nondegenerate ground states, the Hohenberg-Kohn theory is based on two theorems, which legitimize the use of the electron density $\rho(\mathbf{r})$ as basic variable to obtain the ground state energy. The first theorem states: *The external potential $v(\mathbf{r})$ is determined, within a trivial additive constant, by the electron density $\rho(\mathbf{r})$.* Here $v(\mathbf{r})$ does not restrict to the Coulomb potential. The proof of this theorem is quite simple by employing the minimum-energy principle for the ground state. Consider two external potentials $v$ and $v'$ that differ by more than a constant, but both give the same $\rho$ for their ground state. The different Hamiltonians $H$ and $H'$ whose ground state densities are the same then determine two different normalized wave functions $\Psi$ and $\Psi'$. Taking $\Psi'$ as a trial function for

$H$, we would have,

$$\begin{aligned} E_0 < \langle \Psi' | \hat{H} | \Psi' \rangle &= \langle \Psi' | \hat{H}' | \Psi' \rangle + \langle \Psi' | \hat{H} - \hat{H}' | \Psi' \rangle \\ &= E_0' + \int \rho(\mathbf{r})[v(\mathbf{r}) - v'(\mathbf{r})] d\mathbf{r} \quad , \end{aligned} \tag{2.17}$$

where $E_0$ and $E_0'$ are the ground state energies for $\hat{H}$ and $\hat{H}'$, respectively. In the same way, taking $\Psi$ as a trial function for $H'$ we would get,

$$E_0' < \langle \Psi | \hat{H}' | \Psi \rangle = E_0 - \int \rho(\mathbf{r})[v(\mathbf{r}) - v'(\mathbf{r})] d\mathbf{r} \quad . \tag{2.18}$$

Adding Eq. 2.17 and 2.18, we get $E_0 + E_0' < E_0' + E_0$. This contradiction indicates that there cannot be two different $v$ that give the same $\rho$ for their ground states. The first Hohenberg-Kohn theorem thus tell us that the ground state density $\rho$ determines all properties of a system. Then the total energy of a configuration at a certain potential $v$ can be written as,

$$\begin{aligned} E_v[\rho] &= T[\rho] + V_{\mathrm{ne}}[\rho] + V_{\mathrm{ee}}[\rho] \\ &= F_{\mathrm{HK}}[\rho] + \int \rho(\mathbf{r}) v(\mathbf{r}) d\mathbf{r} \quad , \end{aligned} \tag{2.19}$$

where

$$F_{\mathrm{HK}}[\rho] = T[\rho] + V_{\mathrm{ee}}[\rho] \quad . \tag{2.20}$$

$F_{\mathrm{HK}}$ is called *universal functional* of $\rho$ due to its independence on the external potential.

The second Hohenberg-Kohn theorem states: *For a trial density* $\tilde{\rho}(\mathbf{r})$*, such that* $\tilde{\rho}(\mathbf{r}) \geq 0$ *and* $\int \tilde{\rho}(\mathbf{r}) d\mathbf{r} = N$*, then,*

$$E_0 \leq E_v[\tilde{\rho}(\mathbf{r})] \quad , \tag{2.21}$$

*where* $E_v[\tilde{\rho}(\mathbf{r})]$ *is the energy depending on* $v$*.* This theorem is a justification to use the variational principle to determine the ground state energy $E_0$. Based on the first theorem, $\tilde{\rho}$ determines its own potential $\tilde{v}$, Hamiltonian $\hat{\tilde{H}}$ and wave function $\tilde{\Psi}$. Taking $\tilde{\Psi}$ as a trial function for a Hamiltonian ($\hat{H}$) with the true external potential $v$,

$$\langle \tilde{\Psi} | \hat{H} | \tilde{\Psi} \rangle = \int \tilde{\rho}(\mathbf{r}) v(\mathbf{r}) d\mathbf{r} + F_{\mathrm{HK}}[\tilde{\rho}] = E_v[\tilde{\rho}] \geq E_v[\rho] \quad , \tag{2.22}$$

which is the desired result.

Additionally, applying the variational principle with constrained $\int \rho(\mathbf{r}) d\mathbf{r} = N$, the differentiability of $E_v[\rho]$ for the ground state density is satisfying the stationary principle,

$$\delta \{ E_v[\rho] - \mu [ \int \rho(\mathbf{r}) d\mathbf{r} - N ] \} = 0 \quad , \tag{2.23}$$

which gives the Euler-Lagrange equation, and

$$\mu = \frac{\delta E_v[\rho]}{\delta \rho(\mathbf{r})} = v(\mathbf{r}) + \frac{\delta F_{\mathrm{HK}}[\rho]}{\delta \rho(\mathbf{r})} \quad , \tag{2.24}$$

where $\mu$ is the chemical potential.

### 2.2.3 Kohn-Sham Equation

In principle, if we knew the exact *universal functional* ($F_{\mathrm{HK}}$), Eq. 2.23 is an exact equation to obtain the ground-state properties. Unfortunately, this exact $F_{\mathrm{HK}}$ is elusive, leaving the Hohenberg-Kohn theorems without much practical relevance. The break-through came only one year after the HK theorems. In 1965 Kohn and Sham [9] approximated the $F_{\mathrm{HK}}$ functional, and made the theorems practically useful by introducing the concept of a non-interacting reference system. Within this approach, the kinetic energy of the non-interacting reference system still exhibiting the real density $\rho(\mathbf{r})$ can be written as,

$$T_{\mathrm{s}} = -\frac{1}{2}\sum_{i}^{N} < \varphi_i|\nabla^2|\varphi_i > \quad , \tag{2.25}$$

where $\varphi_i$ are single-particle Kohn-Sham orbitals. Here the non-interacting kinetic energy is not equal to the true kinetic energy ($T$) of the interacting system, $T_{\mathrm{s}} \neq T$, and actually $T = T_{\mathrm{s}} + T_{\mathrm{c}}$. Therefore, Kohn and Sham rewrote the universal functional as,

$$F[\rho] = T_{\mathrm{s}}[\rho] + J[\rho] + E_{\mathrm{xc}}[\rho] \quad , \tag{2.26}$$

and the exchange-correlation energy is defined as,

$$E_{\mathrm{xc}}[\rho] = (T[\rho] - T_{\mathrm{s}}[\rho]) + (E_{\mathrm{ee}}[\rho] - J[\rho]) \quad . \tag{2.27}$$

The exchange-correlation energy thus contains everything that is unknown: The non-classical effects of exchange and correlation, which are contributions to the potential energy of the system, and a portion belonging to the kinetic energy. With this formulation, the many-body problem is mapped onto an effective single particle problem. Kohn and Sham thus established that for any real (interacting) system with ground-state density $\rho(\mathbf{r})$ there always exists a noninteracting system with the same ground-state density $\rho(\mathbf{r})$. This leads to the famous Kohn-Sham equation,

$$[-\frac{1}{2}\nabla^2 + V_{\mathrm{eff}}(\mathbf{r})]\varphi_i = \epsilon_i\varphi_i \quad , \tag{2.28}$$

where $\varphi_i$ are the single particle wave functions, or Kohn-Sham orbitals, and $\epsilon_i$ are the Kohn-Sham orbital energies. $V_{\mathrm{eff}}(\mathbf{r})$ is the effective potential, which contains the classical Coulomb potential, exchange-correlation potential and the external potential $V_{\mathrm{ext}}(\mathbf{r})$,

$$V_{\mathrm{eff}}(\mathbf{r}) = \int \frac{\rho(\mathbf{r}')}{|\mathbf{r} - \mathbf{r}'|} d\mathbf{r}' + V_{\mathrm{xc}}(\mathbf{r}) + V_{\mathrm{ext}}(\mathbf{r}) \quad . \tag{2.29}$$

The density of the real system, $\rho(\mathbf{r})$, can be expressed in terms of the Kohn-Sham orbitals, $\rho(\mathbf{r}) = \sum_i^N |\varphi_i(\mathbf{r})|^2$. The exchange-correlation potential, $V_{\mathrm{xc}}(\mathbf{r})$, can be written as,

$$V_{\mathrm{xc}}(\mathbf{r}) = \frac{\delta E_{\mathrm{xc}}[\rho]}{\delta\rho(\mathbf{r})} \quad , \tag{2.30}$$

*i.e.* as the functional derivative of $E_{\rm xc}[\rho]$ with respect to the density. If the exact forms of $E_{\rm xc}$ and $V_{\rm xc}$ were known, the Kohn-Sham strategy would lead to the exact energy, *i.e.* the correct eigenvalue of the Hamilton operator $\hat{H}$ of the Schrödinger equation. The Kohn-Sham approach is thus in principle exact! The approximation only enters when we have to decide on an explicit form for the unknown functional for the exchange-correlation energy $E_{\rm xc}$ and its corresponding potential $V_{\rm xc}$. The central goal of modern density-functional theory is therefore to find better and better approximations to these two quantities.

### 2.2.4 Present-day Exchange-correlation Functionals

The most basic approximation to $V_{\rm xc}$ was introduced by Kohn and Sham in their seminal paper [9]. The so-called local density approximation (LDA) is based on the homogeneous electron gas to approximate the exchange-correlation energy. For an inhomogeneous system, the idea is to view the electron density as locally homogeneous at each point in space. The LDA xc energy then has the form,

$$E_{\rm xc}^{\rm LDA}[\rho] = \int \rho(\mathbf{r})\epsilon_{\rm xc}[\rho(\mathbf{r})]d\mathbf{r} \quad , \tag{2.31}$$

where $\epsilon_{\rm xc}(\rho)$ indicates the exchange-correlation energy per particle of a uniform electron gas of density $\rho$. The corresponding exchange-correlation potential becomes,

$$v_{\rm xc}^{\rm LDA}(\mathbf{r}) = \frac{\delta E_{\rm xc}^{\rm LDA}}{\delta\rho(\mathbf{r})} = \epsilon_{\rm xc}[\rho(\mathbf{r})] + \rho(\mathbf{r})\frac{\partial\epsilon_{\rm xc}(\rho)}{\partial\rho} \quad . \tag{2.32}$$

Moreover, $\epsilon_{\rm xc}(\rho)$ contains two parts: exchange $\epsilon_{\rm x}(\rho)$ part and correlation $\epsilon_{\rm c}(\rho)$ part,

$$\epsilon_{\rm xc}(\rho) = \epsilon_{\rm x}(\rho) + \epsilon_{\rm c}(\rho) \quad , \tag{2.33}$$

where the exchange part $\epsilon_{\rm x}(\rho)$ is expressed as [7, 10],

$$\epsilon_{\rm x}(\rho) = -\frac{3}{4}(\frac{3\rho(\mathbf{r})}{\pi})^{\frac{1}{3}} \quad . \tag{2.34}$$

The correlation part $\epsilon_{\rm c}(\rho)$ can not be expressed by such an explicit functional form. Expressions are only known for the high-density [12, 13] and low-density [14, 15] limit, whereas for intermediate densities only numerical values are known from highly accurate quantum Monte Carlo calculations [11]. This insight was then used to parameterize suitable expressions for DFT-LDA calculations [16, 17].

The LDA gives already surprisingly good results for a wide range of realistic systems, but fails for systems that are far from the uniform electron gas limit like atoms or molecules. A straightforward correction to the LDA is a formal expansion of $E_{\rm xc}$ in gradients of the density. The idea also came from Hohenberg and Kohn [8]. In

general, such a density-gradient expansion (DGE) of the exchange-correlation energy has the form,

$$E_{\rm xc}^{\rm DGE}[\rho] = \int [\epsilon_{\rm xc}^{(0)}(\rho) + \epsilon_{\rm xc}^{(1)}(\rho)\nabla\rho + \epsilon_{\rm xc}^{(2)}(\rho)|\nabla\rho|^2 + ...]d\mathbf{r} \quad . \tag{2.35}$$

However, a first order truncated DGE does not work very well, and sometimes give even worse results than LDA. In order to solve this problem, one can introduce a more generalized expansion and consider *generalized-gradient approximation* (GGA) functionals of the form.

$$E_{\rm xc}^{\rm GGA}[\rho] = \int f(\rho(\mathbf{r}), \nabla\rho(\mathbf{r}))d\mathbf{r} = \int \rho\epsilon_{\rm xc}^{\rm GGA}(\rho(\mathbf{r}), \nabla\rho(\mathbf{r}))d\mathbf{r} \quad . \tag{2.36}$$

As in the LDA, the GGA exchange-correlation energy also divides into two parts: $E_{\rm x}^{\rm GGA}$ and $E_{\rm c}^{\rm GGA}$. There are lots of GGA versions based on different constructions mainly using as many known constraints on the $V_{\rm xc}$. In the present work the functional from Perdew, Burke and Ernzerhof in 1996 (PBE) [18] is almost exclusively used.

# Chapter 3

# (L)APW+lo

From the HK theorems, the electron density determines all system properties. Unfortunately, there is no direct way to obtain the electron density, and it is hard to express the kinetic energy as a functional of the density as well. Therefore, we have to integrate Kohn-Sham wave functions to generate $\rho$ (Eq. 2.12), and insert wave functions into the kinetic potential to get the kinetic energy. In order to convert the corresponding wave function equations into suitably numerically accessible matrix equations, the wave functions and electron densities are expanded into a basis set. Based on the type of basis functions a variety of DFT formulations in numerical codes exist. In this chapter, we will introduce one of the most accurate methods, (L)APW+lo, which is used in the present work.

## 3.1 Bloch's Theorem

The Bloch theorem [20] states that *Any eigenfunction* $\Psi(\mathbf{r})$ *can be written as a product of a function* $\phi_g(\mathbf{r})$ *that has the periodicity of the lattice, and a plane wave* $e^{i\mathbf{g}\cdot\mathbf{r}}$ *with* $\mathbf{g}$ *any vector in reciprocal space,*

$$\Psi(\mathbf{r}) = \phi_{\mathbf{g}}(\mathbf{r})e^{i\mathbf{g}\cdot\mathbf{r}} \quad . \tag{3.1}$$

If the reciprocal vector $\mathbf{g}$ is written as the sum of a vector ($\mathbf{k}$) in the first Brillouin zone and a reciprocal lattice vector $\mathbf{K}$, $\mathbf{g}$=$\mathbf{k}$+$\mathbf{K}$, the Bloch theorem is rewritten as,

$$\begin{aligned} \Psi(\mathbf{r}) \quad = \Psi_{\mathbf{k_n}}(\mathbf{r}) \quad &= \{\phi_{\mathbf{g}}(\mathbf{r})e^{i\mathbf{K}\cdot\mathbf{r}}\}e^{i\mathbf{k}\cdot\mathbf{r}} \\ &= \phi_{\mathbf{k_n}}(\mathbf{r})e^{i\mathbf{k}\cdot\mathbf{r}} \quad , \end{aligned} \tag{3.2}$$

where, $n$ indicates the number of the Brillouin zone where $\mathbf{g}$ is in, and is called *band index.*

The first term in Eq. 3.2 $\phi_{\mathbf{k_n}}(\mathbf{r})$, determines the eigenfunction, $\Psi(\mathbf{r})$. Due to the periodicity of the lattice, the straight idea to get $\phi_{\mathbf{k_n}}(\mathbf{r})$ is to sum over plane waves that have the same periodicity of the lattice. Then,

$$\phi_{\mathbf{k_n}}(\mathbf{r}) = \sum_{\mathbf{K}} c_{\mathbf{K}}^{n,\mathbf{k}} e^{i\mathbf{K}\cdot\mathbf{r}} \quad . \tag{3.3}$$

The expansion of $\Psi_{\mathbf{k_n}}(\mathbf{r})$ becomes,

$$\Psi_{\mathbf{k_n}}(\mathbf{r}) = \sum_{\mathbf{K}} c_{\mathbf{K}}^{n,\mathbf{k}} e^{i(\mathbf{K}+\mathbf{k})\cdot\mathbf{r}} \quad . \tag{3.4}$$

Popular DFT codes like VASP or CASTEP [21] are based on such a plane wave basis sets. Describing the steep potential close to the nuclei (and correspondingly highly oscillating wave functions) is demanding with a pure plane wave basis set, and requires to go to high $\mathbf{K}$ values in Eq. 3.3. When aiming to maintain a full-potential description a suitable approach followed in the (L)APW+lo idea is thus to augment the plane wave basis functions with more localized functions.

## 3.2 Augmented Plane Wave (APW)

Before embarking on the (L)APW+lo method, it is advantageous to discuss the APW method introduced by Slater [22]. Considering the behavior of electrons in space, when electrons are far away from the nuclei, they show the behavior of free electrons, and are then suitably described by plane waves. While close to the nuclei, electrons bind strongly to their nuclei, their behavior is quite as in a free atom and they could be described more efficiently by atomic like functions. Therefore, the whole space can be techniqually divided into two regions, non-overlapping atomic spheres (so-called Muffin-tin (MT) regions) and interstitial (I) region (Fig. 3.1). Correspondingly, the potential in the whole space can be defined as

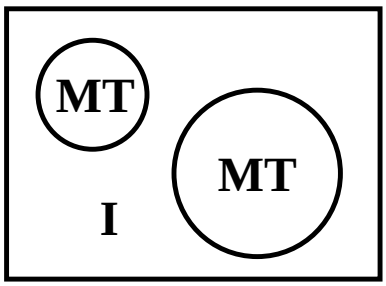


Figure 3.1: Schematic division of space into atomic sphere region (I) and interstitial region (II).

$$V(\mathbf{r}) = \begin{cases} V(\mathbf{r}) & (\mathbf{r} \in \mathrm{MT}) \\ \text{constant} & (\mathbf{r} \in \mathrm{I}) \end{cases} , \tag{3.5}$$

and, two types of basis sets are used in the two different regions,

$$\phi_{\mathbf{k_n}}^{\mathrm{APW}}(\mathbf{r}, \epsilon_l) = \begin{cases} \sum_{lm} A_{lm,\mathbf{k_n}} u_l(r, \epsilon_l) Y_{lm}(\hat{\mathbf{r}}) & (\mathbf{r} \in \mathrm{MT}) \\ \frac{1}{\sqrt{\Omega}} e^{i\mathbf{k_n}\cdot\mathbf{r}} & (\mathbf{r} \in \mathrm{I}) \end{cases} . \tag{3.6}$$

In the atomic spheres (MT), the wave functions are expanded by radial functions times spherical harmonics. $u_l$ is the solution of the radial Schrödinger equation for a spherical potential $[V(r)]$ for energy $\epsilon_l$,

$$-\frac{1}{r^2}\frac{d}{dr}(r^2\frac{du_l}{dr}) + [\frac{l(l+1)}{r^2} + V(r) - \epsilon_l] r u_l = 0 \quad . \tag{3.7}$$

In the interstitial region (I) plane waves are instead used to build the wave function. The coefficients $A_{lm}$ in the atomic sphere expansion are determined by requiring that

the wave functions in the MT and the interstitial regions match each other at the MT boundary [24]. Thus, each plane wave is augmented by an atomic-like function in every atomic sphere and constitutes thus the basis set used to expand the wave function,

$$\Psi(\mathbf{r}) = \sum_n c_n \phi_{\mathbf{k_n}}(\mathbf{r}) \quad . \tag{3.8}$$

The biggest disadvantage in the APW method is that it can not get the eigenvalues from a single diagonalization due to the unknown parameter $\epsilon_l$ in Eq. 3.6. The exact $\epsilon_l$ value, which is what we want to know, is needed to describe the eigenstate $\Psi_{\mathbf{k_n}}(\mathbf{r})$ accurately. Since this energy depends on the function $u_l(r, \epsilon_l)$, the resulting eigenvalue problem is non-linear in energy. One has to set a trial energy for $\epsilon_l$, solve Eq. 3.7 to obtain the APW basis, set up the matrix elements, and compute the determinant $|H - ES|$. If the eigenenergy does not equal $\epsilon_l$, another trial energy must be chosen until the eigenenergy equals $\epsilon_l$. This makes the APW method extremely inefficient.

## 3.3 LAPW

In order to overcome the non-linearity problem in the APW method, Anderson developed the linearized augmented plane wave method (LAPW) [23, 24]. In his idea, the radial function $u_l$ is expanded by a Taylor expansion around $\epsilon_l$,

$$u_l(r, \epsilon_l) = u_l(r, \epsilon_l^1) + (\epsilon_l - \epsilon_l^1)\dot{u}_l(r, \epsilon_l^1) + O((\epsilon_l - \epsilon_l^1)^2) \quad , \tag{3.9}$$

where $\dot{u}_l = \frac{\partial u_l}{\partial \epsilon_l}$. In this case the radial function error is second order, and the energy error is of fourth order [25]. When $\epsilon_l^1$ is set near $\epsilon_l$, the radial function and energy errors are negligible. Substituting Eq. 3.9 into Eq. 3.6, we get the formulation of the LAPW basis set,

$$\phi_{\mathbf{k_n}}^{\mathrm{LAPW}}(\mathbf{r}) = \begin{cases} \sum_{lm}[A_{lm,\mathbf{k_n}} u_l(r, \epsilon_l^1) + B_{lm,\mathbf{k_n}} \dot{u}_l(r, \epsilon_l^1)]Y_{lm}(\hat{\mathbf{r}}) & (\mathbf{r} \in \mathrm{MT}) \\ \frac{1}{\sqrt{\Omega}} e^{i\mathbf{k_n}\cdot\mathbf{r}} & (\mathbf{r} \in \mathrm{I}) \quad . \end{cases} \tag{3.10}$$

In the interstitial region, the basis set is the same as in the APW method, but in the MT spheres, the basis functions not only depend on $u_l$, but also on its energy derivative, $\dot{u}_l$. It is very clear that the LAPW method is thus more flexible than the APW in the MT spheres. To know the exact value for $\epsilon_l$ as in the APW is not important anymore. For a fixed value of $\epsilon_l^1$, the modified basis functions (Eq. 3.9) provide the extra flexibility to cover a large energy region around this linearization energy. In order to determine both $A_{lm,\mathbf{k_n}}$ and $B_{lm,\mathbf{k_n}}$, the functions in the MT spheres are required to match the plane wave function both in value and in slope at the sphere boundary. However, the continuous derivatives require higher plane wave cutoffs to achieve a given level of convergence.

## 3.4 LAPW with Local Orbital (LAPW+LO)

Based on whether or not electrons in an atom participate in the chemical bonding with other atoms, the electrons can be divided into two types. One type of electrons are *core electrons*, which are extremely bound to their nucleus and are thus entirely localized in the MT sphere. The corresponding states are called *core states*. The other type of electrons are *valence electrons*, who are leaking out of the MT sphere and bond with other atoms. However, for many elements, the electrons cannot be clearly distinguished like that. Some states are neither constrained in the core states, nor lie in the valence states and are correspondingly termed *semi-core states*. They have the same angular quantum number $l$ as the valence states but with lower principal quantum number $n$. When applying LAPW on these states, it is thus hard to use one $\epsilon_l^1$ to determine the two *same* $l$ in Eq. 3.10. The dilemma is solved by introducing *local orbitals* (LO), which are defined as

$$\phi_{lm}^{\mathrm{LO}}(r) = \begin{cases} [A_{lm}u_l(r,\epsilon_l^1) + B_{lm}\dot{u}_l(r,\epsilon_l^1) + C_{lm}u_l(r,\epsilon_l^2)]Y_{lm}(\hat{\mathbf{r}}) & (\mathbf{r} \in \mathrm{MT}) \\ 0 & (\mathbf{r} \in \mathrm{I}) \quad . \end{cases} \tag{3.11}$$

Each local orbital is zero in the interstitial region and other atoms' MT sphere. The three coefficients $A_{lm}$, $B_{lm}$ and $C_{lm}$ can be determined by requiring the LO to have both zero value and zero slope at the MT boundary and be normalized.

## 3.5 APW+lo

It has been realized that the standard LAPW method is not the most efficient way to linearize Slater's APW method [27]. Instead, the basis set of the introduced APW+lo [26, 27] method is also energy independent and still has the same basis size as the original APW method. In order to achieve that a new local orbital (lo) is added, which is different from the LOs used to describe semicore states to gain enough variational flexibility in the radial basis functions. The lo definition is,

$$\phi_{lm}^{\mathrm{lo}}(\mathbf{r}) = \begin{cases} [A_{lm}u_l(r,\epsilon_l^1) + B_{lm}\dot{u}_l(r,\epsilon_l^1)]Y_{lm}(\hat{\mathbf{r}}) & (\mathbf{r} \in \mathrm{MT}) \\ 0 & (\mathbf{r} \in \mathrm{I}) \quad . \end{cases} \tag{3.12}$$

The two coefficients $A_{lm}$ and $B_{lm}$ are determined by normalization, and by requiring that the local orbital has zero value at the Muffin-tin boundary. The advantage of the APW+lo method is that it has the same small basis set size as the APW method, and has the same accuracy compared to the LAPW method.

As mentioned by Madsen *et al* [27], it is also possible to use a hybrid basis set, LAPW in combination with APW [(L)APW+lo], and treat the physically important orbitals by the APW+lo method, but the polarization $l$-quantum numbers with LAPW. All the data presented in our work are using this hybrid basis set (L)APW+lo.

## 3.6 Full Potential (L)APW+lo Method

In Eq. 3.5, we supposed the potential is constant in the interstitial region and spherical in the MT region. The accuracy of (L)APW+lo method can be further improved by considering the full potential (FP), and expand it similar to the wave functions,

$$V(\mathbf{r}) = \begin{cases} \sum_{lm} V_{lm}(r) Y_{lm}(\hat{\mathbf{r}}) & (\mathbf{r} \in \text{MT}) \\ \sum_{\mathbf{G}} V_{\mathbf{G}} e^{i\mathbf{G}\cdot\mathbf{r}} & (\mathbf{r} \in \text{I}) \end{cases} , \tag{3.13}$$

This is also called *non-muffin-tin* correction. In this case, the radial function $u_l$ in Eq. 3.7 is not the exact solution inside the MT sphere. It should be evaluated for the true MT potential.

## 3.7 Two Important Basis Set Parameters: Energy Cutoff and K-mesh

In all DFT codes for solid state calculations the energy cutoff ($E_{\text{cut}}$) and k-mesh (or **k**-points) are important basis set parameters to determine the accuracy of the computational results. Both parameters must be tested in DFT calculations in order to find the optimum compromise between accuracy and implied computational burden.

When we use plane waves to construct wave functions, in principle the more plane waves, the better the results are. However, it is not necessary to use infinitely many plane waves to construct the wave function. We can limit the energy cutoff, which describes the number of plane waves used, to an optimum value. The relationship between energy cutoff and plane wave coefficient is,

$$E_{\text{cut}} = \frac{\hbar^2 K_{\text{max}}^2}{2m_{\text{e}}} \quad . \tag{3.14}$$

And the wave function based on $K_{\text{max}}$ is,

$$\psi_{\mathbf{k_n}}(\mathbf{r}) = \sum_{\mathbf{K}}^{\mathbf{K_{max}}} C_{\mathbf{K},\mathbf{k_n}} e^{i(\mathbf{k}+\mathbf{K})\cdot\mathbf{r}} \quad . \tag{3.15}$$

In the FP-(L)APW+lo method this energy cutoff is employed in the interstitial region. Turning to the MT sphere, the spherical harmonics should also be terminated at a maximum $lm$ for the same reason.

The evaluation of the Kohn-Sham equations in a periodic boundary calculation requires many system quantities like the charge density to be integrated over the Brillouin Zone (BZ). Exploring the symmetry of the system, it is more specifically only necessary to integrate over the irreducible part of the Brillouin Zone (IBZ). The integrals are dealt with numerically by summing over a finite number of **k**-points in the IBZ,

$$\int_{\text{IBZ}} \frac{1}{\Omega_{\text{IBZ}}} d\mathbf{k} \rightarrow \sum_{\mathbf{k}} \omega_{\mathbf{k}} \quad . \tag{3.16}$$

Therefore, the denser the k-mesh, the more accurate the integrand is. Similar to $E_{\text{cut}}$, we should also find an optimum k-mesh at which the quantities of interest are converged.

There are two common methods to get **k**-points: The tetrahedron method [28, 29] and the special **k**-points method [30–32]. In our work we use the special **k**-point method according to Monkhorst and Pack [31] throughout. The method generates a uniform **k**-point grid in the full BZ, then uses the space group of the system to rotate the **k**-points into the IBZ, and determine the proper weights, $\omega(\mathbf{k})$, of each special **k**-point by dividing the number of equilibrium **k**-points of a special **k**-point in the BZ by the total number of points in the grid.

In metals, energy bands intersect the Fermi energy. This leads to discontinuities in the occupation and in the integrand on the Fermi surface, and can cause problems with reaching self-consistency due to charge sloshing. We can replace the step function occupation at the Fermi energy with a smoother function, like a Fermi distribution at a finite temperature to solve the problem. After the integration the resulting free energy has then to be extrapolated to $T = 0$ K.

## 3.8 WIEN2k Code

The **WIEN2k** code [33] is based on the FP-(L)APW+lo method. The code can only be applied to systems with periodic boundary conditions and is therefore mainly used for crystal calculations.

The **WIEN2k** code has two main parts (Fig. 3.2). One is the initialization (left part in Fig. 3.2). It is used to check if MT spheres overlap, generate a new structure file according to its space group, detect its symmetry operations, generate a k-mesh in its BZ, and get the input trial density. The other one is the self-consistency cycle (right part in Fig. 3.2). It calculates the potential used in the KS equation, diagonalizes the Hamiltonian and overlap matrices and generates eigenvalues and eigenvectors, integrates all valence states and obtains the valence electron density ($\rho_{\text{val}}$), solves the atomic calculation and gets the core electron density ($\rho_{\text{core}}$), mixes [34] the two electron densities with the old total electron density ($\rho_{\text{old}}$) and gets the new total electron density ($\rho_{\text{new}}$). Thereafter it checks if the properties ($\rho_{\text{new}}$, or $E_{\text{tot}}$, or $F$ ...) of the system are converged, and either stops the self-consistency cycle or starts anew.

Apart from two the main parts, **WIEN2k** has lots of additional packages to evaluate a variety of system properties. This comprises geometry optimization, plotting the density of states (DOS), band structure, electron density, X-ray spectra ...

Two kinds of parallelization modes are implemented in the **WIEN2k** code to increase the calculation efficiency. One is **k**-point parallelization, which distributes the computations for the different irreducible **k**-points over several CPUs. This method is only useful for small calculations and a low communication bandwidth between the CPUs. If we go to big systems with few **k**-points, fine grained parallelization can be additional applied. It diagonalizes the Hamiltonian and overlap matrices for

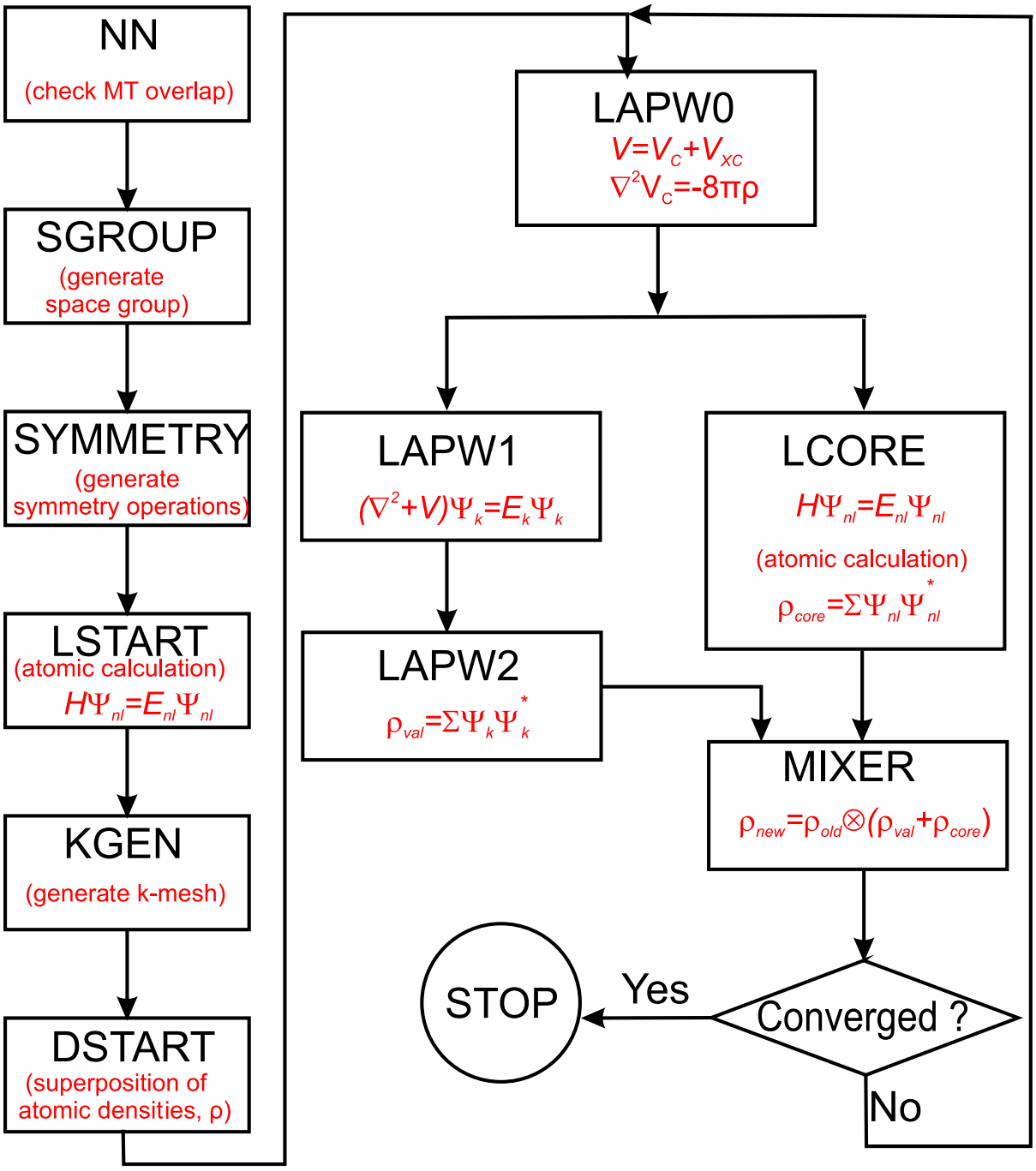


Figure 3.2: Flow chart of the **WIEN2k** code. The left part is the initialization, which is used to get the trial input electron density for starting the self-consistency cycle. The right part is the self-consistency cycle, which is used to converge the electron density.

each **k**-point on different CPUs. The speed of this method strongly depends on the communication between the CPUs, on the number of CPUs and on the matrix size. In order to run the code more efficiently, the **WIEN2k** code can combine the two methods, which separates number of **k**-points on different block of CPUs, and applies the fine grained parallelization on each block of CPUs.

# Chapter 4

# DFT Calculations for Solid Surfaces

Surfaces are generated when we split a bulk crystal. The created surface is the place where molecules from the gas phase or a liquid come into contact with the material. Atoms at the surface will have a lower coordination than those in the bulk. Due to the changed coordination the surface geometry will relax or possibly even reconstruct, to let surface atoms find their new equilibrium positions. For ideal surfaces of cubic crystals, there are two groups, low Miller index (flat) surfaces, (100), (111) and (110) surfaces, and high Miller index (stepped) surfaces. Stepped surfaces can exhibit significantly different properties compared to flat surfaces due to the effect of the defects. In this chapter, we summarize how to construct a stepped surface model within the context of periodic boundary condition electronic structure calculations, and which geometric and electronic structure quantities of surfaces are evaluated in our analysis.

## 4.1 Vicinal Surfaces

Close-packed flat surfaces are generated by cutting a fcc bulk along perfect low Miller index planes, like (100) (left panel in Fig 4.1), (111) or (110) surfaces. Although the investigation of such low-index surfaces can generate a wealth of information on surface properties of materials, they are far away from real surfaces. A real surface exhibits additional features like steps, kinks, or vacancies (Fig. 4.1), which can play an important role for the overall surface properties. It is therefore a key endeavor in current surface science to extend our knowledge toward such defects. In our presented work, we focus on atomic step defects. The role of steps can be particularly suitably studied using *vicinal surfaces*, which exhibit a regular array of steps. Cutting a crystal at a small angle (*miscut angle*) away from a low-Miller-index plane creates such *vicinal surfaces* (Fig. 4.2) (or *stepped surfaces* or *high-Miller-index surfaces*). Vicinal surfaces exhibit atomic terraces with a low-index orientation, and these terraces are separated by either straight or kinked atomic steps.

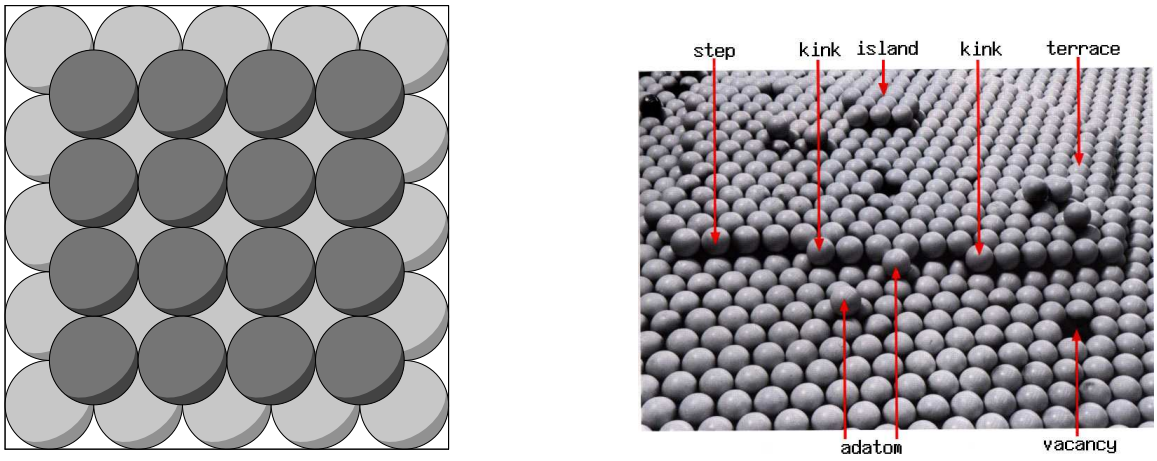


Figure 4.1: Left panel: Top view of a fcc (100) surface (second layer atoms are drawn as light spheres). Right panel: A real surface with steps, kinks, and vacancies.

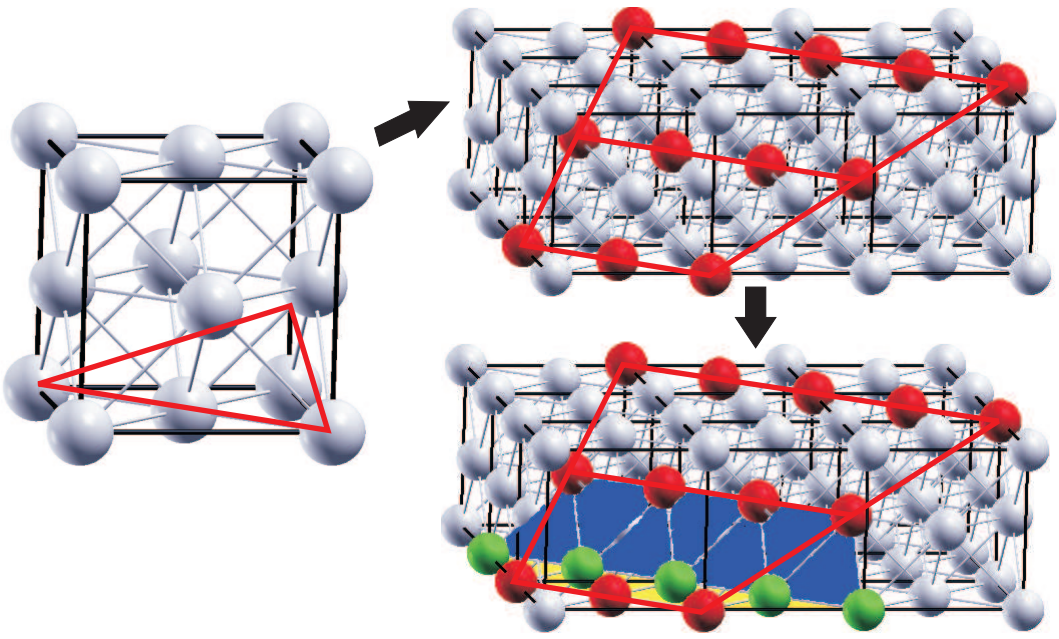

Figure 4.2: Cartoon scheme to create a (113) vicinal surface in a fcc bulk. The left panel is a bulk fcc unit cell. The plane enclosed by red lines is the (113) plane. Expanding the fcc cell 3 times in the x and y directions reveals the (113) plane (top right panel), and atoms on the plane are shown in red color. In the bottom right panel, the yellow plane corresponds to a (100) terrace and the blue one is a (111) step. The green atoms indicate the bottom step edge. The (113) plane can therefore be viewed as two atomic row wide (100) terraces and (111) atomic steps.

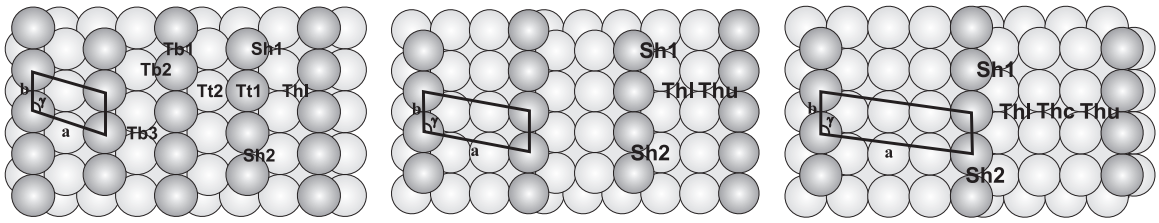


Figure 4.3: Top view of the family of Pd(11$N$) vicinal surfaces, Pd(113), Pd(115) and Pd(117) (from left panel to right panel). Based on the GGA-PBE bulk fcc Pd lattice constant (3.947 Å), the value of $b$ is same in the three cells, 2.79 Å, and $a$ and $\gamma$ are 4.83 Å and $106.79^0$ for Pd(113), 7.38 Å and $100.89^0$ for Pd(115), and 10.06 Å and $97.97^0$ for Pd(117), respectively. The additional nomenclatures will be discussed in Chapter 7.

In our work, we focus on Pd(11$N$) ($N$=3, 5, 7) vicinal surfaces (Fig. 4.3), which can be built in the way described in Fig. 4.2. The family of Pd(11$N$) ($N$=3, 5, 7) vicinal surfaces (top view in Fig. 4.3 and side view in Fig. 7.1) has a similar geometric structure, exhibiting (111) steps and (100) terraces of varying width. There are 2, 3 and 4 atomic rows on the (100) terraces of Pd(113), Pd(115) and Pd(117), respectively. The relationship between the Miller indices of these Pd(11$N$) vicinal surfaces and their constituent low-index micro-facets becomes clear from the vector decomposition $(11N)=n_{\mathrm{row}}\times(002)+1\times(11\bar{1})$, ($N=2n_{\mathrm{row}}-1$, $n_{\mathrm{row}}$=2, 3, 4...), where $n_{\mathrm{row}}$ is the number of atomic rows on the (100) terraces. ($(002)\equiv(100)$ and $(11\bar{1})\equiv(111)$ in cubic symmetry). From the $(1\times1)$ surface unit cells of the different vicinal surfaces, Pd(11$N$) ($N$=3, 5, 7) indicated in Fig. 7.1, the surface unit cell becomes larger and larger, and the interlayer spacing becomes smaller and smaller with increasing $N$. Moreover, the larger the surface unit cell, the smaller the atomic density is, and the more open the surface is.

## 4.2 Surface Models

For surface simulations, there are different models that can be used, most notably the cluster model and the supercell model. Cluster models treat the surface as a small isolated cluster of atoms, one facet of which has the same symmetry and atomic arrangement as the crystal surface intended to study. This model is useful for materials with more localized wavefunctions, such as insulators like MgO [35]. For metal surfaces with de-localized valence wavefunctions, however, it is not suitable, and the supercell model (Fig. 4.4) including slabs and vacua is the more efficient choice. The slab in the supercell is infinite and periodic in the directions parallel to the surface, but finite in the direction perpendicular to the surface.

Such a setup thus enables band formation with the correct dispersions. Two important things should be kept in mind using a supercell model: The vacuum thickness should be large enough to avoid surfaces of consecutive slabs seeing each other, and

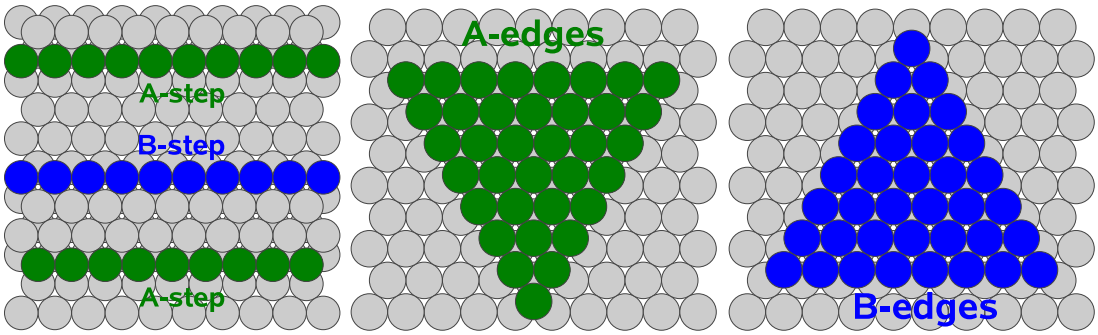


Figure 4.5: Left panel: Striped islands on a fcc(111) surface. The stripes and the valleys between them are both four atomic rows wide. The islands are necessarily bounded by an A (100) (green) and a B (111) (blue) step. Middle and right panels: Two types of triangular islands on an fcc(111) surface, exhibiting (100) (green) and (111) (blue) steps.

the thickness of the slab should also be thick enough to avoid interaction between the two surfaces of one slab. This normally also ensures that the middle layer of the slab exhibits bulk-like properties.

There are three methods to build stepped surfaces in the supercell approach. The first one is a *striped surface* (Fig. 4.5) [38]. Striped surfaces are $(n+1)$ layers thick in cross section through the stripe islands and $n$ layers thick through the trenches in between. On such a striped surface, the disadvantage is that there are necessarily (100) and (111) steps simultaneously present at the two sides of one stripe. The second method to build a stepped surface is via *triangular islands* on the surface (Fig. 4.5) [39]. Such structures contain only one kind of either (100) or (111) steps around each island. This method is useful to differentiate the small energy differences in step formation of (111) and (100) steps, but contains the effect of the step facet edges of the triangle. The third method is via a *slab vicinal surface* as illustrated in Fig. 4.4 and Fig. 7.1. Here, the slab is constructed from the corresponding high Miller-index plane layer by layer. Such a setup allows the investigation of long-range step-step interactions, and also exhibits only one type of step. Additionally, the surface unit cell size is modest. On the other hand, due to the sheared orientation of the supercell, particular care has to be taken to ensure proper **k**-point sampling (Appendix C). The slab vicinal surface model to investigate the properties of vicinal surfaces is used in our study.

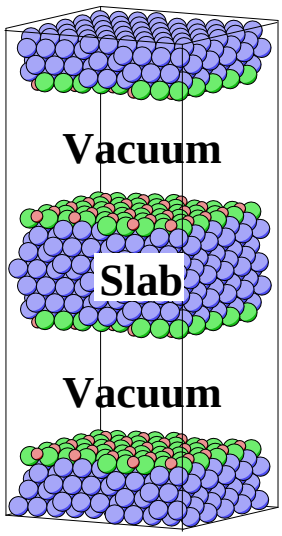


Figure 4.4: Supercell model, including slabs and vacuum.

## 4.3 Surface Minimization

In surface science surfaces are often classified into three kinds: ideal bulk-truncated surfaces, relaxed surfaces and reconstructed surfaces, depending on how they differ from the same planar termination in the bulk. Assuming cleavage of the crystal does not perturb the remaining material at all and the geometrical arrangement of surface atoms is the same as the bulk termination, a surface is called an *ideal surface*. At a metal surface, the electrons are free to rearrange their distribution in space to lower their kinetic energy (Smoluchowski smoothing [44, 45]), which leads to a net force on the ions. The ensuing movement of the atoms in the surface fringe is called *surface relaxation*. If the atomic movement leads even to a change in the symmetry and size of the surface unit cell (*e.g.* through changing bonds), one talks about *surface reconstruction*. Relaxation changes thus only interlayer spacings, while the surface unit cell does not change at all. Neither flat Pd surfaces, nor Pd($11N$) vicinal surfaces are known to reconstruct so far. Therefore, we focus on the varying interlayer spacings as resulting from surface relaxation,

$$\Delta d_{ij} = 100 \times (d_{ij} - d_{\mathrm{b}})/d_{\mathrm{b}} \quad , \tag{4.1}$$

where $d_{\mathrm{b}}$ is the bulk interlayer spacing, and $d_{ij}$ is the interlayer spacing between layers $i$ and $j$ ($i$ and $j$ are the surface layer numbers) after relaxation. With the sign convention behind Eq. 4.1, a minus sign indicates interlayer spacing contraction, while a plus sign indicates expansion. In addition to the varying interlayer spacing, there can be atomic displacements from the bulk position parallel to the surface. Such *registry relaxations* [36], $\Delta r_{ij}$, are defined similar to the interlayer relaxation perpendicular to the surface as,

$$\Delta r_{ij} = 100 \times (r_{ij} - r_{\mathrm{b}})/r_{\mathrm{b}} \quad , \tag{4.2}$$

here, $r_{\mathrm{b}}$ and $r_{ij}$ are the distance between the positions of two atoms in different layers ($i$ and $j$) projected onto the surface plane, before and after surface relaxation, respectively. In the registry relaxation, a minus sign means atoms of neighboring layers try to approach each other compared to their bulk distance, while a plus sign means that atoms go further away from each other.

For finding the equilibrium positions of atoms, the PORT minimization method [46], *a reverse-communication trust-region quasi-Newton method* from the Port library, was used to relax the atomic positions. Almost all geometry optimization approaches base on a harmonic approximation, in which the total energy can be expanded near the minimum as,

$$E = E(\mathbf{R}^*) - \mathbf{F}(\mathbf{R}^*) \cdot (\mathbf{R} - \mathbf{R}^*) + \frac{\mathbf{1}}{\mathbf{2}}(\mathbf{R} - \mathbf{R}^*) \cdot \mathbf{H}(\mathbf{R}^*) \cdot (\mathbf{R} - \mathbf{R}^*) \quad , \tag{4.3}$$

where $E$ is the predicted energy for taking a step $\Delta\mathbf{R}$ ($\Delta\mathbf{R}$=$\mathbf{R} - \mathbf{R}^*$) from the current point, $E(\mathbf{R}^*)$ and $\mathbf{F}(\mathbf{R}^*)$ are the energy and force calculated at the current point and

$\mathbf{H}(\mathbf{R}^*)$ is the Hessian matrix. The most straightforward approach is steepest descent, which takes $\mathbf{H}(\mathbf{R}^*)$ as a unitary matrix and takes a step along the direction of the force,

$$\mathbf{F}(\mathbf{R}) = \mathbf{F}(\mathbf{R}^*) - \mathbf{H}(\mathbf{R}^*) \cdot \mathbf{\Delta R} \quad . \tag{4.4}$$

Looking for the minimum of total energy $E$ means searching for a zero of this force. Hence, we have

$$\mathbf{\Delta R} = \mathbf{H^{-1}}(\mathbf{R}^*) \cdot \mathbf{\Delta F}(\mathbf{R}), \quad (\mathbf{\Delta F}(\mathbf{R}) = \mathbf{F}(\mathbf{R}^*) - \mathbf{F}(\mathbf{R})) \quad . \tag{4.5}$$

The left side indicates the finite step $\mathbf{\Delta R}$ which points to the minimum provided the inverse Hessian matrix and quadratic approximation of $E$ are exact. The most important method to investigate this information is the Broyden-Fletcher-Goldberg-Shanno (BFGS) method [47]. The method iteratively builds up an approximation of $\mathbf{H^{-1}}(\mathbf{R}^*)$ by making use of the forces obtained during previous steps of the structure minimization. This Hessian matrix must remain positive definite in order to guarantee that $E(\mathbf{R})$ deceases as we move into the direction $\mathbf{\Delta R}$. If the step $\mathbf{\Delta R}$ is too large, *i.e.* $E(\mathbf{R})$ is increasing, one has to backtrack trying a smaller step along the same direction to get a lower total energy. The minimization process terminates when all atomic forces for a geometry fall below a certain target value.

However, away from the minimum the true Hessian is not necessarily well approximated by this procedure. If the approximated Hessian is not positive definite, the solution to Eq. 4.5 may even be in the uphill direction and the update procedure can go badly wrong. To circumvent this we can rewrite the Eq. 4.4 as,

$$(\mathbf{R} - \mathbf{R}^*)^{\mathbf{T}} \cdot \mathbf{\Delta F}(\mathbf{R}) = (\mathbf{R} - \mathbf{R}^*)^{\mathbf{T}} \cdot \mathbf{H}(\mathbf{R}^*) \cdot (\mathbf{R} - \mathbf{R}^*) \quad . \tag{4.6}$$

If $\mathbf{H}$ is positive definite, the right-hand side is positive, $(\mathbf{R}-\mathbf{R}^*)^{\mathbf{T}} \cdot \mathbf{H}(\mathbf{R}^*) \cdot (\mathbf{R}-\mathbf{R}^*) > \mathbf{0}$. This is called the *curvature condition*. If instead $(\mathbf{R} - \mathbf{R}^*)^{\mathbf{T}} \cdot \mathbf{H}(\mathbf{R}^*) \cdot (\mathbf{R} - \mathbf{R}^*) < \mathbf{0}$ at some stage, precautions have to be taken to prevent the approximated Hessian to become wrong. The PORT method includes such a curvature condition judgment.

Moreover, moving a full step $\mathbf{\Delta R}$ is often not appropriate; it may be too large. One approach would be to search along the direction of $\mathbf{\Delta R}$, but this can be inefficient since it would involve many calculations along a single direction. An alternative approach is to use what is called *Trust-Region* method. Here one calculates the best step for a quadratic model with the current approximation for the Hessian with the additional constraint that $\|\mathbf{\Delta R}\| \leq \mathbf{R}$, where $\mathbf{R}$ is the trust region radius. If a good step is chosen, the current approximation for the Hessian is good and it is safe to increase the radius; if the step is poor (the total energy increases) the radius is decreased. In one word, PORT is still a BFGS type minimization method but with curvature condition and trust region. In the **WIEN2k** code the PORT minimization method is strongly recommended, and for our purposes it proved to be stable, efficient and did not depend too much on the users input. In our surface simulations, the middle layer in the slab is fixed during relaxation procedure, and the remaining layers are fully relaxed until each force component of each atom decreases below 5 mRy/a.u (1 mRy/a.u=7.20 meV/Å).

## 4.4 Two Key Surface Energetic Properties: $\gamma$ and $E_\mathrm{b}$

The surface relaxation we just described minimizes the forces on the atoms. Energetically, this relaxation process is suitably characterized by the surface energy per unit area, $\gamma$ [37]. (For simplicity, it is often just named *surface energy* though.) It is defined as the surface excess free energy per area of a particular crystal facet. The total energy of a surface is,

$$E = TS - pV + \mu N + \gamma A \quad . \tag{4.7}$$

Since $\gamma$ denotes the cost connected with creating the surface, the most stable surface will minimize $\gamma$. In this respect, it also determines the equilibrium shape of a crystal (Wulff construction [40, 41]), or plays a key role in faceting, roughening, crystal growth phenomena, or surface segregation in binary alloys. Most of the experimental data on absolute surface energies [42] comes from surface tension measurement in the liquid phase extrapolated to zero temperature. This procedure includes a rather large degree of uncertainty and corresponds furthermore to an isotropic crystal.

Using a supercell model containing slabs with two equivalent surfaces (*i.e.* a crystal with inversion symmetry), the surface energy, $\gamma$ at $T = 0$ K of a clean surface, can then be calculated as,

$$\gamma = \frac{1}{2A}(E^\mathrm{total}_\mathrm{slab} - N_s E^\mathrm{total}_\mathrm{bulk}) \quad . \tag{4.8}$$

where $E^\mathrm{total}_\mathrm{slab}$ and $E^\mathrm{total}_\mathrm{bulk}$ are the total energy of the slab and the total energy of a bulk atom, respectively. $N_s$ is the number of atoms in the slab, $A$ is the surface unit area, and the factor $\frac{1}{2}$ is used because the slab has two surfaces.

When atoms or molecules adsorb at surfaces, created bonds with the surface will release energy. The total energy component of this formation energy is called *binding energy*, $E_\mathrm{b}$, which is a function of coverage and distribution of the adsorbates at the surface. In the case of oxygen adsorption, it is written as,

$$E_\mathrm{b} = -\frac{1}{N_\mathrm{O}}\left[E^\mathrm{total}_\mathrm{O/slab} - E^\mathrm{total}_\mathrm{slab} - \frac{N_\mathrm{O}}{2}E^\mathrm{total}_\mathrm{O_2(gas)}\right] \quad . \tag{4.9}$$

Here $N_\mathrm{O}$ is the total number of adsorbed O atoms, $E^\mathrm{total}_\mathrm{O/slab}$, $E^\mathrm{total}_\mathrm{slab}$, and $E^\mathrm{total}_\mathrm{O_2(gas)}$ are the total energies of the surface containing oxygen, of the corresponding clean surface, and of an isolated oxygen molecule, respectively. Since a free $O_2$ molecule is thus used as the zero reference for $E_\mathrm{b}$, a positive binding energy indicates that the dissociative adsorption of $O_2$ is exothermic at $T = 0\,\mathrm{K}$. To obtain the total energy of the isolated $O_2$ molecule, we exploit the relation $E^\mathrm{total}_\mathrm{O_2(gas)} = 2E^\mathrm{total}_\mathrm{O(atom)} - D$, where $E^\mathrm{total}_\mathrm{O(atom)}$ is the total energy of an isolated oxygen atom, and $D$ is the theoretical $O_2$ binding energy. The isolated O atom is then calculated spin-polarized, inside a rectangular cell of side lengths $(12 \times 13 \times 14)$ bohr, $\Gamma$-point sampling of the Brillouin zone and without

spherically averaging the electron density in the open valence shell. For $D$ we employ the previously published ultra-converged GGA-PBE value of 6.202 eV. [96] Compared to the experimental binding energy of 5.12 eV [110], this value shows the well-known, substantial GGA-induced error. With this value Eq. 4.9 can be rewritten as,

$$E_{\mathrm{b}} = -\frac{1}{N_{\mathrm{O}}}(E^{\mathrm{total}}_{\mathrm{O/slab}} - E^{\mathrm{total}}_{\mathrm{slab}}) + (E^{\mathrm{total}}_{\mathrm{O(atom)}} - 3.101\,\mathrm{eV}) \quad . \tag{4.10}$$

## 4.5 Step Formation Energy

The change in the $T = 0$ K surface energies of vicinal surfaces compared to the corresponding terrace surface energies reflects the additional cost due to the atomic steps at the surface. This cost can be expressed by the so-called *step formation energy* [48, 49]. Consider a vicinal surface (Fig. 4.6) exhibiting a periodic succession of terraces with equal widths, separated by steps of monoatomic height. The step energy density (step formation energy per unit length) $\bar{\beta}$ of the vicinal surface is defined by the equation:

$$\bar{\beta} = \beta(\mathbf{n})b - \beta(\mathbf{n_0})s \quad . \tag{4.11}$$

So,

$$\begin{aligned} \beta(\mathbf{n}) &= \beta(\mathbf{n_0})\frac{s}{b} + \frac{\beta(\theta)}{b} \\ &= \beta(\mathbf{n_0})\cos\theta + \bar{\beta}\sin\alpha/h \quad , \end{aligned} \tag{4.12}$$

where $\beta(\mathbf{n})$ and $\beta(\mathbf{n_0})$ is the surface energy (per unit length) of the vicinal surface and the flat terrace surface, respectively. This equation yields the surface energy of vicinal surfaces in terms of the step energy density $\bar{\beta}$. On the other hand, it is useful to consider the step formation energy $E_{\mathrm{step}}$ per step atom rather than the energy density $\bar{\beta}$, $E_{\mathrm{step}} = \bar{\beta}a_0$. Then Eq. 4.12 can be rewritten as,

$$\begin{aligned} E_{\mathrm{step}} &= (\beta(\mathbf{n}) - \beta(\mathbf{n_0})\cos\theta)\frac{a_0 h}{\sin\theta} \\ &= (\beta(\mathbf{n}) - \beta(\mathbf{n_0})\cos\theta)a_0 b \\ &= \gamma_{\mathrm{vicinal}}(\mathbf{n}) - (n_{\mathrm{row}} - 1)\beta(\mathbf{n_0})\mathbf{a_0}\mathbf{b_0} \\ &= \gamma_{\mathrm{vicinal}}(\mathbf{n}) - (n_{\mathrm{row}} - 1)\gamma_{\mathrm{terrace}}(\mathbf{n_0}) - f\gamma_{\mathrm{terrace}}(\mathbf{n_0}) \quad , \end{aligned} \tag{4.13}$$

where $\gamma_{\mathrm{vicinal}}(\mathbf{n})$ and $\gamma_{\mathrm{terrace}}(\mathbf{n_0})$ are the surface energies per atom of the vicinal surface and flat surface, respectively. $n_{\mathrm{row}}$ is the number of atomic rows at terraces. The additional term, $f\gamma_{\mathrm{terrace}}(\mathbf{n_0})$, is a correction for the fact that the step may not rise at a right angle from the terrace. $f$ is a geometrical factor explained in Fig. 4.6. The values for $f$ on different vicinal surfaces can be found in ref. [48]; $f$=1/2 for the ideal vicinal Pd(11$N$) surfaces, $n_{\mathrm{row}}$(100)+(111).

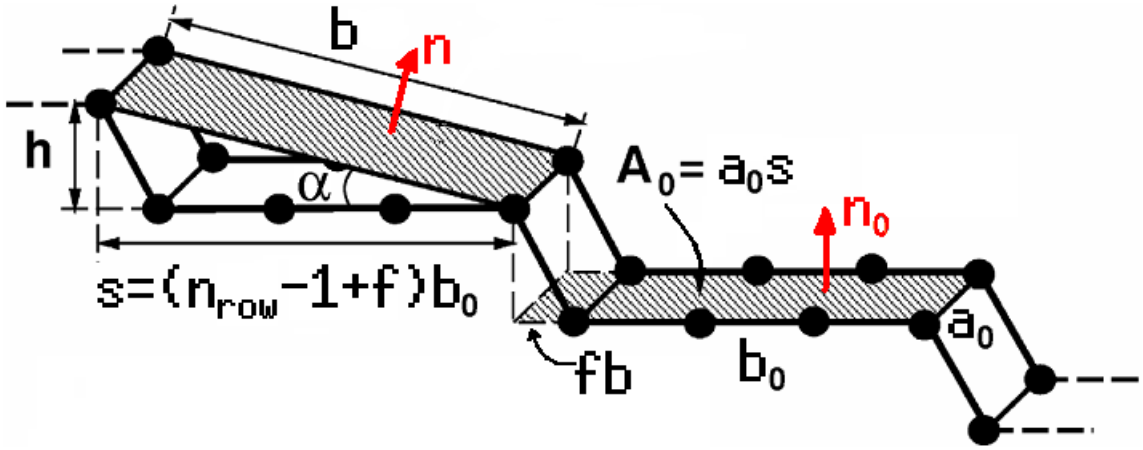


Figure 4.6: Model explaining the geometrical view behind Eq. 4.13. $\mathbf{n}$ and $\mathbf{n}_0$ are the directions normal to the vicinal surface and to the terraces, respectively. $b$ is the distance between two consecutive steps, $b_0$ is the distance between two consecutive atomic rows in a terrace. $a_0$ is the unit along the step edge. $\alpha$ is the miscut angle and $n_{\text{row}}$ is the number of atomic rows, $f$ is a geometrical factor depending on the vicinal surface and $h$ is the height of the steps.

## 4.6 Local Density of States (LDOS)

The local density of electronic states (LDOS), which is the number of electronic states within energy between $E$ and $E + dE$, is an important quantity to analyze the electronic structure. It is defined as,

$$n(\mathbf{r}, \epsilon) = \sum_{i=1}^{\infty} |\varphi_i(\mathbf{r})|^2 \delta(\epsilon - \epsilon_i) \quad , \tag{4.14}$$

where $\varphi_i(\mathbf{r})$ is the single-particle eigenfunction of the Kohn-Sham Hamiltonian, and $\epsilon_i$ is the corresponding eigenvalue. The LDOS exhibits system properties, such as the valence band, conduction band, Fermi energy, bonding region, *etc.* Based on that, we can determine whether the system is a metal, or insulator or semiconductor. In the LAPW method, the muffin-tin sphere is a convenient *local* region to calculate the LDOS of different states projected onto the different atoms. Fig. 4.7 shows the correspondingly computed LDOS of fcc bulk Pd. The valence $d$-band is nicely discerned and the Fermi-level falls at the upper edge, indicating the high filling characteristic for this late transition metal (TM).

## 4.7 Surface Core-level Shifts

Apart from the LDOS, surface core-level shifts (SCLS) [50] are another important quantity that can be used to investigate the electronic structure of surfaces. Although the core orbitals do not take part in the bonding, they are affected by changes in the

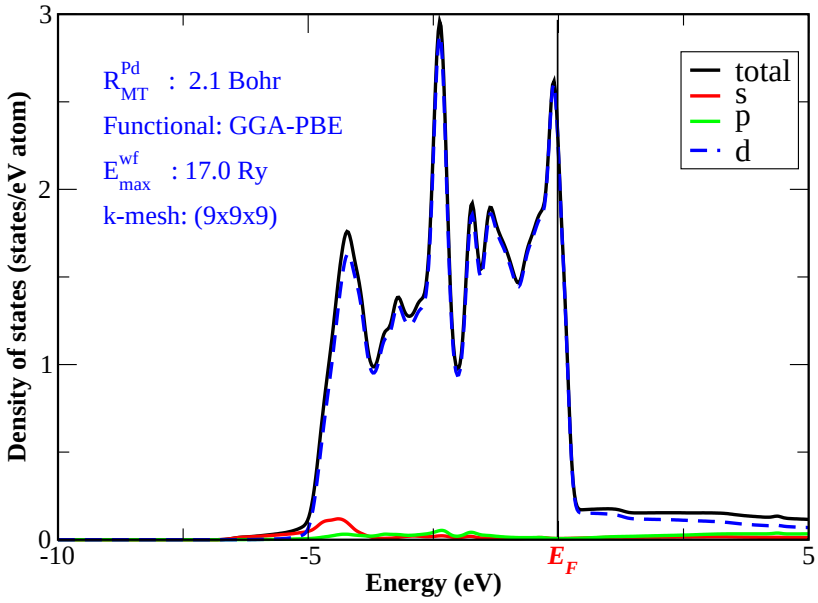


Figure 4.7: Local density of states of bulk fcc Pd (projected onto $s$, $p$ and $d$ atomic orbitals). $s$ and $p$ orbitals have a very small contribution to the total valence DOS, while the Pd $4d$ band is clearly visible. The Fermi level is at its upper end of this band, reflecting the position of Pd in the periodic system of elements.

atomic environment, and as such the core level energies are sensitive local probes of changes in the electronic structure in different environments. Core level energies can be measured for both clean and adsorbate-covered surfaces by high resolution core-level photoemission spectroscopy [52]. The SCLS [51], $\Delta^{\mathrm{SCLS}}$, is defined as the difference in energy that is needed to remove a core electron either from the surface or from a bulk atom,

$$\Delta^{\mathrm{SCLS}} = [E_{\mathrm{surface}}(n_c - 1) - E_{\mathrm{surface}}(n_c)] - [E_{\mathrm{bulk}}(n_c - 1) - E_{\mathrm{bulk}}(n_c)] \quad , \tag{4.15}$$

where $E_{\mathrm{surface(bulk)}}(n_c)$ is the total energy of the system considered as a function of the number of electrons $n_c$ in a particular core level $c$ of a surface or bulk atom, respectively. In DFT calculations, we can rewrite Eq. 4.15 approximately as,

$$\Delta^{\mathrm{SCLS}}_{\mathrm{initial}} = [\epsilon^c_{\mathrm{bulk}} - \epsilon^F_{\mathrm{bulk}}] - [\epsilon^c_{\mathrm{surface}} - \epsilon^F_{\mathrm{surface}}] \quad , \tag{4.16}$$

where, $\epsilon^c_{\mathrm{surface(bulk)}}$ is the KS eigenvalue of the core level $c$ in the surface and bulk, respectively. $\epsilon^F_{\mathrm{surface(bulk)}}$ is the Fermi level in the surface and bulk, respectively. In this SCLS approximation, $\Delta^{\mathrm{SCLS}}_{\mathrm{initial}}$ is one contribution to the measurable SCLS in x-ray photoemission spectroscopy (XPS), where the latter comprises in addition also the screening contribution of the valence electrons in response to the created core hole [50]. For a meaningful comparison with the experimental data, a total SCLS taking

both initial and final state screening effects into account must be used. However, it is not so much this connection to an experimentally accessible quantity that makes us interested in the initial-state SCLS in this work, but rather that the $\Delta^{\mathrm{SCLS}}_{\mathrm{initial}}$ are a very sensitive probe of changes in the local electronic structure of an atom in different environments, which is why we mostly content ourselves here with focusing on the $\Delta^{\mathrm{initial}}_{\mathrm{SCLS}}$ of the $3d$ Pd core level.

In Fig. 4.9, one can see for both clean Pd(111) and Pd(100) that the $4d$ band of the first layer atoms is narrower than those of the deeper lying surface layers. This can be rationalized as follows: The width of the band depends on the overlap or hybridization of orbitals with orbitals from neighboring atoms. The higher the coordination, the more overlap and the broader the band. The reduced coordination of the surface atoms leads therefore to a narrowing of the valence $d$-band. Moreover, because the total number of valence states must be conserved, the narrowed LDOS is enhanced around the Fermi level. In order to keep local charge neutrality, the Pd $d$-band is therefore also slightly shifted to a higher energy (Fig. 4.8), which induces a positive surface potential shift $[\Delta V(r) = V_{\mathrm{surface}}(r) - V_{\mathrm{bulk}}(r)]$ [51, 53]. Since $\Delta V(r)$ is related with the initial-state SCLS ($\Delta$): $\Delta_{3d} \approx -\int dr \Delta V(r) r^2 |R_{3d}(r)|^2$, the changed potential acting on the Pd surface atom $3d$ core levels generates a negative initial surface core level shift. This would be reversed for surface atoms in an early TM (less than half full $d$ band), where the surface potential shift is negative and a positive $3d$ initial-state surface core level shift is induced. The computed initial-state surface core level shift of the $3d$ level is $-0.39$ eV and $-0.50$ eV for the outermost layer of Pd(111) and Pd(100) (with GGA-PBE), respectively. They are therewith much larger than those of the other deeper lying layers, which are nearly zero. Both the LDOS and the SCLS reflect therefore the efficient metallic screening behavior of Pd: Only the first layer atoms are largely affected by the changed coordination and exhibit correspondingly significantly changed parameters. These changes are rapidly screened away by the mobile conduction electrons deeper inside the crystal, and already the 2nd and lower layer atoms approach properties virtually indistinguishable from the ones of bulk atoms. The LDOS of the middle layer atoms in the slab is correspondingly already quite similar to the bulk LDOS (Fig. 4.7).

In additional to the initial SCLS, we need to compute the total SCLS including the final SCLS contribution for comparing with the experimental value. We already know that the final SCLS is induced by the valence screen effect on the creating core in the core level. The screen effect in the energy different in Eq. 4.15 can be determined by the mean value theorem of integration [51],

$$E(n_c - 1) - E(n_c) = \int_{n_c}^{n_c - 1} \frac{\partial E(n')}{\partial n'} dn' \approx -\epsilon_c (n_c - 1/2) \quad . \tag{4.17}$$

In order to implement the final state effect by the DFT calculation, we ionize the interesting core level of atoms by moving 1/2 electron from the core to the valence band.

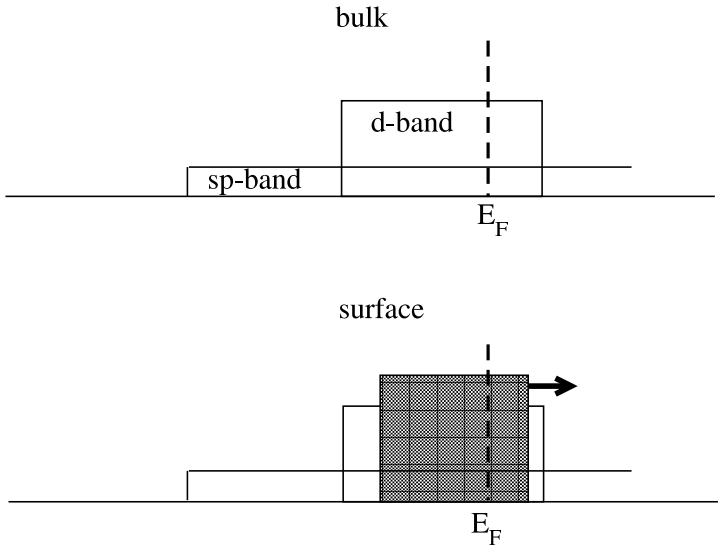


Figure 4.8: Cartoon using the rectangular $d$-band model to illustrate the $d$-band surface shift in late TM (more than half full $d$ band). In order to maintain the same number of occupied states up to $E_F$, the narrowed surface band (dash shading) shifts up in energy.

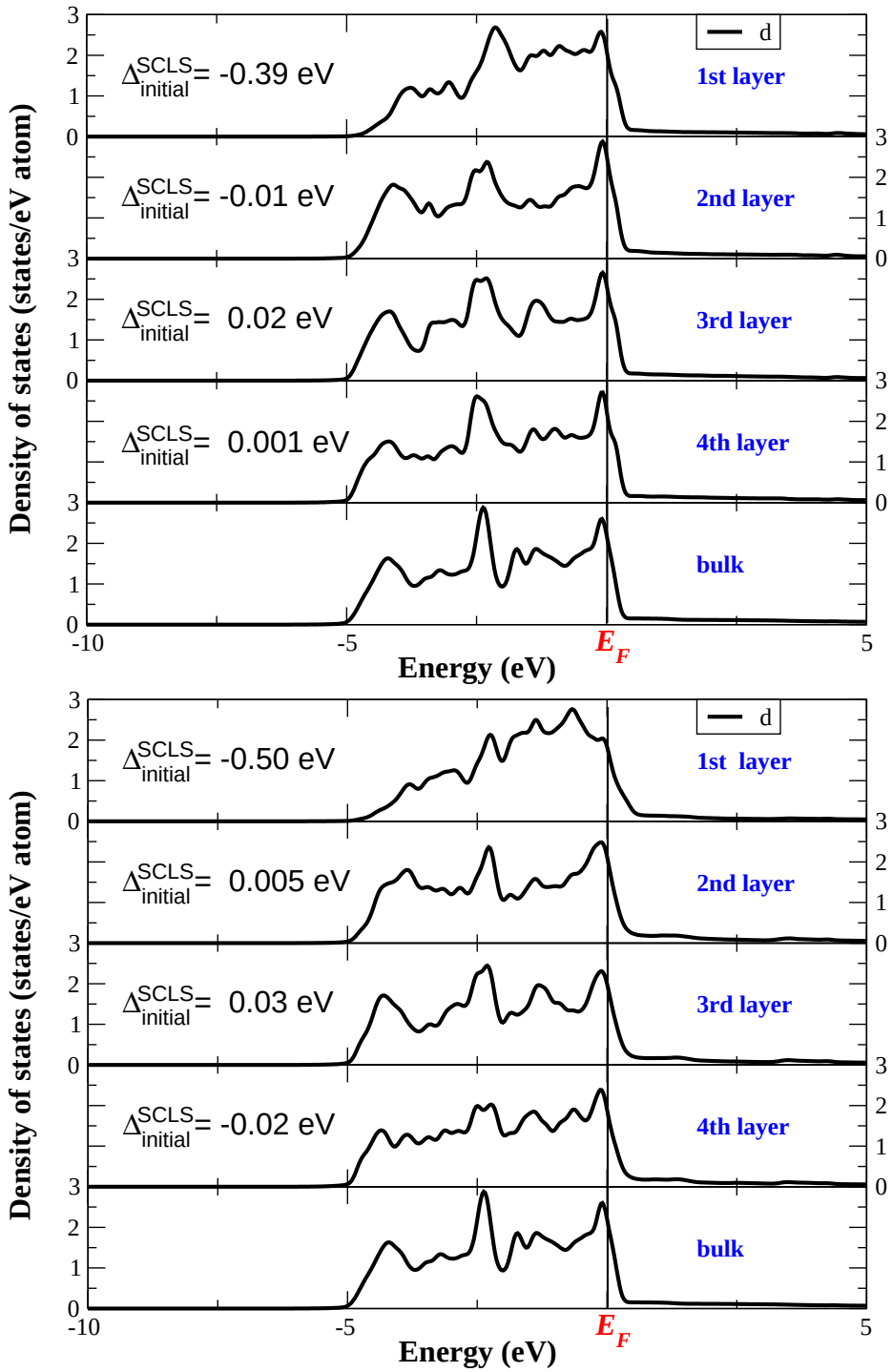


Figure 4.9: Local density of states of different layers for Pd(111) [top panel] and Pd(100) [bottom panel]. The LDOS of the outermost layer is significantly narrower than those of the other layers, while the LDOS of the middle layer is already similar to the bulk DOS. Additionally shown are the $3d$ initial-state surface core level shifts $\Delta^{\mathrm{SCLS}}_{\mathrm{initial}}$ of the corresponding layers.

# Chapter 5

# First-principles Statistical Mechanics

DFT has proven to be a useful tool to investigate the electronic structure of materials. However, it provides only the total energy and is thus not directly applicable to situations at finite temperature [54]. Moreover, due to the unfortunate scaling of DFT, the accessible system sizes are limited. One would therefore often like to separate off large, but homogenous parts of the system and treat them only as reservoirs. For these cases, a suitable approach is first-principles statistical mechanics in which DFT is combined with concepts from thermodynamics or statistical mechanics. We will use such approaches in this work to account for the effect of realistic gas-phases with pressures of the order of atmospheres and elevated temperatures (*ab-initio thermodynamics* [55, 57, 58]), and to account for the effect of configurational entropy in the adsorbate ensemble (*ab-initio statistical mechanics*).

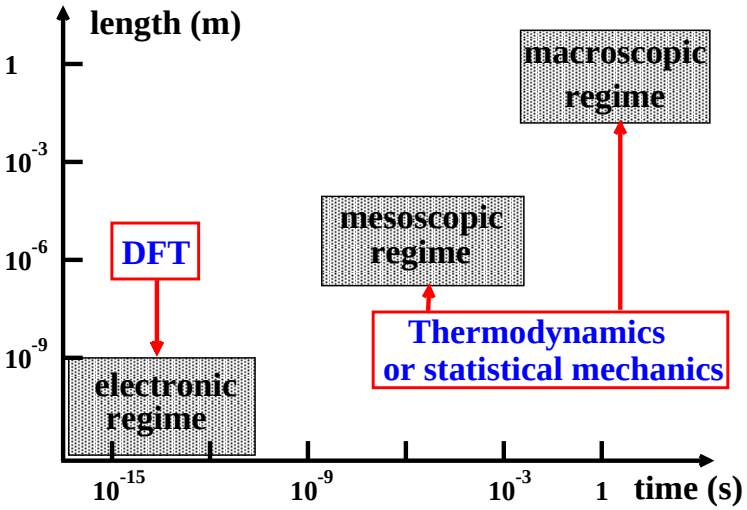


Figure 5.1: Schematic view of three regimes in the (length,time) space and methods used to simulate the corresponding regimes. The molecular processes occur in the *electronic regime*, whereas their statistical interplay develops in the *mesoscopic* and *macroscopic* regime.

## 5.1 Ab-initio Atomistic Thermodynamics

The total energies obtained by DFT correspond to the Helmholtz free energy at $T = 0$ K and neglecting the zero-point energy (ZPE). The effect of temperature and the ZPE can be drawn from calculating the potential energy surface (PES) at different atomic positions. A finite gas-phase pressure can be considered by assuming the surface to be in equilibrium with a reservoir exhibiting the appropriate thermodynamic potential.

If we correspondingly extend the surface energy definition of Eq. 4.8, we obtain the surface energy for oxygen adsorption at Pd surfaces in the $(T, p)$ ensemble. Substituting the Gibbs free energy definition $G(T, p) = E - TS + pV$ into Eq. 4.7, we get

$$\gamma = \frac{1}{2A}(G_{\mathrm{O/Pd(slab)}}(T,p) - N_{\mathrm{Pd}}\mu_{\mathrm{Pd}} - N_{\mathrm{O}}\mu_{\mathrm{O}}) \quad , \tag{5.1}$$

where $\mu_{\mathrm{Pd}}$ and $\mu_{\mathrm{O}}$ are the chemical potentials of Pd and oxygen atoms, respectively. $N_{\mathrm{Pd}}$ and $N_{\mathrm{O}}$ are the number of Pd and O atoms in the adsorption system, respectively. The area $A$ and the factor $1/2$ have the same meaning as in Eq. 4.8. Assuming the surface to be in equilibrium with the underlying metal bulk, $\mu_{\mathrm{Pd}}$ is determined by the Pd bulk atoms. The vibrational entropic and $pV$ terms in this bulk Gibbs free energy and the surface Gibbs free energy are rather similar. We therefore approximate the difference between these two quantities entering Eq. 5.1 by their leading total energy terms: $(G_{\mathrm{O/slab}}(T,p) - N_{\mathrm{Pd}}\mu_{\mathrm{Pd}}) \approx (E^{\mathrm{total}}_{\mathrm{O/slab}} - N_{\mathrm{Pd}}E^{\mathrm{total}}_{\mathrm{bulk}})$, and then arrive at,

$$\gamma = \frac{1}{2A}(E^{\mathrm{total}}_{\mathrm{O/Pd(slab)}} - N_{\mathrm{Pd}}E^{\mathrm{total}}_{\mathrm{bulk}} - N_{\mathrm{O}}\mu_{\mathrm{O}}) \quad . \tag{5.2}$$

Subtracting the surface energy of the clean surface, and supposing the number of Pd atoms in the O-covered slab and clean slab to not change, we get the Gibbs free energy of adsorption,

$$\Delta G(T,p) = \gamma - \gamma_{\mathrm{clean}} \approx -\frac{1}{2A}(E^{\mathrm{total}}_{\mathrm{O/Pd(slab)}} - E^{\mathrm{total}}_{\mathrm{Pd(slab)}} - N_{\mathrm{O}}\mu_{\mathrm{O}}) \quad . \tag{5.3}$$

Assuming the surface in equilibrium with the surrounding gas-phase the $\mu_{\mathrm{O}}$ can be written as,

$$\mu_{\mathrm{O}}(T,p) = \frac{E^{\mathrm{total}}_{\mathrm{O_2(gas)}}}{2} + \Delta\mu_{\mathrm{O}} \quad . \tag{5.4}$$

Substituting into Eq. 5.3, and exploiting the definition for the binding energy we arrive at,

$$\begin{aligned} \Delta G(\Delta\mu_{\mathrm{O}}) &= -\frac{1}{2A}(E^{\mathrm{total}}_{\mathrm{O/Pd(slab)}} - E^{\mathrm{total}}_{\mathrm{Pd(slab)}} - N_{\mathrm{O}}(\frac{E^{\mathrm{total}}_{\mathrm{O_2(gas)}}}{2} + \Delta\mu_{\mathrm{O}})) \\ &= \frac{N_{\mathrm{O}}}{2A}(E_{\mathrm{b}} + \Delta\mu_{\mathrm{O}}) \quad . \end{aligned} \tag{5.5}$$

Table 5.1: $\Delta\mu_O(T, p^0)$ in the temperature range of interest to our study. The entropy and enthalpy changes used to obtain $\Delta\mu_O(T, p^0)$ are taken from [59] at $p^0$= 1 atm.

| $T$ | $\Delta\mu_O(T, p^0)$ | T | $\Delta\mu_O(T, p^0)$ |
|---|---|---|---|
| 100 K | -0.08 eV | 600 K | -0.61 eV |
| 200 K | -0.17 eV | 700 K | -0.73 eV |
| 300 K | -0.27 eV | 800 K | -0.85 eV |
| 400 K | -0.38 eV | 900 K | -0.98 eV |
| 500 K | -0.50 eV | 1000 K | -1.10 eV |

The chemical potential of an oxygen atom in an ideal gas, $\Delta\mu_O(T, p)$, can be obtained using [55]

$$\Delta\mu_O(T, p) = \Delta\mu_O(T, p^0) + \frac{1}{2}k_B T ln(\frac{p_{O_2}}{p^0}) \quad , \tag{5.6}$$

where $p^0$= 1 atm, and $\Delta\mu_O(T, p^0)$ can be found in thermochemical tables [59]. We list some values for $\Delta\mu_O(T, p^0)$ of interest to our work in Table 5.1.

Eq. 5.5 can be used in a most straight forward way to determine the most stable surface structure by comparing the stability of different adsorbate phases depending on the gas phase condition, $\Delta\mu_O(T, p)$, and using the surface energy of the corresponding clean slab as reference energy. Fig. 5.2 illustrates this with the phase diagram of oxygen adsorption at the Pd(100) surface, which clearly shows three stable regions: The clean Pd(100) surface, as well as a $p(2\times2)$ and a $c(2\times2)$ adsorbate phase, which will be explained in more detail below [87–90, 92, 93].

## 5.2 Ab-initio Statistical Mechanics

In the above described formulation, the atomistic thermodynamics approach enables a first consideration of a surrounding environment. It is, however, restricted in its predictive character to those structures that are included in the comparison, *i.e.* it cannot predict unanticipated stable structures. The neglect of the surface configurational entropy furthermore limits its use for elevated temperature, *e.g.* order-disorder transitions in the adsorbate ensemble cannot be treated. In order to overcome these shortcomings, we use the first-principles Lattice Gas Hamiltonian (FP-LGH) approach in combination with Monte Carlo (MC) simulations to investigate corresponding phenomena.

### 5.2.1 Canonical Monte Carlo (CMC) [61, 62]

If we first want to explicitly address temperature effects on a fixed adsorbate ensemble, the appropriate ensemble to study thermodynamically is the ($NVT$) ensemble with

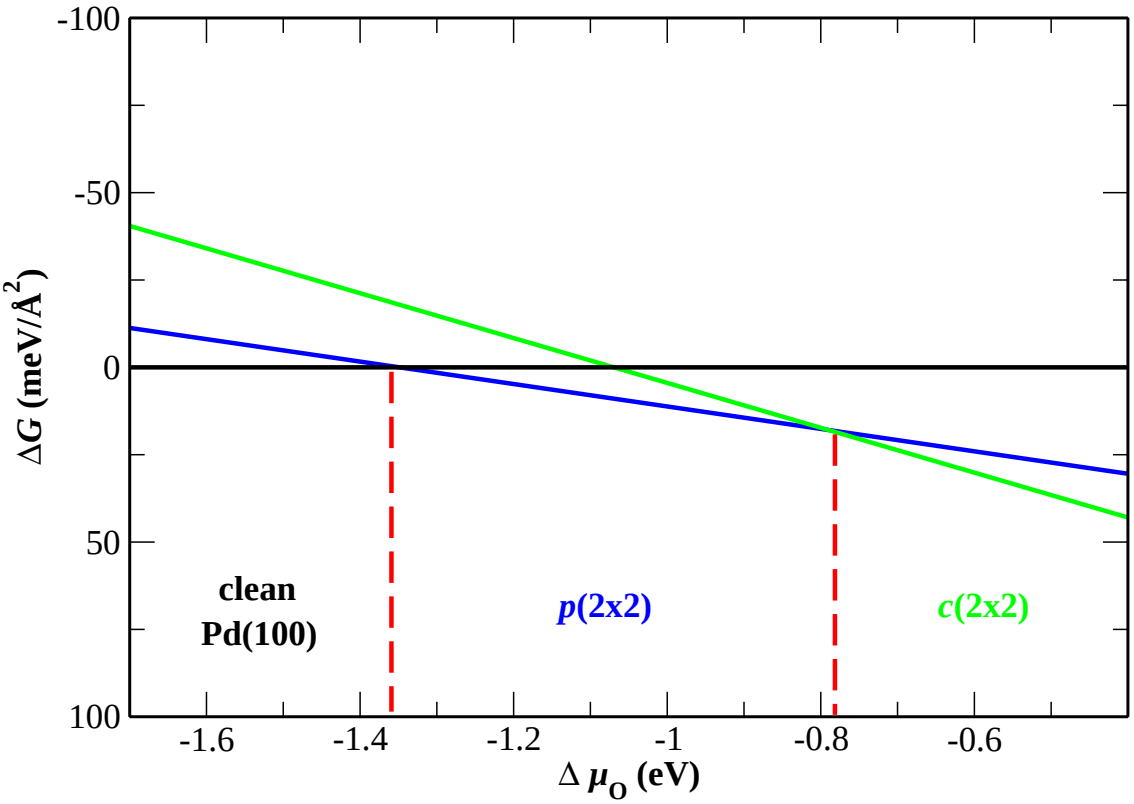


Figure 5.2: Phase diagram of on-surface oxygen atom adsorption at the Pd(100) surface. At low chemical potentials, the clean Pd(100) surface is the stablest structure $(-\infty, -1.35)$; with increasing chemical potential, oxygen atoms start to adsorb at the surface and build a $p(2 \times 2)$ configuration $(-1.35, -0.79)$; at further increased chemical potential, the $c(2 \times 2)$ configuration $(-0.79, +\infty)$ is coming out.

fixed number of particle $N$, fixed volume $V$, and fixed temperature $T$. The central quantity in this so-called canonical ensemble is the partition function,

$$Z = \sum_{\nu} e^{-E_\nu / k_B T} = \sum_{\nu} e^{-\beta E_\nu}, \quad (\beta = 1/k_B T) \quad . \tag{5.7}$$

where $E_\nu$ are the energies of the system states of interest and $k_B$ is the Boltzmann constant, $1.38 \times 10^{-23}$ J/K.

In this work, these system states of interest are any configuration of the adsorbates on the surface, ordered or disordered. For the moment we neglect vibrational contributions to the free energy, so that these system states are characterized by their total energy $E_\nu$. We will thus intend to evaluate through $Z$ the configurational entropy, and through $F = -kTlnZ$ the Helmholtz free energy. In more practical terms, we wish to evaluate the expectation value of any observable quantity $Q$ in the corresponding $(NVT)$ ensemble,

$$< Q >= \sum_{\nu} Q_\nu p_\nu = \frac{1}{Z} \sum_{\nu} Q_\nu e^{-\beta E_\nu} \quad , \tag{5.8}$$

where, $Q_\nu$ is the value of $Q$ in state $\nu$. The straight idea to calculate $< Q >$ is to calculate $Z$, $\sum_\nu Q_\nu e^{\beta E_\nu}$, and get $< Q >$. Unfortunately, it is tedious to calculate the integrand, and the scaling is (grid points)$^{\text{dimension}}$ for a grid-based techniques numerical integration. An efficient numerical approach is instead to resort to *Monte Carlo (MC)* simulations. The basic idea behind Monte Carlo simulations is to simulate the *random* thermal fluctuations of the system from state to state over the course of an experiment. In principle, one has to average the quantity of interest over all states $\nu$ of the system, and the real $< Q >$ is obtained when $\nu \to \infty$. However, this is only tractable for a very small system. For a large system, a much more efficient way would be to average only over the subset of system states, which have the largest contribution to the average quantity. The Monte Carlo technique thus works by choosing a subset of states at random from some probability distribution $p_\nu$ and thereby achieves an importance sampling. Hence, Eq. 5.8 is rewritten as,

$$Q_M = \frac{\sum_{i=1}^{M} Q_{\nu_i} p_{\nu_i}^{-1} e^{-\beta E_{\nu_i}}}{\sum_{i=1}^{M} p_{\nu_i}^{-1} e^{-\beta E_{\nu_i}}} \quad , \tag{5.9}$$

where, $Q_M$ is an *estimator*. If $M$ is large enough and nearly all important states are included, $Q_M$ will approach the real $< Q >$. Particularly important is to realize that for $Q_M$ to be a good estimator, one does not need the numerator and denominator in Eq. 5.9 to well approximate the infinite sums separately, but for a converged $< Q >$ only a well converged ratio of the two is necessary. Metropolis [64] devised an efficient Monte Carlo scheme to sample such a ratio. This so-called *Metropolis Algorithm* is described as follows:

1. If there are $N$ particles in the system, and its total energy is $E_1$, we can give this configuration a probability distribution, $p_\nu = e^{-E_1\beta}$.

2. Randomly create a new configuration, and calculate the total energy of the new configuration, $E_2$. If $E_2$ is lower than $E_1$, accept the trial, and update the old configuration to the new one. Otherwise, accept the trial with a probability ($e^{-\beta\Delta E}$, $\Delta E = E_2 - E_1$). In practice this is realized by comparing $e^{-\beta\Delta E}$ with a random number (between 0 and 1). If $e^{-\beta\Delta E}$ is larger than the random number, accept the trial, and update the old configuration to the new one, otherwise reject the trial and continue with the old configuration.

3. Add the current configuration to the sums in Eq. 5.9.

4. Loop steps 1 to 3 steps until the estimator is converged to a given precision.

Since the system is allowed to visit any configuration in this scheme, it is clear that a large enough number of trials will enable the system to reach any phase space point of the system if the way to create new configuration is chosen appropriately. Hence, the method is *ergodic*.

### 5.2.2 Grand-Canonical Monte Carlo (GCMC)

In typical adsorption studies, the adsorbates do not only move at the surface, but also exchange with the gas-phase represented by a constant temperature and pressure. The appropriate ensemble to consider in this case is the grand-canonical ensemble ($\mu VT$), which means that chemical potential ($\mu$), volume ($V$) and temperature ($T$) are fixed. The Metropolis scheme detailed in the previous sections can be readily extended to evaluate this ensemble as well. The corresponding grand-canonical Monte Carlo procedure is the following for a gas-phase reservoir characterized by the chemical potential $\Delta\mu(T,p)$ and again disregarding vibrational contributions to the free energy of the adsorbed particles for the time being:

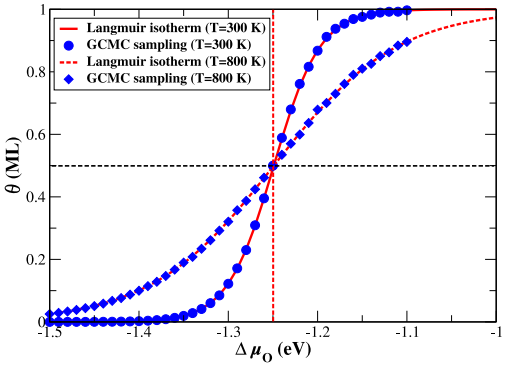


Figure 5.3: $\theta$ vs. $\Delta\mu$ from the Langmuir adsorption isotherm Eq. 5.10 (red solid line (300 K), red dashed line (800 K)) and GCMC simulation (blue dots (300 K), blue diamond (800 K)), respectively.

1. Prepare an initial configuration, containing $N$ particles with total energy of $E_1$.

2. In the ($\mu TV$) ensemble, three cases can lead to new trial configurations: redistribution of the fixed number of particles at the surface, remove a particle from the surface, or add a particle to the surface. Each of the procedures has the same probability.

1). Removal: Randomly choose a particle, and move it from the surface to the reservoir. Then, calculate the total energy of this $(N-1)$ particle configuration, $E_2$, and the energy difference, $\Delta E = (E_2 + \Delta\mu) - E_1$. If $\Delta E < 0$, accept the removal. Otherwise, the removal should be accepted with a probability, $e^{-\beta\Delta E}$.

2). Addition: Randomly select an empty site, and add a particle from the reservoir to this site. The total energy of the new $(N+1)$ particle configuration, $E_2$, and the energy difference, $\Delta E = E_2 - (E_1 - \Delta\mu)$, are calculated. If $\Delta E < 0$, accept this addition. Otherwise, the addition should be accepted by a probability, $e^{-\beta\Delta E}$.

3). Diffusion: The same procedure as in CMC (see section 5.2.1).

3. Loop steps 1) to 3) until the observable $Q_M$ is converged to a descried accuracy.

A simple numerical test to illustrate the GCMC approach is to evaluate the adsorption isotherm $(\Delta\mu, \theta)$, where $\theta$ is the coverage, for a lattice gas without lateral interactions. This model can also be evaluated analytically, leading to the Langmuir adsorption isotherm [76],

$$\theta = \frac{1}{1 + e^{\frac{E_0 - \Delta\mu}{k_B T}}} \quad , \tag{5.10}$$

where, $\theta$ is the coverage, $E_0$ is the binding energy of an adsorbated particle at the surface, and $\Delta\mu$ is the chemical potential difference to the particle in the gas-phase.

Fig. 5.3 shows a comparison of corresponding numerical GCMC results to the

analytical curve at $T = 300$ K and 800 K. The simulation cell was a square lattice of dimension (40×40). Based on the probabilities of removal and addition, in the low chemical potential ($\Delta\mu < E_0$) region, the probability to accept remove a particle from the surface is larger than adding a particle. This leads to $\theta < 0.5$ ML. On the contrary, when $\Delta\mu$ is larger than $E_0$, the probability to accept adding a particle to the surface is larger than removing a particle, and then the coverage is larger than 0.5 ML. At the point, $\Delta\mu = E_0$, the probabilities to accept removal and addition are equal and the equilibrium coverage is 0.5 ML. Furthermore, Fig. 5.3 shows that the curve at high $T$ is more spread than at low $T$. This reflects the increased configurational entropy contribution at the higher temperature. Nevertheless, all curves must cross the ($E_0$, 0.5 ML) point.

### 5.2.3 First-principles Lattice-gas Hamiltonian (FP-LGH)

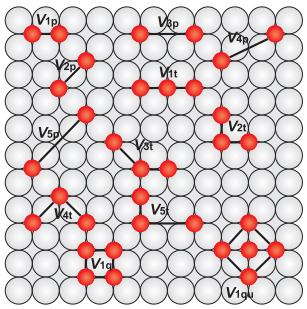


Figure 5.4: Schematic view of lateral interaction figures for adatoms at a fcc (100) surface.

While the importance sampling achieved by the described Metropolis schemes makes the evaluation of averaged properties in the ($NVT$) and ($\mu VT$) ensemble much more efficient, the total number of energy evaluations required is still untraceable for larger systems, if the total energies are provided directly from electronic structure calculations. In addition, due to the periodic boundary conditions the latter can only provide the energetics for ordered adsorbate configurations with rather small unit-cell sizes. For adsorption systems with site-specific adsorption this problem can be solved by resorting to a lattice model and expand the energy of any given configuration in terms of occupations in the lattice. This is the idea behind the *Lattice-Gas Hamiltonian* (LGH) [65−67] or *Cluster Expansion* (CE) approach, in which the total energy depends on an infinite expansion in terms of pair interactions, and many-body interactions, such as trio (three-body) interactions, quattro (four-body) interactions, and so on between well defined sites at the surface. As soon as the lateral interaction potentials are known, the total energy can be evaluated by a simple summation for any given configuration on the lattice, so that a manyfold evaluation of this Hamiltonian as required for MC simulations becomes readily possible.

Fig. 5.4 illustrates such a LGH model for adsorption of particles at a fcc (100) surface into the fourfold hollow sites. The LGH is then written (again neglecting vibrational contributions to the free energies for this time being):

$$E = \sum_{i=1}^{N} E_i^{\text{on-site}} n_i + \sum_{i \neq j} V_{\text{p}}(i,j) n_i n_j + \sum_{i \neq j \neq k} V_{\text{t}}(i,j,k) n_i n_j n_k + ..... \qquad (5.11)$$

where, $E_i^{\text{on-site}}$ is the on-site energy, and $V_{\text{p}}$ and $V_{\text{t}}$ are pair and trio interactions, respectively. Formally, higher and higher order interaction terms (quattro, quinto, ...)

would follow in this infinite expansion. $n_i$ is set as 1 or 0 according to site $i$ being occupied or empty. In the LGH, the periodic boundary condition (Fig 5.5) should be considered in Eq. 5.11, which means that apart from the interactions between atoms in the simulation cell (green arrows), also the interactions with atoms in the neighboring image cells (blue arrows) should be considered.

As has been noted, the LGH expansion is in principle infinite including higher order interaction terms. In practice, the expansion must (and can) be truncated after a finite number of terms. One crucial objective to determine a reliable LGH is thus to identify which terms can be truncated. For a given truncated LGH the accuracy of the predicted total energies depends then on the accuracy of the considered lateral interactions, which is thus the second central objective to fit a reliable LGH. Traditionally, these parameters are adjusted in order to fit a variety of experimental data such as phase diagrams, heats of adsorption, or thermal desorption data. Although useful, such an approach is clearly not necessarily predictive in nature, nor the parameters unique, and may thus not capture the physics of the microscopic processes that are behind the best-fit adjusted effective parameters.

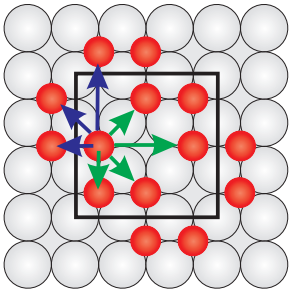

Figure 5.5: Schematic illustration of periodic image lateral interactions in the simulation cell. Green arrows are pair interactions in the simulation cell, while blue arrows are image pair interactions.

In recent years, algorithmic advances and increased computational power have made it possible to determine the lateral interactions alternatively from first-principles. Most notably, these are approaches that parameterize LGHs with DFT energetics. This is called *First-principles LGH* approach. In the FP-LGH, various ordered configurations at different coverages are calculated by DFT. For each configuration, the binding energy is expanded as a cluster expansion using Eq. 5.11. The on-site energies and lateral interactions can then be extracted by fitting to a sufficiently large number of such computed binding energies for different configurations. There are thus two crucial aspects that determine the reliability of this approach: One is which and how many lateral interactions play a role in determining accurate total energies. In other words, where should the CE be truncated? And the second one is which and how many DFT calculations are required to identify optimum lateral interactions. Obviously, the two questions are related to each other. In the next two sections, we are going to address these two intertwined topics.

### 5.2.4 Leave-one-out Cross-validation: Identify Optimum Lateral Figures

Suitable guidance for the question which lateral interactions should be considered in the truncated LGH expansion can be obtained by assessing the predictive character of the expansion. In other words, how well can the energetics of configurations that were

not used in the fitting of the lateral interactions be predicted. Due to the high cost of the underlying DFT calculations, it is not desirable to calculate a larger number of configurations as a test set with which this predictive character can be evaluated. Instead, one would want to use each computed configuration in the actual training set used to determine the lateral interactions. For such cases the predictive character can be assessed through cross-validation (CV) scores. The simplest one, the leave-one-out CV (LOO-CV) is defined as:

$$CV = \sqrt{\frac{1}{N}\sum_{i=1}^{N}(E_{\mathrm{b}}^{\mathrm{DFT}}(i) - E_{\mathrm{b}}^{\mathrm{LGH}}(i))^2} \quad . \tag{5.12}$$

where $N$ is the number of calculated ordered configurations. $E_{\mathrm{b}}^{\mathrm{DFT}}(i)$ and $E_{\mathrm{b}}^{\mathrm{LGH}}(i)$ are the binding energies of the $i$th configuration by DFT calculation and evaluated from the LGH expression for this configuration, respectively. This method means that least-squares fitting (LSF) is applied on $(N-1)$ configurations to get the lateral interactions, and the remaining configuration is used to check the fitting data with an *expected error*. In more detail, the procedure of LOO-CV is: First, calculate $N$ ordered configurations by DFT, and prepare a large pool of lateral interaction figures (like Fig. 5.4 or Fig. 6.1) according to the studied system. Second, randomly choose $m$ lateral interaction figures from the pool. Instead of fitting them by least-square-fitting using ALL calculated configurations, leave the $i$th configuration out, use the rest $(N-1)$ configurations to fit the selected $m$ figures by LSF, use the left out configuration to check the fitting data and get one expected error, $(E_{\mathrm{b}}^{\mathrm{DFT}}(i) - E_{\mathrm{b}}^{\mathrm{LGH}}(i))^2$. Then leave another configuration out, and fit the same $m$ figures by the now remaining $(N-1)$ configurations by LSF, use the left out configuration to check the new fitting data and get another expected error. This loop is run until each configuration has been left out once and finally all expected errors are summed and averaged to produce the final CV score for the considered set of $m$ lateral interactions. Then choose another group of $m$ figures from the cluster pool, start anew, and get another CV score. This is equally done for all sets with $m-1$, $m+1$, $m-2$, $m+2$ ... *etc.* lateral interactions and finally the set of lateral interactions with the smallest CV score is identified as the optimum one.

### 5.2.5 Direct Enumeration: Validate the Set of DFT Input Structures

The LOO-CV identifies the optimum set of lateral interaction figures that minimizes the fitting errors for a given set of calculated configurations. This leaves the question, whether the configurations provide an ideal and sufficient set of input structures. One possibility to check on this is by assessing whether the LGH predicts the same set of ordered ground-state structures at $T$=0 K than the DFT input data. For our adsorption studies this is suitably evaluated through the formation energy, $\Delta E_f$ [69],

which is in general defined as an excess energy with respect to the equivalent amounts of pure constituents,

$$\Delta E_f = \frac{1}{N_\mathrm{t}}[E^\mathrm{total}_\mathrm{O/slab} - \theta E^\mathrm{total}_{(1\times1)-\mathrm{O/slab}} - (1-\theta)E^\mathrm{total}_\mathrm{slab}] \quad . \tag{5.13}$$

As in Eq. 4.9, $E^\mathrm{total}_\mathrm{O/slab}$ is the total energy for a specific adsorbate configuration with $N_\mathrm{O}$ O atoms per surface unit-cell (corresponding to a coverage $\Theta = N_\mathrm{O}/N_\mathrm{t}$ with $N_\mathrm{t}$ the number of sites per surface unit-cell), $E^\mathrm{total}_\mathrm{slab}$ is the total energy of the clean surface, and $E^\mathrm{total}_{(1\times1)-\mathrm{O/slab}}$ is the total energy of the full monolayer $(1\times1)$-O configuration. With this definition, $\Delta E_f$ reflects the relative stability of a particular configuration with respect to phase separation into a fraction $\theta$ of the full monolayer configuration and a fraction $(1-\theta)$ of the clean surface, and we can relate it to the binding energy of the configuration by

$$\Delta E_f = \theta\left[E_{\mathrm{b,O/slab}} - E_{\mathrm{b},(1\times1)-\mathrm{O/Pd(100)}}\right] \quad . \tag{5.14}$$

Plotting the formation energy vs. coverage is very convenient to determine the *DFT ground state line* (or *convex hull*) [78]. As illustrated in Fig. 5.6, assume there are two stable configurations ($\theta_1$,$\Delta E_{f1}$) and ($\theta_2$,$\Delta E_{f2}$), and they define the DFT ground state line (dashed line in Fig. 5.6). Any formation energy ($\Delta E_{f0}$) of a configuration at any coverage ($\theta_0$) that lies on the dashed line can be easily derived by,

$$\Delta E_{f0} = \frac{\Delta E_{f2} - \Delta E_{f1}}{\theta_2 - \theta_1} \times \theta_0 \quad . \tag{5.15}$$

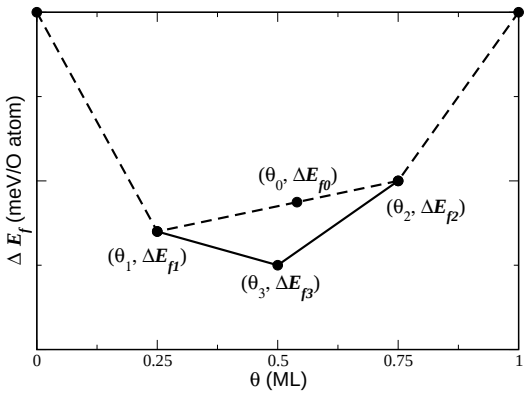


Figure 5.6: Schematic illustration of the idea behind a of convex hull and the ground line determined by formation energies.

Therefore, the ground state line divides the whole $(\theta, \Delta E_f)$ space into a unstable configuration region above the DFT ground line, and a stable configuration region below the line at least with respect to the existing DFT data (which here comprises only two configurations). If we now compute a third configuration ($\theta_3$,$\Delta E_{f3}$) that lies below the ground-state line a new stable structure is found and the convex hull/ground-state line must be redrawn (solid line in Fig. 5.6). For any newly computed configuration we can thus quickly assess whether it constitutes a stable structure at $T = 0$ K or not.

The LGH expansion should obviously predict the same stable structures as the DFT input data. An additional benefit is that with the LGH many more configurations within much larger unit-cells can be computed. By directly enumerating all such configurations within unit-cells with a certain maximum area, one can quickly check the consistency of the LGH with the DFT data. If there is LGH configuration that

leaks below the DFT ground-state line, the corresponding structure is obviously an important motif not yet included in the DFT input data set or it is an artifact of the present LGH expansion. In either case, this identifies a structure (or structural motif) that should be computed and included in the DFT input data set. For a refined LGH based on this new input data set, the procedure is repeated and again checked whether it predicts structures below the DFT ground-state line. This iterative scheme is done until DFT and LGH predict a consistent set of ground-state structures.

### 5.2.6 Two Properties to Monitor Phase Transitions: $\Psi$ and $C_V$

Using a validated first-principles LGH in either canonical or grand-canonical MC simulations enables the study of critical phenomena at surfaces, like the order-disorder transition in the adsorbate ensemble. For this two central quantities that we will evaluate in the MC simulations are order parameters sensitive to the lateral periodicities at the surface ($\Psi$)[70–73] and the specify heat capacity ($C_V$).

Corresponding order parameters can be derived from Fourier theory for the periodicity of the ordered configuration of interest. Considering our two-dimensional periodic surfaces, the Fourier transformation should act on each dimension of the surface unit-cell. In this work, we are only interested in surface unit-cells with equal periodicity in both dimensions. We can correspondingly concentrate on a square Fourier matrix ($\mathbf{F}$) [68] written as:

$$\mathbf{F} = \begin{pmatrix} w^{0\cdot 0} & w^{0\cdot 1} & ... & w^{0\cdot(N_{\mathrm{FFT}}-1)} \\ w^{1\cdot 0} & w^{1\cdot 1} & ... & w^{1\cdot(N_{\mathrm{FFT}}-1)} \\ . & . & . & . \\ . & . & . & . \\ . & . & . & . \\ w^{(N_{\mathrm{FFT}}-1)\cdot 0} & w^{(N_{\mathrm{FFT}}-1)\cdot 1} & ... & w^{(N_{\mathrm{FFT}}-1)\cdot(N_{\mathrm{FFT}}-1)} \end{pmatrix} \quad , \tag{5.16}$$

where $w^{r\cdot c} = e^{-\frac{r\times c\times 2\pi i}{N_{\mathrm{FFT}}}}$: $N_{\mathrm{FFT}}$ indicates the periodicity in units of the surface unit-cell vector. In order to make a suitable transform according to our magnetization matrix $\mathbf{M}$ defined later, the Fourier transformed matrix ($\mathbf{R}$) is written as, [68]

$$\mathbf{R} = \mathbf{F} * (\mathbf{F} * \mathbf{M^T})^{\mathbf{T}} \quad . \tag{5.17}$$

where the superscript $\mathbf{T}$ denotes transposed the matrices transport without conjugation, which means that the operation only exchanges the rows and columns.

In our case the ordered arrangements of interest are $p(2\times 2)$ and $c(2\times 2)$ ordered adlayers as depicted in Fig. 5.7. In order to evaluate a suitable order parameter we apply the so-called renormalization group [70, 75], which divides the unit cell into several sub-lattices, $a, b$ *etc* (Fig. 5.7). Supposing there are $N_{\mathrm{sub}}$ sub-lattices, we use $M_a$, $M_b$ *etc* to indicate the total magnetization of the corresponding sub-lattices.

(The magnetization value of each site is 1 or $-1$ depending if the sites are occupied or empty.) The magnetization matrix of a configuration cell is thus expressed by a $(N_{\rm sub} \times N_{\rm sub})$ size matrix,

$$\mathbf{M} = \frac{1}{N_{\rm sub}} \begin{pmatrix} M_a & M_b & ... \\ ... & ... & ... \\ ... & ... & ... \end{pmatrix} \quad , \tag{5.18}$$

which has the same arrangement in its rows and columns as the unit-cell lattice at the surface. Correspondingly, the Fourier transform is written as a $(N_{\rm sub} \times N_{\rm sub})$ matrix as well. After transforming Eq. 5.17, the remaining non-zero elements in the matrix $\mathbf{R}$ compare to the frequencies, and are partly degenerate. Summing all these non-zero parts and normalizing so that the stable arrangement yields an order parameter of 1, we arrive at the final order parameter $\Psi$.

If we apply this general recipe to the $p(2 \times 2)$ ordered arrangement shown in the left panel of Fig. 5.7, we identify first $N_{\rm sub}$=4 sub-lattices, $a, b, c$ and $d$. $M_a$, $M_b$, $M_c$ and $M_d$ are the corresponding magnetizations of the $a, b, c$ and $d$ sub-lattices in the simulation cell, respectively, and the magnetization matrix reads,

$$\mathbf{M}_{p(2\times2)} = \frac{1}{4} \begin{pmatrix} M_a & M_b & M_a & M_b \\ M_c & M_d & M_c & M_d \\ M_a & M_b & M_a & M_b \\ M_c & M_d & M_c & M_d \end{pmatrix} \quad , \tag{5.19}$$

Correspondingly, we can write its Fourier matrix as,

$$\mathbf{F}_{p(2\times2)} = \begin{pmatrix} 1 & 1 & 1 & 1 \\ 1 & e^{-\frac{\pi i}{2}} & e^{-\pi i} & e^{-\frac{3\pi i}{2}} \\ 1 & e^{-\pi i} & e^{-2\pi i} & e^{-\pi i} \\ 1 & e^{-\frac{3\pi i}{2}} & e^{-\pi i} & e^{-\frac{\pi i}{2}} \end{pmatrix}. \tag{5.20}$$

Substituting $\mathbf{M}_{p(2\times2)}$ and $\mathbf{F}_{p(2\times2)}$ into Eq. 5.17, we get,

$$\mathbf{R}_{p(2\times2)} = \begin{pmatrix} M_a + M_b + M_c + M_d & 0 & M_a - M_b + M_c - M_d & 0 \\ 0 & 0 & 0 & 0 \\ M_a + M_b - M_c - M_d & 0 & M_a - M_b - M_c + M_d & \\ 0 & 0 & 0 & 0 \end{pmatrix}. \tag{5.21}$$

Neglecting the constant part, $M_a + M_b + M_c + M_d = \theta \cdot N_{\rm t}$ ($N_{\rm t}$: the total number of sites in the simulation cell), the order parameter at 0.25 ML can be written as,

$$\Psi_{p(2\times2)} = \sqrt{(\Psi_1)^2 + (\Psi_2)^2 + (\Psi_3)^2} \quad , \tag{5.22}$$

where $\Psi_1 = M_a - M_b + M_c - M_d$, $\Psi_2 = M_a + M_b - M_c - M_d$, and $\Psi_3 = M_a - M_b - M_c + M_d$. Normalizing Eq. 5.22 to the most stable configuration, $p(2 \times 2)$ (left panel in Fig.

5.7), which gives $M_a = \frac{N_t}{4}$ and $M_b = M_c = M_d = -\frac{N_t}{4}$, we thus obtain $\Psi^{max}_{p(2\times2)} = \frac{3}{4N_t}$. Correspondingly, Eq. 5.22 is rewritten as,

$$\Psi_{p(2\times2)} = \frac{3}{4N_t}\sqrt{(\Psi_1)^2 + (\Psi_2)^2 + (\Psi_3)^2} \quad . \tag{5.23}$$

In the same spirit, for the $c(2 \times 2)$ ordered arrangement shown in the right panel in Fig. 5.7, we can identify 2 sub-lattices, $N_{sub}$=2, and the magnetization matrix is,

$$\mathbf{M}_{c(2\times2)} = \frac{1}{2}\begin{pmatrix} M_a & M_b \\ M_b & M_a \end{pmatrix} \quad , \tag{5.24}$$

Correspondingly, its Fourier matrix is,

$$\mathbf{F}_{c(2\times2)} = \begin{pmatrix} 1 & 1 \\ 1 & -1 \end{pmatrix}. \tag{5.25}$$

Substituting $\mathbf{M}_{c(2\times2)}$ and $\mathbf{F}_{c(2\times2)}$ into Eq. 5.17, we get,

$$\mathbf{R}_{c(2\times2)} = \begin{pmatrix} M_a + M_b & 0 \\ 0 & M_a - M_b \end{pmatrix}. \tag{5.26}$$

Neglecting the constant part, $M_a + M_b = \theta \cdot N_t$ ($N_t$: the total number of sites in the simulation cell), its order parameter is written as, $\Psi_{c(2\times2)} = \sqrt{(M_a - M_b)^2}$, where $M_a$ and $M_b$ indicate the total magnetization of $a$ and $b$ sub-lattices in the simulation cell, respectively. Normalizing this formula to the most stable $c(2 \times 2)$ configuration at this coverage, which gives $M_a = \frac{N_t}{2}$ and $M_b = -\frac{N_t}{2}$, we thus obtain $\Psi^{max}_{c(2\times2)} = \frac{1}{N_t}$ and arrive at the final order parameter at 0.5 ML,

$$\Psi_{c(2\times2)} = \frac{1}{N_t}\sqrt{(M_a - M_b)^2} \quad . \tag{5.27}$$

Such order parameters are perfect to determine the critical temperature for the order-disorder transition, if the periodicity of the ordered structure is known. Essentially, these order parameters are equivalent to the superstructure spot intensities in low-energy electron diffraction (LEED) experiments [74]. However, if the periodicity of the ordered structure is unknown, monitoring the specific heat capacity $C_V$ is another suitable approach, which is instead sensitive to the mean squared fluctuations in energy [75]. This quantity is defined as,

$$\begin{aligned} C_V &= \frac{< E^2 > - < E >^2}{k_B T^2} \\ &= \frac{\frac{\sum_i^M E_i^2}{M} - (\frac{\sum_i^M E_i}{M})^2}{k_B T^2} \quad , \end{aligned} \tag{5.28}$$

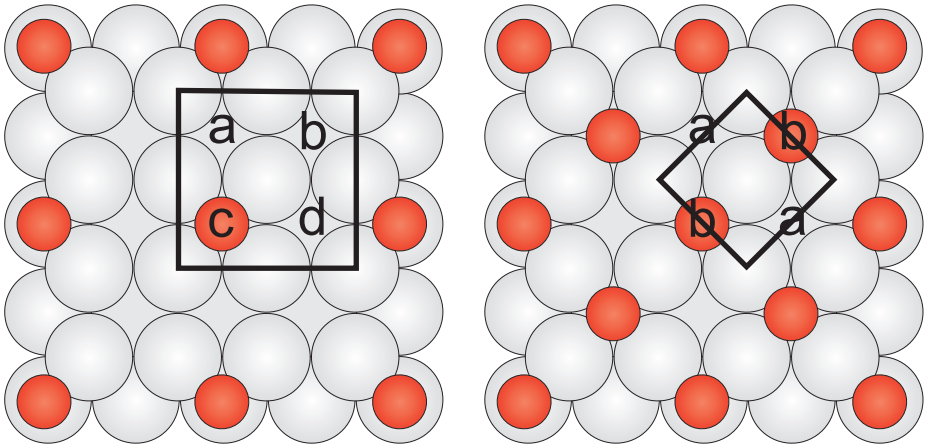


Figure 5.7: Schematic top view illustrating the division into sub-lattices for the $p(2 \times 2)$ (left panel) and $c(2 \times 2)$ structures (right panel) on a fcc (100) surface. There are 4 and 2 sub-lattices for the $p(2 \times 2)$ and $c(2 \times 2)$ configurations, respectively. $a, b, c$ or $d$ indicate the name of one kind of sub-lattice. (Large spheres Pd atoms, small spheres O adatoms)

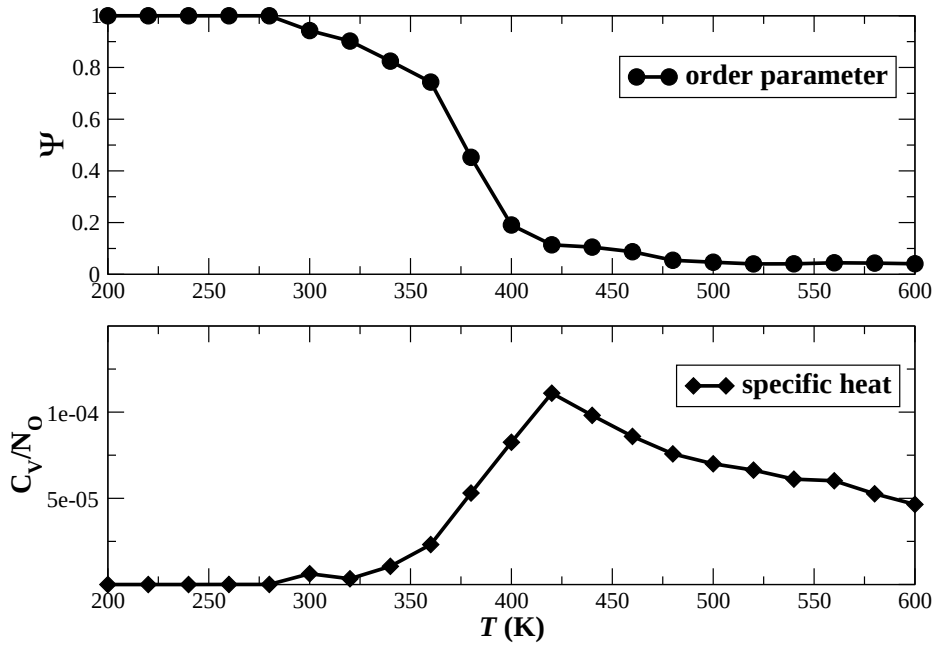


Figure 5.8: Illustration of how the order parameter $\Psi$ (upper panel) and the specific heat $C_V$ (lower panel) identify the order-disorder transition of a $p(2 \times 2)$ structure at a cubic (100) surface with $\theta = 0.25$ ML. As a toy model we consider a strongly repulsive first nearest neighbor pair interaction (-200 meV) and a smaller repulsive second nearest neighbor pair interaction (-50 meV) between adatoms adsorbed into the hollow sites of the (100) surface. Evaluating $\Psi$ and $C_V$ over $10^8$ MC steps and in a (60×60) simulation cell, both properties yield a critical temperature (taken from the inflection point for $\Psi$ and from the peak for $C_V$) that is identical to within 40 K.

where, $< E >$ and $< E^2 >$ are the average energy and the mean squared energy, respectively, and $M$ is the number of MC steps. Fig. 5.8 illustrates an example of how $\Psi$ and $C_V$ identify the order-disorder transition.

Furthermore, for a (100) surface including one (111) step, in order to study the (111) step effects on the mesoscopic adsorption properties at the (100) surface, we need to define a property that is sensitive to the local environment. For this we employ the specific heat per atom resolved for each row parallel to the (111) step, $C_V^{\mathrm{row}}$. Since the number of atoms in each row is then no longer constant during the MC simulation we thus rewrite Eq. 5.28 as

$$C_V^{\mathrm{row}_j} = \frac{1}{kT^2}\left[\frac{\sum_{i=1}^{M}\left(\frac{E_i^{\mathrm{row}_j}}{\sqrt{N_i^{\mathrm{row}_j}}}\right)^2}{M} - \left(\frac{\sum_{i=1}^{M}\frac{E_i^{\mathrm{row}_j}}{\sqrt{N_i^{\mathrm{row}_j}}}}{M}\right)^2\right] \quad , \tag{5.29}$$

where, $N_i^{\mathrm{row}_j}$ and $E_i^{\mathrm{row}_j}$ are the number of atoms and the total energy in the $j$th row at the $i$th MC step. (See the test for O-Pd(100) in Appendix D.)

# Part II

# Ordering Behavior of Oxygen Atoms at the Pd(100) Surface

# Chapter 6

# On the Accuracy of First-Principles Lateral Interactions: Oxygen at Pd(100)

Lateral interactions between species adsorbed at solid surfaces are crucial microscopic quantities that have been the target of surface science studies for a long time.[76] These interactions govern both the equilibrium, as well as the non-equilibrium ordering behavior of the adsorbates, and thereby critically influence the surface function and properties in important applications like heterogeneous catalysis. Traditionally, considerable efforts have been devoted to determine lateral interactions empirically from experimental data, *e.g.* from temperature programmed desorption or low energy electron diffraction (LEED) measurements. In order to simplify the inherently indirect determination from sparse experimental data, the assumption of exclusively pairwise interactions between the adsorbed species has often been applied. As we described in Chapter 5, an emerging alternative is to determine the lateral interactions within a first-principles LGH approach. Since the accuracy of the determined lateral interactions should be of the order of $k_B T$ to properly describe the thermal ordering, a concern with this approach has been whether the employed first-principles energetics is actually accurate enough.

Within this context, the work described in this chapter has a methodological and a materials science motivation. The methodological motivation is to scrutinize both the assumption of exclusively pairwise interactions, and the accuracy with which the first-principles LGH approach can provide the lateral interactions. For this purpose we concentrate on a simple model case, namely the on-surface ordering of atomic adsorbates at a (100) cubic surface, for which extensive studies with model interactions have already been performed.[79–86] To make contact with a specific material and with experiment, we specifically choose the on-surface adsorption of oxygen at Pd(100), for which detailed experimental data on the ordering behavior is available [87]. Since in this system higher oxygen coverages above $\theta \sim 0.5$ monolayers [ML, defined with respect to the number of Pd atoms in one layer of Pd(100)] induce structures containing

incorporated oxygen atoms [87–91], we concentrate on the low coverage regime. For this regime, two ordered structures have hitherto been characterized experimentally [87–90, 92, 93]: A $p(2\times2)$-O structure at 0.25 ML and a $c(2\times2)$-O structure at 0.5 ML, both with O adsorbed in the on-surface fourfold hollow sites. The material science motivation of our first-principles LGH study is then to extract the lateral interactions operating between the adsorbed O atoms at the surface and to study the ordering behavior they imply. Specifically, this is to see whether we can confirm the experimentally determined ordered structures, as well as the critical temperatures for the order-disorder transition in the low coverage regime.

# 6.1 Computational Details

## 6.1.1 Lattice-Gas Hamiltonian for O-Pd(100)

Employing the concept of a lattice-gas Hamiltonian for the O-Pd(100) system, the total free binding energy of any configuration is expanded into a sum of discrete interactions between the on-surface hollow lattice sites. For this one component system with only one site type, this energy reads

$$N_{\mathrm{O}}F_{\mathrm{b}} = F_{\mathrm{b}}^{\mathrm{on-site}}\sum_{i} n_i \;+\; \sum_{u=1}^{\mathrm{r}} V_{u,\mathrm{p}} \sum_{(i<j)_u} n_i n_j \;+\; \sum_{u=1}^{\mathrm{q}} V_{u,\mathrm{t}} \sum_{(i<j<k)_u} n_i n_j n_k + \ldots \quad , \tag{6.1}$$

where the site occupation numbers $n_i = 0$ or 1 indicate whether site $i$ in the lattice is empty or occupied, with a total of $N_{\mathrm{O}}$ sites occupied, and $F_{\mathrm{b}}^{\mathrm{on-site}}$ is the free energy of an isolated species at the hollow lattice site, including static and vibrational contributions. There are $r$ pair interactions with two-body (or pair) interaction energies $V_{u,\mathrm{p}}$ between species at $u$th nearest neighbor sites, and $q$ trio interactions with $V_{\mathrm{t,u}}$ three-body interaction energies. The sum labels $(i<j)_u$ [and $(i<j<k)_u$] indicate that the sums run over all pairs of sites $(ij)$ (and three sites $(ijk)$) that are separated by $u$ lattice constants, and the summation is done such, that each pair (or trio) of occupied sites contributes exactly once to the lattice energy.[94]

To quantify the effect that truncating the infinite expansion in Eq. 6.1 has on the accuracy, we rely on the concept of leave-one-out cross validation (LOO-CV) to identify the most important interactions out of a larger pool of possible interactions. Figure 6.1 illustrates the lateral interactions contained in this pool, which range from pair interactions up to the fifth nearest neighbor, via all trio interactions up to second nearest neighbor, to several compact quattro and one quinto interaction. The pool focuses thus on short- to medium-ranged interactions. Interactions at larger distances can be substrate-mediated elastic or of electronic origin [95], but for the present system we do not expect such interactions to play a role on the accuracy level of interest to this study.

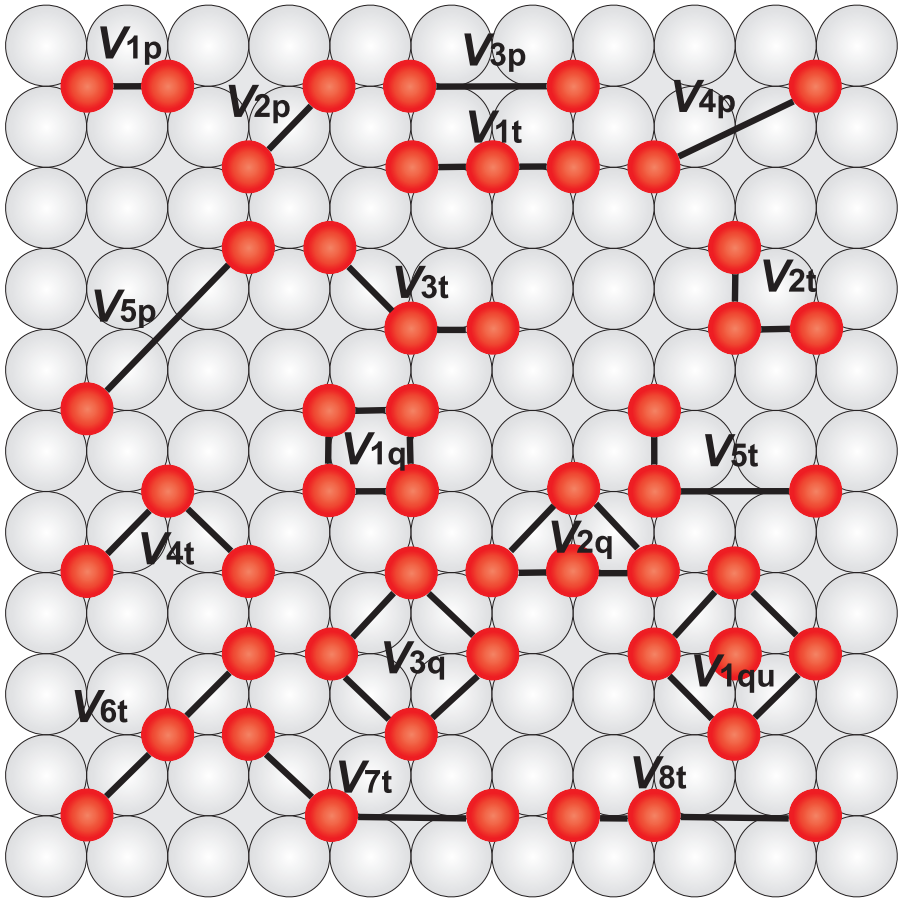


Figure 6.1: Top view of the Pd(100) surface, illustrating the considered pool of 17 lateral interactions between O atoms in on-surface hollow sites. $V_{m,\mathrm{p}}$ $(m = 1, 2, 3, 4, 5)$ are the two-body (or pair) interactions at first, second, third, fourth and fifth nearest neighbor distance. $V_{n,\mathrm{t}}$, $V_{n,\mathrm{q}}$, $V_{n,\mathrm{qu}}$ are considered compact trio, quattro and quinto interactions, respectively. Light grey spheres represent Pd atoms, and small dark grey (red) spheres O atoms.

### 6.1.2 Static and Vibrational Average Binding Energy

In order to generate a quantitatively accurate LGH, we parameterize the unknown lateral interaction energies contained in the LGH by first-principles calculations. The central quantities required for this parameterization are computed average free binding energies for a set of ordered configurations of O adsorbed at Pd(100). We write this average free binding energy as

$$F_{\mathrm{b}}(T) \;=\; E_{\mathrm{b}} + F_{\mathrm{b}}^{\mathrm{vib.}}(T) \quad , \tag{6.2}$$

separating the total and vibrational contributions, $E_{\mathrm{b}}$ and $F_{\mathrm{b}}^{\mathrm{vib.}}(T)$ respectively. The former contribution is obtained from Eq. 4.9. In order to determine the vibrational contribution to the average free binding we use the phonon density of states $\sigma(\omega)$ and

write the vibrational free energy as

$$F^{\text{vib.}}(T) \;=\; \int d\omega \; F(T,\omega)\; \sigma(\omega) \quad , \tag{6.3}$$

where

$$F^{\text{vib.}}(T,\omega) = \hbar\omega \left(\frac{1}{2} + \frac{1}{e^{\beta\hbar\omega}-1}\right) - k_B T \left[\frac{\beta\hbar\omega}{e^{\beta\hbar\omega}-1} - \ln(1-e^{-\beta\hbar\omega})\right] \tag{6.4}$$

is the vibrational free energy of an harmonic oscillator of frequency $\omega$. [55] $k_B$ is the Boltzmann constant, and $\beta = 1/(k_B T)$ the inverse temperature. The vibrational contribution to the average binding energy can then be written in exactly the same way as Eq. 4.9, namely

$$\begin{aligned} F_{\text{b}}^{\text{vib.}}(T) &= -\frac{1}{N_{\text{O}}}\left[F^{\text{vib.}}_{\text{O/Pd(100)}}(T) - F^{\text{vib.}}_{\text{Pd(100)}}(T) - \frac{N_{\text{O}}}{2} F^{\text{vib.}}_{\text{O}_2\text{(gas)}}(T)\right] \qquad (6.5)\\ &= -\frac{1}{N_{\text{O}}}\int d\omega \; F^{\text{vib.}}(T,\omega) \; \left[\sigma_{\text{O/Pd(100)}}(\omega) - \sigma_{\text{Pd(100)}}(\omega) - \frac{N_{\text{O}}}{2}\sigma_{\text{O}_2\text{(gas)}}(\omega)\right] \quad . \end{aligned}$$

To evaluate this contribution in practice one must thus determine the difference of the surface phonon density of states of the adsorbate covered and of the clean surface, $\sigma_{\text{O/Pd(100)}}(\omega)$ and $\sigma_{\text{Pd(100)}}(\omega)$ respectively, as well as the vibrational frequencies of the gas phase molecule contained in $\sigma_{\text{O}_2\text{(gas)}}(\omega)$.

### 6.1.3 Total Energy Calculations

The total energies required to evaluate Eq. 4.9 are obtained by DFT calculations within the (L)APW +lo scheme [33], using the (GGA-PBE) [18] for the exchange-correlation functional. All surface structures are modeled in a supercell geometry, employing fully-relaxed symmetric slabs (with O adsorption on both sides of the slab) consisting of five (100) Pd layers with an optimized bulk lattice constant of $a = 3.947$ Å (neglecting bulk zero-point vibrations) (see Appendix A). A vacuum region of $\geq 10$ Å ensures the decoupling of consecutive slabs. The (L)APW+lo basis set parameters are listed as follows (see Appendix B): Muffin tin spheres for Pd and O are $R^{\text{Pd}}_{\text{MT}} = 2.1$ bohr and $R^{\text{O}}_{\text{MT}} = 1.1$ bohr, respectively, the wave function expansion inside the muffin tin spheres is done up to $l^{\text{wf}}_{\text{max}} = 12$, and the potential expansion up to $l^{\text{pot}}_{\text{max}} = 6$. The energy cutoff for the plane wave representation in the interstitial region between the muffin tin spheres is $E^{\text{wf}}_{\text{max}} = 20$ Ry for the wave functions and $E^{\text{pot}}_{\text{max}} = 196$ Ry for the potential. Monkhorst-Pack (MP) grids are used for the Brillouin zone integrations. Specifically, we use a $(12 \times 12 \times 1)$ grid for the calculation of $(1 \times 1)$ surface unit-cells. For the larger surface cells, care is taken to keep the reciprocal space point sampling identical by appropriately reducing the employed k-meshes.

For the calculation of the adsorbate vibrational modes, the dynamical matrix is set up by displacing the O atom from its equilibrium position in 0.05 Å steps. Anticipating

Table 6.1: Calculated binding energies $E_b$ (in meV/O atom) for O adsorption in on-surface hollow or bridge sites. The nomenclature and geometric arrangement in the surface unit-cell for the five ordered adlayers at hollow sites are explained in Fig. 6.2.

| | $(3 \times 3)$-O | $p(2 \times 2)$-O | $c(2 \times 2)$-O | $(2 \times 2)$-3O | $(1 \times 1)$-O |
|---|---|---|---|---|---|
| $\theta$ | 0.11 ML | 0.25 ML | 0.50 ML | 0.75 ML | 1.00 ML |
| hollow | 1249 | 1348 | 1069 | 643 | 344 |
| bridge | 1024 | 961 | 801 | 573 | 378 |

a good decoupling of the vibrational modes due to the large mass difference between Pd and O, the positions of all atoms in the substrate below the adsorption site are kept fixed in these calculations. The frequencies and normal modes are then obtained by subsequent diagonalization of the dynamic matrix.

### 6.1.4 Monte Carlo Simulations

Once a reliable set of interactions has been established, evaluating the LGH for any configuration on the lattice corresponds merely to performing an algebraic sum over a finite number of terms, cf. Eq. 6.1. Due to this simplicity, the LGH can be employed to evaluate the system partition function. Here this is done by canonical Monte Carlo (CMC) simulations for O coverages up to $\theta = 0.5$ ML. The employed lattice size was $(40 \times 40)$ with periodic boundary conditions (see Appendix D). Metropolis sampling used 2000 MC passes per lattice site for equilibration, followed by 10000 MC passes per site for averaging the thermodynamic functions. Increasing any of these numerical parameters led to identical results on the accuracy level of interest to this study, *i.e.* here primarily critical temperatures that are converged to within 5-10 K.

For fixed coverage on the surface, ordered structures are identified by evaluating order parameters sensitive to lateral periodicities. We compute the $p(2 \times 2)$ [$\Psi_p(2 \times 2)$, Eq. 5.23] and $c(2 \times 2)$ [$\Psi_{c(2\times2)}$, Eq. 5.27] order parameters as a function of temperature, and the critical temperature for the order-disorder transition is defined by the inflection point where $\Psi_{p(2\times2)}$ or $\Psi_{c(2\times2)}$ go to zero. In parallel, we also derive the critical temperature from evaluating the specific heat, obtaining values that are identical to within 10 K with those inferred from the order parameters (see Appendix D).

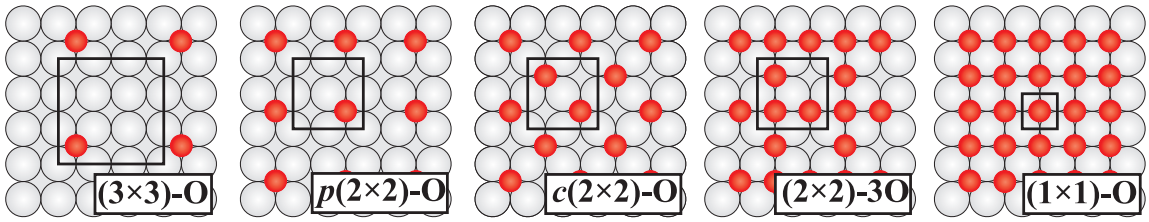


Figure 6.2: Top view of 5 ordered adlayers with O in on-surface hollow sites. The coverage of each configuration from left to right panel is 1/9, 1/4, 1/2, 3/4 and 1 ML, respectively. Light grey spheres represent Pd atoms, small dark grey (red) spheres O atoms, and the black lines indicate the surface unit-cells.

## 6.2 First-Principles Lattice-gas Hamiltonian for O at Pd(100)

### 6.2.1 Energetics of On-Surface Adsorption

Owing to the tendency of oxygen atoms to prefer highly coordinated binding sites at late transition metal surfaces, the high-symmetry fourfold hollow sites appear as the most likely adsorption sites at Pd(100). On the other hand, one cannot exclude *a priori* that the twofold bridge sites are not also metastable, *i.e.* local minima of the potential energy surface. To test this, we slightly displaced a bridge site O adatom in a $p(2 \times 1)$ configuration [(hol-hol)-2 in Table 6.2] laterally towards a neighboring hollow site. The resulting forces relaxed the adatom back to the ideal bridge position, so that at least in this configuration the bridge site is not just a mere transition state, *i.e.* a saddle point of the potential energy surface. As this might also be true for bridge site adsorption in other (local) O adatom arrangements, we calculated the binding energetics of O atoms in the fourfold hollow and in the twofold bridge sites for 5 different ordered overlayers spanning the coverage range up to one ML. The periodicities of these overlayers are explained for the case of hollow site adsorption in Fig. 6.2, and Table 6.1 summarizes the calculated binding energies.

For lower coverages the fourfold hollow site is energetically clearly more stable, which suggests an insignificant contribution of bridge sites to the ordering behavior at coverages up to around 0.5 ML, even if the latter are always metastable sites. Although the reversal of the energetic order between hollow and bridge sites at $\theta = 1$ ML seen in Table 6.1 is intriguing, it clearly occurs in a coverage range where surface oxide formation and eventually three-dimensional oxide cluster growth takes place.[90, 91] Since our interest lies in the on-surface ordering behavior at low coverages, we will therefore focus the LGH expansion for the moment exclusively on adsorption into the fourfold hollow sites, and return to the role of bridge site O atoms in section 6.2.4.

As the next step in the LGH parameterization, average binding energies for different ordered configurations with O atoms in on-surface hollow sites and with surface unit-cells up to $(3 \times 3)$ were correspondingly computed (Table 6.2, and Appendix E).

Table 6.2: Binding energy ($E_b^{DFT}$) for ordered O-Pd(100) configurations with O in the hollow sites at various coverages ($\theta$) and using different functionals (GGA and LDA) and different energy cutoffs. The last two configurations are used to test the derived optimum lateral interaction figures (see text). Top views of all structures can be found in Appendix E.

| Configuration | $\theta$ (ML) | $E_b$ (meV/O atom) | | | | | | | |
|---|---|---|---|---|---|---|---|---|---|
| | | GGA-PBE | | | | | | LDA | |
| | | 18 Ry | | 20 Ry | | 22 Ry | | 20 Ry | |
| | | $E_b$ | $\Delta E_b$ | $E_b$ | $\Delta E_b$ | $E_b$ | $\Delta E_b$ | $E_b$ | $\Delta E_b$ |
| (hol-hol)-1 | 1/9 | 1320 | 0 | 1249 | 0 | 1208 | 0 | 1968 | 0 |
| (hol-hol)-2 | 1/4 | 1409 | 88 | 1349 | 100 | 1312 | 104 | 2069 | 101 |
| (hol-hol)-3 | 1/2 | 1127 | −194 | 1069 | −180 | 1033 | −175 | 1743 | −225 |
| (hol-hol)-4 | 3/4 | 701 | −619 | 644 | −605 | 610 | −598 | 1233 | −735 |
| (hol-hol)-5 | 1 | 405 | −915 | 345 | −905 | 310 | −898 | 914 | −1053 |
| (hol-hol)-6 | 1/2 | 960 | −361 | 897 | −352 | 861 | −347 | 1583 | −385 |
| (hol-hol)-7 | 1/3 | 900 | −420 | 839 | −411 | 802 | −406 | 1527 | −441 |
| (hol-hol)-8 | 2/3 | 808 | −512 | 750 | −499 | 714 | −493 | 1366 | −602 |
| (hol-hol)-9 | 1/6 | 1355 | 35 | 1296 | 47 | 1257 | 49 | 2019 | 51 |
| (hol-hol)-10 | 1/3 | 1261 | −59 | 1204 | −45 | 1167 | −41 | 1389 | −74 |
| (hol-hol)-11 | 1/3 | 1253 | −67 | 1193 | −56 | 1155 | −53 | 1896 | −72 |
| (hol-hol)-12 | 1/2 | 955 | −365 | 900 | −349 | 864 | −343 | 1535 | −433 |
| (hol-hol)-13 | 1/2 | 1071 | −249 | 1013 | −236 | 977 | −231 | 1671 | −297 |
| (hol-hol)-14 | 2/3 | 781 | −539 | 723 | −526 | 687 | −521 | 1346 | −622 |
| (hol-hol)-16 | 1/8 | 1377 | 57 | 1316 | 67 | 1277 | 70 | 2028 | 60 |
| (hol-hol)-17 | 1/4 | 1275 | −45 | 1219 | −31 | 1182 | −26 | 1898 | −69 |
| (hol-hol)-18 | 1/4 | 1216 | −104 | 1156 | −93 | 1118 | −90 | 1856 | −112 |
| (hol-hol)-19 | 1/4 | 1377 | 57 | 1317 | 68 | 1279 | 71 | 2054 | 87 |
| (hol-hol)-20 | 3/8 | 1223 | −97 | 1162 | −88 | 1127 | −80 | 1861 | −107 |
| (hol-hol)-21 | 5/8 | 868 | −452 | 811 | −438 | 775 | −432 | 1442 | −526 |
| (hol-hol)-22 | 2/9 | 1201 | −119 | 1135 | −114 | 1096 | −111 | 1832 | −136 |
| (hol-hol)-23 | 2/9 | 1301 | −20 | 1237 | −12 | 1199 | −9 | 1939 | −28 |
| (hol-hol)-24 | 4/9 | 1089 | −231 | 1026 | −223 | 997 | −221 | 1692 | −276 |
| (hol-hol)-26 | 2/3 | 781 | −539 | 719 | −530 | 682 | −526 | 1357 | −611 |
| (hol-hol)-27 | 2/3 | 768 | −552 | 706 | −543 | 668 | −539 | 1348 | −619 |
| (hol-hol)-15 | 2/3 | | | 725 | −524 | | | | |
| (hol-hol)-25 | 4/9 | | | 947 | −302 | | | | |

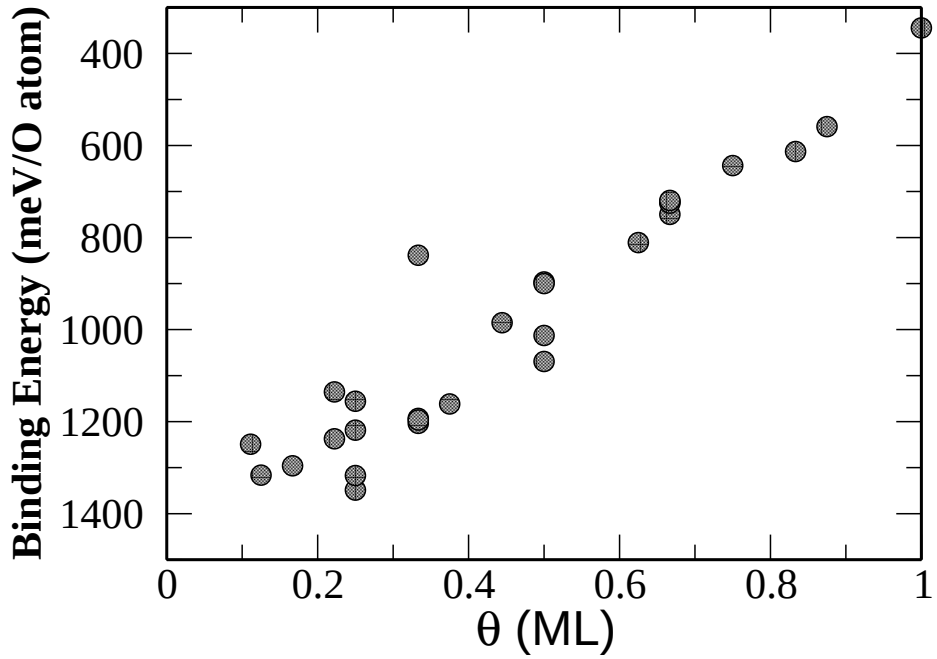


Figure 6.3: Coverage ($\theta$) dependence of the calculated DFT binding energies of the 25 ordered configurations with O atoms in on-surface hollow sites listed in Table 6.2.

Despite our focus on the lower coverage regime, the set does comprise structures with coverages up to 1 ML, since these structures are required during the LGH parameterization to determine in particular the higher-order many-body interactions occurring in (locally) denser adatom arrangements. In most cases configurations that we initially prepared with high coverage of on-surface O atoms were truly metastable, in the sense that they relaxed into geometries where all O atoms remained in the on-surface hollow sites. However, some structures directly relaxed into geometries with O incorporated below the first Pd layer. Since the O-O interaction in these structures does not correspond to the physical situation we want to describe (and would thus mess up the chosen LGH), we excluded these configurations from our set (using a strongly enlarged Pd first interlayer distance as criterion). This left a set of 25 configurations with on-surface O atoms, which was subsequently used in the parameterization of the LGH. The binding energy data of this set is compiled in Table 6.2 and Fig. 6.3, and indicates already overall strongly repulsive lateral interactions, which reduce the binding energy with increasing coverage by up to 1 eV.

### 6.2.2 Lateral Interactions

In order to determine the lateral interaction energies in the LGH, we employ Eq. 6.1 to write down the LGH expression for each of the ordered configurations calculated by DFT (including the interactions with the periodic images in the neighboring cells) see

Appendix E. Neglecting the vibrational contributions in Eq. 6.2 for the moment, we equate the right hand side of Eq. 6.1 with $N_{\mathrm{O}} E_{\mathrm{b}}$ for the corresponding configurations and arrive at a system of linear equations that can be solved for the unknown values of the lateral interaction energies. As was noted, the crucial aspects of this procedure are therefore i) the number and type of interactions included in the LGH expansion, and ii) the number and type of ordered configurations that are computed with DFT to determine the values of these interaction energies. In the following we show how i) is addressed by leave-one-out cross-validation, and ii) is aided by a search for the LGH "ground state" structures and an iterative refinement of the input structure set.

**Leave-one-out Cross-validation (LOO-CV)**

In a truncated LGH expansion with finite ranged interactions, sparse configurations will exhibit a lattice energy that is simply $N_{\mathrm{O}}$ times the on-site energy, as soon as all adsorbed species have distances from each other that exceed the longest range considered interaction. We therefore fix the on-site energy $E_{\mathrm{b}}^{\mathrm{on-site}}$ in Eq. 6.1 to be the DFT binding energy computed for 1/9 ML coverage, cf. Fig. 6.2 and Table 6.1. In this particular $(3 \times 3)$-O configuration, the minimum distance between O adatoms is 8.37 Å, *i.e.* six nearest neighbor sites away. This is larger than the farthest reaching interaction contained in our pool of lateral interactions, cf. Fig. 6.1, so that fixing $E_{\mathrm{b}}^{\mathrm{on-site}}$ to the 1/9 ML $(3 \times 3)$-O binding energy should prevent fitting noise into this parameter.

To get some guidance as to which could be the leading lateral interactions to be included in the LGH expansion, we estimate the predictive power of the LGH by the concept of leave-one-out cross-validation [78, 97–100], Eq. 5.12. In the present work, the sum runs over the remaining $N = 24$ ordered configurations that were calculated with DFT (apart from the 1/9 ML coverage structure used already for $E_{\mathrm{b}}^{\mathrm{on-site}}$), and which have DFT calculated binding energies $E_{\mathrm{b}}^{\mathrm{DFT}}(i)$. The CV score is intended to be a measure of the predictive power of a LGH expansion considering a given set of lateral interactions. In general, one would expect sets containing too few interactions to be too inflexible and thus leading to a high CV score, whereas sets containing too many interactions as loosing their predictive power through overfitting and thereby also leading to a high CV score. The hope is thus to identify the optimum set of considered interactions as that set that minimizes the CV score.

Within this approach, we evaluate the CV score for any set of interactions out of the larger pool of 17 lateral interactions shown in Fig. 6.1. Table 6.3 summarizes these scores subdivided into the optimum sets containing $m$ lateral interactions, *i.e.* listed are the sets that yield the lowest CV score for any arbitrary combination of $m$ lateral interactions out of the total pool of 17. For these sets, we then determine the values of the considered lateral interactions by least-squares fitting to the computed DFT binding energies of all $N = 24$ ordered configurations and also include them in Table 6.3. The minimum CV score reached indeed decreases initially upon adding more interactions to the set, and then increases again for sets containing more than 10

Table 6.3: List of the sets containing $m$ lateral interactions, together with their CV scores and the values determined for the lateral interaction energies (no entry at a position in the table means that this interaction is not contained in the set. Lateral interactions shown in Fig. 6.1, but not shown here are never selected out of the pool). Negative values for the interaction energies indicate repulsion, positive values attraction. The sets shown are those that minimize the CV score among all possible sets containing $m$ lateral interactions out of the pool of 17 shown in Fig. 6.1. The first line for each set corresponds to the data obtained by fitting to 24 ordered DFT configurations, while the second line is obtained after adding 2 additional DFT configurations to the fit (see text). Units for the CV score and lateral interactions are meV.

| m | CV | pair | | | | | trio | | | | | | | quattro | |
|---|---|---|---|---|---|---|---|---|---|---|---|---|---|---|---|
| | score | $V_{1p}$ | $V_{2p}$ | $V_{3p}$ | $V_{4p}$ | $V_{5p}$ | $V_{1t}$ | $V_{2t}$ | $V_{3t}$ | $V_{4t}$ | $V_{5t}$ | $V_{6t}$ | $V_{7t}$ | $V_{1q}$ | $V_{2q}$ |
| 7 | 31 | −344 | −130 | 52 | 14 | | −120 | 132 | −54 | | | | | | |
| | 32 | −338 | −126 | 50 | 16 | | −114 | 117 | −51 | | | | | | |
| 8 | 20 | −324 | −126 | 50 | 16 | | −138 | 120 | −57 | | | | | | 68 |
| | 22 | −314 | −122 | 46 | 18 | | −138 | 108 | −57 | | | | | | 80 |
| 9 | 16 | −292 | −90 | 50 | 10 | | −168 | 60 | −48 | | | −51 | | | 80 |
| | 16 | −296 | −92 | 50 | 10 | | −162 | 63 | −48 | | | −51 | | | 76 |
| 10 | 17 | −290 | −92 | 50 | 10 | | −168 | 60 | −48 | | 1 | −51 | | | 80 |
| | 17 | −298 | −92 | 50 | 10 | | −162 | 69 | −51 | | | −54 | | −28 | 80 |
| 11 | 18 | −284 | −90 | 46 | 12 | 6 | −171 | 57 | −51 | | −3 | −54 | | | 88 |
| | 18 | −296 | −92 | 48 | 10 | 2 | −165 | 69 | −48 | | | −54 | | −28 | 84 |
| 12 | 20 | −292 | −70 | 50 | 8 | 2 | −168 | 486 | −264 | 414 | | −36 | −216 | | 88 |
| | 19 | −296 | −92 | 48 | 10 | 2 | −165 | 69 | −51 | | −3 | −54 | | −32 | 84 |

interactions. Another gratifying feature is that almost always the same interactions are picked out of the pool, *i.e.* the optimum set for $m + 1$ interactions corresponds mostly to those interactions already contained in the optimum set for $m$ interactions plus one additional one. Only very rarely is an interaction that is contained in the optimum $m$ set not selected in the optimum $m + 1$ set. And if this happens, this concerns lateral interactions for which only very small values are determined, and which are thus anyway not meaningful within the uncertainties of our approach. Also in a physical picture, the determined values for the lateral interactions appear quite plausible for $m$ up to 11. The pairwise interactions decrease with increasing distance, and the leading higher-order trio and quattro interactions are smaller in size than the most dominant nearest-neighbor pair interaction. The quinto interaction contained in the pool of possible interactions is never selected. In contrast, the $m = 12$ set shows already clear signs of linear dependencies, with some trio interactions suddenly exhibiting very large values. This continues for expansions containing even more interactions (not listed in Table 6.1), which exhibit more and more obviously meaningless lateral interaction energies.

Another equally important feature of the expansions up to $m = 11$ is the stability of the determined lateral interaction values against adding further interactions to the set. In particular for the optimum sets close to the overall CV minimum, *i.e.* for $m$ equal to 9 or 10, adding another lateral interaction to the set changes the values for the dominant interactions by less than 2 meV. A similar behavior is obtained

for another test to which we subject our expansion: Having calculated another two DFT configurations (the last two configurations in Table 6.2), we increased the set of DFT configurations employed in the fit to $N = 26$ and repeated the entire CV score evaluation. The results are also included in Table 6.3 and show only minimal variations for the sets up to $m = 11$. Almost always the same lateral interactions are picked out of the pool and also their values change by less than 10 meV compared to the previous procedure employing 24 DFT configurations. For the set $m = 12$, adding the two DFT input energies removes the linear dependencies and brings the set back in line with the other sets with fewer interactions. These findings suggest that the expansions are also stable against adding further DFT configurations and we finally identify the set containing 9 lateral interactions and using 24 DFT configurations to determine their values as our optimum LGH expansion.

### Ground State Search

Before moving to the ordering behavior at finite temperatures, a crucial test for the validity of the LGH expansion is that it gives the correct ordered ground states at $T = 0\,\mathrm{K}$, *i.e.* the lowest-energy structures at a given coverage. Here, this refers in particular to the ground states predicted by the DFT energetics, since the latter is the input with which the LGH expansion must be consistent. Obviously, if the energetic order of competing configurations is wrong at the DFT level (*e.g.* due to the employed approximate xc-functional), there is no hope that a correct LGH expansion could cure this problem. To this end, it is useful to replot the DFT database shown in Fig. 6.3 in form of a formation energy plot [78] (Eq. 5.14).

Plotting $\Delta E_f$ versus coverage as done in Fig. 6.4 allows to identify the ground states, *i.e.* lowest-energy ordered phases, that are predicted by the present DFT data set, as those lying on the convex hull.[78] As apparent from Fig. 6.4 the convex hull formed by the DFT data set exhibits three ordered ground states (apart from the trivial ones at the ends of the considered coverage range). Consistent with existing experimental data, these are the $p(2 \times 2)$-O ordered phase at $\theta = 0.25\,\mathrm{ML}$, and the $c(2 \times 2)$-O ordered phase at $\theta = 0.5\,\mathrm{ML}$. A third ordered structure, $(2 \times 2)$-3O at $\theta = 0.75\,\mathrm{ML}$, is at best metastable, since it falls already in the coverage range above $\sim 0.5\,\mathrm{ML}$, for which surface oxide formation sets in.

Using Eq. 5.14 we can evaluate formation energies using the binding energies obtained from the LGH expansion. Since the evaluation of the latter is numerically significantly less demanding, we can sample a much larger configuration space in this case. To this end, we directly enumerate all combinatorially possible ordered structures in surface unit-cells of any symmetry and with a surface area smaller or equal to a $(4 \times 4)$ cell and with O coverages up to 1 ML. The final self-consistent direct enumeration data are also shown in Fig. 6.4. If we first focus on the coverage range up to 0.5 ML, we find the obtained LGH data to be fully consistent with the DFT ground state line. Namely, there is no structure predicted by the LGH expansion that would have an energy that is lower than the DFT convex hull, and the LGH Hamiltonian

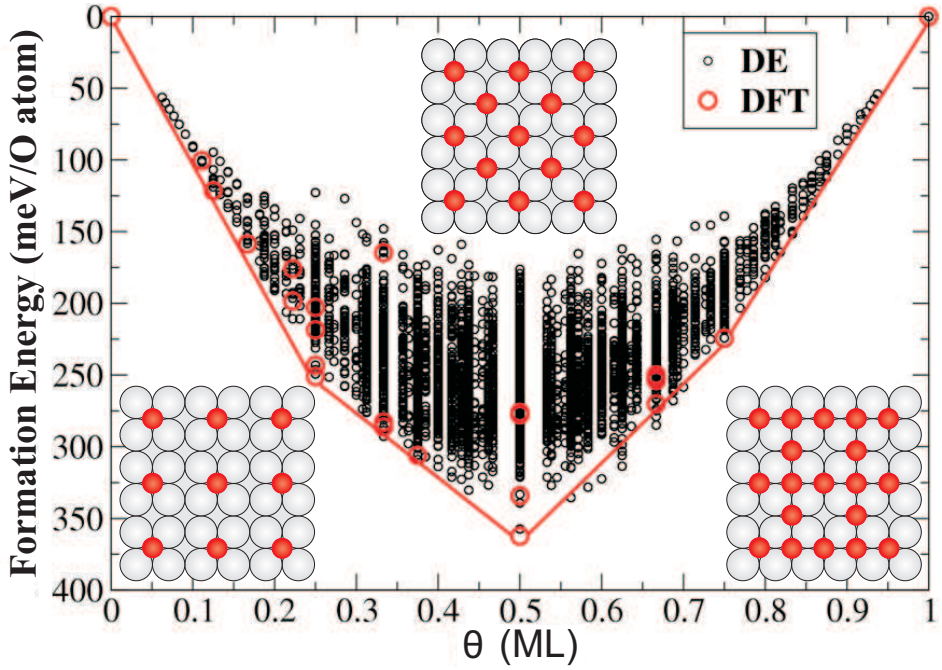


Figure 6.4: Formation energies $\Delta E_f$ as computed with DFT for the 25 ordered configurations shown in Fig. 6.2 (big (red) circles), as well as for all configurations obtained by direct enumeration and using the LGH expansion (small (black) circles), see text. The red line is the convex hull for the DFT data, identifying three ordered ground states shown as insets: $p(2\times 2)$-O at $\theta = 0.25$ ML (left inset), $c(2\times 2)$-O at $\theta = 0.5$ ML (top inset), and $(2\times 2)$-3O at $\theta = 0.75$ ML (right inset). Pd = large, light spheres, O = small, dark (red) spheres.

yields therefore exactly the same ordered ground states as the DFT input data.

In fact, this is not a coincidental result demonstrating the reliability of the achieved LGH expansion, but the end product of an iterative procedure. We used the consistency with the DFT ground state line as another criterion to judge whether more DFT ordered configurations are required as input to the LGH expansion. Initially we had started with a smaller number of DFT configurations as the set discussed above. Having gone through the same CV score evaluation, we had identified an optimum LGH expansion, but had then obtained LGH data points in the direct enumeration leaking below the DFT ground state line. Interpreting the corresponding structures as important input to the LGH expansion, we would ideally calculate them with DFT and add them to the DFT data set used for the LGH expansion. This was, unfortunately, not always possible, when the structures predicted by the LGH had surface unit-cells that exceeded our computational capabilities. In such cases, we looked for other structures in smaller unit-cells, which still contained what we believed were the relevant motifs and computed those with DFT. This procedure was repeated several times, each time adding new structures to the DFT data base, until the present consistent result was obtained.

In the coverage range above $\sim 0.5\,\mathrm{ML}$, the situation is not that perfect. As apparent from Fig. 6.4 there are still several LGH structures slightly below the DFT ground state line. Unfortunately, further improvement along the sketched lines is inhibited by the above described propensity of structures in this coverage range to directly relax into geometries with O incorporated below the first Pd layer. This renders it very tough to provide new on-surface O/Pd(100) structures to the data base and improve on the present LGH expansion. Although not completely satisfying, we therefore contend ourselves with the achieved expansion. Particular care should therefore be exerted, when aiming to use it to describe the higher coverage regime, since denser adatom arrangements can presumably not be fully reliably described. However, due to the overall strongly repulsive interactions, the local occurrence of such denser arrangements at lower coverages is rather unlikely in the MC simulations. Correspondingly, we do expect the results obtained from our expansion to be reliable for the coverage range below $\sim 0.5\,\mathrm{ML}$, on which we focus in the present work.

### 6.2.3 Order-disorder Transition

Having established the ground state ordered structures we proceed to study the ordering behavior at finite temperatures. Experimentally, this was investigated in the coverage range up to 0.6 ML by Chang and Thiel [87]. For defined initial coverages at the surface, they identified the presence of ordered phases at the surface by monitoring LEED superstructure spots corresponding to the different periodicities, and the critical temperatures $T_c(\theta)$ for the order-disorder transition were determined by the inflection point of the vanishing spot intensities at increasing temperatures. Avoiding the O-induced reconstruction at higher coverages, we focus here on the data in the coverage range $\theta < 0.35\,\mathrm{ML}$, in which the $p(2\times 2)$ or a coexistence of $p(2\times 2)$ and $c(2\times 2)$ phases form the ordered structures at low temperatures, cf. Fig. 6.4. For this coverage range, Chang and Thiel determined the onset of desorption in their ultra-high vacuum experiments at much higher temperatures than the order-disorder transition. [87] From this we assume that in the experiments, the coverage at the surface remained essentially constant at the initially prepared coverage value for all temperatures up to the critical temperatures for the order-disorder transition.

The experimental conditions are simulated by canonical MC runs for fixed coverages and at various temperatures. With the definitions in Eqs. 5.23 and 5.27, our order parameters are equivalent to LEED spot intensities, so that the determined critical temperatures for the order-disorder transition can be directly compared to the experimental values. Figure 6.5 shows the $T_c(\theta)$ curve obtained with the optimum LGH expansion together with a reproduction of the experimental data. Overall, we observe very good agreement, both with respect to the absolute temperature values and the trend of increasing critical temperatures with coverage. The largest deviation of about 250 K results at $\theta = 0.25\,\mathrm{ML}$, where theory predicts a small peak in the critical temperature, which is absent in the experimental data and which we discuss in §6.4. Apart from this feature, the agreement with the experimental $T_c(\theta)$ data is

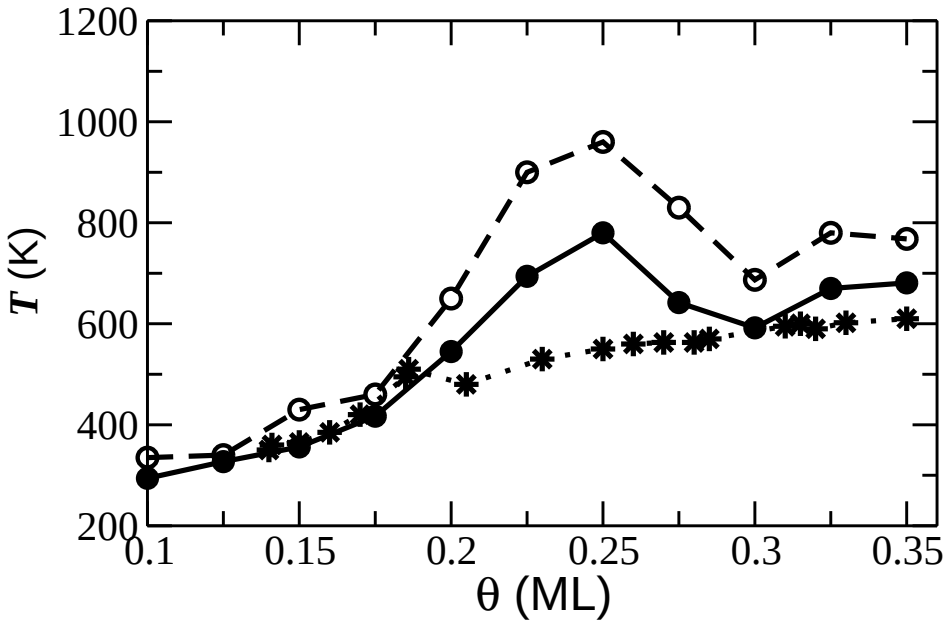


Figure 6.5: $\theta - T$ diagram of the critical temperatures $T_c$ for the order-disorder transition. Shown with stars are the experimental data from Ref. [87], and with solid circles the values obtained when using the optimum LGH expansion. Additionally shown by empty circles are the values obtained when using the LDA as exchange-correlation functional in the DFT calculations (see text).

quite satisfying, if not quantitative.

### 6.2.4 Population of Bridge Sites

The LGH+MC simulations up to now have exclusively focused on O adsorption into the fourfold on-surface hollow sites. The already good agreement obtained with existing experimental data, together with the significantly lower stability of the energetically next favored high-symmetry bridge sites apparent in Table 6.1, seem to suggest that the on-surface low coverage ordering can indeed be understood in terms of the most stable hollow sites only. To verify the implied negligible population of (possibly metastable) bridge sites, even up to the critical temperatures of the order-disorder transition, we proceed by including these sites into the LGH expansion. Since the intention is at this point only to check on the influence of a population of these sites, we consider a reduced pool of possible lateral interactions between O atoms adsorbed in bridge sites (left panel in Fig. 6.6), consisting of the equivalents to the hollow-hollow pair and trio interactions shown in Fig. 6.1. Due to the twofold symmetry of the bridge sites, two different forms at the same interatomic distance exist for some of the interactions, and in addition there is a lateral interaction $V_{0\mathrm{p}}$(br-br) (right panel in Fig. 6.6) at the very short distance of $a/2$ between O atoms sitting in immediately adjacent bridge sites coordinated to the same Pd atom.

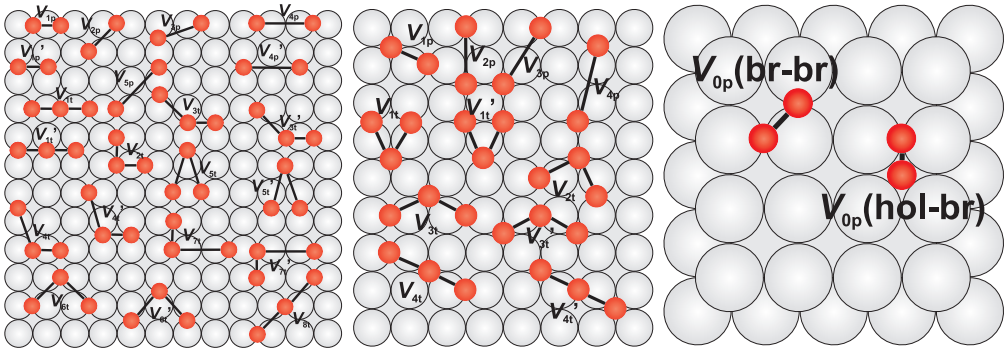


Figure 6.6: Considered lateral interaction figures for bridge-bridge sites (left panel), hollow-bridge sites (middle panel) and infinitely repulsive pair interactions (right panel) on (100) surface. Due to space limitation, we omit the labeling by (br-br) in the left panel, and (hol-br) in the middle panel.

However, when computing with DFT configurations containing such closely neighboring O atoms at a site distance of $a/2$, we always found them to be unstable against relaxation. During the geometry optimization the O atoms moved to sites further apart, indicating a sizable repulsive $V_{0\mathrm{p}}$(br-br). Focusing therefore on 18 ordered configurations (see Appendix E) that do not contain O adatoms at such close distance, the best sets with a varying total number of lateral interactions are determined via LOO-CV in the same manner as for the hollow-hollow interactions. Similar to the results in Table 6.3, the different expansions yield consistently the same two dominant lateral interactions, namely the first-nearest neighbor pair $V_{1\mathrm{p}}(\mathrm{br}-\mathrm{br})$ and second-nearest neighbor pair $V_{2\mathrm{p}}(\mathrm{br}-\mathrm{br})$ interactions. Both are largely repulsive, with $V_{1\mathrm{p}}(\mathrm{br}-\mathrm{br}) \approx -400\,\mathrm{meV}$ and $V_{2\mathrm{p}}(\mathrm{br}-\mathrm{br}) \approx -120\,\mathrm{meV}$. Turning to the leading lateral interactions between O atoms adsorbed in hollow and bridge sites (middle panel in Fig. 6.6), we again found that structures with O atoms in directly adjacent bridge and hollow sites at the very short distance of $a/\sqrt{8}$ [$V_{0\mathrm{p}}$(hol-br): right panel in Fig. 6.6] are not stable against structural relaxation. As for the other interactions, this time the first-nearest neighbor pair interaction and one compact trio interaction turn out to be dominant in the LOO-CV based LGH expansion procedure. They are also largely repulsive, with values of $\approx -240\,\mathrm{meV}$ and $-280\,\mathrm{meV}$, respectively.

We therefore approximately consider the interactions involving bridge site O atoms in the MC simulations by excluding configurations with O atoms at the above described shortest $a/2$ and $a/\sqrt{8}$ distances between bridge-bridge and bridge-hollow site pairs, respectively. In addition, the two next dominant lateral interactions for bridge-bridge and bridge-hollow pairs are explicitly accounted for using the values stated above. The consecutive MC simulations (Fig. 6.7) show virtually no change in the ground state ordered structures and critical temperatures in the coverage range up to $\theta = 0.35\,\mathrm{ML}$. The overall largely repulsive interactions together with the significantly less stable on-site energy compared to adsorption in the hollow sites, efficiently prevents any significant population of bridge sites. For all temperatures up to the

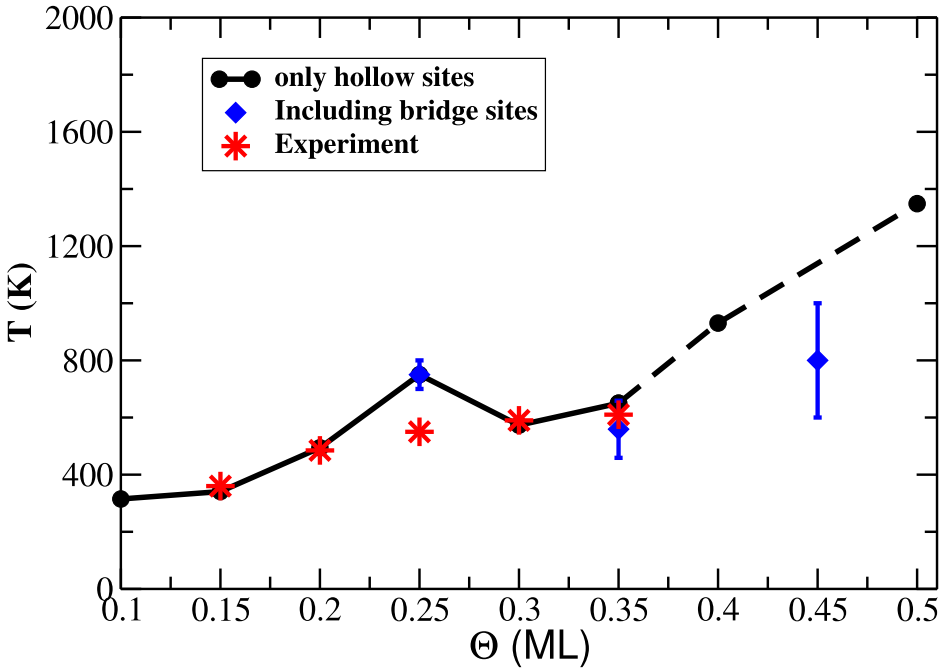


Figure 6.7: Critical temperatures for 0.25, 0.35 and 0.45 ML coverages considering a population of bridge site. The error bars reflect the observed variations in the critical temperature when varying the bridge site lateral interactions as described in the text.

order-disorder transition, we find less than 10 % of the available bridge sites occupied with O atoms, with the highest populations obtained for the larger coverages in the considered range. To make sure that these results are not affected by the uncertainty in the approximately determined lateral interactions, we varied the value of each of the four lateral interactions by ±50 meV and each time reran the MC simulations. This had no influence on the findings, so that we do not expect them to be invalidated by the crude way of how the bridge-bridge and bridge-hollow interactions are considered. Instead, we conclude that up to coverages of $\theta \approx 0.35$ ML and up to the critical temperatures for the order-disorder transition, a population of (possibly metastable) bridge sites plays no role for the on-surface ordering behavior.

## 6.3 Accuracy of First-principles Lateral Interactions

The agreement with the experimental low coverage phase diagram (ground state structures and critical temperatures) suggests that the determined *set* of first-principles lateral interactions is quite reliable. In order to get a better understanding of the explicit uncertainties of the different parameters in this set, we return to a critical discussion of all approximations entering the LGH approach, and scrutinize their in-

fluence on the lateral interaction values. Uncertainties arise on the one hand side due to the truncated LGH expansion and the finite number of configurations employed to parameterize it, and on the other hand due to the approximate first-principles energetics, both with respect to total and vibrational free energy contributions.

### 6.3.1 Uncertainties in the LGH Expansion Procedure

Table 6.3 provides detailed information about the influence of most approximations in the LGH expansion procedure. Inspecting the basically indistinguishable CV score for the expansions with $m = 9$, 10, and 11, one might take the scatter in the correspondingly extracted lateral interactions as a rough measure for the uncertainty introduced by truncating the LGH expansion after a finite number of terms. Concerning the finite number of DFT configurations employed in the parameterization, the achieved consistency of the DFT and LGH ground state line illustrated in Fig. 6.4 gives some indication as to the minimum number of configurations that is required. Correspondingly, the differences in the lateral interaction values determined when extending this minimum set by two further configurations (upper vs. lower line for each expansion in Table 6.3) may be taken as reflecting the uncertainty due to employing a finite number of DFT configurations in the parameterization.

This leaves as remaining *ad hoc* feature of our expansion procedure the decision to not include the on-site energy into the fit, but instead fix it at the value of the sparsest DFT configuration computed, *i.e.* the $(3 \times 3)$-O structure at 1/9 ML. To this end, we redid all LGH expansions in Table 6.3 using the same LOO-CV procedure, but this time including the $(3\times3)$-O structure into the set of DFT configurations and including the on-site energy $E_{\mathrm{b}}^{\mathrm{on-site}}$ into the fit. The results are remarkably consistent, in the sense that the obtained lateral interactions differ in all cases by less than 15 meV from the values compiled in Table 6.3, and for the expansions with $m = 9$, 10, 11 the on-site energy is in fact determined at values that are within 15 meV of the computed binding energy of the $(3\times3)$-O structure. For expansions using fewer lateral interaction figures ($m < 9$) this becomes progressively worse, and the increasing inflexibility of the few-interaction expansions starts to shift errors between the on-site energy and the lateral interactions in an uncontrolled way. We therefore conclude that for expansions with a sufficient number of interaction figures it apparently makes very little difference to include or not include the on-site energy into the fit; the expansions are stable in this respect. In view of the significantly different inaccuracies in the determination of the on-site energy and lateral interactions discussed below, we nevertheless prefer to fix the on-site energy at the value of the sparsest DFT configuration computed.

Summarizing the discussion on the uncertainties in the LGH expansion and parameterization procedure, we estimate the uncertainty introduced by the various approximations to be of the order of 10-20 meV in the dominant lateral interactions. When using the first-principles lateral interactions to determine quantities describing the mesoscopic ordering behavior, this uncertainty needs to be taken into account. Figure 6.8 illustrates this for the determined critical temperatures for the order-disorder

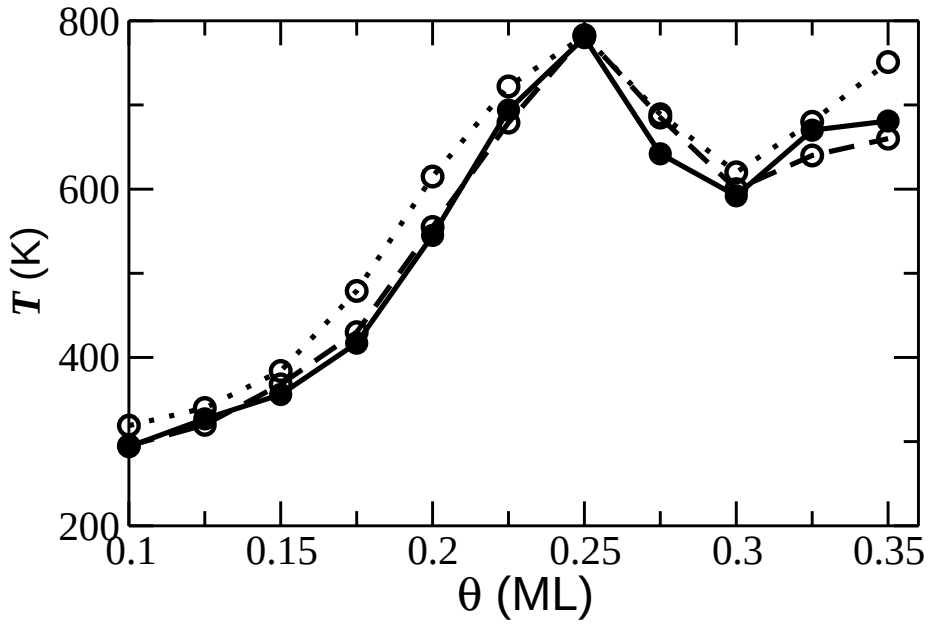


Figure 6.8: $\theta - T$ diagram of the critical temperatures $T_c$ for the order-disorder transition. Compared are the curves obtained when using the first-principles lateral interactions for different LGH expansions compiled in Table 6.3 and each time using 24 DFT configurations in the parameterization: Solid line, full circles: $m = 9$; dashed line, empty circles: $m = 10$; dotted line, empty circles: $m = 11$.

transition by comparing the results obtained for the different LGH expansions with $m = 9$, 10, and 11 in Table 6.3, for which the extracted lateral interactions exhibit a scatter of about the estimated magnitude. The critical temperatures show a variation of less than 100 K and the overall form of the $T_c(\theta)$-curve is almost untouched. The systematics of the present LGH expansion procedure provides thus an error-controlled link between the electronic structure calculations and the mesoscopic statistical simulations, which allows to assess which quantities can be determined with which uncertainty for a given accuracy of the underlying first-principles energetics.

### 6.3.2 Uncertainties in the First-principles Energetics

The energetic parameters in the LGH expansion in Eq. 6.1 comprise total and vibrational free energy contributions. Uncertainties in our approach arise therefore out of the treatment of the vibrational free energy contribution and the approximate DFT energetics, where the latter contains uncertainties due to the numerical setup and due to the approximate exchange-correlation functional. We will discuss these three sources of uncertainties subsequently.

### Vibrational Free Energy Contribution

Separating each of the energetic parameters in the LGH (i.e $F_{\mathrm{b}}^{\mathrm{on-site}}$, $V_{\mathrm{p}}$, $V_{\mathrm{t}}$, ...) into a total energy term and a term due to the vibrational free energy contribution, one arrives at a LGH expansion for the total binding energies and a LGH expansion for the vibrational free binding energies. In section 6.2 the vibrational part was completely neglected by equating the right hand side of Eq. 6.1 solely to the $N_{\mathrm{O}}E_{\mathrm{b}}$ of the different computed configurations. The formally correct procedure would be to evaluate for each configuration also the vibrational free energy contribution to the binding energy, $F_{\mathrm{b}}^{\mathrm{vib.}}(T)$, and consider it in the parameterization. As apparent from Eq. 6.5, what determines this vibrational contribution are the changes of the vibrational modes during adsorption. Since this will predominantly concern the adsorbate-derived vibrational modes, we estimate the order of magnitude of this contribution by the zero point energy ($E^{\mathrm{ZPE}}$) difference arising from the change of the $O_2$ stretch frequency, $\omega_{\mathrm{O_2(gas)}}$, to the O-substrate stretch mode, *i.e.* we approximate Eq. 6.5 roughly with

$$\begin{aligned} F_{\mathrm{b}}^{\mathrm{vib.}}(T) &\sim -\frac{1}{N_{\mathrm{O}}}\left[E^{\mathrm{ZPE}}_{\mathrm{O/Pd(100)}} - \frac{N_{\mathrm{O}}}{2}E^{\mathrm{ZPE}}_{\mathrm{O_2(gas)}}\right] \\ &\sim -\frac{1}{N_{\mathrm{O}}}\sum_{i=1}^{N_{\mathrm{O}}}\frac{\hbar}{2}\left[\omega_{\mathrm{O/Pd(100)}}(i) - \frac{1}{2}\omega_{\mathrm{O_2(gas)}}\right] \quad , \end{aligned} \tag{6.6}$$

where $\omega_{\mathrm{O/Pd(100)}}(i)$ is the O-substrate stretch frequency of the $i$th adsorbed O atom in the corresponding configuration. Within the frozen substrate approximation we calculate the latter stretch mode in good agreement to the experimental data [101] as $\hbar\omega_{p(2\times2)} = 50\,\mathrm{meV}$ in the $p(2\times2)$-O configuration and $\hbar\omega_{c(2\times2)} = 33\,\mathrm{meV}$ in the $c(2\times2)$-O configuration. Compared to the computed stretch frequency of $\hbar\omega_{\mathrm{O_2(gas)}} = 190\,\mathrm{meV}$ of the $O_2$ molecule, this yields an estimated vibrational contribution to the binding energy of $-(\hbar\omega_{p(2\times2)}-\hbar\omega_{\mathrm{O_2(gas)}}/2)/2 = 23\,\mathrm{meV}$ and $-(\hbar\omega_{c(2\times2)}-\hbar\omega_{\mathrm{O_2(gas)}}/2)/2 = 31\,\mathrm{meV}$ per O atom for the two configurations, respectively. In the LGH expansion these contributions get separated into a non-coverage dependent part, which enters the on-site energy, and a coverage-dependent part, which enters the lateral interactions. Taking the difference between the estimated $p(2\times2)$-O and the $c(2\times2)$-O vibrational free energy contributions as a measure of the coverage dependence we thus arrive at an uncertainty of $\sim 5\,\mathrm{meV}$ in the lateral interactions and an uncertainty of $\sim 30\,\mathrm{meV}$ in the on-site energy due to the neglect of vibrational contributions in our approach. The on-site energy is thus much more affected by the predominantly non-coverage dependent shift in vibrational frequency from the $O_2$ stretch to the O-substrate stretch mode.

### Numerical Uncertainties in the DFT Energetics

Turning to the effect of the approximate DFT total energies, we first distinguish between numerical inaccuracies which arise out of the finite basis set, the **k**-point sampling or the chosen supercell geometries, and the more fundamental uncertainty

due to the employed approximate xc functional. In principle, the numerical inaccuracies can be reduced to whatever limit desired, although this may quickly lead to unfeasible computations in practice. In this respect, the finite slab and vacuum thicknesses employed in our supercell setup are the end result of extensive test calculations (see Appendix B), in which these quantities were progressively increased until the relative binding energies were converged to the desired limit of $\pm 10\,\mathrm{meV/O}$ atom. An important point to note concerning the **k**-point sampling is that compatible k-meshes must be employed in calculations involving different surface unit-cells. Compatible in this respect means that always the same points within the Brillouin zone are sampled, even when the latter changes its size due to the different periodicity of the real-space surface unit-cell. As long as this is considered, we found only a negligible influence on the LGH parameters, when increasing the **k**-point density to higher values than the one of our standard computational setup described in section 6.1. This leaves as most notable numerical approximation the finite energy cutoff for the plane wave representation in the interstitial region between the muffin tin spheres in the (L)APW+lo scheme. To this end, we repeated the LGH expansion with the optimum $m = 9$ lateral interaction figure set, cf. Table 6.3, using as input the 24 DFT configurations with total energies computed self-consistently at cutoffs of 18 Ry, 20 Ry and 22 Ry (20 Ry corresponding to our standard basis set size) (Table 6.2). The variations in the determined values for all lateral pair, trio and quattro interactions are within 5 meV. In contrast, what changes notably is the on-site energy (determined by the $(3 \times 3)$-O structure). With increasing cutoff, its value decreases by more than 100 meV, and from the convergence pattern using energy cutoffs up to 30 Ry we expect it to decrease by another $\sim 50\,\mathrm{meV}$, when extrapolating to infinite cutoff. The reason for this different convergence behavior is again that the on-site energy gathers all non-coverage dependent contributions. As such, it includes also all the inaccuracies in the description of the isolated $O_2$ molecule, the total energy of which enters the binding energy of all DFT configurations used in the parameterization alike. The slow convergence of the on-site energy is therefore mainly caused by the known slow convergence in the description of the gas phase molecule. At feasible basis set sizes (for full potential calculations of the present system), the lateral interactions can therefore again be determined at a much higher accuracy than the on-site energy.

### Approximate Exchange-correlation Functional

The uncertainty introduced by the approximate xc functional can not be determined in a comparably quantitative manner as for the numerical approximations, since the exact functional is not known. In order to get at least a feeling for the scatter in the results when using different present-day xc functionals, we evaluated the lateral interactions also within the local density approximation (LDA)[17], which is a functional that by its very construction is known to yield significantly different adsorbate binding energies than the hitherto employed GGA-PBE functional. Most prominently, the two functionals yield *e.g.* binding energies for the free $O_2$ molecule that differ

Table 6.4: First-principles lateral interactions obtained using the LDA and the GGA-PBE as exchange-correlation functional for the optimum set of $m = 9$ interaction figures determined in Table 6.3. Additionally shown are the values obtained, when restricting the LGH expansion in Eq. 6.1 to pairwise interactions only. Units are meV.

| Functional | | pair | | | | trio | | | | quattro |
|---|---|---|---|---|---|---|---|---|---|---|
| | $E_b^{\mathrm{on-site}}$ | $V_{1\mathrm{p}}$ | $V_{2\mathrm{p}}$ | $V_{3\mathrm{p}}$ | $V_{4\mathrm{p}}$ | $V_{1\mathrm{t}}$ | $V_{2\mathrm{t}}$ | $V_{3\mathrm{t}}$ | $V_{6\mathrm{t}}$ | $V_{2\mathrm{q}}$ |
| GGA | 1249 | −292 | −90 | 50 | 10 | −168 | 60 | −48 | −51 | 80 |
| LDA | 1968 | −344 | −128 | 54 | 10 | −168 | 72 | −45 | −45 | 64 |
| GGA, pair only | 1249 | −360 | −128 | 48 | – | – | – | – | – | – |
| LDA, pair only | 1968 | −410 | −160 | 52 | – | – | – | – | – | – |

by 1.35 eV (!) when computed with our accurate full-potential (L)APW+lo scheme. All 24 DFT input configurations were correspondingly calculated fully relaxed (Table 6.2) using the LDA and the LDA optimized lattice constant ($a = 3.836$ Å). Using their energetics in the LGH expansion procedure, we obtain the lateral interaction energies compiled in Table 6.4 for the previously discussed optimum set with $m = 9$ interaction figures.

Comparing to the results obtained before using the GGA-PBE as xc functional, also compiled in Table 6.4, one clearly observes a similar pattern as before for the numerical uncertainties in the sense that the difference between the two xc functionals shows up predominantly in the on-site energy. In fact, the lateral pair, trio and quattro interactions are strikingly little affected, considering that the two xc functionals yield adsorbate binding energies that differ on the order of $\sim 0.7$ eV. The reason is again as before, *i.e.* most of this variation arises out of the description of the free gas phase molecule, which affects all computed configurations alike and therefore solely enters the non-coverage dependent LGH parameter $E_{\mathrm{b}}^{\mathrm{on-site}}$. The known larger variation of adsorbate binding energies when using different present-day xc functionals is often put forward as a generic argument against the reliability or usefulness of first-principles lateral interactions. At least for the present system, we can now qualify this concern. Our analysis shows that the on-site energy can indeed not be determined with a high accuracy, cf. Table 6.4. However, the lateral interactions themselves can be. For the O/Pd(100) system, the uncertainty due to the approximate xc functional seems to be of the order of 50 meV for the dominant pair interactions. The farther ranging and higher-order interaction terms in Table 6.4 exhibit intriguingly an even smaller scatter.

The largely different accuracy with which on-site energy and lateral interactions can be determined allows also to scrutinize when the first-principles parameters may be employed to reliably describe mesoscopic system quantities. We focus here on the effect of the approximate xc functional, since this leads to a larger uncertainty compared to the discussed treatment of the vibrational free energy contributions and the numerical inaccuracies in the total energies. Since the on-site energy has no

effect on the order-disorder transition in a canonic adsorbate ensemble, the small variation in the lateral interaction energies exhibited in Table 6.4 rationalizes the good agreement with the experimental critical temperatures. Using the determined LDA interaction values we indeed obtain a $T_c(\theta)$ curve that is very similar to GGA-PBE as shown in Fig. 6.5: The overall shape of the curve including the peak structure is completely preserved, and the absolute $T_c$ values are merely shifted by up to 200 K to higher temperatures. This variation may thus be taken as an indication of the accuracy with which this quantity can presently be calculated from first-principles. For other quantities, where the on-site energy enters explicitly, this accuracy will be significantly worse. Staying with the presently available experimental data for the O/Pd(100) system [87], this would *e.g.* be the case when aiming to compute the measured temperatures for oxygen desorption, where the on-site energy enters explicitly.

One can, of course, always argue in terms of a smaller uncertainty by favoring a particular approximate xc functional over others (*e.g.* because the functional is known to reproduce well similar system quantities). In the sense of first-principles theory, the more appropriate approach would, however, be to eliminate errors by using higher-level theory. In this respect, one could suitably exploit a finding like for the present system that most of the xc uncertainty gets concentrated in the on-site energy by *e.g.* computing only the latter with a higher-level technique (or appropriate xc-correction scheme [102]) and using the already quite accurate lateral interactions determined by present-day xc functionals.

## 6.4 Comparison to Empirical Parameters

Instead of a first-principles determination, the traditional method to obtain the strengths of lateral interactions has been to adjust the predictions from atomistic lattice-gas models to experimental observations of the coverage and temperature dependence of on-surface ordering. To keep the number of free fit parameters low, the focus has often been on pair interactions only, *i.e.* Eq. 6.1 was truncated after the pair terms, and usually also only the dominant short-ranged pair interactions were considered. In this respect, extensive model studies [79–86] have shown that the $p(2\times2)$ and $c(2\times2)$ ordering frequently found at (100) cubic metal surfaces requires nearest neighbor repulsions that are so strong that they effectively yield a site exclusion ($-V_{1\mathrm{p}} >> k_BT$), as well as weaker second nearest neighbor repulsions. In order to produce a true $p(2\times2)$ ordering further interactions are required. This can either be a third nearest neighbor attraction, or a fourth nearest neighbor repulsion, or more generally a combination of these interactions that fulfills $V_{3\mathrm{p}} - V_{4\mathrm{p}}/2 > 0$.[82, 86]

Comparing with our first-principles data compiled in Table 6.4, we see that they perfectly fit into this expected qualitative pattern: Strong first nearest neighbor repulsion, weaker second nearest neighbor repulsion, and the combination $V_{3\mathrm{p}} - V_{4\mathrm{p}}/2$ is attractive. However, differences arise when turning to a more detailed modeling of

the experimental O/Pd(100) phase diagram of Chang and Thiel [87]. For a lattice-gas model considering nearest-neighbor site exclusion and finite second and third nearest neighbor interactions, Liu and Evans showed that the best overall topological agreement with the experimental phase diagram is achieved for $V_{3p} \approx -V_{2p}$.[86] In particular, the position of the disordered to $c(2 \times 2)$-O transition line shifts notably with the ratio of $-V_{2p}/V_{3p}$, and for a ratio of $\sim 1$ the $T_c(\theta)$ curve no longer exhibits the peak structure at $\theta = 0.25\,\mathrm{ML}$ visible in the first-principles curve in Fig. 6.5. Since this resembles the shape of the experimental curve better, it could indicate that the calculated first-principles ratio of $-V_{2p}/V_{3p} \approx 3$ is too large. On the other hand, it is intriguing to see that both LDA and GGA-PBE yield roughly the same $-V_{2p}/V_{3p}$ ratio and in turn clearly a peak in the $T_c(\theta)$ curve, cf. Fig. 6.5. Since Chang and Thiel discuss also a rather large uncertainty of $\sim 0.05\,\mathrm{ML}$ in their experimental coverage calibration [87], a careful remeasurement of the experimental $T_c(\theta)$ curve would thus be very interesting to fully settle this point.

A much more fundamental difference between the set of empirical and first-principles lateral interactions is that the former is restricted to just pairwise interactions. To test the validity of this frequently applied approximation, we restrict our LGH expansion to pair interactions up to third nearest neighbors and repeat the parameterization using exactly the same 24 DFT configurations as in section 6.2. The resulting interactions are also compiled in Table 6.4, using the LDA or GGA-PBE as xc functional. Comparing with the values obtained for each functional from the proper LGH expansion (and using exactly the same first-principles input), we note significant differences. The dominant short-ranged interactions are overestimated, in the case of the first nearest neighbor pair interaction by $\sim 60\,\mathrm{meV}$. Overall, the lateral interactions are too repulsive, which is a consequence of them having to mimic the effect of the neglected overall repulsive trio interactions. As expected, the true microscopic lateral interactions are thus blurred by spurious contributions arising from the invalid assumption that lateral interactions at metal surfaces could be expressible in pair-only terms. The invalidity of this assumption is already clearly demonstrated by the similar magnitude of the dominant trio interactions ($V_{1t}, V_{2t}$, *etc.* in Table 6.4) compared to the dominant short-ranged pair interactions, which necessarily reduces pair-only restricted expansions to a set of *effective* parameters at best.

The deficiencies introduced by such an effective description are not only the lack of microscopic meaning of the lateral interactions themselves, but also errors in the mesoscopic system properties calculated with these interactions. This is again exemplified for the order-disorder transition in Fig. 6.9, which shows that the $T_c(\theta)$ curve derived from the pair-only lateral interactions in Table 6.4 differs notably from the curve derived from the corresponding proper LGH expanded lateral interactions. The critical temperatures are up to 350 K higher, even though being based on exactly the same first-principles energetics. The shortcomings due to the restricted LGH can also not be overcome, when turning to a completely empirical approach and adjusting the lateral interaction values to reproduce experiment. Within the above described lattice-gas model with pair interactions to third nearest neighbor and fitting to the

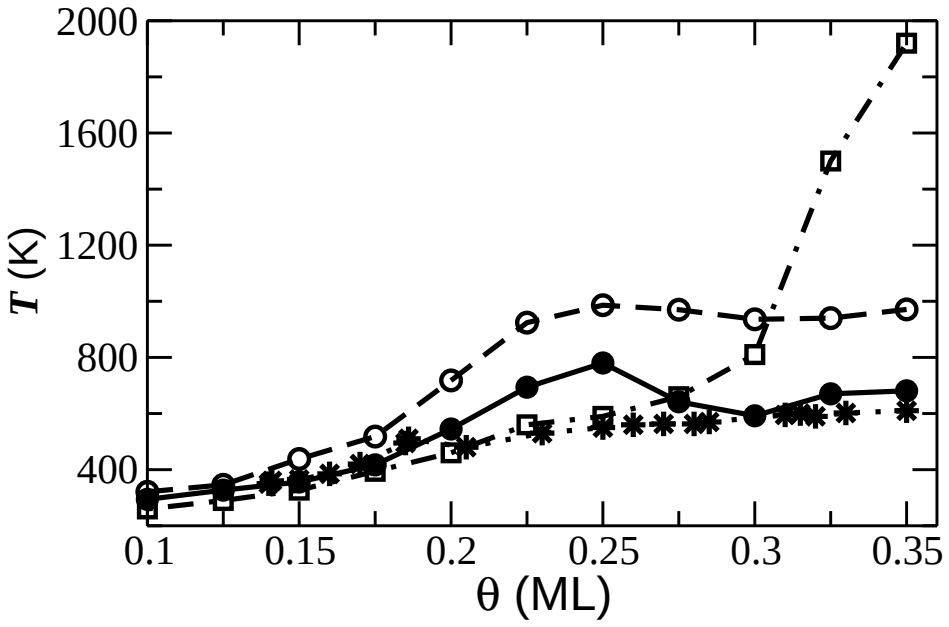


Figure 6.9: $\theta - T$ diagram of the critical temperatures $T_c$ for the order-disorder transition. Shown with stars are the experimental data from Ref. [87], and with solid circles the values obtained when using the optimum GGA-based LGH expansion, cf. Table 6.4. These curves are compared to those obtained, when considering only pair interactions in the LGH: Using the GGA values compiled in Table 6.4 (empty circles), or the empirically adjusted values by Liu and Evans (empty squares), see text.

critical temperatures in the coverage range below 0.25 ML, Liu and Evans determined $V_{1p} \approx 500$ meV and $V_{3\mathrm{p}} = -V_{2\mathrm{p}} \approx 40$ meV [86], *i.e.* lateral interactions that differ considerably from the first-principles values compiled in Table 6.4. As apparent from Fig. 6.9, these empirical parameters do indeed lead to an excellent fit of the experimental $T_c(\theta)$ curve in the coverage range up to 0.25 ML. However, outside the fitted coverage range, the effective description rapidly breaks down and predicts a critical temperature curve in qualitative disagreement with experiment. Already at a coverage of 0.35 ML, *i.e.* only 0.1 ML outside the fitted coverage range, the predicted critical temperature for the order-disorder transition is wrong by 1200 K.

The spurious contributions contained in the effective pair interactions also prohibit a systematic determination of which pairwise interactions to consider. In the systematic LGH expansion detailed in section 6.2, the lateral interactions are chosen out of a larger pool of lateral interactions and the ultimately determined pair interactions decrease in magnitude with distance. In contrast, when we extend the pair-only expansion to include the fourth and fifth nearest neighbor interaction, we obtain a negligible $V_{4\mathrm{p}}$ of -2 meV, but a $V_{5\mathrm{p}}$ of -18 meV. The spurious contributions contained in the effective $V_{5\mathrm{p}}$ thus feign that such far ranging interactions are significant, whereas the proper first-principles LGH expansion shows no significant interactions between

adsorbates at distances larger than the fourth nearest neighbor site. In empirical approaches this uncertainty (or degree of arbitrariness) as to which interactions to consider is even further aggravated, since there are typically several sets of pairwise interactions which equally well fit the less stringent mesoscopic ordering behavior.

## 6.5 Conclusions

Summarizing this chapter, we have presented a first-principles lattice-gas Hamiltonian study of the on-surface ordering behavior of O adatoms at the Pd(100) surface. A key feature of the approach is the systematics of the LGH expansion, both with respect to the selection of the considered lateral interactions and with respect to the ordered configurations, the DFT energetics of which is employed in the parameterization. In contrast to empirical or semi-empirical *ad hoc* parameterizations the approach does provide an error-controlled link between the electronic structure regime and the system's mesoscopic ensemble properties. Carefully scrutinizing the approximations entering at the level of the underlying DFT energetics, at the LGH interface and in the statistical simulations, we identify the approximate exchange-correlation functional employed to obtain the DFT energetics as the major source of uncertainty in the approach. This uncertainty affects predominantly the on-site energy, and only to a much lesser degree the lateral interactions themselves. Comparing LDA and GGA exchange-correlation functionals, we estimate the accuracy of the latter to be within $\sim 60\,\mathrm{meV}$ for the present system. This shows that the known much larger variation of adsorbate binding energies with different xc functionals can not be used to uncritically question the reliability or usefulness of lateral interactions derived from first-principles *per se*.

The rather high accuracy of the first-principles lateral interactions also rationalizes the obtained good agreement with the experimental low coverage phase diagram for the O/Pd(100) system, *i.e.* the ground state ordered structures and critical temperatures for the order-disorder transition. An important feature of the set of lateral interactions is that it contains many-body interactions of comparable magnitude to the dominant short-ranged pair interactions. This demonstrates the invalidity of the assumption of exclusively pairwise interactions between adsorbates at metal surfaces that is frequently applied in empirical approaches. Indeed, when restricting the LGH expansion to just pairwise lateral interactions, we find that this results in effective interactions which contain spurious contributions that are of equal size, if not larger than any of the uncertainties *e.g.* due to the approximate xc functional. These effective parameters lack microscopic meaning and lead to uncontrolled errors in the mesoscopic system properties calculated with them. In the present system, this is illustrated clearly by critical temperatures that are up to 350 K higher than the ones obtained with the proper set of lateral interactions, even though both sets were based on exactly the same first-principles energetics.

We conclude that at least for the present system, an appropriate first-principles sta-

tistical mechanics framework and present-day DFT energetics can determine lateral interactions at least as reliably as the traditional empirical approaches, and without suffering from the non-uniqueness in the selection of pairwise-additive adspecies interactions which reasonably fit available data.

# Part III

# Ordering Behavior of Oxygen Atoms under the Influence of a Step

# Chapter 7

# Oxygen Adsorption at Pd(11$N$)($N$=3,5,7) Vicinal Surfaces

Important materials processes and functions like oxide formation or oxidation catalysis have motivated a wealth of Surface Science studies on low Miller index surfaces of late transition metals (TMs) and their interaction with oxygen.[104] In recent years, experimental work has been increasingly complemented by independent information from first-principles theoretical studies, which appropriately account for the band structure of the TMs through supercell setups with periodic boundary conditions.[105] En route towards an atomic-scale understanding of real TM surfaces, investigating the role of defects like steps, kinks or vacancies with similar rigor and detail as established for the low-index surfaces becomes a key endeavor. With respect to catalysis and oxide formation, such defects are frequently discussed as playing a prominent role, *e.g.* in form of active sites facilitating molecular dissociation or as nucleation centers.[104, 106, 107]

As discussed in Chapter 4, steps and kinks are suitably studied at high-index vicinal surfaces, which contain regular arrays of steps of specific orientation, separated by terraces of specific width. The advantage of these surfaces is that they (ideally) only contain one defined type of step in always the same local environment, and are amenable to periodic boundary supercell calculations. The disadvantage is that the extracted step properties can be masked by step-step interactions at decreasing terrace widths. This holds in particular, since one would precisely try to perform first-principles calculations addressing a certain step type by employing vicinal surfaces with a minimum terrace width, in order to reduce the computational burden. In this respect and as a prelude to the LGH parameterization including a step performed in the following chapter, we concentrate here on a systematic study of a family of vicinal surfaces that always exhibit the same step type, but terraces of increasing width. Examining the geometric and electronic structure of the clean and oxygen-covered surfaces, we can then extract by how much the local properties at a given step are affected by the presence of the neighboring steps.

Specifically, we use DFT to study the series of vicinal Pd(11$N$) ($N$=3,5,7) surfaces,

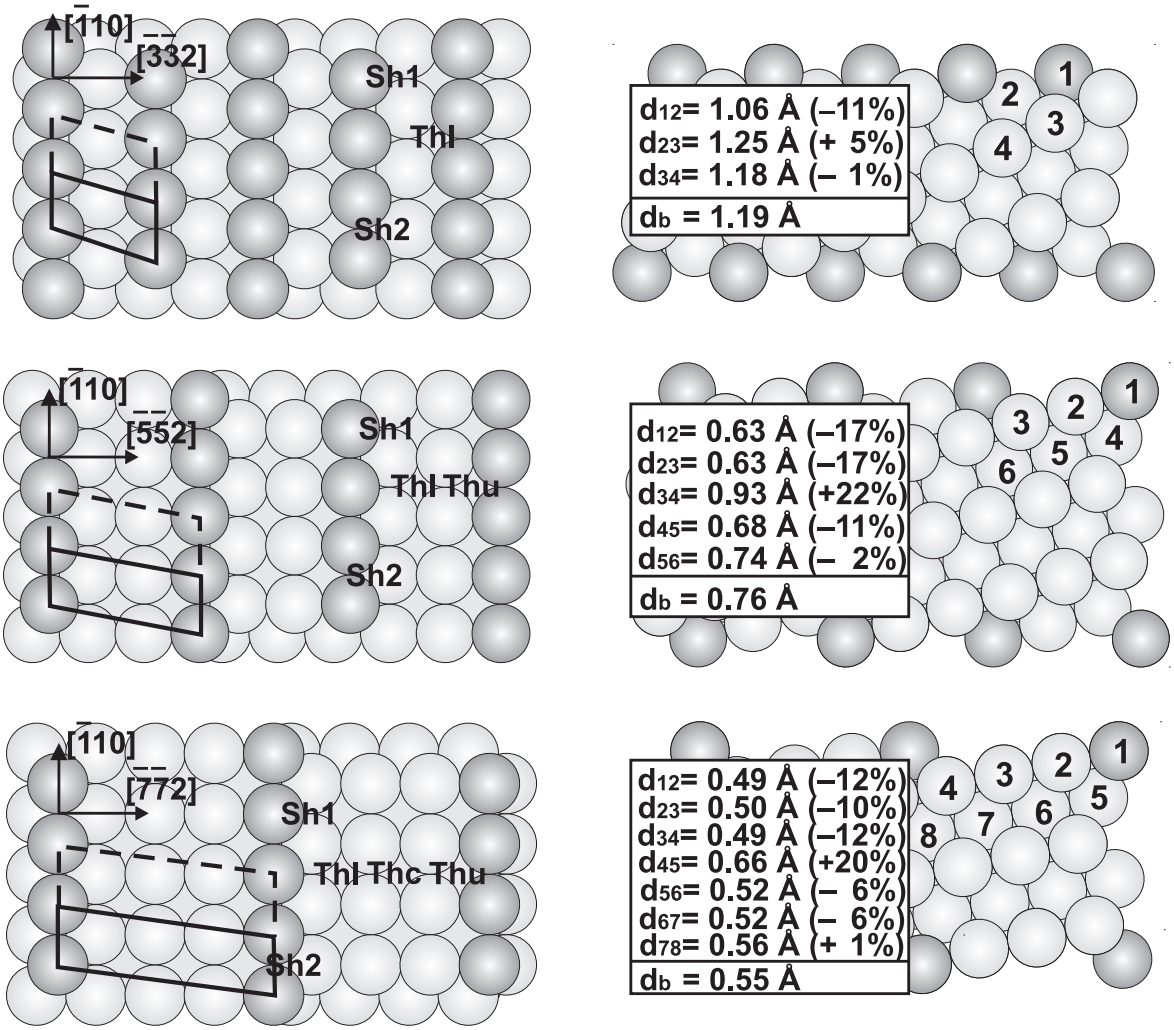


Figure 7.1: Top and side views of the atomic geometry of the family of Pd(11$N$) surfaces ($N$=3 [top panel], 5 [middle panel], 7 [bottom panel]) surfaces. Light grey spheres represent Pd atoms, while the Pd step atoms are shown in grey, to better illustrate the step structure in the top view. Additionally shown in the top view are the $(1 \times 1)$ and $(1 \times 2)$ surface unit-cells (solid and dashed lines, respectively), as well as the high-symmetry sites for oxygen adsorption considered (see text). The side view includes also the layer numbering and the relaxed spacings $d_{ij}$ between layers $i$ and $j$ (and in parenthesis the percent change $\Delta d_{ij}$ with respect to the bulk interlayer spacing $d_b$).

additionally comparing them to the low-index Pd(100) and Pd(111) surfaces. Figure 7.1 explains the geometric structure of the vicinals, which exhibit (111) steps and (100) terraces with 2, 3 and 4 atomic rows for Pd(113), Pd(115) and Pd(117), respectively. Besides the surface energetics and geometric structure with and without oxygen adsorbates, we also study the local density of states (LDOS) and initial-state surface core-level shifts (SCLS) as measures of the surface electronic structure. Apart from insight into details of the oxygen-metal chemical bond, our major conclusion in this part of the work is that the oxygen adsorption properties at the (111) step of Pd(117) (with 4 atomic row terraces) are already very little disturbed by the presence of the neighboring steps of the vicinal.

## 7.1 Computational Details

As Chapter 6, the DFT calculations were also performed within the FP-(L)APW+lo scheme [33], using the (GGA-PBE)[18] for the exchange-correlation (xc) functional. All surfaces were modeled by supercells, employing symmetric slabs (with O adsorption on both sides of the slab) and a minimum vacuum thickness of 12 Å to ensure the decoupling of consecutive slabs. The slab thickness was 7 layers for Pd(111) and Pd(100), 9 layers for Pd(113), 17 layers for Pd(115) and 19 layers for Pd(117), cf. Fig. 7.1. For the oxygen adsorption studies the thickness of the Pd(113), Pd(115) and Pd(117) slabs was increased to 13, 17, and 23, respectively. All structures were fully relaxed, keeping only the atomic positions in the central two slab layers at their fixed bulk positions.

The (L)APW+lo basis set parameters are as follows (see Appendix C): $R_{\mathrm{MT}}^{\mathrm{Pd}} = 2.1\,\mathrm{bohr}$, $R_{\mathrm{MT}}^{\mathrm{O}} = 1.1\,\mathrm{bohr}$, wave function expansion inside the muffin tin spheres up to $l_{\mathrm{max}}^{\mathrm{wf}} = 12$, and potential expansion up to $l_{\mathrm{max}}^{\mathrm{pot}} = 6$. The energy cutoff for the plane wave representation in the interstitial region between the muffin tin spheres was $E_{\mathrm{wf}}^{\mathrm{max}} = 20\,\mathrm{Ry}$ for the wave functions and $E_{\mathrm{pot}}^{\mathrm{max}} = 196\,\mathrm{Ry}$ for the potential. The core states are treated fully relativistic, while the semi-core and valence states are treated within a scalar relativistic approximation, *i.e.* spin-orbit coupling is included (neglected) for the core (semi-core and valence) states. Monkhorst-Pack (MP) grids were used for the Brillouin zone integrations. Specifically, we used $(6 \times 10 \times 1)$, $(4 \times 10 \times 1)$ and $(3 \times 10 \times 1)$ grids for the calculations of $(1 \times 1)$ surface unit-cells of Pd(113), Pd(115), and Pd(117), respectively. The selected calculations on Pd(100) and Pd(111) used for the comparison with low-index surfaces were done with a $(12 \times 12 \times 1)$ grid. For the larger surface cells, the grids were reduced accordingly to keep the same sampling of the reciprocal space.

Limitations in the numerical accuracy of our results come predominantly from the finite (L)APW+lo basis set and the supercell geometry. We performed extensive test calculations to estimate the importance of the various numerical approximations. Our tests concentrated on the convergence of the crucial energetic quantities of our study, using the surface energies of all five surfaces, as well as the oxygen binding

energy in the Thu and Sh2 site (see Fig. 7.1 and definition below) in $(1 \times 1)$ unit-cells on the vicinals as representatives. Naming here only the factors that are most critical for the convergence, we increased the employed cutoff for the plane-wave basis set systematically from 20 to 30 Ry, doubled the k-mesh density, and tested slab thicknesses with up to twice as many layers. From all these tests we estimate that our reported surface energies are converged to within 2 meV/Å$^2$, and the O binding energies to within 150 meV/O atom. However, much more important for our study comparing the properties at different surfaces and sites are relative binding energy and surface energy *differences*. For these differences, a large part of the uncertainty, *e.g.* due to the description of the isolated O atom, cancels out, and our tests show that the numerical uncertainty for $\Delta E_\mathrm{b}$ of O atoms at different sites or at different surfaces is $\pm 50$ meV/O atom, and the relative surface energy differences are converged to within 0.5 meV/Å$^2$. As will become apparent below, this does not affect our discussion and conclusions.

## 7.2 Clean Vicinal Surfaces

### 7.2.1 Geometric Structure

The obtained surface relaxation pattern for the low-index Pd(100) and Pd(111) surfaces is as expected in view of the trend understanding over the late 4*d* TMs *e.g.* discussed by Methfessel, Hennig and Scheffler [114]. For both surfaces we obtain only insignificant ($< 1\,\%$) variations in the interlayer spacings of the topmost layers with respect to the bulk value.

Turning to the surface relaxation for the three vicinal surfaces, our results are summarized aside with the geometry side views in Fig. 7.1. One can clearly discern that the largest deviations from the bulk spacing are concentrated to those layers, in which the atoms have a lower coordination than in the bulk. When performing our slab thickness tests, we also fully relaxed slabs with up to twice as many layers as those shown in Fig. 7.1. However, no changes in the interlayer spacings were observed compared to the values listed in Fig. 7.1, and the deeper layers showed insignificant relaxations. Focusing therefore on the larger relaxations in the topmost layers, we notice that the signs of the percent changes $\Delta d_{ij}$ of the interlayer spacings compared to the bulk spacing exhibit a certain pattern. Starting with the topmost layer distance, we namely have $-+-$ for Pd(113), $--+-$ for Pd(115) and $---+-$ for Pd(117), where "$-$" corresponds to a contraction and "$+$" to an expansion of the interlayer spacing.

There are two theoretical models that explain these sequences as a consequence of Smoluchowski's ideas of charge smoothing, *cf.* Fig. 7.2, (or equivalently, in a chemical language, through the bond-order bond-length correlation concept) [115–117]: The *atom rows* model [118] predicts that for a surface with $n_\mathrm{row}$ atomic rows on the terraces, the first $(n_\mathrm{row} - 1)$ topmost interlayer spacings exhibit a contraction,

Table 7.1: Comparison of the multilayer relaxation sequence of the Pd(11$N$), ($N = 3, 5, 7$) vicinals to the key quantities of the atom-rows model [118] and NN coordination model [119]. A "−" in the relaxation sequence stands for a contraction of the corresponding interlayer spacing, and a "+" for an expansion. $n_{\mathrm{row}}$ is the number of atomic rows on the terraces and $n_{\mathrm{NN}}$ the number of undercoordinated layers at the surface. For comparison, the coordination is 12 in the fcc bulk, and 8 for a (100) terrace atom.

| Vicinal Surface | $n_{\mathrm{row}}$ | NN Coordination For Topmost Layers | $n_{\mathrm{NN}}$ | Relaxation Sequence |
|---|---|---|---|---|
| Pd(113) | 2 | 7, 10, 12, 12, ... | 2 | $-+-$ |
| Pd(115) | 3 | 7, 8, 10, 12, 12, ... | 3 | $--+-$ |
| Pd(117) | 4 | 7, 8, 8, 10, 12, 12, ... | 4 | $---+-$ |

Table 7.2: Computed surface energies of the low-index Pd(100) and Pd(111) surfaces, as well as of the three vicinal (Pd(11$N$), ($N = 3, 5, 7$)) surfaces. Bulk-truncated refers to a bulk-truncated surface geometry, while relaxed corresponds to a fully relaxed surface geometry. We present all values in meV/Å$^2$ and in eV/surface atom.

| meV/Å$^2$ | Pd(111) | Pd(113) | Pd(115) | Pd(117) | Pd(100) |
|---|---|---|---|---|---|
| Bulk-truncated | 87.9 | 100.3 | 99.4 | 99.1 | 96.4 |
| Relaxed | 87.9 | 98.3 | 97.3 | 97.4 | 96.3 |
| eV/atom | Pd(111) | Pd(113) | Pd(115) | Pd(117) | Pd(100) |
| Bulk-truncated | 0.59 | 1.30 | 2.01 | 2.76 | 0.75 |
| Relaxed | 0.59 | 1.27 | 1.97 | 2.71 | 0.75 |

while the $n_{\mathrm{row}}$th one expands. The *nearest-neighbor (NN) coordination* model [119] focuses instead on those surface layers which have a NN coordination smaller than the bulk. For a surface where the $n_{\mathrm{NN}}$ topmost layers are undercoordinated, the topmost ($n_{\mathrm{NN}} - 1$) interlayer spacings are then expected to contract, while the $n_{\mathrm{NN}}$th one expands. As apparent from Table 7.1 the multilayer relaxation sequences obtained for the present family of Pd(11$N$) vicinals conforms with both models, which is no surprise, since for the case of (111) steps the atom-rows model is actually a special case of the more general NN coordination concept.

### 7.2.2 Energetics and Electronic Structure

Table 7.2 summarizes the computed surface energies of the three vicinal surfaces and compares them to the surface energies of the two low-index surfaces Pd(100) and Pd(111). Due to the negligible layer relaxation of the latter two surfaces, a full

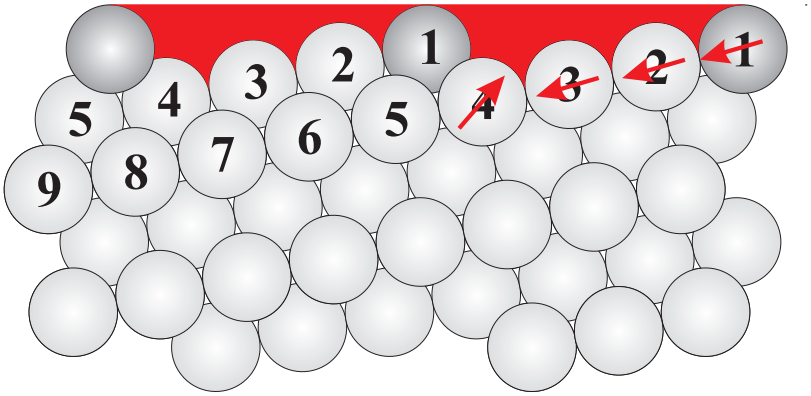


Figure 7.2: Smoluchowski smoothing picture behind the observed relaxation patterns illustrated for the Pd(117) surface: The undercoordinated terrace atoms, 1, 2, 3 and 4, will contribute electrons to diminish the density gradient in the trench (indicated schematically by the red region). Correspondingly, the interlayer electron density below these atoms will decrease. Trying to preserve the bulk electron density value, an inward relaxation of the atoms results, and the interlayer spacing decreases. The inward movement of these atoms are assisted by a concomitant outward movement of atom 4. As a result of all these movements (schematically indicated by the red arrows), including registry relaxation Eq. 4.2, on Pd(117) the first 3 layers will relax inward, while the 4th layer will move out.

relaxation of the surface geometry has only a negligible effect on their surface energy. As expected, this is different for the more open vicinal surfaces, where the atomic relaxation leads to some lowering. The values obtained for Pd(111) and Pd(100), 0.59 eV/atom and 0.75 eV/atom respectively, are in good agreement ($\pm 5\,\%$) with recent other DFT-GGA studies [113, 120, 121]. However, they are significantly different to two earlier trend studies, namely the linear-muffin-tin-orbital (LMTO) GGA work by Vitos *et al.* (Pd(111) 0.82 eV/atom; Pd(100) 1.15 eV/atom)[123], and the LMTO work by Methfessel, Hennig and Scheffler employing the local-density approximation (LDA)[122] to the xc functional (Pd(111) 0.68 eV/atom; Pd(100) 0.89 eV/atom)[114]. To assess the effect of the different approximate xc functional in the latter study, we recomputed the surface energies with the LDA and using the optimized LDA lattice constant (3.84 Å). The obtained values of 0.77 eV/atom for Pd(111) and 1.02 eV/atom for Pd(100) are again in good agreement with recent other LDA studies [113, 124]. However, although the values are significantly different to the GGA numbers, they cannot resolve the discrepancy with respect to the early LDA work by Methfessel and coworkers. Instead, it seems to be the non-relativistic treatment of the valence and semi-core electrons in the latter work that is behind the difference. When deliberately switching off the scalar relativistic treatment employed in our work, we obtain values of 0.69 eV/atom (Pd(111)) and 0.88 eV/atom (Pd(100)) that are now very close to those obtained by Methfessel and coworkers. While we are therefore able to resolve the difference with respect to this work, we are unable to account for the discrepancy with respect to the TB-LMTO work by Vitos *et al.*. As already discussed by Da Silva,

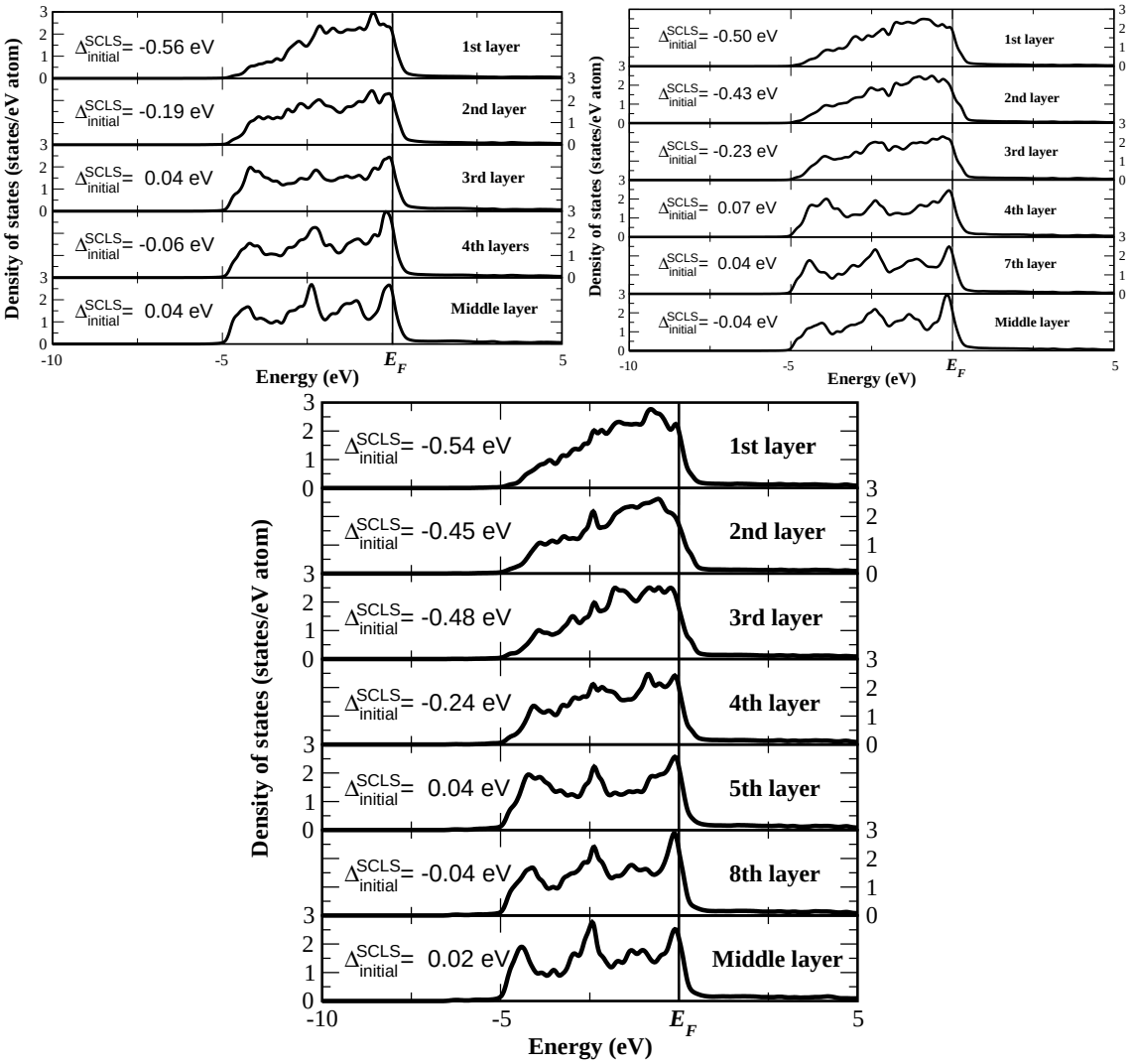


Figure 7.3: Local density of states (LDOS) in the different layers in Pd(113) (top left panel), Pd(115) (top right panel) and Pd(117) (bottom panel). Taking the Pd(117) DOS as example, one observes that compared to the bulk-like LDOS in the central layer of the slab, the topmost four surface layers (corresponding to undercoordinated step and terrace atoms) exhibit a significant narrowing of the valence 4$d$ band. The ensuing shift of the center of gravity of the valence 4$d$ band induces a non-negligible shift $\Delta^{\rm SCLS}_{\rm initial}$ in the 3$d$ core-level positions with respect to the value in a bulk Pd atom. Note the similarity of the $\Delta^{\rm SCLS}_{\rm initial}$ exhibited by the two terrace atoms in Pd(117), 2nd and 3rd row, to the one of the topmost layer atoms in an infinite Pd(100) terrace, $\Delta^{\rm SCLS}_{\rm initial} = -0.50\,$eV. Equivalent features are seen in the LDOS of Pd(113) and Pd(115).

Stampfl and Scheffler [113], the reason might be that the atomic sphere approximation (ASA) employed by Vitos *et al.* does not allow for sufficient flexibility of electronic relaxation at the surface.

As for the vicinal surfaces, the sequence of Pd(113), Pd(115) and Pd(117) surface energies is $\gamma_{113} > \gamma_{115} \approx \gamma_{117}$, instead of the more intuitive $\gamma_{117} > \gamma_{115} > \gamma_{113}$. However the trend is similar as in vicinal Cu(11$N$) surfaces [106]. Although the Pd(115) and Pd(117) are more open than Pd(113), the surface of the vicinal surface becomes more and more flat increasing terraces width. The surface energy of Pd(117) is already very similar to the Pd(100) surface energy. With increasing (100) terraces (more and more atomic rows on the terraces, $N \geq 7$), the surface energy of the vicinal surface obviously approaches the surface energy of the Pd(100) surface. On the other hand, the surface energies sequence gives already a first hint as to the influence of neighboring steps. In this respect, the obtained rather similar values in meV/Å$^2$, cf. Table 7.2, suggest that step-step interactions are rather small despite the small terrace widths of these surfaces. This finding is in full agreement with a preceding tight-binding study by Raouafi *et al.*, which also determined negligible step-step interactions at $n_{\rm row}(100)\times(111)$ vicinals of Rh, Pd and Cu [125]. Moreover, using the computed surface energies for the Pd(11$N$) vicinal surfaces (Table 7.2), the step formation energy can be evaluated for $n_{\rm row}$=2, 3, 4 based on Eq. 4.13. If the step-step interaction energy is sufficiently short-ranged, this will already be sufficient to isolate *e.g.* $E^{111}_{\rm step}$.

There are only 2 atomic rows per terrace on the Pd(113) surface, and inspection of Fig. 7.1, suggests to view this as (111) steps and (100) terraces. However, if viewed after 180$^0$ degree rotation, it may alternatively be considered as (100) steps and (111) terraces, and the factor $f$ in Eq. 4.13 is changed to 2/3 [48]. One may therefore use this surface to get two step formation energies, (111) and (100), which due to the proximity of the steps will however not be well converged to the isolated case yet. The other Pd(11$N$) vicinal surfaces with larger (100) terraces exactly show only (111) steps and (100) terraces. Table 7.3 summarizes the step formation energies extracted using the calculated unrelaxed and relaxed surface energies of the Pd(11$N$) family, and compares with step formation energy values in the literature. (The factor $f$ is no longer exactly 1/2 for $n_{\rm row}(100)\times(111)$ and 2/3 for $n_{\rm row}(111)\times(100)$ in relaxed vicinal surfaces). Although our results for $E^{111}_{\rm step}$ ($n_{\rm row}$=4) (GGA-PBE) compare well with the LMTO-GGA study of Vitos et al. [48], the differences to the TB-LDA [125] are substantial (factor 2). While potential other sources for this discrepancy could be the use of unrelaxed surfaces at experimental lattice constants in *ref.* [48], the major source is presumably the different choice of xc functional, namely the LDA. This is already reflected by their much larger surface energy of Pd(113) [1.533 eV/atom], compared with our value of 1.30 eV/atom, in good agreement with 1.27 eV/atom in *ref.* [127]. As apparent from Table. 7.3, although the difference of $E^{111}_{\rm step}$ on the three Pd(11$N$) surfaces is very small, it still shows a trend with the step formation energy on Pd(113) being larger than on Pd(115) or Pd(117), indicating short-ranged repulsive step-step interactions [125, 126]. Moreover, $E^{111}_{\rm step}$ on Pd(115) and Pd(117) is almost the same, suggesting that at the larger terrace widths only a very small step-step interaction is left. Our $E^{111}_{\rm step}$ results on Pd(11$N$) show thus the same trend as those reported in *ref.* [125] for the family of Rh(11$N$) and Cu(11$N$) surfaces. Although

Table 7.3: Step formation energies at the different vicinal surfaces (Table 7.2) extracted via Eq. 4.13 and using either the ideal geometrical factor for the nonrelaxed surface, or taking $f$ from our relaxed surface geometries. Additionally shown are values from the literature.

| $E_{\text{step}}$ | Pd(113) ($n_{\text{row}}$=2) | | Pd(115) ($n_{\text{row}}$=3) | | Pd(117) ($n_{\text{row}}$=4) | | Vitos [48] LMTO-GGA ($n_{\text{row}} \to \infty$) | Raouafi [125] TB-LDA ($n_{\text{row}} \to \infty$) |
|---|---|---|---|---|---|---|---|---|
| | unrelax | relax | unrelax | relax | unrelax | relax | unrelax | unrelax |
| $f_{111}$ | 1/2 | 0.526 | 1/2 | 0.527 | 1/2 | 0.513 | 1/2 | 1/2 |
| $E_{\text{step}}^{111}$ (eV/atom) | 0.175 | 0.125 | 0.135 | 0.07 | 0.125 | 0.08 | 0.106 | 0.289 |
| $f_{111}$ | 2/3 | 0.688 | — | —- | — | —- | 2/3 | 2/3 |
| $E_{\text{step}}^{100}$ (eV/atom) | 0.317 | 0.274 | —- | —- | — | —- | 0.460 | 0.425 |

our data allows only to extract $E_{\text{step}}^{100}$ for $n$=2, *i.e.* with a presumably non-negligible step-step interaction, it is interesting to use it to comment on an observation made in *ref.* [38]: There it was reported that the average of (111) and (100) step formation energies of Cu, Pt and Al (using the striped model) scale approximately as 7% of the cohesive energy of the corresponding metal [38]. For our Pd(113) case, the average of the (111) and (100) step formation energies is 0.246 eV/atom, while the computed cohesive energy is 3.38 eV/atom. Correspondingly, we obtain for this fraction 7.3%, which agrees well with the observation in *ref.* [38]. Still, as mentioned in *ref.* [38], our number has to be seen in light of the uncertainty due to the certainly present step-step interaction at the short terrace widths of the Pd(113) surface.

Apart from surface energies and step formation energies, the fast decay of the local perturbation introduced by the (111) step is also nicely discerned in the surface electronic structure. Figure 7.3 shows the local density of states (LDOS) calculated inside the muffin tin spheres of the atoms in the various surface layers at Pd(11$N$). Taking the Pd(117) LDOS as example, one observes that compared to the bulk-like LDOS of the central layer in the slab, only the topmost four layers corresponding to step or terrace atoms with reduced NN coordination show a significant variation, predominantly in form of a narrowing of the valence 4$d$ band. The band narrowing induces a shift in the position of the core-levels, *cf.* section 4.7. With our SCLS definition, the valence $d$ band narrowing at the Pd surface leads to a negative shift, and we focus in this work in particular on the SCLS exhibited by the 3$d$ Pd levels.

We note that the $\Delta_{\text{initial}}^{\text{SCLS}}$ exhibited by the eightfold coordinated 2nd and 3rd layer terrace atoms at Pd(117), cf. Fig. 7.3, are already quite similar to the one we compute for a topmost layer atom in an infinite Pd(100) terrace, $-0.50\,$eV/atom. In contrast, all deeper layers with 12fold bulk-like coordination exhibit only insignificant shifts. Table 7.4 shows that the nearest-neighbor coordination is in fact the overriding

Table 7.4: Initial-state surface core-level shifts $\Delta^{\mathrm{SCLS}}_{\mathrm{initial}}$ for the topmost layers with reduced NN coordination, cf. Table 7.1, at the low-index and vicinal surfaces. All values are given in eV.

| $\Delta^{\mathrm{SCLS}}_{\mathrm{initial}}$ | Pd(111) | Pd(113) | Pd(115) | Pd(117) | Pd(100) |
|---|---|---|---|---|---|
| 1st | -0.39 | -0.56 | -0.50 | -0.54 | -0.50 |
| 2nd | | -0.19 | -0.43 | -0.45 | |
| 3rd | | | -0.23 | -0.48 | |
| 4th | | | | -0.24 | |

Table 7.5: Binding energies of oxygen atoms at the different highly-coordinated terrace and step sites of the three Pd(11$N$) ($N$=3,5,7) surfaces, see Fig. 7.1 for an illustration of all sites and the employed nomenclature. Listed are results for the adsorption of one oxygen atom per $(1 \times 1)$ and $(1 \times 2)$ surface unit-cell. At the Pd(113) surface, the Thu and Thl sites coincide, which is why only one value is given. All values are in eV.

| $(1 \times 1)$ | Sh1 | Sh2 | Thu | Thl | Thc |
|---|---|---|---|---|---|
| Pd(113) | 0.82 | 0.87 | 0.60 | | |
| Pd(115) | 0.80 | 0.89 | 0.84 | 0.52 | |
| Pd(117) | 0.83 | 0.94 | 0.86 | 0.57 | 0.80 |
| $(1 \times 2)$ | Sh1 | Sh2 | Thu | Thl | Thc |
| Pd(113) | 1.08 | 1.17 | 0.96 | | |
| Pd(115) | 1.04 | 1.17 | 1.27 | 0.92 | |
| Pd(117) | 1.05 | 1.22 | 1.27 | 0.98 | 1.25 |

parameter determining the initial-state SCLSs at all surfaces studied here. Comparing to the NN coordination listed in Table 7.1, one even finds a roughly linear relation of the $\Delta^{\mathrm{SCLS}}_{\mathrm{initial}}$ with the number of NN Pd atoms, which indicates that perturbations further away than the immediate NN shell are rapidly screened away.

## 7.3 Oxygen Adsorption at Vicinal Surfaces

### 7.3.1 Binding Energy

Interested in evaluating the effect of the nearby steps in the series of Pd(11$N$) surfaces, we consider the adsorption of oxygen as a probe of the local chemical properties. On Pd(113) there have the least number of inequivalent adsorption sites among the Pd(11$N$)surfaces (Fig. 4.3 and 7.1). Focusing on the oxygen adsorption on all kinds of sites on the Pd(113) surface, and trying to get some hints of the oxygen adsorption on the vicinal surfaces, which adsorption sites are the important ones for us, we

Table 7.6: Binding energy of oxygen adsorption at different sites on Pd(113)(1×1) (Fig. 4.3).

| | Sh2 | Sh1 | Thl | Tb1 | Tb2 | Tb3 | Tt1 | Tt2 |
|---|---|---|---|---|---|---|---|---|
| $E_b$ (eV) | 0.87 | 0.82 | 0.60 | 0.67 | 0.66 | 0.81 | -0.40 | 0.05 |

summarize all the binding energies of the oxygen adsorption at the different sites on the Pd(113) surface in Table 7.6. In Table 7.6 the binding energies show that the Sh2 site where the oxygen atom is coordinated to two step atoms is the most stable one on Pd(113), and the next most stable one is the Sh1 site where the oxygen atom is coordinated to one step atoms. And the binding energy of Tb3 site which at the bridge site of bottom step edge has a similar value as the Sh1 site. This is because the two sites have the similar adsorption environment (Fig. 4.3), and after relaxation the oxygen at the Tb3 site will move to the Sh1 site. From the binding energies of oxygen at Pd(113), which indicates that hollow sites *i.e.* have the largest binding energies. For this we focus on the binding of atomic O to the highly-coordinated high-symmetry sites offered by the vicinal surfaces, namely the fourfold coordinated hollow sites on the terraces and the threefold coordinated hollow sites at the steps, *cf.* Fig. 7.1. Apart from Sh2 and Sh1 sites, at the Pd(117) surface, there are three terrace hollow sites, one at the lower edge of the step (Thl), one at the upper edge of the step (Thu) and one in the center of the terrace (Thc). Due to the reduced terrace width, there are only Thl and Thu sites at Pd(115), and at Pd(113) the lower and upper edge terrace hollow sites coincide. To analyze the effect of coverage we calculated the binding energy of one oxygen atom at any of these sites both in $(1 \times 1)$ and $(1 \times 2)$ surface unit cells. In the prior, all sites of one type are then covered, *e.g.* all Sh1 sites along a step, while in the latter occupied sites alternate with empty ones, *e.g.* one Sh1 site covered, the neighboring one empty *etc.*

The obtained binding energies are compiled in Table 7.5 and can be understood in a rather simple and local picture. Central for the stability at a given site are the number of directly coordinated surface Pd atoms and their respective Pd coordination ($n$fold coordinated terrace or step atoms). Sites which are identical with respect to these criteria exhibit binding energies that are almost degenerate within our numerical accuracy (±50 meV/O atom). Prominent examples are the similar binding energies at the Sh1 site at all three surfaces (binding to one 7fold coordinated step and two 10fold coordinated terrace atoms) and at the Sh2 site at all three surfaces (binding to two 7fold coordinated step and one 10fold coordinated terrace atom). Due to the narrow terrace widths this equivalence is only established for the Thu (and separately for the Thl) sites at the Pd(115) and Pd(117) surfaces. There, Thl corresponds to binding to two 8fold coordinated and two 10fold coordinated terrace atoms, while Thu corresponds to binding to two 7fold coordinated step atoms and two 8fold coordinated terrace atoms. The binding site Thc in the center of a terrace (coordination

to four 8fold terrace atoms) develops only at the Pd(117) surface, but is then already comparable to the fourfold hollow site at Pd(100), corresponding to an infinite terrace width. We arrive at this assessment from calculating $(3 \times 1)$ and $(4 \times 1)$ overlayers at Pd(100) with one oxygen atom per surface unit-cell. The obtained binding energies are 0.84 eV/O atom and 0.85 eV/O atom, respectively, which shows that the lateral interactions between the neighboring O atoms along the long axis of the unit-cell are already negligible. On the other hand, these binding energies are very close to the one computed for the Thc site at Pd(117), 0.80 eV/O atom, revealing an only marginal influence of the neighboring steps in the latter case. Furthermore, the predominant role of the local coordination seems to hold independently of the coverage, since our calculations in $(1 \times 2)$ surface unit-cells, *cf.* Table 7.5, show exactly the same pattern. In this case, we compute an O binding energy of 1.29 eV/O atom in a $(3 \times 2)$ overlayer on Pd(100), which is again very similar to the value of 1.25 eV/O atom at the Thc site.

Also the stability ordering among the different site types largely follows a local coordination picture, when recognizing that the bonding is stronger to lower-coordinated Pd atoms than to higher-coordinated ones. Correspondingly, the Sh2 site is more stable than the Sh1 (bonding to two step atoms vs. bonding to one step atom), while the ordering among the terrace sites goes with decreasing stability as Thu, Thc and Thl. Interestingly, the most stable terrace site (Thu) is slightly more stable than the most stable step site (Sh2) at the lower $(1 \times 2)$ coverage studied, while this order is reversed at the higher $(1 \times 1)$ coverage. This might again be explained in a local coordination picture, when realizing that in the $(1 \times 1)$ arrangement, neighboring O atoms in rows of any of the terrace sites share two Pd atoms, while in rows of either of the two step sites they share only one Pd atom. In terms of a bond-order conservation picture, it is then intelligible that equivalent terrace sites are $\sim 0.4$ eV/O atom less stable in the denser $(1 \times 1)$ overlayer compared to the $(1 \times 2)$ one, while for the step sites this reduction is only $\sim 0.25$ eV/O atom. With the Thu site only slightly more favorable than the Sh2 site in the $(1 \times 2)$ arrangement, the smaller reduction for the Sh2 site when going to the dense $(1 \times 1)$ arrangement leads then to slight preference for the Sh2 site. We speculate that this change in the stability ordering of terrace and step sites with coverage may lead to interesting ordering phenomena. Addressing this topic requires a proper evaluation of the partition function, on which we focus in the next chapter.

### 7.3.2 Geometric and Electronic Structure

The calculated relaxed surface geometries also reflect the local coordination picture developed in the previous section. Focusing first on the O-Pd bond lengths, the data for the $(1 \times 1)$ O overlayers compiled in Table 7.7 clearly reveals two trends (equivalent results are obtained for the $(1 \times 2)$ O overlayers): Longer O-Pd bond lengths are found at higher coordinated adsorption sites (fourfold terrace sites vs. threefold step sites), and shorter bond lengths result in bonds to lower coordinated Pd atoms (7fold

Table 7.7: O-Pd bond lengths (in Å) at the different sites in $(1 \times 1)$ overlayers. The shorter bond lengths are always to the lower coordinated Pd atoms, *cf.* Fig. 7.1 and Table 7.2. At the Pd(113) surface, the Thu and Thl sites coincide, which is why only one set of values is given.

| | Sh1 | Sh2 | Thu | Thl | Thc |
|---|---|---|---|---|---|
| Pd(113) | 1.97/2.02/2.02 | 1.98/1.98/2.02 | 2.00/2.00/2.47/2.47 | | |
| Pd(115) | 1.99/2.01/2.01 | 1.99/1.99/2.03 | 2.15/2.15/2.14/2.14 | 2.05/2.05/2.30/2.30 | |
| Pd(117) | 1.98/2.01/2.01 | 1.98/1.98/2.03 | 2.15/2.15/2.14/2.14 | 2.05/2.05/2.30/2.30 | 2.13/2.13/2.16/2.16 |

coordinated step atoms vs. 8 or 10fold coordinated terrace atoms). Equivalent sites at the different surfaces that possess the same coordination and hence similar binding energies as discussed above, also exhibit similar bond lengths. The local geometry at the Sh1 and Sh2 sites is thus the same at all three vicinals, and so is the one at the Thu and Thl sites at Pd(115) and Pd(117). Since the bonds to lower coordinated Pd atoms are shorter, the threefold step sites Sh1 and Sh2 are not exactly threefold, but a slightly shorter bond length results to the step atoms. The same occurs for the terrace sites, where the inequivalence of the Thl site at the bottom of the step is most pronounced: Here, the O atom is significantly shifted away from ideal fourfold site, away from the step and towards the terrace center. Just as with respect to the binding energies, the Thc site is already very much comparable in its local geometry to the fourfold hollow site at a similarly covered Pd(100) surface: For $(3 \times 1)$ and $(4 \times 1)$ overlayers with one O atom per surface unit-cell we compute bond lengths of 2.14 Å, which are almost identical to the 2.13 Å/2.16 Å found at Pd(117). Interestingly, this bond length similarity to the low-index surfaces holds even for the threefold step sites Sh1 and Sh2, which exhibit bond lengths that are very close to the $\approx 2$ Å computed for the threefold hollow sites in various overlayers on Pd(111) [111].

The chemisorption of oxygen also induces substantial changes in the relaxation pattern of the underlying Pd substrate atoms. Similar to the situation at lower coverages at the low-index Pd(111) [111] and Pd(100) surfaces, the main effect of the adsorbed oxygen is to pull the directly coordinated Pd atoms out of the surface. However, while primarily at Pd(100) this leads simply to a significant expansion of the first layer spacing ($\Delta d_{12} = +12\,\%$ at $(1 \times 1)$ coverage), the relaxation is more complicated at the more open vicinal surfaces, which also allow for quite some lateral displacements of the Pd atoms. The corresponding data is shown in Fig. 7.4 for O adsorption in the most stable step and terrace site, Sh2 and Thu respectively, and compiled in Table 7.8 for all adsorption sites. Due to the lateral displacements, the oxygen-induced changes in the relaxation pattern also propagate much further than just the nearest-neighbor Pd shell. Here, the locality is thus not that pronounced, but apparently this has no significant consequences on the afore discussed binding energies.

The perturbation in the electronic system created by the chemisorbed oxygen atom is again very localized, as is nicely reflected in the layer-resolved LDOSs. Figure 7.5 exemplifies this for oxygen at the Sh2 step and Thc terrace site at Pd(117).

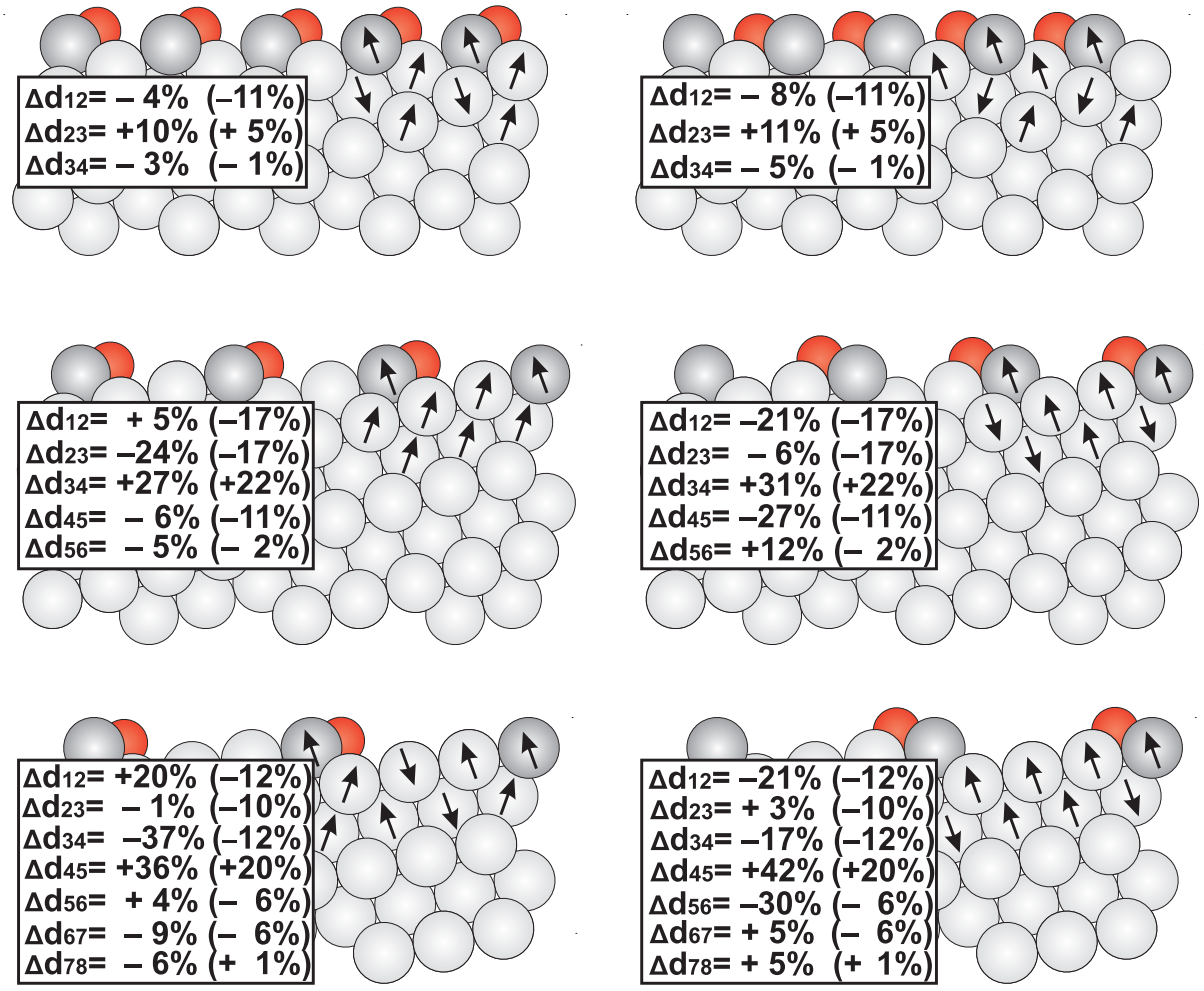


Figure 7.4: Geometry side views for adsorption in the Sh2 (left panels) and Thu (right panels) sites in $(1 \times 1)$ overlayers at the Pd(113) [top panels], Pd(115) [middle panels], and Pd(117) [bottom panels]. The insets show the percent change of the layer spacings with respect to the bulk spacing $\Delta d_{ij}$. For comparison, the value in parenthesis gives the corresponding $\Delta d_{ij}$ of the clean surface. The arrows indicate the direction of the substrate atom displacement (including the lateral relaxation) with respect to the position in the clean surface. Light grey spheres represent Pd atoms, grey spheres Pd step atoms, and small dark (red) spheres O atoms.

Table 7.8: Surface relaxation pattern of the Pd(11$N$) ($N = 3, 5, 7$) vicinal surfaces, both for the clean surfaces and with a $(1 \times 1)$ O overlayer adsorbed. Shown are the interlayer spacings $d_{ij}$ (see Fig. 7.1 for a definition of the layer numbers), as well as in parenthesis the percent change $\Delta d_{ij}$ with respect to the interlayer spacing $d_b$ in the bulk, *cf.* Eq. 4.1. See Fig. 7.1 for an illustration of the various adsorption sites.

| Pd(113) | Sh1 | Sh2 | Thu/Thl | clean |
|---|---|---|---|---|
| $d_{12}$ ($\Delta d_{12}$) | 1.09 Å (−9%) | 1.15 Å (−4%) | 1.10 Å (−8%) | 1.06 Å (−11%) |
| $d_{23}$ ($\Delta d_{23}$) | 1.32 Å (+11%) | 1.31 Å (+10%) | 1.32 Å (+11%) | 1.25 Å (+5%) |
| $d_{34}$ ($\Delta d_{34}$) | 1.11 Å (−7%) | 1.15 Å (−3%) | 1.12 Å (−5%) | 1.18 Å (−1%) |
| $d_{45}$ ($\Delta d_{45}$) | 1.23 Å (+3%) | 1.21 Å (+2%) | 1.23 Å (+3%) | 1.19 Å (0%) |
| $d_{56}$ ($\Delta d_{56}$) | 1.17 Å (−2%) | 1.19 Å (0%) | 1.18 Å (−1%) | 1.19 Å (0%) |

| Pd(115) | Sh1 | Sh2 | Thu | Thl | clean |
|---|---|---|---|---|---|
| $d_{12}$ ($\Delta d_{12}$) | 0.74 Å (−2%) | 0.79 Å (+5%) | 0.60 Å (−21%) | 0.64 Å (−15%) | 0.63 Å (−17%) |
| $d_{23}$ ($\Delta d_{23}$) | 0.62 Å (−19%) | 0.58 Å (−24%) | 0.71 Å (−6%) | 0.73 Å (−4%) | 0.63 Å (−17%) |
| $d_{34}$ ($\Delta d_{34}$) | 0.95 Å (+24%) | 0.97 Å (+27%) | 1.00 Å (+31%) | 0.82 Å (+8%) | 0.93 Å (+22%) |
| $d_{45}$ ($\Delta d_{45}$) | 0.70 Å (−7%) | 0.71 Å (−6%) | 0.55 Å (−27%) | 0.85 Å (+11%) | 0.68 Å (−11%) |
| $d_{56}$ ($\Delta d_{56}$) | 0.71 Å (−6%) | 0.72 Å (−5%) | 0.85 Å (+12%) | 0.62 Å (−19%) | 0.74 Å (−2%) |
| $d_{67}$ ($\Delta d_{67}$) | 0.83 Å (+9%) | 0.81 Å (+7%) | 0.77 Å (+1%) | 0.81 Å (+6%) | 0.79 Å (+4%) |
| $d_{78}$ ($\Delta d_{78}$) | 0.72 Å (−5%) | 0.74 Å (−2%) | 0.74 Å (−2%) | 0.80 Å (+5%) | 0.75 Å (−2%) |

| Pd(117) | Sh1 | Sh2 | Thu | Thc | Thl | clean |
|---|---|---|---|---|---|---|
| $d_{12}$ ($\Delta d_{12}$) | 0.66 Å (+20%) | 0.66 Å (+20%) | 0.44 Å (−21%) | 0.48 Å (−13%) | 0.48 Å (−12%) | 0.49 Å (−12%) |
| $d_{23}$ ($\Delta d_{23}$) | 0.52 Å (−6%) | 0.54 Å (−1%) | 0.57 Å (+3%) | 0.51 Å (−7%) | 0.46 Å (−16%) | 0.50 Å (−10%) |
| $d_{34}$ ($\Delta d_{34}$) | 0.29 Å (−47%) | 0.35 Å (−37%) | 0.46 Å (−17%) | 0.51 Å (−7%) | 0.51 Å (−8%) | 0.49 Å (−12%) |
| $d_{45}$ ($\Delta d_{45}$) | 0.80 Å (+46%) | 0.75 Å (+36%) | 0.78 Å (+42%) | 0.65 Å (+18%) | 0.70 Å (+28%) | 0.66 Å (+20%) |
| $d_{56}$ ($\Delta d_{56}$) | 0.59 Å (+8%) | 0.57 Å (+4%) | 0.39 Å (−30%) | 0.64 Å (+17%) | 0.49 Å (−11%) | 0.52 Å (−6%) |
| $d_{67}$ ($\Delta d_{67}$) | 0.45 Å (−18%) | 0.50 Å (−9%) | 0.58 Å (+5%) | 0.36 Å (−34%) | 0.66 Å (+20%) | 0.52 Å (−6%) |
| $d_{78}$ ($\Delta d_{78}$) | 0.49 Å (−11%) | 0.52 Å (−6%) | 0.58 Å (+5%) | 0.63 Å (+15%) | 0.40 Å (−28%) | 0.56 Å (+1%) |
| $d_{89}$ ($\Delta d_{89}$) | 0.69 Å (+25%) | 0.61 Å (+12%) | 0.58 Å (+5%) | 0.59 Å (+6%) | 0.60 Å (+10%) | 0.56 Å (+1%) |

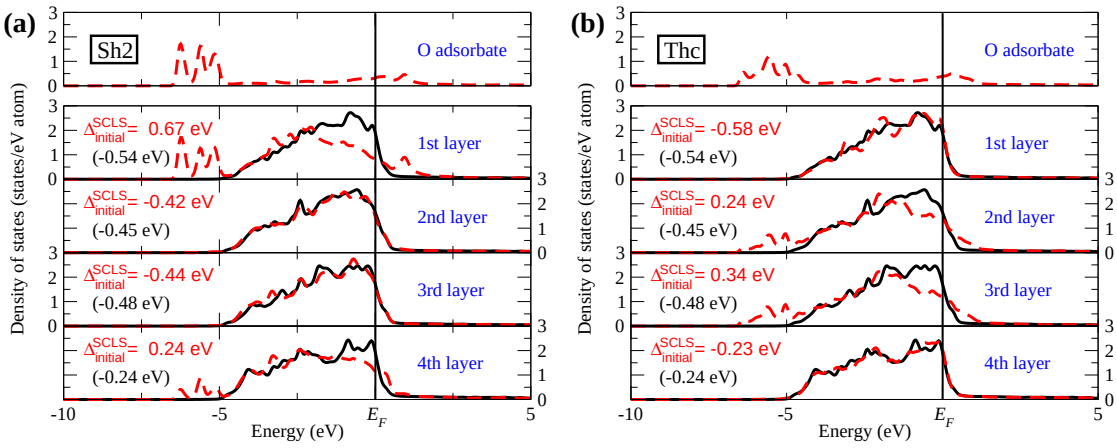


Figure 7.5: Oxygen-induced changes in the local density of states (LDOS) and initial-state SCLSs. Shown are the data for oxygen adsorption into the Sh2 step (left panels) and Thc terrace site (right panels) at Pd(117). Dashed lines correspond to the LDOS with the O adsorbate (inside the O muffin tin in the top panel and inside the Pd muffin tin in all other panels), solid lines correspond to the clean surface. The $\Delta^{\mathrm{SCLS}}_{\mathrm{initial}}$ exhibited by the Pd terrace atoms directly coordinated to the O atom in the Thc site, layers 2 and 3, are very similar to the 0.32 eV computed for the directly-coordinated Pd atoms in a $(3 \times 1)$ O-overlayer at Pd(100). The values in parenthesis give the initial-state SCLSs at the clean surface for comparison.

In both cases, the local density of states is primarily affected in the surface layers corresponding to the Pd atoms directly coordinated to the O adsorbate, namely layers 1 and 4 for the Sh2 site, and layers 2 and 3 for the Thc site, cf. Fig. 7.1. In these layers, we find O-Pd bonding states just below and antibonding states just above the nearly fully occupied Pd 4$d$ band. In the shown LDOS for the $(1 \times 1)$ overlayer, the bonding states show some substructure due the presence of a noticeable oxygen-oxygen interaction along the rows in the short direction of the surface unit-cell. This leads to the formation of an adsorbate band structure as previously discussed for high-coverage O overlayers at the low-index Pd(111) surface [111]. The surface layers corresponding to atoms not belonging to the immediate NN shell of the oxygen adsorbate show only insignificant variations in the LDOS compared to the case of the clean surface, as does the LDOS in the deeper layers. Correspondingly, it is also only the directly coordinated surface layers that exhibit appreciable adsorbate-induced changes in the initial-state SCLSs, cf. Fig. 7.5. The widening of the $d$-band leads then to more positive shifts compared to the clean surface SCLSs [51]. The stronger the formed O-Pd bond, the larger the disturbance of the local potential and the larger the ensuing shift. In this respect, we find O-induced shifts, *i.e.* a change of $\Delta^{\mathrm{SCLS}}_{\mathrm{initial}}$ compared to the value at the clean surface, of +1.21 eV and +0.48 eV at the 7fold and 10fold coordinated Pd atoms to which the O atom binds in the Sh2 site, and shifts of +0.69 eV and +0.82 eV at the two types of 8fold terrace Pd atoms to which the O atom binds in the Thc site. This indicates a significantly different bonding of the O atom to the different NN Pd atoms, which correlates with the varying O-Pd bond lengths shown in Table 7.7 and suggests that the 7fold coordinated step atoms may offer a stronger bonding compared to the higher-coordinated terrace atoms. That the overall binding energy at the Sh2 site is nevertheless still comparable to the most stable terrace sites, cf. Table 7.5, results simply because the latter offer a higher (fourfold) coordination to Pd atoms compared to the threefold sites at the (111) step.

The perturbation due to oxygen adsorption at all other investigated sites is as localized as in the just discussed case of the Sh2 and Thc sites. In all cases, we only find significant O-induced shifts in the initial-state SCLS at the directly coordinated Pd atoms. Just as for the binding energies and O-Pd bond lengths, also these SCLSs are very similar for adsorption into equivalent sites at the three vicinal surfaces. In a $(3 \times 1)$ overlayer at Pd(100) we compute an O-induced SCLS shift of +0.82 eV exhibited by the directly coordinated Pd atoms, which is again very similar to the above cited values for O adsorption into the Thc terrace site at a Pd(117) surface. This corroborates our understanding that the neighboring steps have already a negligible influence on the O bonding at this site in the center of an only four atomic row wide terrace.

## 7.4 Conclusions

In this Chapter we presented a DFT-GGA study addressing the on-surface adsorption of oxygen at Pd(11$N$) ($N$=3,5,7) vicinal surfaces. Apart from providing detailed insight into the oxygen-metal chemical bond, our particular interest was to investigate the influence on the adsorption properties by the neighboring steps that are separated by 2, 3 and 4 atomic row wide terraces at the three surfaces, respectively. The computed data on binding energies, local density of states and initial-state surface core-level shifts points at a very localized perturbation created by the chemisorbed oxygen atoms, primarily concentrating on the nearest neighbor Pd atoms. Central for the stability at a given site are then the number of directly coordinated surface Pd atoms (threefold hollow sites at the (111) steps vs. fourfold hollow sites at the (100) terraces) and their respective Pd coordination ($n$fold coordinated Pd terrace or step atoms). Sites which are equivalent with respect to these criteria exhibit binding energies that are degenerate to within 70 meV/O atom. Examples are the step sites at all three vicinal surfaces, while the hollow site in the center of the four atomic row (100) terrace at Pd(117) is already very much comparable to the ones at the low-index Pd(100) surface. Interestingly, the stability at the threefold (111) step sites is very similar to the stability at the fourfold (100) terrace sites, and their energetic order depends on the local oxygen concentration. The ruling lateral interactions will thus critically determine the ordering behavior under the influence of a step, and it is this ordering behavior which we address in the next chapter.

# Chapter 8

# Decoration of a (111) Step at Pd(100) by Oxygen Atoms

As prominent defects at solid surfaces atomic steps are commonly perceived as playing some kind of special, if not decisive role for the surface properties or function in materials science applications. When it comes to the interaction with a reactive environment, steps are viewed as providing particularly active sites which can have a pronounced effect on the catalytic activity or act as nucleation centers for adsorbate-induced morphological transitions with oxide formation or corrosion in our oxygen-rich atmosphere as well-known examples. When aiming to qualify this role at the atomic scale an important first task is to identify the structure and composition at the step edge under realistic gas-phase conditions. On the modeling side, the first-principles atomistic thermodynamics approach [67] has brought considerable progress to this end for ideal low-index surfaces. In its prevalent form, this approach compares the stability of a variety of structural models in contact with a given gas-phase reservoir. Extending it to the study of steps depends then only on the ability to perform the underlying electronic structure calculations for corresponding structural models. For metal surfaces, one viable route to this is to resort to supercell geometries for vicinal surfaces, *i.e.* to compute periodic arrays of steps that can be suitably cast into a periodic boundary condition framework. Unfortunately, the high computational cost connected to such inherently large supercell calculations severely limits both the accessible surface unit-cell sizes and total number of structural models that can be computed. This prevents to date a proper exploration of the huge configurational space of possible step structures and allows at best for approximate treatments of entropic effects at elevated temperatures.

In this chapter we address these limitations by suitably combining the thermodynamic approach with a first-principles parameterized lattice-gas Hamiltonian (LGH) [67]. The concept is illustrated with the application to the on-surface oxygen adsorption at Pd(100), and there specifically to the decoration of close-packed (111) steps in an oxygen atmosphere. In Chapter 7 we proved that the binding properties at the center of (100) terraces of Pd(117) are little disturbed by the neighboring steps. Then

we employ large-scale density-functional theory (DFT) calculations for corresponding low-index O-Pd(100) and vicinal O-Pd(117) to determine the lateral interactions between adsorbates at the (100) terrace sites and at sites close to or at a (111) step. In a first stage the resulting multi-site LGH is then used to generate a large pool of possible structural models with varying on-surface O content. Within the thermodynamic framework the stability of these models is evaluated for a wide range of gas-phase conditions and compared to known more complex O-induced reconstructions at the low-index surface, namely an ultrathin $(\sqrt{5} \times \sqrt{5})R27^\circ$ (henceforth simply termed $\sqrt{5}$) surface oxide) and thick bulk-like PdO films [90, 91]. Intriguingly, this identifies a distinct range of O chemical potentials where a characteristic zigzag step decoration is most stable. Explicitly accounting for the configurational entropy we confirm with grand-canonical Monte Carlo (GCMC) simulations that this ordered structure is indeed stable up to quite elevated temperatures, in fact up to even higher temperatures than the concurrent ordered adsorbate structure at the Pd(100) terrace. At near atmospheric pressures such temperatures around and above 1000 K are representative for catalytic applications like the high-temperature combustion of methane [136], for which our study thus provides first insight into the structure and composition at a prominent defect on the working surface.

# 8.1 Computational Details

## 8.1.1 Total Energy Calculations

Again, we employ the **WIEN2k** code based on FP-(L)APW+lo, using GGA-PBE as the exchange-correlation factional, for the total energy calculations of various ordered oxygen structures at Pd(117) (see Appendix F). All surface structures are modeled in a supercell geometry, employing full-relaxed symmetric slabs (with O adsorption on both sides of the slab) consisting of 23 Pd(117) layers with an optimized bulk lattice constant of a= 3.947 Å. A minimum vacuum region of 12 Å ensures the decoupling of consecutive slabs. The (L)APW+lo basis set are listed as following: $R_{\mathrm{MT}}^{\mathrm{Pd}}$=2.1 bohr, $R_{\mathrm{MT}}^{\mathrm{O}}$=1.1 bohr, wave function expansion inside the muffin tin spheres up to $l_{\mathrm{max}}^{\mathrm{wf}}$=12, and potential expansion up to $l_{\mathrm{max}}^{\mathrm{pot}}$=6. The energy cutoff for the plane wave representation in the interstitial region between muffin tin spheres was $E_{\mathrm{max}}^{\mathrm{wf}}$=20 Ry for the wave functions and $E_{\mathrm{max}}^{\mathrm{pot}}$=196 Ry for the potential. Monkhorst-Pack (MP) grids were used for the Brillouin zone integrations. Specially, we use a (3×12×1) [1] for the calculation of the Pd(117)(1×1) surface unit cell. For the larger surface cells, care was taken to keep the reciprocal space point sampling identical by appropriately reducing the employed k-meshes, *e.g.* the k-meshes are changed to (3×6×1) and (3×4×1) for Pd(117)(1 × 2) and Pd(117)(1 × 3) surface unit-cell respectively. The total energy of the isolated $O_2$ molecule is obtained just as in Chapter 4.

[1] The k-mesh used in this chapter is different to the k-mesh in Chapter 7, which was $(6 \times 10 \times 1)$, for reasons which will be detailed below.

In order to explicitly account for the different hollow sites (Sh2, Sh1, Thu, Thc and Thl) at Pd(117), instead of using the average binding energy as in Eq. 4.10, we are going to use the total binding energy to do the comparison, and extract the lateral interactions. The total binding energy is defined as,

$$E_{\rm b}^{\rm tot} = -\frac{1}{2}\left[E_{\rm O/Pd(117)}^{\rm total} - E_{\rm Pd(117)}^{\rm total} - \frac{N_{\rm O}}{2}E_{\rm O_2(gas)}^{\rm total}\right] \quad , \tag{8.1}$$

where $N_{\rm O}$ is the total number of oxygen atoms in the supercell. $E_{\rm O/Pd(117)}^{\rm total}$, $E_{\rm Pd(117)}^{\rm total}$ and $E_{\rm O_2(gas)}^{\rm total}$ are the total energy of the adsorption system, of the corresponding clean system and of an isolated oxygen molecule, respectively. And the factor $\frac{1}{2}$ accounts for the fact that oxygen atoms adsorb at both sides of the symmetric slab.

### 8.1.2 Lattice-gas Hamiltonian for O-Pd(117)

Within the LGH approach, the free binding energy of any O-Pd(117) configuration can be written as the following cluster expansion formula,

$$F_{\rm b}^{\rm tot} = \sum_{i}^{\rm site} F_i^{\rm on-site} n_i + \sum_{l=1}^{\rm r}\sum_{(i<j)_l}^{\rm site} V_{l,{\rm p}}^{(i,j)} n_i n_j + \sum_{m=1}^{\rm q}\sum_{(i<j<k)_m}^{\rm site} V_{m,{\rm t}}^{(i,j,k)} n_i n_j n_k + ... \quad , \tag{8.2}$$

where $F_i^{\rm on-site}$ is the free energy of an isolated oxygen at site $i$, and for simplicity, we use 1, 2, 3, 4, and 5 to distinguish Thu, Thc, Thl, Sh2 and Sh1, the five hollow sites, respectively. For the nomenclatures of pair ($V_{l,{\rm p}}^{(i,j)}$) and triple ($V_{m,{\rm t}}^{(i,j,k)}$) interactions, the subscripts have the same meaning as the CE on the Pd(100) surface (Fig. 6.1): the $l$th pair interaction, and the $m$th triple interaction; and the superscripts indicate the pair interaction involves two sites $i$ and $j$, and the trio interaction involves three sites $i$, $j$ and $k$. The value of $n_{i,(j,k)}$ is 1 or 0 if the site $i,(j,k)$ is occupied or empty. The sum labels $(i<j)_l$ [or $(i<j<k)_m$] indicate that the sums run over all pairs of sites $(ij)$ (and three sites $(ijk)$) that are separated by the $l$ (or $m$) lateral figure, and the summation is done such, that each pair (or trio) of occupied sites contributes exactly once to the lattice energy.

We consider pair interactions between any combination of sites up to distances that correspond to the third nearest neighbor (NN) shell, as well as the most compact many-body interactions in form of trio interactions between any three site combination within a second NN shell distance. The resulting 70 inequivalent lateral interaction figures compiled in Fig. 8.1. As we mentioned the lateral interaction figure nomenclature contains the information of which kind interaction it is and which sites are involved. Taking $V_{\rm 2p}^{12}$ as an example, the subscript 2p indicates this is a second nearest neighbor (2NN) pair interaction, and the superscript 12 indicates that this 2NN interaction is between Thu (1) and Thc (2) sites. Different to the Pd(100) surface, the present (111) steps divide the (100) surface into upper terraces and lower terraces.

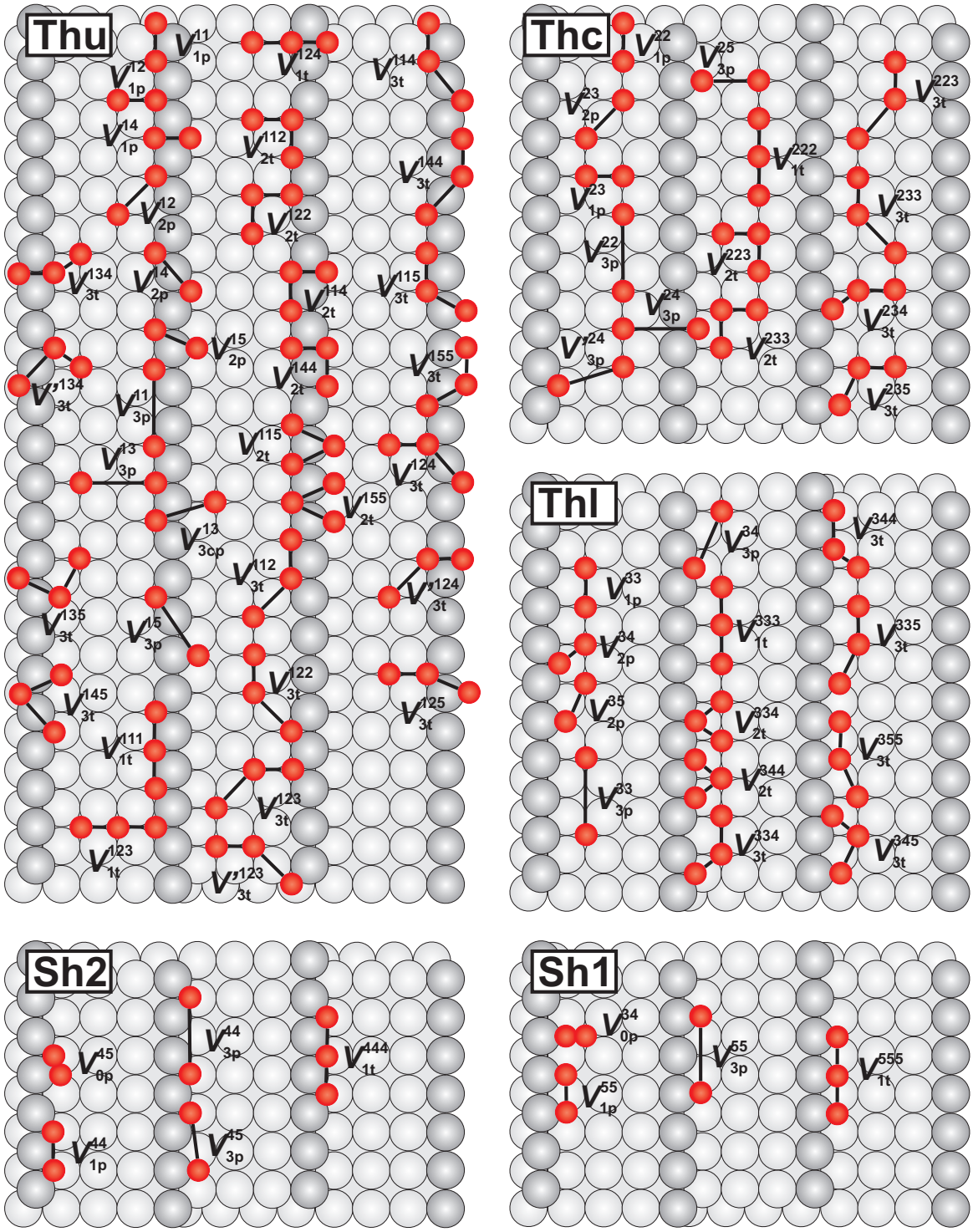


Figure 8.1: 70 step-influenced lateral interaction figures, including up to 3rd NN pair interactions and compact trios up to 2nd NN interactions. Light grey spheres represent Pd atoms, grey spheres Pd step atoms, and small dark (red) spheres O atoms. See text for the explanation nomenclature.

Table 8.1: Total binding energies of one oxygen atom at different sites in Pd(117)$(1 \times 1)$, $(1 \times 2)$ and $(1 \times 3)$ cells. Due to the different k-meshes, the binding energies in this table are slightly different to the ones in Table 7.5. The labels in parenthesis correspond to the names of the structures in Appendix F. (Unit: meV)

| | Sh2 | Sh1 | Thu | Thc | Thl |
|---|---|---|---|---|---|
| 1O−Pd(117)$(1 \times 1)$ | 953 | 845 | 876 | 819 | 595 |
| | (V7-4) | (V7-5) | (V7-1) | (V7-2) | (V7-3) |
| 1O−Pd(117)$(1 \times 2)$ | 1242 | 1073 | 1308 | 1279 | 1012 |
| | (V7-16) | (V7-17) | (V7-13) | (V7-14) | (V7-15) |
| 1O−Pd(117)$(1 \times 3)$ | 1286 | 1106 | 1265 | 1264 | 1009 |
| | (V7-50) | (V7-51) | (V7-47) | (V7-48) | (V7-49) |

This gives rise to additional lateral interactions across the (111) steps, like $V_{3\mathrm{cp}}^{13}$ (the pair interaction between Thu and Thl sites at consecutive (100) terraces). Due to the finite width of the terraces at Pd(117), there are furthermore interaction figures like $V_{1\mathrm{t}}^{123}$ that span across the entire terrace and involve both Thu sites at the upper edge and Thl sites at the lower step edge of the step. Such interaction figures will never be used in the LGH simulations with very large terrace widths presented below. However, in order to extract meaningful values for the other interaction figures from the Pd(117) DFT data, they need to be accounted for. Based on Eq. 8.2 and Fig. 8.1, the cluster expansion of each configuration is presented at the right side of each structure in the Appendix F.

## 8.2 First-principles Lattice-gas Hamiltonian for O at Pd(117)

### 8.2.1 Energetics for O−Pd(117)

The total binding energies of various ordered configurations of oxygen adsorption at Pd(117) computed within our DFT approach are also compiled in Appendix F. Table 8.1 collects just the binding energies of one oxygen atom at different sites in the Pd(117)(1×1), (1×2) and (1×3) cells. The binding energies of one oxygen atom at the (100) terraces in a Pd(117)$(1 \times 3)$ supercell, Thu and Thc sites, are degenerate, 1265 and 1264 meV, and they are quite similar to the binding energy of an isolated oxygen atom at the ideal Pd(100) surface, 1249 meV. This energetic value further supports the conclusion in Chapter 7, that the binding properties at the center of the (100) terraces of Pd(117) are only little different to oxygen at the Pd(100) surface, and are little disturbed by the neighboring steps. While for Sh2 and Sh1 or Thl, *i.e.* positions that are at the (111) steps or near to the steps, the oxygen binding

energetics is much different to O-Pd(100) due to the influence of the (111) steps.

All relaxed O-Pd(117) structures were carefully examined, and in some high coverage configurations the adsorbed O atoms induce large bucklings of the surrounding Pd atoms, so as to relax below the surface. Since this is not the physics of on-surface adsorption that we want to describe with the LGH, such configurations were − similarly to the procedure in Chapter 6 − excluded from the input data set.

Moreover, in configurations including the $V_{0\mathrm{p}}^{35}$ or $V_{0\mathrm{p}}^{45}$ lateral figure (Fig. 8.1), the oxygen atoms at Thl or Sh1 sites directly relaxed to the nearest hollow sites along the (100) terraces. This reflects very large repulsive interactions between O atoms at such short distances, which we correspondingly model in the LGH by setting $V_{0\mathrm{p}}^{35}$ or $V_{0\mathrm{p}}^{45}$ to infinite repulsion. This leaves a total of 105 DFT structures (see Appendix F) to obtain the lateral interactions (Fig. 8.1) at the (111) step region.

### 8.2.2 Lateral Interactions for O−Pd(117)

As we discussed in Chapter 6, whether or not including the on-site energy into the fitting group does not affect the final results. From Table 8.1, we deduce that the (1×3) cell is large enough to avoid all significant lateral interactions shown in Fig. 8.1, and we therefore take the binding energies of 1O-Thu-Pd(117)(1×3)(V7-13 in Appendix F), 1O-Thc-Pd(117)(1×3)(V7-14 in Appendix F), 1O-Thl-Pd(117)(1×3)(V7-15 in Appendix F), 1O-Sh2-Pd(117)(1×3)(V7-16 in Appendix F) and 1O-Sh1-Pd(117)(1×3)( V7-17 in Appendix F) as the on-site energies for the Thu, Thc, Thl, Sh2, and Sh1 sites, respectively.

Excluding these 5 on-site structures, the remaining 68 lateral interactions are then determined by least-squares fitting to the remaining 100 DFT ordered structures, following the same procedure outlined in Chapter 6. Table 8.2 summarizes the thereby obtained interaction values. We again calculate the LOO-CV score (Eq. 5.12) as a first indication of the reliability of the resulting LGH expansion. The CV score is 29 meV/O atom, which provides a measure for the average accuracy with which the LGH can predict the energetics of adatom configurations not included in the fitting procedure. There are a number of interaction figures in the set for Pd(117) that have a direct equivalent at the ideal Pd(100) surface. This concerns all interactions between the 3 different hollow sites Thu, Thc and Thl. Supporting our approach we find the interactions that only involve the Thc sites (pairs: $V_{1\mathrm{p}}^{22}$, $V_{3\mathrm{p}}^{22}$. trios: $V_{1\mathrm{t}}^{222}$) to be very similar to these parameters extracted in the LGH expansion at the ideal Pd(100) surface. This shows that not only the on-site energy, but also the lateral interactions of this site in the middle of the (100) terrace are already little disturbed by the presence of the neighboring steps. Interestingly, the same similarity holds also for all interactions involving the Thu site at the upper rim of the step edge. Also here, we extract pair interactions and trio interactions that are within 30 meV identical to those between hollow sites at Pd(100). Effectively, this thus leaves three adsorption sites that are noticeably affected by the step, the two step sites Sh1 and Sh2, and the fourfold site Thl at the lower rim of the step edge.

Table 8.2: Extracted on-site energies at Thu, Thc, Thl, Sh2 and Sh1 sites, and lateral interactions as represented in Fig. 8.1. (Unit: meV)

| On-site | $E_{\mathrm{Thu}}^{\mathrm{on-site}}$ | $E_{\mathrm{Thc}}^{\mathrm{on-site}}$ | $E_{\mathrm{Thl}}^{\mathrm{on-site}}$ | $E_{\mathrm{Sh2}}^{\mathrm{on-site}}$ | $E_{\mathrm{Sh1}}^{\mathrm{on-site}}$ |
|---|---|---|---|---|---|
| (meV) | 1265 | 1264 | 1009 | 1286 | 1106 |

| pair | $V_{1\mathrm{p}}^{11}$ | $V_{1\mathrm{p}}^{12}$ | $V_{1\mathrm{p}}^{14}$ | $V_{2\mathrm{p}}^{12}$ | $V_{2\mathrm{p}}^{14}$ | $V_{2\mathrm{p}}^{15}$ | $V_{3\mathrm{p}}^{11}$ | $V_{3\mathrm{p}}^{13}$ | $V_{3\mathrm{cp}}^{13}$ | $V_{3\mathrm{p}}^{15}$ |
|---|---|---|---|---|---|---|---|---|---|---|
| (meV) | -299 | -283 | -420 | -90 | 133 | 41 | 41 | 80 | -49 | -10 |
| pair | $V_{1\mathrm{p}}^{22}$ | $V_{1\mathrm{p}}^{23}$ | $V_{2\mathrm{p}}^{23}$ | $V_{3\mathrm{p}}^{22}$ | $V_{3\mathrm{p}}^{24}$ | $V'^{24}_{3\mathrm{p}}$ | $V_{3\mathrm{p}}^{25}$ | $V_{1\mathrm{p}}^{33}$ | $V_{2\mathrm{p}}^{34}$ | $V_{2\mathrm{p}}^{35}$ |
| (meV) | -298 | -413 | -150 | 20 | 7 | -11 | 23 | -138 | -212 | -119 |
| pair | $V_{3\mathrm{p}}^{33}$ | $V_{3\mathrm{p}}^{34}$ | $V_{1\mathrm{p}}^{44}$ | $V_{3\mathrm{p}}^{44}$ | $V_{3\mathrm{p}}^{45}$ | $V_{1\mathrm{p}}^{55}$ | $V_{3\mathrm{p}}^{55}$ | | | |
| (meV) | 13 | -21 | -274 | -53 | -70 | -19 | -66 | | | |

| trio | $V_{1\mathrm{t}}^{111}$ | $V_{1\mathrm{t}}^{123}$ | $V_{1\mathrm{t}}^{124}$ | $V_{2\mathrm{t}}^{112}$ | $V_{2\mathrm{t}}^{122}$ | $V_{2\mathrm{t}}^{114}$ | $V_{2\mathrm{t}}^{144}$ | $V_{2\mathrm{t}}^{115}$ | $V_{2\mathrm{t}}^{155}$ |
|---|---|---|---|---|---|---|---|---|---|
| (meV) | -145 | -155 | -258 | 63 | 52 | 93 | 94 | -59 | 84 |
| trio | $V_{3\mathrm{t}}^{112}$ | $V_{3\mathrm{t}}^{122}$ | $V_{3\mathrm{t}}^{123}$ | $V'^{123}_{3\mathrm{t}}$ | $V_{3\mathrm{t}}^{114}$ | $V_{3\mathrm{t}}^{144}$ | $V_{3\mathrm{t}}^{115}$ | $V_{3\mathrm{t}}^{155}$ | $V_{3\mathrm{t}}^{124}$ |
| (meV) | -14 | -16 | -38 | -26 | 2 | 18 | -40 | -35 | -28 |
| trio | $V'^{124}_{3\mathrm{t}}$ | $V_{3\mathrm{t}}^{125}$ | $V_{3\mathrm{t}}^{134}$ | $V'^{134}_{3\mathrm{t}}$ | $V_{3\mathrm{t}}^{135}$ | $V_{3\mathrm{t}}^{145}$ | $V_{1\mathrm{t}}^{222}$ | $V_{2\mathrm{t}}^{223}$ | $V_{2\mathrm{t}}^{233}$ |
| (meV) | -98 | -144 | -80 | -78 | -61 | 62 | -166 | 116 | 125 |
| trio | $V_{3\mathrm{t}}^{223}$ | $V_{3\mathrm{t}}^{233}$ | $V_{3\mathrm{t}}^{234}$ | $V_{3\mathrm{t}}^{235}$ | $V_{1\mathrm{t}}^{333}$ | $V_{2\mathrm{t}}^{334}$ | $V_{2\mathrm{t}}^{344}$ | $V_{3\mathrm{t}}^{334}$ | $V_{3\mathrm{t}}^{344}$ |
| (meV) | -30 | -53 | 128 | -72 | -285 | 131 | 8 | -45 | 89 |
| trio | $V_{3\mathrm{t}}^{335}$ | $V_{3\mathrm{t}}^{355}$ | $V_{3\mathrm{t}}^{345}$ | $V_{1\mathrm{t}}^{444}$ | $V_{1\mathrm{t}}^{555}$ | | | | |
| (meV) | -79 | -28 | 73 | -5 | -66 | | | | |

Table 8.3: Comparison of equivalent lateral interaction figures involving Thu and Thc sites at O-Pd(117) and the hollow sites at O-Pd(100). The additional data in the parentheses are the corresponding values. (Unit: meV)

| O-Pd(100) | O-Pd(117) | | | | | |
|---|---|---|---|---|---|---|
| $V_{1\mathrm{p}}$ (-292) | $V_{1\mathrm{p}}^{11}$ | (-299) | $V_{1\mathrm{p}}^{22}$ | (-298) | $V_{1\mathrm{p}}^{12}$ | (-283) |
| $V_{2\mathrm{p}}$ (-90) | $V_{2\mathrm{p}}^{12}$ | (-90) | | | | |
| $V_{3\mathrm{p}}$ (50) | $V_{3\mathrm{p}}^{11}$ | (41) | $V_{3\mathrm{p}}^{22}$ | (20) | | |
| $V_{1\mathrm{t}}$ (-168) | $V_{1\mathrm{t}}^{111}$ | (-145) | $V_{1\mathrm{t}}^{222}$ | (-166) | | |
| $V_{2\mathrm{t}}$ (60) | $V_{2\mathrm{t}}^{112}$ | (63) | $V_{2\mathrm{t}}^{122}$ | (52) | | |
| $V_{3\mathrm{t}}$ (-48) | $V_{3\mathrm{t}}^{112}$ | (-14) | $V_{3\mathrm{t}}^{122}$ | (-16) | | |

### 8.2.3 Vibrational Contribution to the Lateral Interactions

The energetic parameters in Eq. 8.2 comprise total and vibrational free energy contributions. In addition to the total energy based lateral interactions discussed in the last section, we also account for the vibrational contribution in an approximate way, following the procedure detailed in Chapter 6. This means that we account for the leading vibrational contribution which gets concentrated in the on-site energy by adding the ZPE correction due to the change of the $O_2$ stretch frequency to the O-substrate stretch frequency (Eq. 6.7).

In order to obtain an estimate of this stretch mode we focus on configurations with one O atom at the Sh2 site in a $(1 \times 2)$ cell (V7-16 in Appendix F), and one O atom at the Thu site in a $(1 \times 2)$ cell (V7-13 in Appendix F), as well as on one configuration involving two O atoms at Thu and Sh2 sites in a $(1 \times 2)$ cell (V7-23 in Appendix F). In line with the conclusions taken in Chapter 6 we obtain only small differences in the stretch modes of both the step atom (Sh2) and the terrace site atom (Thu) at the two computed coverages ($\sim$ 5 meV difference each). On the other hand, the modes at the 3-fold step and 4-fold hollow sites are slightly different ($\sim$ 20 meV at the step and $\sim$ 30 meV at the terrace). Correspondingly, we account for the vibrational contribution to zeroth order by correcting the on-site energies at the step sites (Sh1 and Sh2) by 20 meV and correcting the on-site energies at the terrace sites (Thu, Thc, Thl) by 30 meV.

### 8.2.4 Validation by Direct Enumeration

In the work on the ordering behavior of oxygen at the Pd(100) surface in Chapter 6, there was only one kind of important adsorption site, the hollow site. Focusing on the order-disorder transition at constant number of adsorbed O atoms, we could there focus on the formation energy, Eq. 5.13 to check on the consistency of the DFT input structures and the ground-state structures predicted by the LGH via direct enumeration, see Chapter 6.2.2. In this Chapter we are more interested in the ordering behavior in a grand-canonical ensemble, *i.e.* allowing for particle exchange with the surrounding gas-phase. We therefore use here the Gibbs free energy of adsorption defined as Eq. 8.3 to validate our O-Pd(117) DFT input data set.

$$\begin{aligned} \Delta G(\Delta\mu_{\mathrm{O}}) &\approx -\frac{1}{2A}(E^{\mathrm{total}}_{\mathrm{O/Pd(117)}} - E^{\mathrm{total}}_{\mathrm{Pd(117)}} - \frac{N_{\mathrm{O}}}{2}E^{\mathrm{total}}_{\mathrm{O_2(gas)}} - N_{\mathrm{O}}\Delta\mu_{\mathrm{O}}) \\ &= \frac{1}{2A}(2E^{\mathrm{tot}}_{\mathrm{b}} + N_{\mathrm{O}}\Delta\mu_{\mathrm{O}}) \quad , \end{aligned} \tag{8.3}$$

where $E^{\mathrm{total}}_{\mathrm{O/Pd(117)}}$, $E^{\mathrm{total}}_{\mathrm{Pd(117)}}$, $E^{\mathrm{total}}_{\mathrm{O_2(gas)}}$, and $E^{\mathrm{tot}}_{\mathrm{b}}$ have the same meaning as in Eq. 8.1. $\Delta\mu_{\mathrm{O}}$ is the oxygen chemical potential, $A$ is the surface unit area, and $N_{\mathrm{O}}$ is the total number of the oxygen atoms in the supercell.

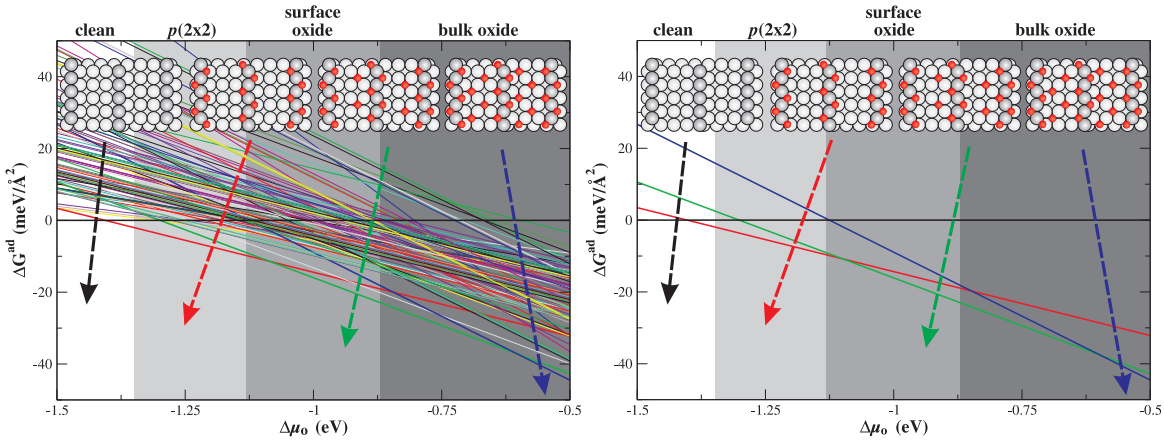


Figure 8.2: Phase diagrams of DFT calculations (left panel) and of corresponding DE data (right panel). The structures on the top of each panel show the most stable structures in different oxygen chemical as obtained in previous work (ref. [60]). In the DE phase diagram, we only show the lines of the most stable configurations.

Using all DFT structures to construct the thermodynamic phase diagram we compare this to the phase diagram obtained when directly enumerating any ordered structure that can be produced in a Pd(117)$(1 \times 3)$ cell with the LGH energetics. Similar to Chapter 6 we did this in an iterative fashion, by starting with a small group of DFT input structures to construct the LGH. Using this LGH for the DE method to obtain $\Delta G$ for all arbitrary configurations within a $(1 \times 3)$ cell, we then plotted the DE thermodynamic phase diagram, and compared it to the DFT phase diagram. If new configurations showed up, they were calculated by DFT. Then, including this new DFT data to get a new LGH, the DE was redone until DFT and DE phase diagrams agreed with each other.

Finally, the left and right panels in Fig. 8.2 illustrate the DFT phase diagram and the direct enumeration phase diagram using the the final LGH presented in Sections 8.2.1 and 8.2.2, respectively. The nice agreement between the two phase diagrams indicates that our DFT input set is able to parameterize a LGH that gives a sequence of most stable structures at different $\Delta\mu_O$ that is consistent with the original DFT input set. At this stage we content ourselves with this similarity and defer a discussion of the physics of this phase diagram to Section 8.3.2 below.

### 8.2.5 Treating the Boundary for Surfaces with Wider Terrace Width

The parameterization of the LGH was exclusively done using DFT data for the Pd(117) surface. If one wants to employ this LGH to also simulate the ordering

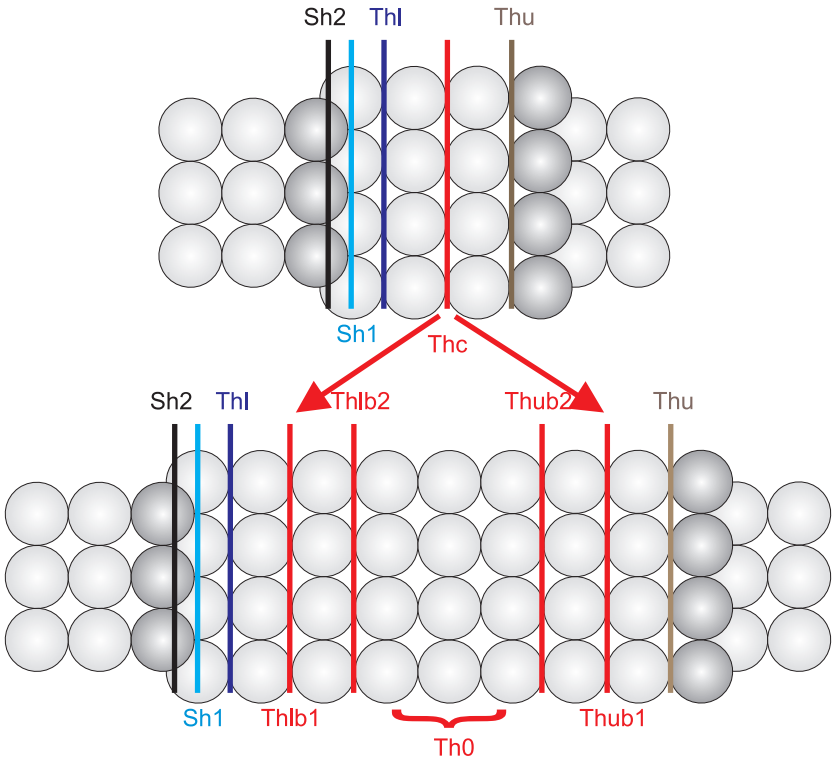


Figure 8.3: Schematic top view of the sites at the 4 atomic row (100) terraces at (117) and the site types at wider terrace width. Sh2, Sh1, Thu, Thc and Thl have the same meaning as usual, whereas on a wider (100) terrace, the Thc sites have to be divided into different sites, Thlb1, Thlb2, Th0, Thub1, and Thub2, according to their distance to the step. For the presently employed range of lateral interactions (up to 3rd NN pairs) all sites marked as Th0 are indistinguishable from hollow sites at a (100) surface. "b" indicates the boundary between Thl and Th0, or between Thu and Th0.

behavior of O atoms at vicinals with a wider terrace width − or ultimately the ordering behavior of O atoms at an isolated step at Pd(100) − one further issue needs to be addressed. As illustrated in Fig. 8.3 a wider terrace width gives rise to two additional rows of sites that for the employed pool of short-ranged interactions can have lateral interactions that are neither covered by the (117)-derived interactions, nor the (100)-derived interactions. If we take for example the Thl sites, the farthest reaching interaction in form of the third NN pair interaction reaches to the sites Thlb2, *i.e.* one needs an interaction $V_{3\mathrm{p}}$ Thl-Thlb2. On the other hand, what we only have are either the interaction $V_{3\mathrm{p}}$ from Pd(100), which is not entirely correct since the Th0 site is not a terrace site. Or we have the interaction $V_{3\mathrm{p}}^{13}$, which is neither entirely correct since the Thlb2 site is not a Thu site. Fortunately, as discussed before, in many cases the involved lateral interactions are very similar. What we therefore did in practice was to either always approximate the unknown boundary interactions by the equivalent interactions from the Pd(100) LGH, or to always approximate the unknown boundary interactions by the equivalent interactions from the (117) LGH. The obtained results

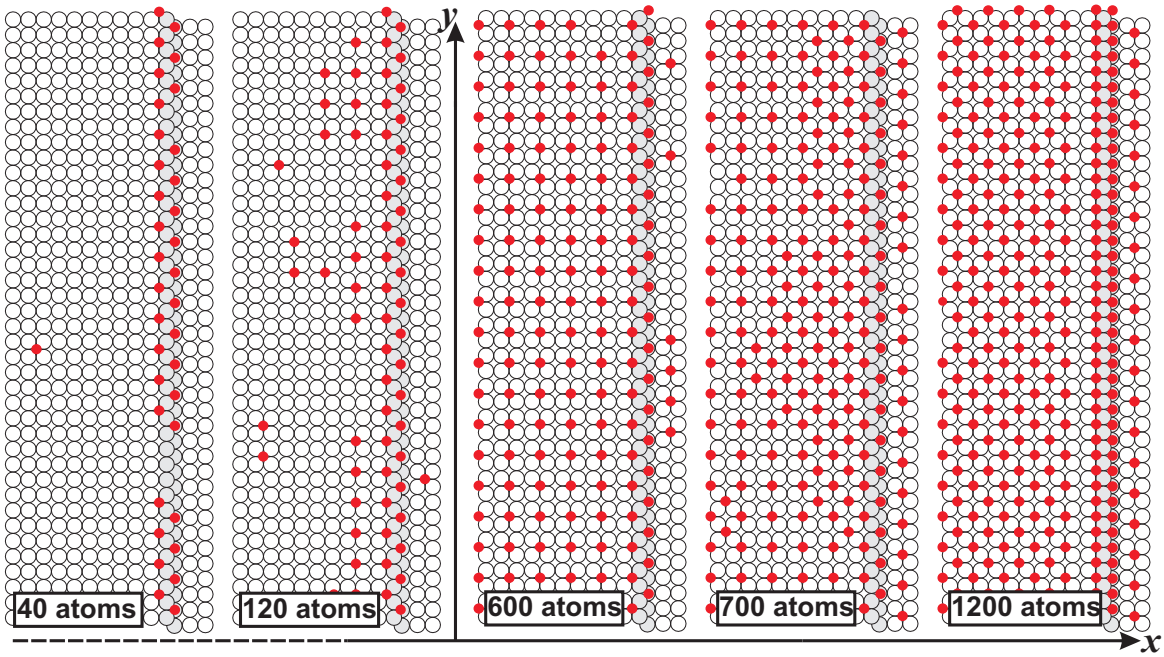


Figure 8.4: Schematic top views showing the results of simulated annealing runs with different number of oxygen atoms in $(60 \times 40)(100)$ cell with one (111) step inside. Shown are the results after the temperature quenching had reached room temperature (300 K). In order to save space, each panel only shows one (111) step (grey region) and 10 rows away from the (111) step at the (100) terrace. The two perpendicular lines are $x$ and $y$ directions. The additional data are the total number of oxygen atoms in the simulation cells.

were in both cases very similar so that we concentrate in the remainder of this chapter on presenting the results for the case, where the interactions in the boundary region were approximated with the values form the Pd(100) LGH.

## 8.3 Ordering Behavior of Oxygen Near a (111) Step at Pd(100)

### 8.3.1 Simulated Annealing Simulation: Identify Low-energy Step structures

In a first stage we exploit the low computational cost to evaluate the established first-principles multi-site LGH to extensively explore the huge configuration space and identify low-energy ordered step structures. This is achieved by simulated annealing runs in periodic boundary condition simulation cells containing $(60 \times 40)$ (100) surface unit-cells and one (111) step along the shorter cell axis (see Appendix D). For fixed and initially random O coverages ranging up to a half filling of all terrace hollow sites $10^8$ MC steps are used to continuously quench from an initial temperature of

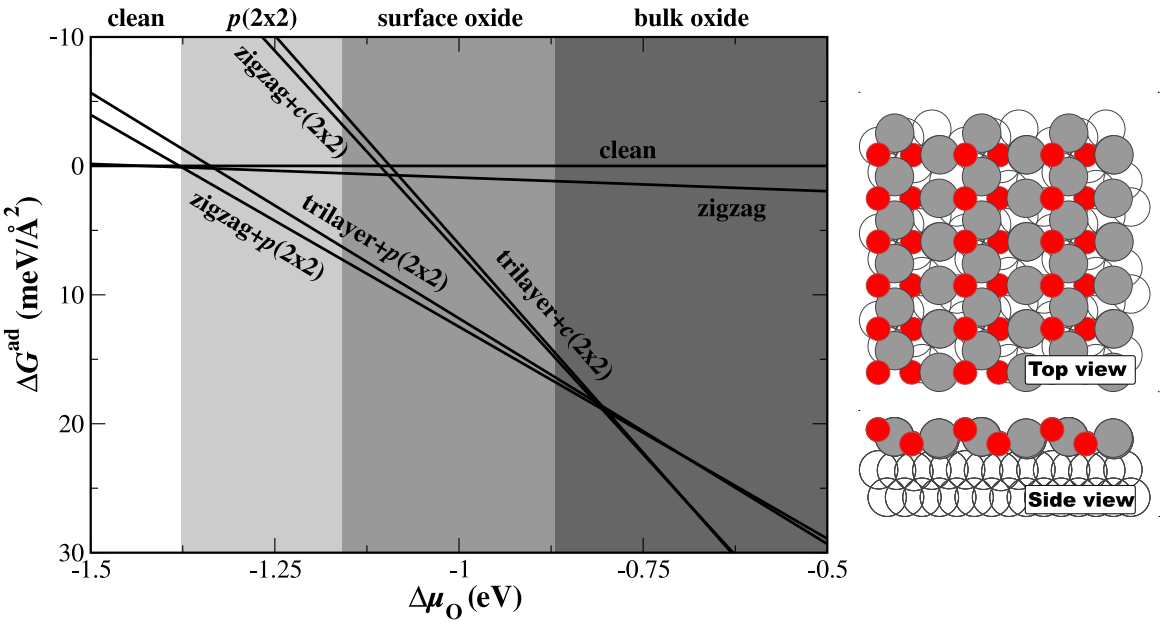


Figure 8.5: Computed Gibbs free energy of adsorption $\Delta G^{\mathrm{ad}}$ for O adsorbate structures at a (111) step at Pd(100) and using the clean surface as zero reference (left panel). Using the nomenclature defined in Fig. 8.6 the labels refer to the structure at the step and at the neighboring terrace, *e.g.* zigzag+$p(2 \times 2)$ stands for a zigzag step decoration coexisting with the $p(2 \times 2)$ adsorbate ordering at the terrace. Additionally indicated by differently shaded backgrounds are the stability regions obtained for the ideal Pd(100) surface in previous work [58, 135], namely those of the $p(2 \times 2)$ overlayer, of the surface oxide structure (right panel) and of a thick bulk-like PdO film.

2000 K. Depending on the O content, these simulations unanimously lead to patches of increasing size of four distinct ordered structures that are schematically shown in Fig. 8.4 and 8.6. At the lowest coverages the O adatoms quickly decorate the Thu and Sh2 sites at the (111) step in a characteristic zigzag structure with $(2 \times 1)$ periodicity (the first left panel in Fig. 8.4). At increasing coverages domains of the experimentally well characterized $p(2 \times 2)$ overlayer [90] start to form at the (100) sites next to the upper edge of the fully zigzag decorated step (the second left panel in Fig. 8.4). After the $p(2 \times 2)$ extends over the whole (100) terrace, further adding oxygen atoms leads to the zigzag decorated step hand in hand with the $c(2 \times 2)$ domain (the second right panel in Fig. 8.4). Only once the O content in the simulation cell exceeds the one required to fully cover the entire terrace with the $c(2 \times 2)$ structure, does a further decoration of Thu and Sh2 step sites occur. This results in a (1x1) periodic step structure, which we henceforth term trilayer.

### 8.3.2 Stability of Zigzag Decorated Step

For the identified structural models we now account for the effect of a finite gas-phase environment through the atomistic thermodynamics approach [67]. Here, the surface

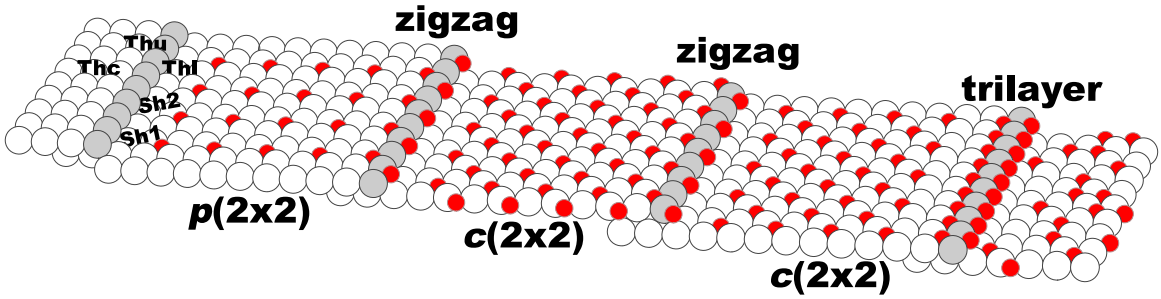


Figure 8.6: Schematic view of a Pd(100) surface with (111) steps. Shown are the five distinct adsorption sites considered in the first-principles lattice-gas Hamiltonian: The fourfold coordinated (100) hollow sites at the terraces (Thc), at the upper (Thu) and lower (Thl) rim of the step, as well as the two threefold (111) hollow sites at the step edge, one with a coordination to two step atoms (Sh2) and one with a coordination to one step atom (Sh1). Additionally represented are five characteristic ordered structures discussed in the text: A $p(2 \times 2)$ and a $c(2 \times 2)$ adsorbate phase at the (100) terrace, a zigzag structure where the step is decorated with O atoms in alternating Thu and Sh2 sites, and a trilayer structure where all Thu and Sh2 are occupied (Pd = large spheres, Pd step atoms = large dark spheres, O = small spheres).

is considered to be in equilibrium with an oxygen gas-phase reservoir characterized by a chemical potential $\Delta\mu_O(T, p)$ summarizing the two-dimensional dependence on pressure $p$ and temperature $T$. In its prevalent form this approach neglects the effect of configurational entropy at the surface and then simplifies to computing the Gibbs free energy of adsorption for any ordered structural model at any given $\Delta\mu_O(T, p)$ from its corresponding binding free energy [55, 56]. This allows to readily compare the stability of most distinct structural models over a wide range of gas-phase conditions, and is thus ideally suited to also assess under which gas-phase conditions the surface structure and composition at the step is appropriately described by our on-surface LGH model. We correspondingly employ this approximate approach here not only to obtain a first understanding of the stability of the presented step models, but also to contrast this with the stability ranges of more complex O-rich phases identified previously for the ideal Pd(100) surface [58, 135]. Specifically, these are the $\sqrt{5}$ surface oxide structure (the right panel in Fig. 8.5), which corresponds to a sub-nanometer thin film of PdO(101) on the surface [91], and bulk PdO to represent thick bulk-like oxide films. The results are summarized in Fig. 8.5 and reveal a large stability range of the zigzag decoration of the (111) step, which over most of this range coexists with the $p(2 \times 2)$ adsorbate phase on the (100) terrace. The trilayer arrangement becomes only more favorable at quite elevated chemical potentials and coexists then directly with the denser $c(2 \times 2)$ overlayer on the terrace. In light of the also shown stability ranges of the oxidic phases at ideal Pd(100) we can therefore identify quite a range of gas-phase conditions ($-1.43\,\mathrm{eV} < \Delta\mu_O < -1.16\,\mathrm{eV}$) that are not yet O-rich enough to induce oxide formation and where the zigzag step decoration is not just due to kinetics, but instead represents a thermodynamically stable phase in its own right.

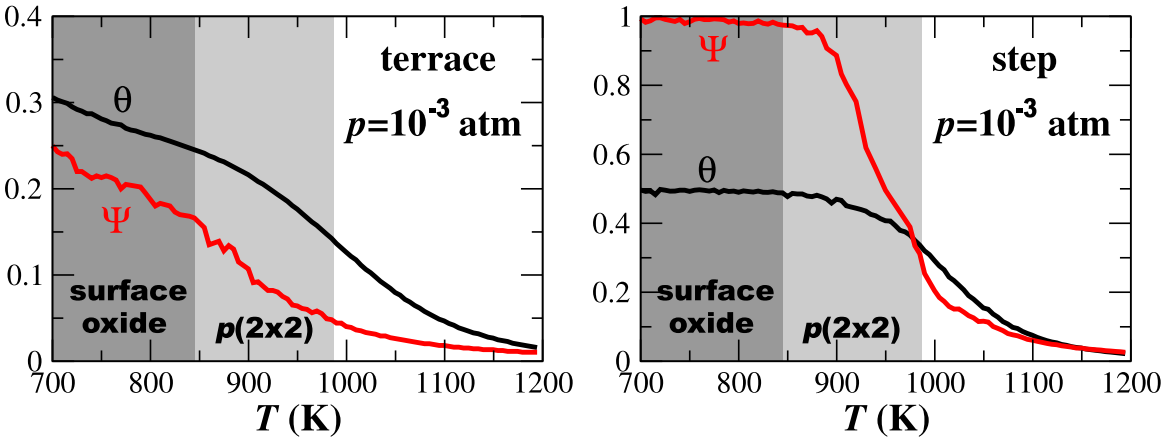


Figure 8.7: Average coverage (black lines) and order parameter (red lines) for the terrace (left panel) and step (left panel) sites as determined by grand-canonical MC simulations for a fixed oxygen pressure of $10^{-3}$ atm. The order parameters are sensitive to the lateral periodicities of the $(2 \times 1)$ zigzag step structure and the $p(2 \times 2)$ arrangement at the terrace, respectively. The coverages are normalized to the full occupation of all Sh2+Thu step sites and the full occupation of all hollow terrace sites. Vertical lines indicate the stability range as determined in Fig. 8.5. Equivalent results are obtained for simulations at $p = 10^{-5}$ and $p = 1$ atm, with corresponding variations of the critical temperatures of the order of 100 K.

In contrast, the elevated $\Delta\mu_O(T, p)$ at which the trilayer arrangement at the step becomes more favorable than the zigzag decoration fall well into the stability range of the oxidic surface reconstructions. This suggests an interpretation of the trilayer structure in form of a kinetic precursor in the oxide formation process, and in this respect it is intriguing to note that its geometric structure coincides in fact with one row of the $\sqrt{5}$ surface oxide (the right panel in Fig. 8.5).

At near atmospheric pressures the stability range of the zigzag step decoration ($-1.43\,\text{eV} < \Delta\mu_O < -1.16\,\text{eV}$) corresponds to rather elevated temperatures of the order of 1000 K [55, 56]. At such temperatures, configurational entropic effects can not be uncritically dismissed. We therefore scrutinize the insight provided by the approximate thermodynamic approach by fully accounting for such effects with grand-canonical MC simulations based on the first-principles LGH. In these simulations, the effect of the (111) step on the adsorbate ensemble in its vicinity is evaluated by separately monitoring the order and coverage for each row of sites (Eq. 5.29) parallel to the step edge using equivalent simulation cells as for the simulated annealing runs. Interestingly, the disturbance exerted by the step is found to be rather short ranged on the accuracy level of interest to this study. Already four atomic rows away from the immediate step edge the computed critical temperatures are to within $\pm 50$ K identical to those obtained at the ideal Pd(100) surface (Appendix D).

We correspondingly restrict the discussion on the ordering behavior directly at the step row itself, contrasting it with the ordering behavior at a row of ideal Pd(100)

hollow sites far away from the step. The results for a pressure $p = 10^{-3}$ atm are shown in Fig. 8.7. Since the prevalent ordered structures in the corresponding $(T, p)$-range are the $p(2 \times 2)$ at the terrace and the $(2 \times 1)$ zigzag decoration at the step order parameters that are sensitive to these lateral periodicities can be suitably employed to determine the critical temperature for the order-disorder transition at fixed oxygen pressure (Chapter 5: the order parameter for $p(2\times2)$ periodicity on terrace is Eq. 5.23 and the order parameter for the zigzag structure has the same formula as in Eq. 5.27). In addition to the GCMC results in Fig. 8.7, we also convert the thermodynamic oxygen chemical potentials of $p(2 \times 2)$-(100) (light grey block) and $\sqrt{5}$ surface oxide (grey block) into the temperatures at $10^{-3}$ atm. They are (987 K, $10^{-3}$ atm) for $p(2 \times 2)$ and (846 K, $10^{-3}$ atm) for the surface oxide.

From Fig. 8.7 we see that at the chosen pressure all temperatures below 846 K fall into the stability regime of the $\sqrt{5}$ surface oxide, which we cannot model with the present on-surface LGH. Focusing therefore on the temperatures above this limit we see that the stability range of the $p(2 \times 2)$ phase at the terrace predicted by the atomistic thermodynamics approach is an artifact of the neglected configurational entropy. In the GCMC simulations that explicitly account for this entropic contribution we indeed find a coverage of O atoms in hollow sites in this temperature range that corresponds to the coverage of the $p(2 \times 2)$ phase. However, over the entire temperature range above 846 K the order parameter has already decreased to small values, *i.e.* there is no long-range order at these temperatures anymore. The real population at the Pd(100) terraces is thus a low-coverage of disordered O atoms in hollow sites. This is much in contrast to the situation at the step, where a high order parameter indicates that the ordered zigzag structure is indeed stable even at these elevated temperatures. The order-disorder transition as reflected by the order parameter occurs only at temperatures around 950 K, where then also desorption of the on-surface oxygen atoms occurs.

## 8.4 Conclusion

Through a combination of first-principles statistical mechanics techniques we are therefore able to identify a wide range of environmental conditions, in which (111) steps at Pd(100) will be decorated by a characteristic zigzag oxygen structure. This includes near atmospheric pressures and temperatures around and above 1000 K, *i.e.* gas-phase conditions that are representative for an important catalytic process like the high-temperature combustion of methane, and Fig. 8.9 shows a schematic perspective view of the resulting surface structure and composition under these conditions. Due to the low energetic cost of the close-packed steps, this defect will be a frequent structural motif at the surface with corresponding potential influence on the function in such applications. In this respect it is interesting to notice that the same ordered zigzag O structure was recently characterized at the (111) steps of Pd(111) vicinals in the same range of oxygen chemical potentials, albeit at lower temperatures

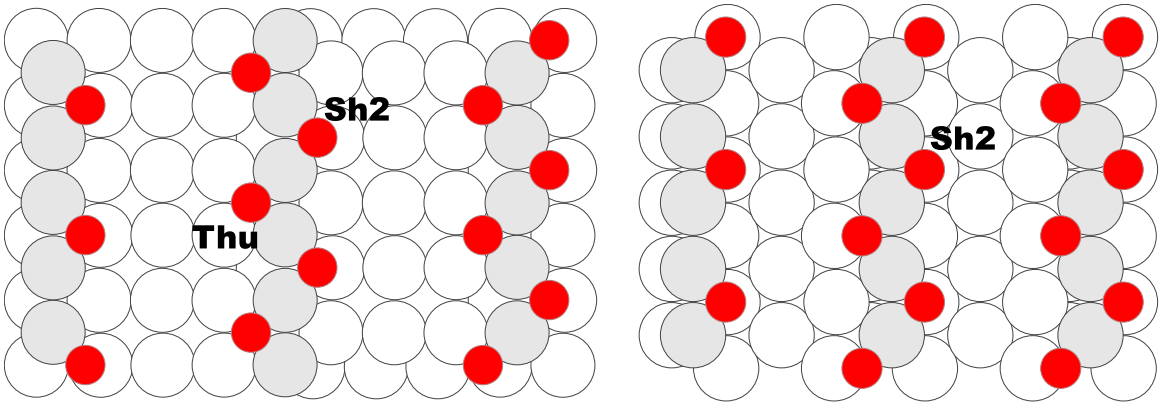


Figure 8.8: Two Pd vicinal structures used to calculate the O 1*s* surface-core level shifts for comparison. Left panel: the zigzag structure of O-Pd(117), which exhibits (111) steps and (100) terraces. Right panel: zigzag structure of O-Pd(221), which exhibits (111) steps and (111) terraces.

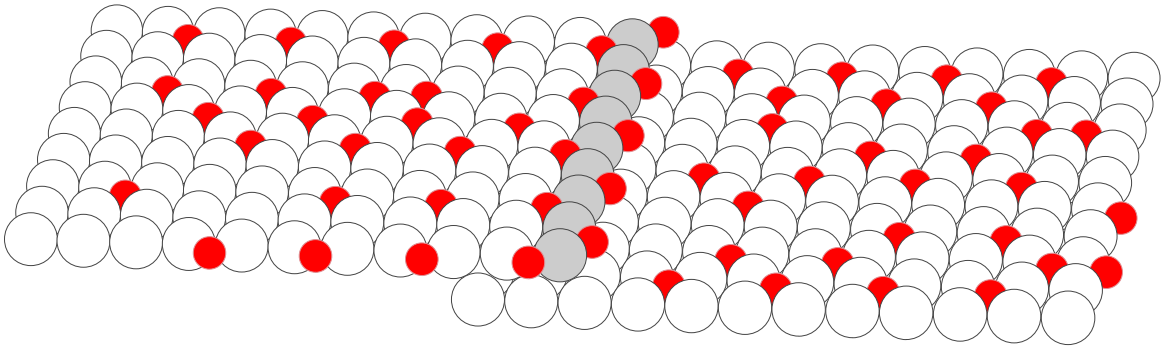

Figure 8.9: Schematic perspective view of the surface under gas-phase conditions representative of high-temperature methane combustion.

[137]. Using our LAPW/APW+lo DFT setup we compute initial and final state O 1*s* core level shifts [51] that are identical to within 40 meV for the O atoms adsorbed at the geometrically equivalent Sh2 step sites in the two structures (Fig. 8.8). Since core level shifts are a sensitive probe of the local bonding properties, this suggests highly similar reactivities of the oxygen atoms adsorbed at the decorated (111) steps at both prominent facets of Pd nanoparticles. If these oxygen atoms play a determining role for the catalytic function, this similarity would then provide an intriguing atomic-scale interpretation for the enigmatic structure insensitivity reported recently for the high-temperature methane combustion [136]. While our study focuses on establishing a first methodological access to determine the structure and composition of a prominent defect like atomic steps at surfaces exposed to realistic environments, this immediately exemplifies the far-reaching insight that this kind of first-principles

statistical mechanics approach can provide.

# Chapter 9

# Summary and Outlook

The aim of the present thesis was to establish a first methodological access to a first-principles based treatment of a prominent defect like atomic steps at single-crystal surfaces, when the latter are exposed to realistic gaseous environments. This methodological work was illustrated and carried out using an oxygen gas-phase and the close-packed (111) step at Pd(100) as example. Specific conclusions, also on the physics regarding this model system, were already presented at the end of each chapter, which is why we restrict this final chapter to an outlook of only the methodological aspects.

Addressing a defect at a metal single-crystal facet exposed to a gaseous environment requires to combine two, somehow conflicting aspects, even if only targeting a situation in thermodynamic equilibrium. In order to obtain a reliable energetics one needs to resort to first-principles electronic structure calculations, nowadays typically achieved using density-functional theory. In order to properly account for entropic effects at finite temperatures one needs to evaluate the partition function, nowadays *e.g.* with Monte Carlo techniques. Even though the latter enable already a most efficient sampling, they still typically need a number of total energy evaluations that far exceeds present day computational facilities. At metal surfaces this is particularly pronounced since large (and thus highly expensive) supercell calculations are required to capture the metallic band structure at the extended surface. While this makes already the treatment of entropic effects at ideal single-crystal surfaces highly challenging, one has to resort to even much larger supercell calculations of vicinal surfaces to capture an extended defect like atomic steps within the underlying periodic boundary condition framework.

In the present thesis we therefore employed an intermediate step in form of a coarse-grained lattice-gas Hamiltonian. Once parameterized with first-principles data from the supercell calculations, the algebraic form of the LGH allows easily for the manifold of total energy evaluations required in the statistical simulations. The crucial aspects in this approach are then the parameterization of the LGH, and for the aspired predictive character of the theory how the uncertainties in the underlying electronic structure calculations propagate to the mesoscopic simulation results. We showed how both aspects can be systematically addressed in the case of the ideal Pd(100)

surface. The increased complexity when also accounting for the step forced us already to a much less rigorous approach there. The significantly increased number of lateral interactions makes checks on the truncated LGH more cumbersome and dictates also a significantly larger number of large supercell calculations. While conceptually straightforward, the approach gets therefore more and more limited in practice when moving to ever more complex scenarios, *e.g.* co-adsorption in mixed environments or a coexistence of various defects like steps, vacancies or facet edges. This is not to mention the complications that would come into play, if the gaseous environment would lead to structural rearrangements beyond the simple adlayer formation addressed here.

In this respect, our finding that most of the error due to the approximate DFT exchange-correlation functional only propagates to the on-site energy and most short-ranged lateral interactions could indicate an intriguing possibility. If this finding is indeed of more general nature, it suggests than one could *e.g.* only use a lower level treatment to determine most of the increasing number of lateral interactions in more complex systems, whereas a much small number of high accuracy electronic structure calculations would be required to accurately determine the on-site and shortest-ranged interactions. With the present thesis as basis, it remains to future studies to further explore this.

# Part IV

# Appendix

# Appendix A

# Bulk Pd

Palladium (Pd) is a late $4d$ transition element. Its atomic number is 46 and its atomic configuration is [Kr]$4d^{10}$. In the periodic table of the elements, its nearest neighbors are Rh ([Kr]$5s^1 4d^8$) and Ag ([Kr]$5s^1 4d^{10}$). Bulk palladium crystallizes in the face-centered cubic (fcc) structure and the experimental value for the palladium lattice constant is $a_{\text{exp}}$=3.8903 Å[138]. In order to study the bulk properties of Pd we use the following (L)APW+lo computational parameters: A muffin-tin radius $R_{\text{MT}}^{\text{Pd}}$=2.1 bohr (1 Å=0.529177 bohr) is used throughout[1]. Using basis set parameters as determined in a previous PhD thesis [139], total energies at different lattice constants were calculated using the Wien2k code [33]. The equilibrium unit cell volume $V_0$ (connected to the equilibrium lattice constant $a_0$ by $a_0^3 = V_0$ in the cubic structure) is determined by minimization of the total energy function, $E(V)$. The bulk modulus $B(T, V)$ is then related to the curvature of the total energy function $E(V)$ at the equilibrium value.

$$B(T, V) = V \frac{\partial^2 E}{\partial V^2}\Big|_T \tag{A.1}$$

In practice, one evaluates the energy for different unit cell volumes (different lattice constants), and then fits them using an equation of state of the solid. The lattice constant of the Pd cubic unit cell was varied from 3.611 Å to 4.403 Å in 0.1 Å steps, and more points were used near the experimental lattice constant (3.8903 Å). The equilibrium value was then obtained using a Murnaghan equation of state fit [140−142] (Eq. A.2). We additionally varied the number of data points actually used in the Murnaghan fit (Fig. A.1 and Fig. A.2) to ensure that this had no influence on the final equilibrium lattice constant.

$$E(V) = E(V_0) + \frac{B_0 V}{B_0'(B_0' - 1)}[B_0'(1 - \frac{V_0}{V}) + (\frac{V_0}{V})^{B_0'} - 1] \tag{A.2}$$

[1]From the experimental Pd lattice constant, the maximum $R_{\text{MT}}$ without overlapping sphere is 2.5 bohr. However at surfaces and in particular in oxygen chemisorption studies the $R_{\text{MT}}$ is also limited by the quite short Pd-O bond length (∼3.8 bohr). Accounting also for the expected significant relaxation at vicinal surfaces, we therefore chose the smaller value of 2.1 bohr, which then also allows for a reasonable O muffin-tin radius.

where $B_0'$ is the derivative of the bulk modulus with respect to pressure $p$=0. In Fig. A.1 and Fig. A.2, the equilibrium lattice constant is determined as 3.95 Å and 3.84 Å using GGA-PBE and LDA as exchange-correlation (xc) functionals, respectively.

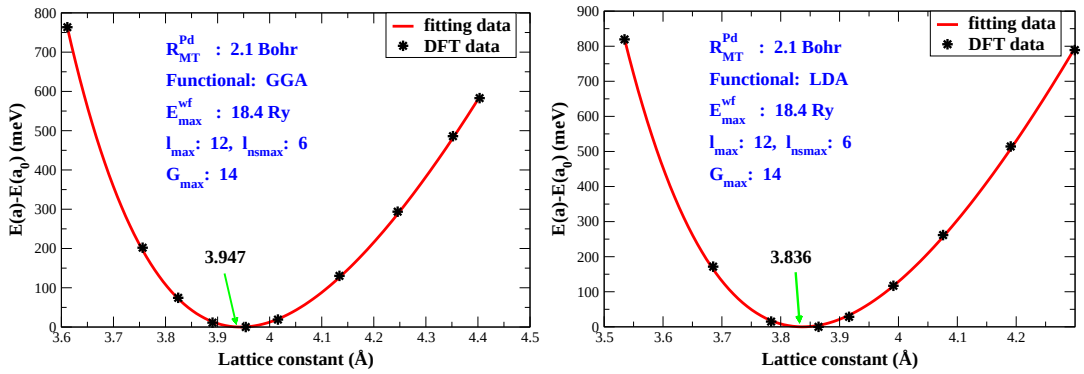


Figure A.1: Determination of the equilibrium lattice constant for the fcc Pd structure for the GGA-PBE and LDA functional by Murnaghan fitting (Eq. A.2): $a_0^{\mathrm{GGA}}$=3.947 Å, $a_0^{\mathrm{LDA}}$=3.836 Å.

The reason why atoms can combine together to construct a solid is that the total energy of the solid is lower than the sum of the energies of the corresponding isolated atoms. In other words the solid is more stable. The process is exothermic, and the released excess energy is called *cohesive energy*. It is defined as,

$$E_{\mathrm{coh}} = -(E_{\mathrm{bulk}}(a_0) - \sum_i E^i_{\mathrm{iso}}) \tag{A.3}$$

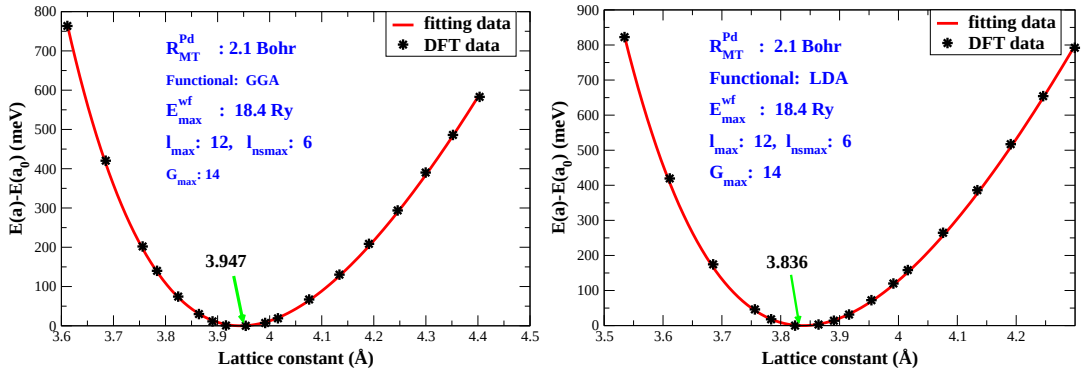


Figure A.2: Determination of the equilibrium lattice constant for the fcc Pd structure for the GGA-PBE and LDA functional with more points than in Fig. A.1. $a_0^{\mathrm{GGA}}$=3.947 Å, $a_0^{\mathrm{LDA}}$=3.836 Å.

Table A.1: Comparison of calculated lattice constant and bulk modulus using the GGA-PBE and LDA functional with experimental data.

| | Experiment [20, 138] | GGA-PBE | $\Delta_{\mathrm{GGA-PBE}}$ | LDA | $\Delta_{\mathrm{LDA}}$ |
|---|---|---|---|---|---|
| $a_0$ (Å) | 3.89 | 3.95 | 1.4% | 3.84 | -1.4% |
| $B_0$ (Mbar) | 1.80 | 1.57 | -13.8% | 2.16 | 20% |
| $E_{\mathrm{coh}}$ (eV/atom) | 3.94 | 3.68 | -6.6% | 5.08 | 28.9% |

where $E_{\mathrm{bulk}}(a_0)$ indicates the total energy of the bulk, $i$ indicates the number of atoms in the bulk, and $E^i_{\mathrm{iso}}$ is the total energy of isolated element atom, $i$. The total energy of an isolated Pd atom is calculated with a supercell geometry *i.e.* a Pd atom is placed in the center of a huge periodically repeating unit cell. The cell size (12 bohr × 13 bohr × 14 bohr) is used to avoid interaction with the periodic images. The non-cubic size of the cell is used to prevent the Wien2K code from symmetry averaging the electron density. In the absence of dispersion in the small Brillouin zone, one k-point at $(\frac{1}{2},\frac{1}{2},\frac{1}{2})$ is enough for this calculation, which in addition is performed spin-polarized to account for the proper Hund occupation of the orbitals. With this procedure, values of $E^{\mathrm{GGA}}_{\mathrm{coh}}$=3.68 eV/atom and $E^{\mathrm{LDA}}_{\mathrm{coh}}$=5.08 eV/atom were computed for the cohesive energy with GGA-PBE and LDA, respectively. The experimental value of the bulk Pd cohesive energy is 3.94 eV/atom [20]. The lattice constant, bulk modulus and cohesive energy from experiment, GGA-PBE and LDA calculations are tabulated in Table A.1, from which the known overbinding of the LDA and overcorrection of the GGA-PBE become apparent [108, 109, 112, 113]. On the other hand, the data in Table A.1 are in excellent agreement with a previous study in the group using the earlier WIEN97 LAPW code, which gave $a = 3.944\,\text{Å}$ and $B = 1.63\,\text{MPa}$, respectively [111].

# Appendix B

# Low-index Pd Surfaces

## B.1 Clean Surfaces

Using the calculated equilibrium bulk Pd fcc lattice constant, we construct Pd(111) and Pd(100) slabs using each time 5 layers (Fig. B.1). The surface unit area is 6.75 Å$^2$ (GGA-PBE) and 6.37 Å$^2$ (LDA) for Pd(111), while it is 7.79 Å$^2$ (GGA-PBE) and 7.36 Å$^2$ (LDA) for Pd(100).

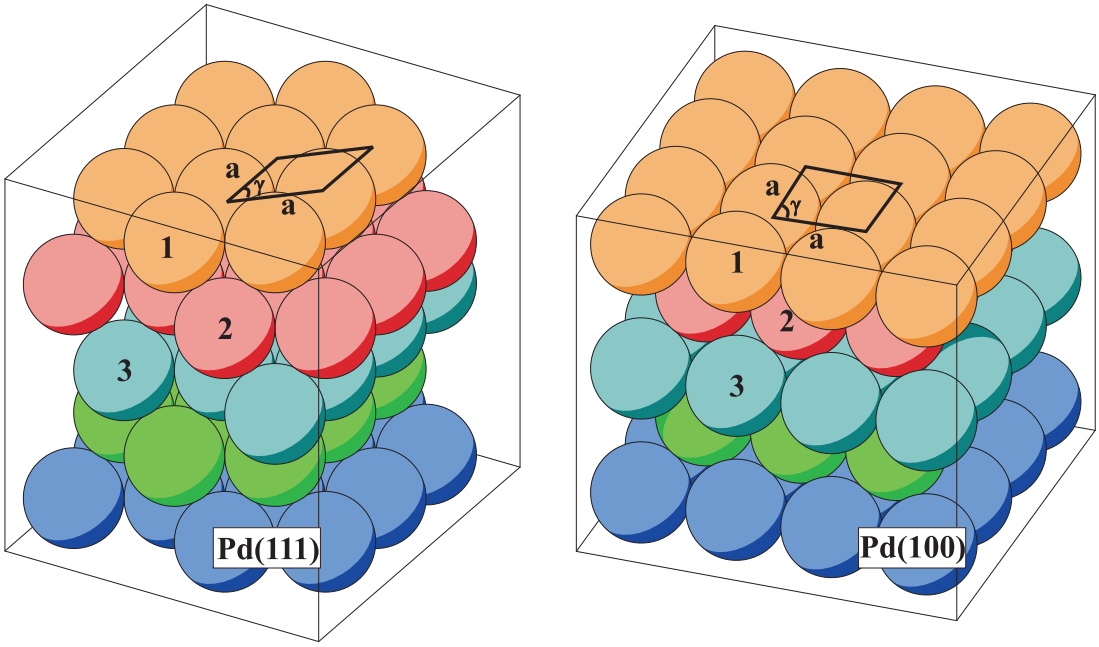


Figure B.1: Schematic figures of the Pd(111) [left] and Pd(100) [right] slab structures. For the GGA-PBE functional the in-plane surface unit-cell parameters are: Pd(111), a=2.79 Å, $\gamma = 60^0$; Pd(100), a=2.79 Å, $\gamma = 90^0$.

The surface energy is obtained via Eq. 4.8 for different energy cutoffs ($E^{\mathrm{wf}}_{\mathrm{max}}$) and

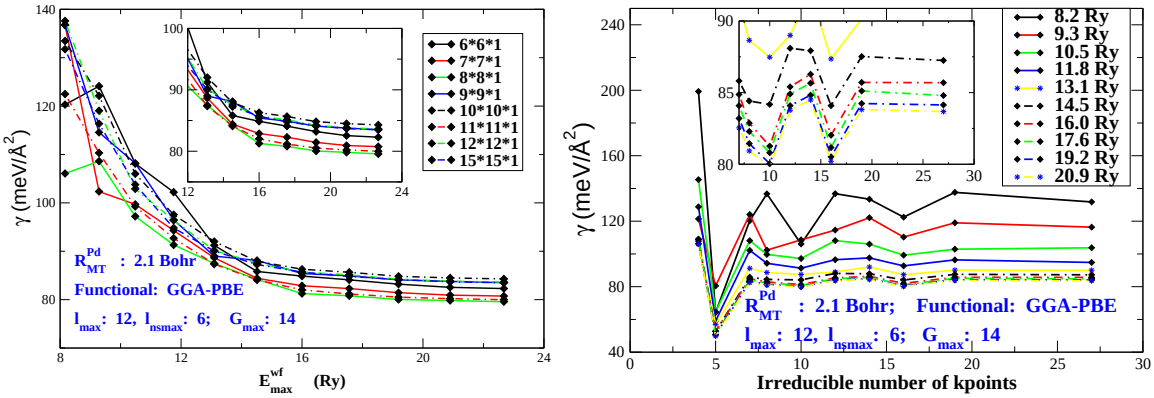


Figure B.2: Convergence test for the optimal energy cutoff and **k**-points on a 5 layer Pd(111) slab using the GGA-PBE functional.

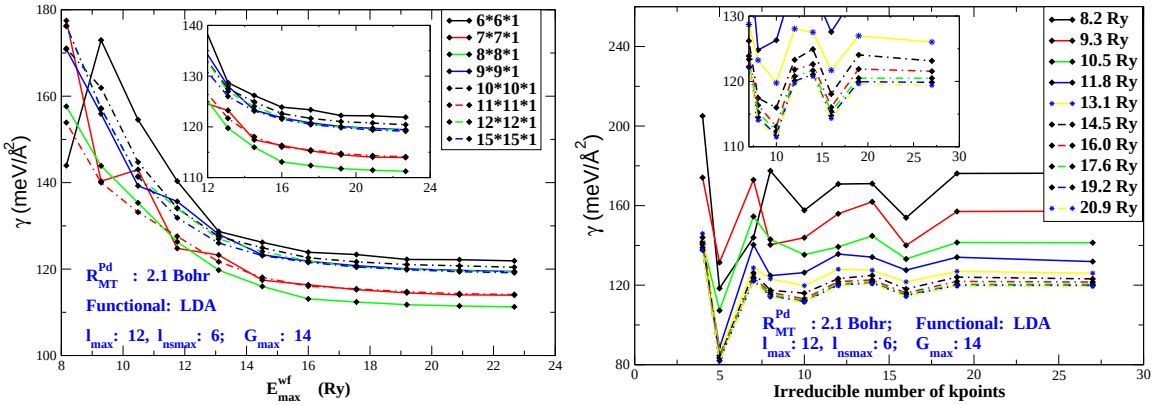


Figure B.3: Convergence test for the optimal energy cutoff and **k**-points on a 5 layer Pd(111) slab using the LDA functional.

**k**-points to find out the convergence behavior with respect to these basis set parameters. Fig. B.2 shows corresponding curves of the surface energy versus $E^{\rm wf}_{\rm max}$ (**k**-points) for different **k**-points ($E^{\rm wf}_{\rm max}$) and the GGA-PBE functional. In the left figure (energy cutoff test), the surface energy is rapidly decreasing with increasing $E^{\rm wf}_{\rm max}$, but converges to within $\pm 5$ meV/Å$^2$ when $E^{\rm wf}_{\rm max}$ reaches 16.0 Ry. In the right figure of Fig. B.2 (**k**-points test), the curve oscillates very fast with increasing irreducible number of **k**-points when $E^{\rm wf}_{\rm max}$ is small. For larger energy cutoff ($\geq$16.0 Ry), all curves are, however, converged very well for meshes containing more than 12 irreducible **k**-points [k-mesh: $(9 \times 9 \times 1)$]. Similar tests, but using the LDA functional are shown in Fig B.3, arriving at a similar conclusion. With basis sets exceeding $E^{\rm wf}_{\rm max}$=16.0 Ry and 12 irreducible **k**-points the surface energy of Pd(111) can therefore be converged to within $\pm 5$ meV/Å$^2$.

In the same way, we tested the energy cutoff and **k**-points convergence for Pd(100)

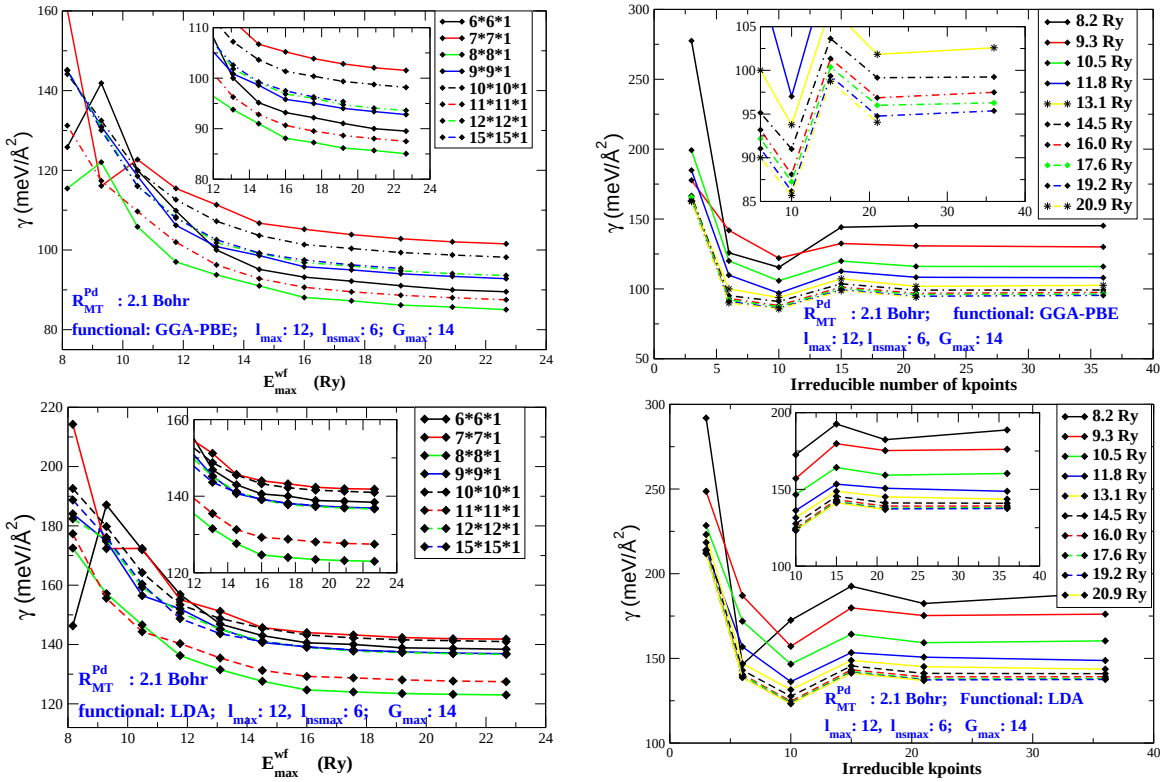


Figure B.4: Convergence test for the optimal energy cutoff and **k**-points on a 5 layer Pd(100) slab using the GGA-PBE (upper two panels) and the LDA (lower two panels) functional.

using again the GGA-PBE and LDA functional. From Fig. B.4, it can be discerned that again a convergence to within $\pm 5$ meV/Å$^2$ can be reached for $E^{\mathrm{wf}}_{\mathrm{max}}$=16.0 Ry and more than 15 irreducible **k**-points (k-mesh: $(9 \times 9 \times 1)$).

As mentioned before, the number of layers in the slab is another important parameter in the surface simulation. In our slab model, we therefore increased the number of layers to construct different slabs (3, 5, 7, 9 and 11 layers of Pd(111) and Pd(100) slabs), while keeping the total thickness of the supercell (slab+vacuum) fixed. The vacua in all cases are large enough (>13 Å in the Pd(111) supercell and >11 Å in the Pd(100) supercell) to avoid the interaction between surfaces of consecutive slabs (see vacuum tests below). The optimal basis set parameters from the above tests were used to calculate the Pd(111) and Pd(100) surface energies of the different slabs, both with the GGA-PBE and LDA functional. As apparent from Fig. B.5, the curves show a small oscillation with the number of layers, but the differences are very small ($\pm 2$ meV/Å$^2$ for GGA-PBE and $\pm 5$ meV/Å$^2$ for LDA). 5 layers is therefore good enough for the clean surface calculation. Addressing finally the finite vacuum thickness, we used 7 layer slabs and halved and doubled the standard vacuum thickness. As apparent from Table B.2, the surface energy of each kind of low-Miller-index surface is hardly changed (within $\pm 1$ meV/Å$^2$) when the vacuum thickness is larger than 10 Å.

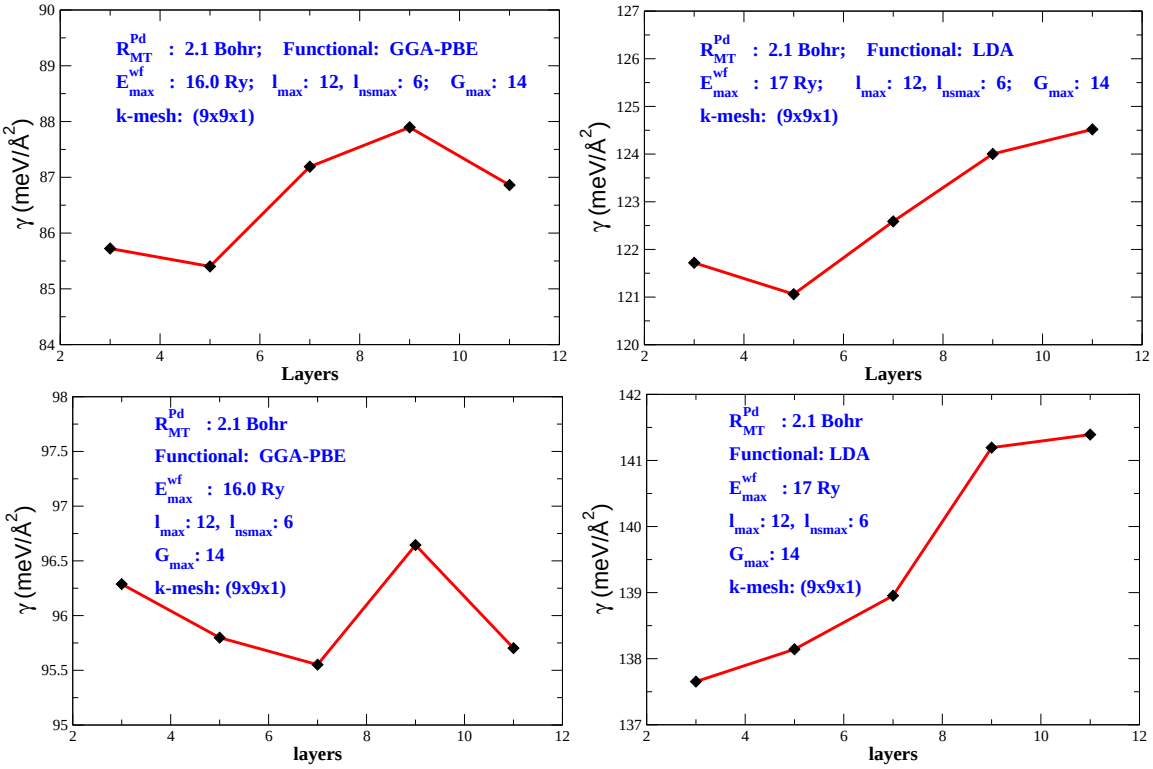


Figure B.5: Convergence test for the optimal layer number for Pd(111) (upper two panels for the GGA-PBE and LDA functional, respectively) and Pd(100) (lower two panels for the GGA-PBE and LDA functional, respectively). Note the scale on the y-axis.

Table B.1: Optimized basis set parameters for the clean Pd(111) and Pd(100) surface.

| | | $E^{\mathrm{wf}}_{\mathrm{max}}$ (Ry) | k-mesh | $K_{\mathrm{irre}}$ | layers |
|---|---|---|---|---|---|
| Pd(111) | GGA | 16.0 | $(9 \times 9 \times 1)$ | 12 | 5 |
| | LDA | 16.0 | $(9 \times 9 \times 1)$ | 12 | 5 |
| Pd(100) | GGA | 16.0 | $(9 \times 9 \times 1)$ | 15 | 5 |
| | LDA | 16.0 | $(9 \times 9 \times 1)$ | 15 | 5 |

The determined basis set and supercell parameters are finally collected in Table B.1. With these parameters the computed values for the surface energy are 87 meV/Å$^2$ and 96 meV/Å$^2$ for Pd(111) and Pd(100) within the GGA-PBE, respectively. They are much smaller than the corresponding values in the LDA calculation, 122 meV/Å$^2$ and 139 meV/Å$^2$ in our work or corresponding LDA results from ref. [114, 123] for Pd(111) and Pd(100), respectively. As expected the surface energy of Pd(100) is larger than the one of Pd(111), as the Pd(100) surface is more open than the Pd(111) surface (seen definition of *open* surfaces in Chapter 4).

Table B.2: Surface energies for various vacuum thicknesses (7 layer Pd(111) and Pd(100) slabs in supercells using the GGA-PBE functional).

| | Pd(111) | | | Pd(100) | | |
|---|---|---|---|---|---|---|
| Vacuum (Å) | 11 | 23 | 46 | 10 | 20 | 41 |
| $\gamma$ (meV/Å$^2$) | 86.8 | 87.2 | 87.3 | 96.5 | 96.4 | 96.7 |

## B.2 Oxygen at Pd(100)

The basis set parameter tests for the calculations with adsorbed oxygen at the Pd(100) surface use the binding energy ($E_\mathrm{b}$) as the central quantity. In these calculations, the clean surface calculation for each configuration has the corresponding same basis set parameters as its adsorption configuration. We choose 3 representative configurations, 1O-Pd(100)(1×1), $p(2\times2)$ and $c(2\times2)$, to carry out energy cutoff tests (left panel of Fig. B.6). From the figure, the absolute binding energies of each configuration show a slow convergence. The relative binding energies of each configuration compared to the 1O-Pd(100)$(1\times1)$ configuration, however, are converged very well to within 10 meV/O atom above 20 Ry. For the determination of lateral interactions, it is primarily those energy differences that matter and we correspondingly use 20 Ry as the optimum energy cutoff for all DFT calculations. At this cutoff, Fig. B.6 shows that the absolute binding energy is converged to within 150 meV/O atom. A similar test for the k-mesh summarized in the right panel of Fig. B.6 reveals a (12×12×1) mesh as the optimum k-mesh. One reason for that is that the binding energies are converged to within 5 meV/O atom, and another one is **k**-points compatibility for various O-Pd(100) cells. In these cells, the k-meshes of configurations are different due to the different Brillouin zone sizes. Our target is to get consistent lateral parameters from the binding energies of configurations. In these cells to cancel the error from different BZ sampling one uses compatible k-meshes and the (12×12×1) mesh can be suitably divided by all our calculated surface unit cells. For example, the compatible k-mesh of O-Pd(100)(3×3) is $(4\times4\times1)$, and so on.

Fig. B.7 shows the layer and vacuum thickness tests for the 1O-Pd(100)(1×1) configuration with full surface relaxation. The binding energies are converged to within 15 meV/O atom for slabs with more than 5 layers. When the vacuum thickness is larger than 10 Å, the binding energies are also fully converged. The thereby determined computational setup for O-Pd(100) is the following: 20 Ry energy cutoff, compatible k-meshes to a $(12\times12\times1)$ grid in (1×1) cells, 5 layer slabs, and 12 Å vacuum thickness.

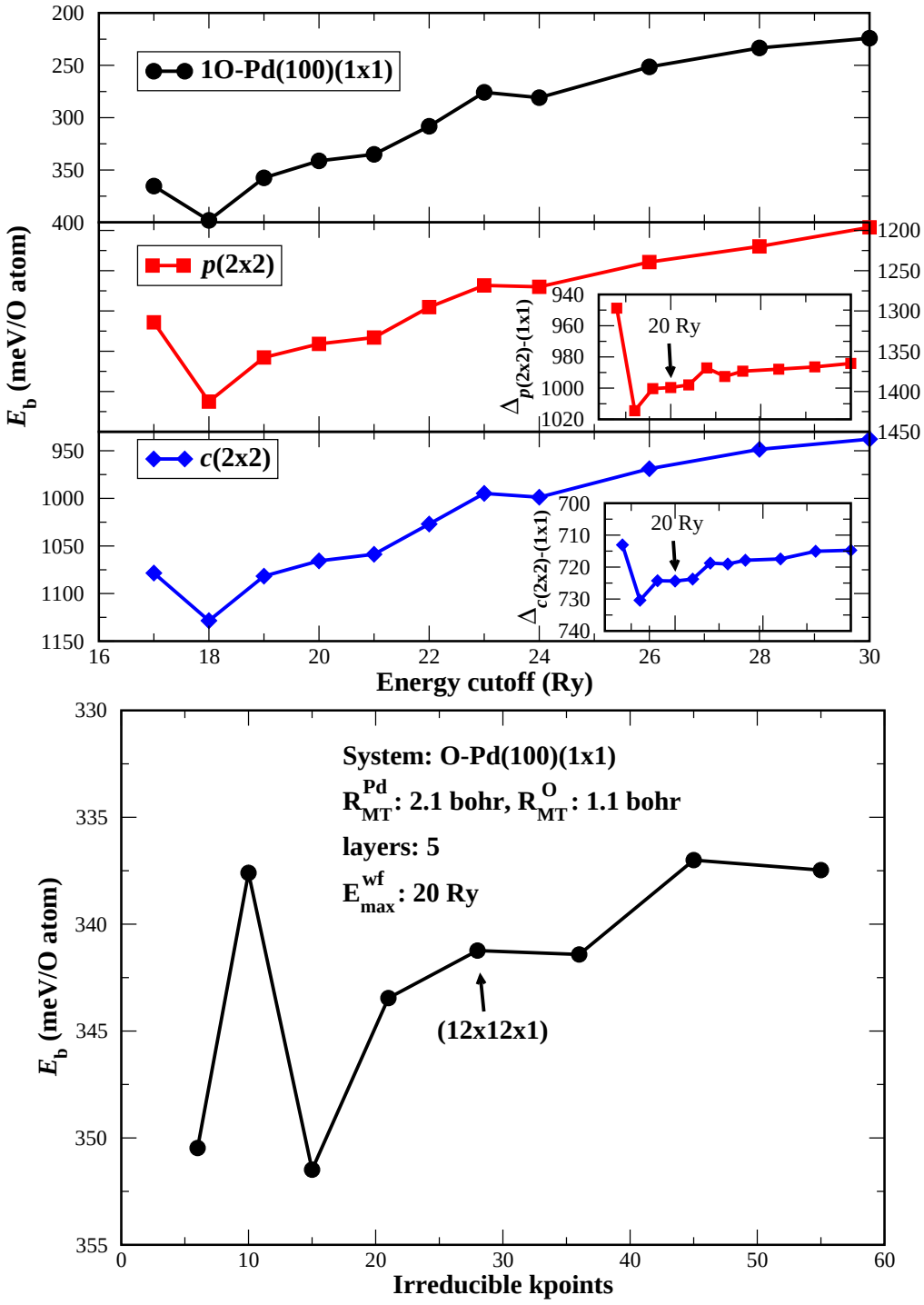


Figure B.6: Top panel: Cutoff convergence test for the 1O-Pd(100)(1×1), $p(2\times2)$,and $c(2\times2)$ oxygen adsorption configurations. Above 20 Ry, the relative binding energies (insert panels) compared to the binding energy of 1O-Pd(100)(1×1) are converged to within 10 meV/O atom. Bottom panel: k-mesh test for 1O-Pd(100)(1×1). (12×12×1) is selected as the optimum k-mesh.

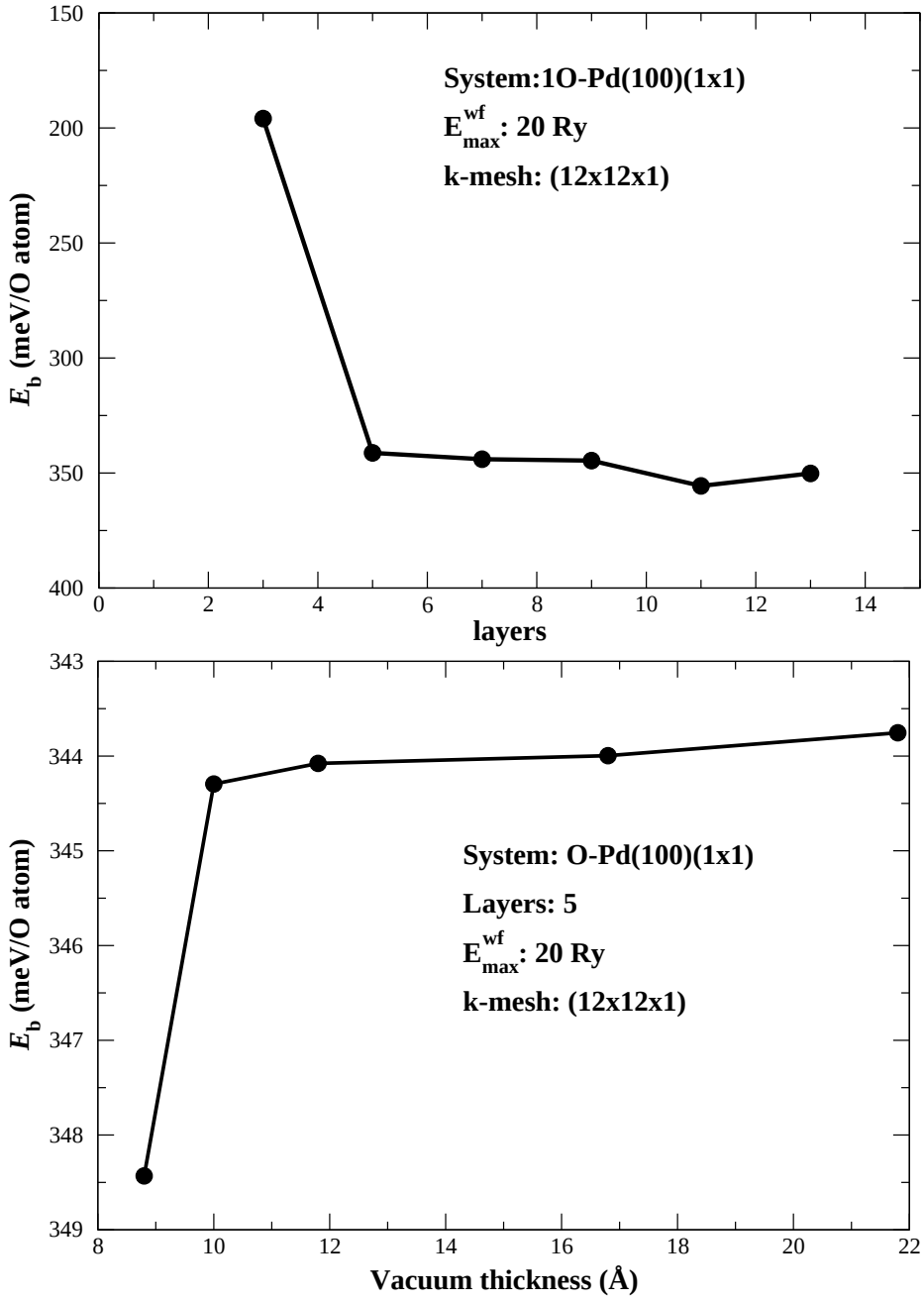


Figure B.7: Top panel: Convergence test for the optimum number of layers for 1O-Pd(100)(1×1) configuration. Bottom panel: Vacuum thickness test.

# Appendix C

# Pd(11$N$) Vicinal Surfaces

## C.1 Clean Pd(11$N$) Vicinal Surfaces

Similar to the low-index surfaces we have to test the important computational parameters to ensure the convergence of the targeted surface properties. For the surface energy $\gamma$ we again focus on energy cutoff and **k**-point sampling. For these tests we use 5, 7 and 9 layer slabs for Pd(113), Pd(115) and Pd(117), respectively, which corresponds each time to the least number of layers possible, while maintaining a bulk-like coordination for the center layer in the slab. The vacuum thickness is about 20 Å, 28 Å, and 23 Å in Pd(113), Pd(115), and Pd(117), respectively. Figures C.1, C.2 and C.3 show the convergence of $\gamma$ [1] with energy cutoff and number of k-points for the Pd(113), Pd(115) and Pd(117) surface, respectively. In all these cases, the surface energy is converged to within $\pm 0.5$meV/Å$^2$ for $E_{\rm max}^{\rm wf} \geq$20 Ry. A similar convergence is reached for k-meshes exceeding k-meshes of $(6 \times 10 \times 1)$ for Pd(113) [2], $(2 \times 9 \times 1)$ for Pd(115), and $(2 \times 7 \times 1)$ for Pd(117), which corresponds to 32, 14 and 8 irreducible **k**-points, respectively.

For the calculation of $\gamma$, one needs not only the total energy of the slab $E_{\rm slab}^{\rm total}$, but also the total energy of a bulk atom $E_{\rm bulk}^{\rm total}$. In Fig C.1, C.2 and C.3 we used for this simply the result of a normal fcc bulk unit cell calculation. That this is not an optimum choice becomes apparent, when testing the slab thickness below. With increasing number of slab layers (while always keeping the vacuum thickness above 11 Å) the surface energy becomes larger and larger (upper panel in Fig. C.4), as discussed in *ref.* [143]. The reason lies in the slightly different sampling of the Brillouin zones in the bulk and in the surface calculation: The respective Brillouin zones are

[1] For simplicity, $E_{\rm bulk}^{\rm total}$ of fcc Pd bulk is used from a calculation with a regular fcc bulk unit cell. As described below it is more appropriate to use $E_{\rm bulk}^{\rm total}$ from a bulk calculation with a supercell geometry equivalent to the slab orientation to obtain compatible k-meshes. However, this does not affect the basis set convergence tests for one fixed slab width we are interested in here.

[2] In Fig. C.1 the k-meshes are tested in two different ways: One is using non-comparable k-meshes for the cubic fcc bulk Pd calculation, the other one is using equivalent k-meshes for the slab bulk calculation. (see discussion below)

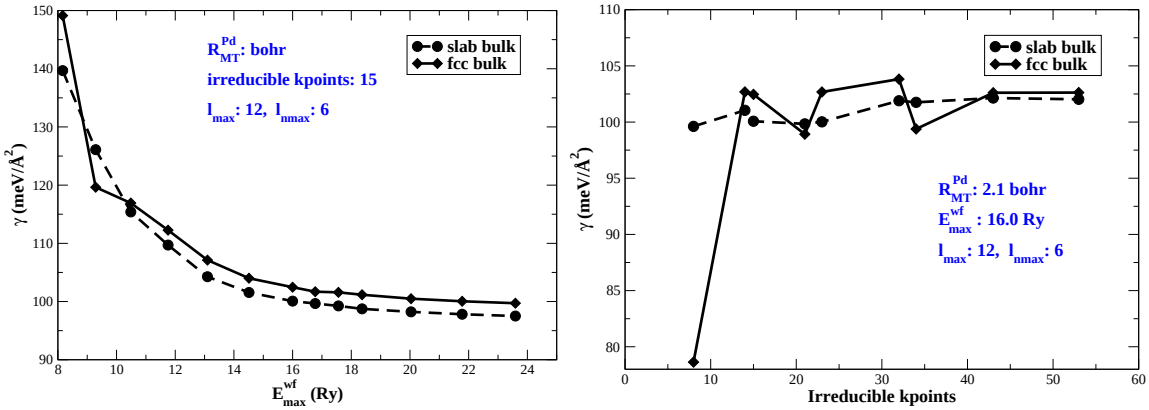


Figure C.1: Energy cutoff ($E^{\rm wf}_{\rm max}$) and irreducible k-point convergence tests for Pd(113). For a convergence within $\pm 0.5$meV/Å$^2$, the optimal energy cutoff is $E^{\rm wf}_{\rm max}$=20 Ry, and the optimal irreducible k-point number is (k-mesh: $6\times10\times1$), corresponding to 32 irreducible **k**-points. Red curve and black curve are the surface energies from fcc bulk and slab bulk calculation, respectively. (see footnote 2)

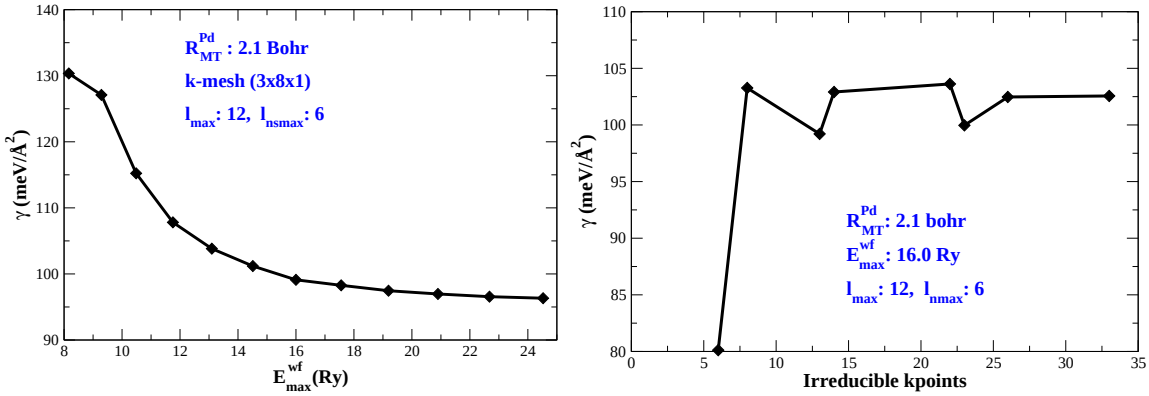


Figure C.2: Energy cutoff ($E^{\rm wf}_{\rm max}$) and irreducible k-point convergence tests for Pd(115). For a convergence within $\pm 0.5$meV/Å$^2$, the optimal energy cutoff is $E^{\rm wf}_{\rm max}$=20 Ry, and the optimal irreducible k-point number is 14 (k-mesh: $3\times9\times1$), corresponding to 14 irreducible **k**-points.

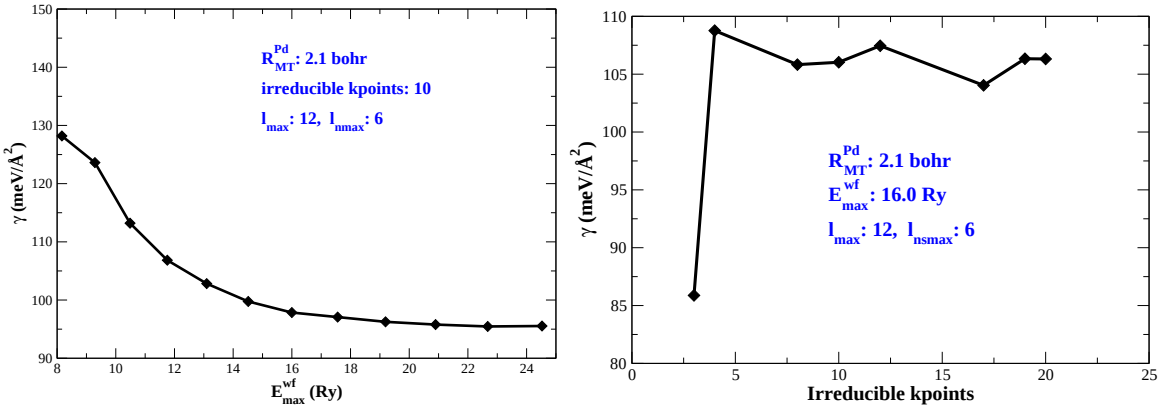


Figure C.3: Energy cutoff ($E^{\rm wf}_{\rm max}$) and irreducible k-point tests for Pd(117). For a convergence within $\pm 0.5$meV/Å$^2$, the optimal energy cutoff is $E^{\rm wf}_{\rm max}$=20 Ry, and the optimal irreducible k-point number is 8 (k-mesh: $2\times7\times1$), corresponding to 8 irreducible **k**-points.

oriented differently and the Monkhorst-pack grids sample different points. Therefore the contribution of bulk-like atoms in the middle of the slab does not cancel, as they are described slightly differently by the two k-meshes. Consequently the surface energy diverges. This problem can be resolved by using for $E_{\text{bulk}}^{\text{total}}$ the total energy of an atom in a *slab bulk*, *i.e.* building a bulk Pd structure by completely filling a vicinal supercell layer by layer. The smallest number of layers required in the supercell is determined by the Miller indices of the vicinal surface, $1^2 + 1^2 + n_{\text{row}}^2$. Then the k-meshes of the two structures, slab bulk and surface slab, are equivalent, *e.g.* $(6 \times 10 \times 2)$ and $(6 \times 10 \times 1)$ in Pd(113), which minimizes errors from the k-point sampling. The surface energy obtained with this procedure is converged to within 1 meV/Å$^2$ already for the 5 layer slab (lower panel in Fig. C.4). In the same way, we can get similarly converged surface energies for Pd(115) (upper panel in Fig. C.5) and Pd(117) (lower panel in Fig. C.5). Equivalent k-meshes for the two structures, slab and bulk, in the surface energy equation Eq. 4.8 are therefore very important to generate converged curves. Analyzing the relaxed slabs in more detail, we find no further geometry relaxation after 9 layers, 17 layers and 19 layers for Pd(113), Pd(115) and Pd(117), respectively. Similarly, the k-meshes for the three vicinal surfaces must also be as commensurate as possible, in order to allow a meaningful comparison of the surface energetics of the three surfaces. If we take the k-mesh of Pd(113), $(6 \times 10 \times 1)$, as the standard, the task is to find the corresponding k-meshes on Pd(115) and Pd(117) using the relation of the surface unit cells. As apparent from Fig. 4.3 the angle $\gamma$ is similar in the three surface unit cells, and the $b$ distance of the three Pd(11$N$) surfaces is equal. The **k**-point sampling in this direction should therefore be equal, namely 10. Along the other direction, $a$, the proportion of their distances is about 9:14:19, therefore the **k**-point along this direction is 4 and 3 for Pd(115) and Pd(117), respectively. The equivalent k-meshes of Pd(113), Pd(115) and Pd(117) surfaces are therefore $(6 \times 10 \times 1)$, $(4 \times 10 \times 1)$ and $(3 \times 10 \times 1)$, respectively. Similar to the vacuum thickness test carried out for Pd(111) and Pd(100), we increased and decreased the vacuum thickness in the vicinal supercells. The resulting surface energies are summarized in Table C.1, from which it becomes clear that the effect of vacuum thickness beyond 10 Å is virtually zero ($< 1$ meV/Å$^2$). Therefore the vacuum thickness used already before in the basis set tests for the clean vicinal Pd(11$N$) surfaces is large enough to avoid the interaction between two consecutive slabs

All basis sets used in the Pd(11$N$) vicinal surface calculations and the corresponding surface energies are summarized in Table C.2. The final surface energies for the three vicinal surfaces are 100.3 meV/Å$^2$, 99.4 meV/Å$^2$, and 99.1 meV/Å$^2$, respectively. They are smaller than the surface energies of the corresponding bulk-truncated vicinal surfaces (Table C.2). Obviously the surface relaxation stabilizes the surfaces. Pd(113) has the highest surface energy among all the surfaces, which is significantly larger than the one of the close-packed Pd(111) surface. However, for increasing (100) terraces width, the surface energy of Pd(11$N$) becomes smaller, and we observe the trend, $\gamma_{113} > \gamma_{115} \approx \gamma_{117}$.

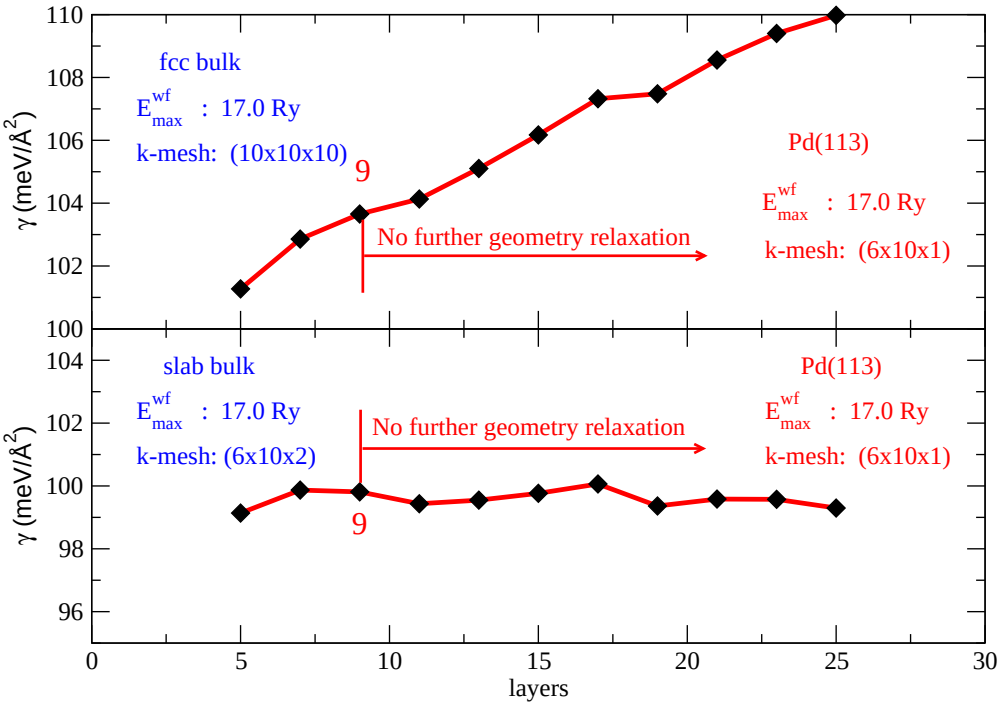


Figure C.4: Surface energy convergence with number of slab layers for the Pd(113) vicinal surface. Upper panel: Surface energy using $E_{\text{bulk}}$ from a bulk fcc Pd unit cell calculation. Lower panel: Surface energy using $E_{\text{bulk}}$ from a slab bulk calculation.

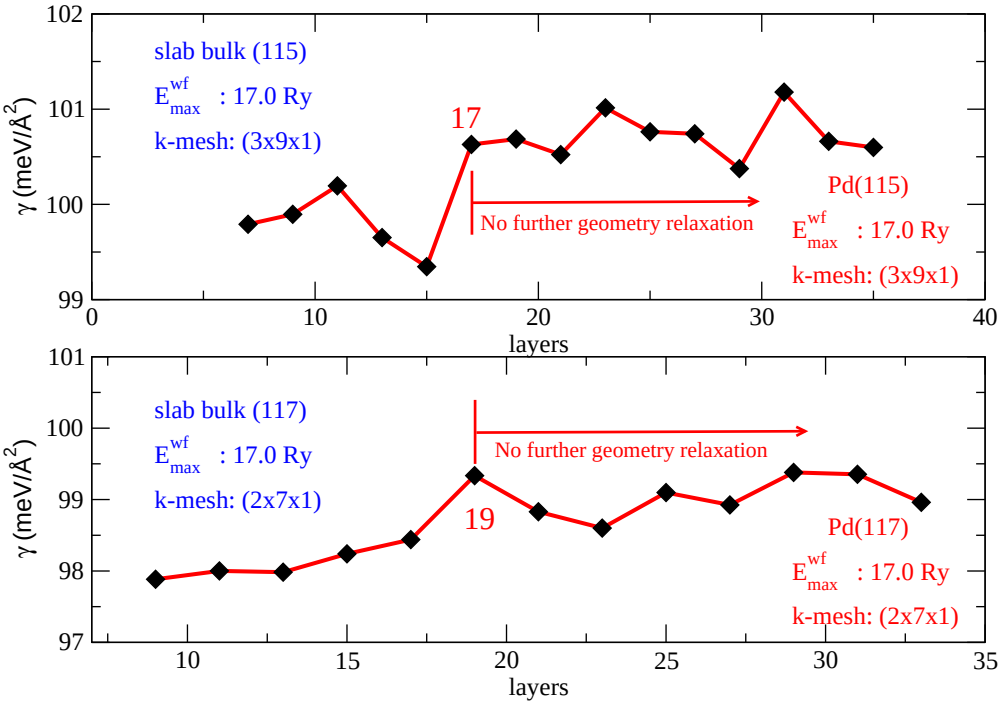


Figure C.5: Surface energy vs. slab layers for Pd(115) (upper panel) and Pd(117) (lower panel), and using $E_{\text{bulk}}^{\text{total}}$ from a slab bulk calculation.

Table C.1: Surface energies of the Pd(11$N$) ($N$=3, 5, 7) vicinal surfaces for different vacuum thicknesses, and using $E_{\max}^{\mathrm{wf}}$=17 Ry and a $(6 \times 10 \times 1)$, $(3 \times 9 \times 1)$ and $(2 \times 7 \times 1)$ for Pd(113), Pd(115) and Pd(117), respectively.

| | Pd(113) | | | Pd(115) | | | Pd(117) | | |
|---|---|---|---|---|---|---|---|---|---|
| Vacuum (Å) | 15 | 30 | 46 | 11 | 22 | 32 | 12 | 24 | 35 |
| $\gamma$ (meV/Å$^2$) | 99.6 | 99.8 | 99.7 | 100.4 | 100.6 | 100.6 | 99.2 | 99.3 | 99.3 |

Table C.2: Computed surface energies of different low-index and vicinal surfaces using optimum basis sets. (The k-meshes of Pd(11$N$) are equivalent).

| | Pd(111) | Pd(113) | Pd(115) | Pd(117) | Pd(100) |
|---|---|---|---|---|---|
| $E_{\max}^{\mathrm{wf}}$ (Ry) | 20 | 20 | 20 | 20 | 20 |
| k-meshes | $(9 \times 9 \times 1)$ | $(6 \times 10 \times 1)$ | $(4 \times 10 \times 1)$ | $(3 \times 10 \times 1)$ | $(9 \times 9 \times 1)$ |
| layers | 7 | 9 | 17 | 19 | 7 |
| vacuum (Å) | 23 | 30 | 22 | 24 | 20 |
| $\gamma_{\mathrm{unrelax}}$ (meV/Å$^2$) | 87.9 | 100.3 | 99.4 | 99.1 | 96.4 |
| $\gamma_{\mathrm{relax}}$ (meV/Å$^2$) | 87.9 | 98.3 | 97.3 | 97.4 | 96.3 |

## C.2 Oxygen at Pd(11$N$) Vicinal Surfaces

With respect to oxygen adsorption at the vicinal surfaces, we focus our convergence tests on two representative adsorption sites, namely the Thu and Sh2 sites. We test the convergence with the energy cutoff by computing the binding energy in a $(1 \times 1)$ cell.

The k-meshes are the same as the optimal values for the clean vicinal surfaces, $(6 \times 10 \times 1)$, $(3 \times 9 \times 1)$ and $(2 \times 7 \times 1)$ for oxygen adsorption on Pd(113), Pd(115) and Pd(117), respectively. The slab thicknesses are 13, 17 and 23 layers, and the corresponding vacuum thicknesses are 25 Å, 20 Å and 20 Å for Pd(113), Pd(115) and Pd(117), respectively. From Fig. C.6, it becomes clear that the absolute binding energies of the oxygen atoms at each site show the same convergence trend. Unfortunately, both of them converge quite slowly, and the $E_{\max}^{\mathrm{wf}}$ curves show a convergence to within 50 meV only above 26 Ry. In contrast, the relative binding energy difference between the two sites (insert panel in Fig. C.6) is already converged to within 5 meV above 20 Ry. In our work we focus on the most favorable site for the oxygen atoms on the Pd(11$N$) surfaces. This trend only requires converged relative binding energies and we choose 20 Ry as the optimal energy cutoff for the oxygen adsorption at Pd(113), which yields accurate relative binding energy differences at an affordable computational time. In the same spirit, we calculate the binding energy of oxygen

at the Sh2 site on Pd(115) and Pd(117) (Fig. C.7), and compare the results with the binding energies at the same site on Pd(113) (insert panel in Fig. C.7). From the figure we see that the absolute binding energy of oxygen on Pd(115) and Pd(117) shows a similar trend as oxygen on Pd(113): slow convergence of the absolute values, while the relative differences reach a convergence to within 5 meV at $E_{\max}^{\mathrm{wf}}$=20.0 Ry. We conclude that for our study 20 Ry is an optimal energy cutoff for the oxygen adsorption on all three Pd(11$N$) surfaces.

Next, the required number of slab layers are tested using the other optimal parameters (energy cutoff and k-mesh) of the clean vicinal surfaces. The thickness of the chosen supercell is 40.47 Å, 33.43 Å and 33.16 Å for the oxygen adsorption on Pd(113), Pd(115) and Pd(117), respectively. This size is kept fixed despite the increasing number of slab layers. Although the vacuum thickness becomes thus smaller and smaller, the least vacuum thickness is 12 Å, 11 Å and 16 Å for oxygen on Pd(113), Pd(115) and Pd(117), respectively, which is still large enough (see vacuum test below). For the oxygen adsorption on Pd(113) surface we also increased the k-mesh from ($6 \times 10 \times 1$) to ($8 \times 14 \times 1$) to check if the old k-mesh is good enough for the adsorption system. In Fig. C.8 the binding energy curves at the two adsorption sites (Sh2 and Thu) are nicely converged with increasing number of slab layers. The two curves show the same convergence trend, and the binding energy is converged to within 10 meV already for 13 layers for the two adsorption sites. Moreover, the high k-mesh ($8 \times 14 \times 1$) generates the same trend as the lower k-mesh ($6 \times 10 \times 1$) does, and the binding energies from the two k-meshes are nearly the same, when the number of layers is more than the optimal layers. We therefore identify the ($6 \times 10 \times 1$) mesh as good enough to study the oxygen adsorption at Pd(113). In the same way, we increase the ($3 \times 9 \times 1$) and ($2 \times 7 \times 1$) meshes to ($4 \times 12 \times 1$) and ($3 \times 10 \times 1$) to check the **k**-points sampling for oxygen at Pd(115) and Pd(117), respectively (Fig. C.9). The binding energies of the two kinds of k-meshes are similar, and the difference is less than 20 meV throughout. Therefore, ($3 \times 9 \times 1$) and ($2 \times 7 \times 1$) k-meshes are enough to study the oxygen adsorption at Pd(115) and Pd(117), respectively. Fig. C.9 (oxygen adsorption on Pd(115) and Pd(117)) shows furthermore the same trend as oxygen adsorption on Pd(113): The two binding energy curves at the two adsorption sites rapidly converge with increasing number of slab layers, and the binding energy is converged to within 10 meV for the same optimal layer number. Therewith, 17 layers and 23 layers are the optimal number of slab layers for the oxygen adsorption on Pd(115) and Pd(117), respectively. Finally, we test the vacuum thicknesses of the three kinds of oxygen adsorption systems by increasing and decreasing the vacuum thickness. All corresponding binding energies are tabulated in Table C.3, from which it is clear that the effect of vacuum thickness is negligible (<10 meV) beyond 12 Å, 10 Å and 10 Å for the oxygen adsorption at the Sh2 site on Pd(113), Pd(115) and Pd(117), respectively. As mentioned in the tests of clean Pd(11$N$) vicinal surfaces, in order to compare quantities, like binding energies, in the family of Pd(11$N$) vicinal surfaces the k-meshes of the three adsorption systems should be comparable. Therefore, ($6 \times 10 \times 1$), ($4 \times 10 \times 1$) and ($3 \times 10 \times 1$) are used for the oxygen adsorption on Pd(113), Pd(115) and Pd(117),

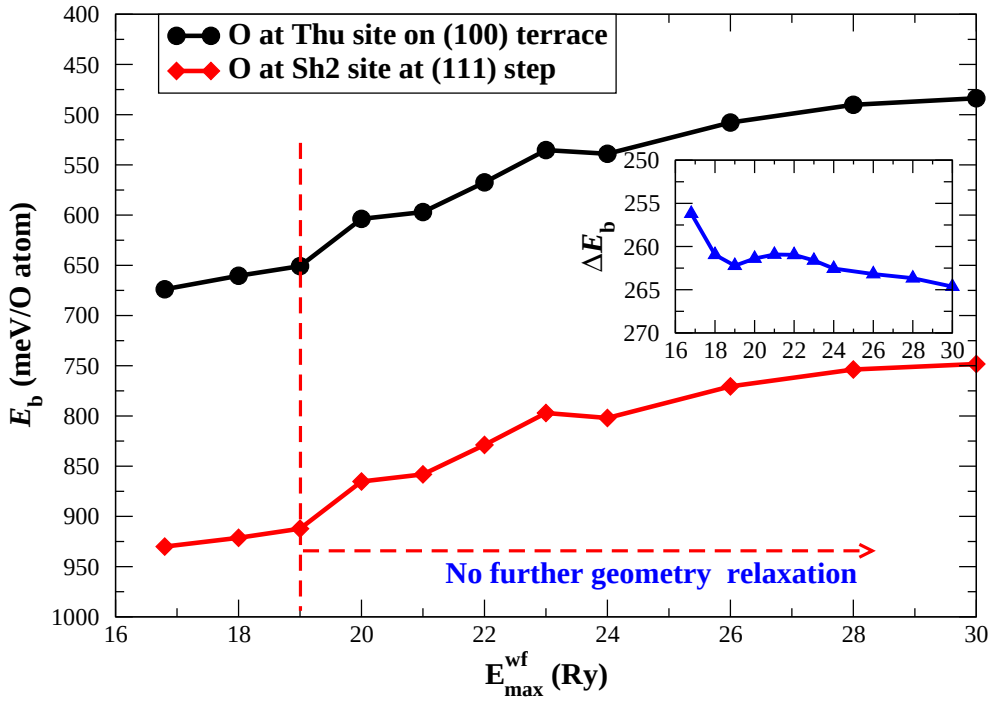


Figure C.6: Absolute binding energies of oxygen adsorbed at the Sh2 and Thu sites at Pd(113) with different energy cutoff values. The insert panel shows the relative binding energy of the two sites.

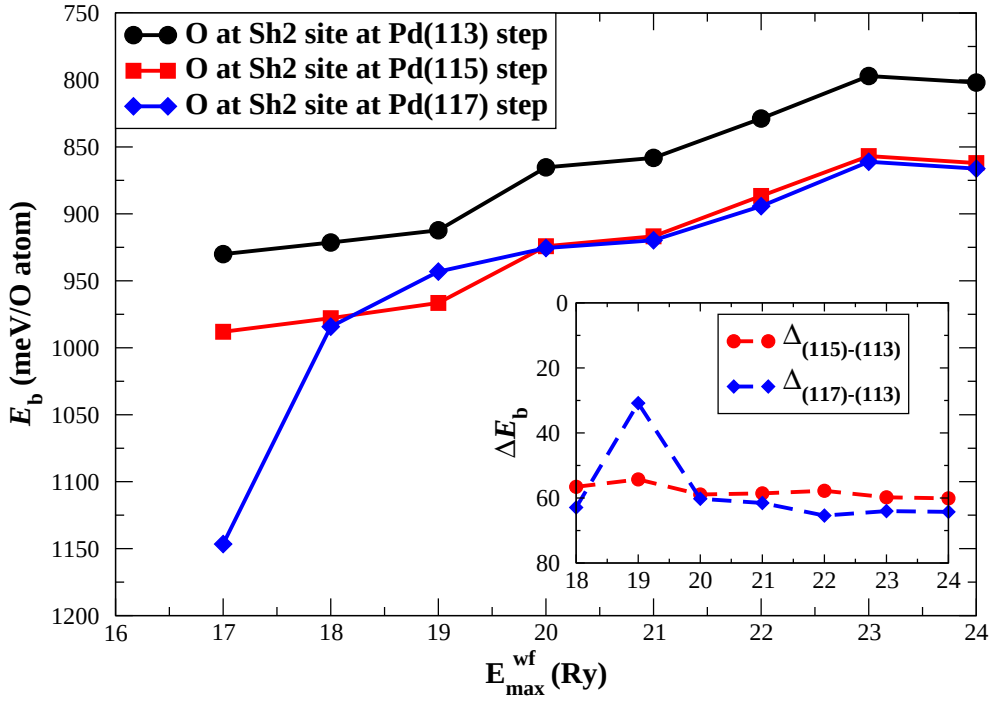


Figure C.7: Binding energy vs. energy cutoff for oxygen adsorbed at the Sh2 site at Pd(113), Pd(115) and Pd(117). The insert shows the relative binding energy with respect to oxygen at the Sh2 site at Pd(113).

Table C.3: Binding energies for various vacuum thicknesses in supercells for the oxygen adsorption at the Sh2 site.

| | 1O-Pd(113)(1×1) | | | 1O-Pd(115)(1×1) | | | 1O-Pd(117)(1×1) | | |
|---|---|---|---|---|---|---|---|---|---|
| Vacuum (Å) | 37 | 25 | 12 | 30 | 20 | 10 | 30 | 20 | 10 |
| $E_b$ (meV) | 875 | 875 | 874 | 923 | 924 | 929 | 927 | 926 | 933 |

Table C.4: Optimal basis set parameters of oxygen adsorption on Pd(11$N$) surfaces.

| | energy cutoff (Ry) | k-mesh | vacuum thickness (Å) | slab layers |
|---|---|---|---|---|
| 1O-Pd(113)(1×1) | 20 | $6 \times 10 \times 1$ | 25 | 13 |
| 1O-Pd(115)(1×1) | 20 | $4 \times 10 \times 1$ | 20 | 17 |
| 1O-Pd(117)(1×1) | 20 | $3 \times 10 \times 1$ | 20 | 23 |

respectively. At last, we summarize the optimal basis set parameters in Table C.4.

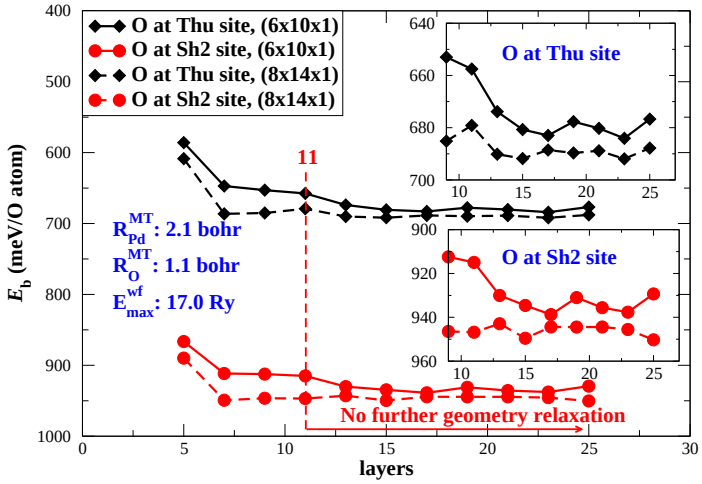


Figure C.8: Convergence of the binding energy with increasing number of slab layers for oxygen adsorption at the two adsorption sites (Sh2 and Thu) on Pd(113) surface. Solid and dashed lines indicate two kinds of k-meshes, $(6 \times 10 \times 1)$ and $(8 \times 14 \times 1)$, respectively.

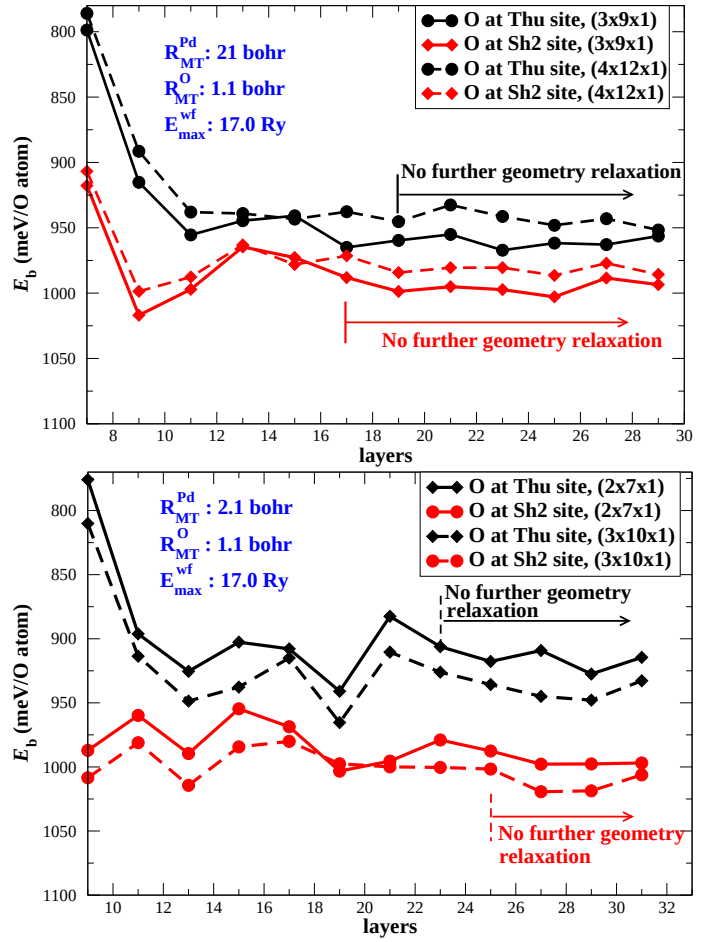


Figure C.9: Convergence of the binding energy with the number of slab layers for oxygen adsorption at Sh2 and Thu sites on Pd(115) (upper panel) and on Pd(117) (lower panel).

# Appendix D

# Monte Carlo Simulations

## D.1 Equilibration

The average quantities obtained from our MC simulations should reflect the equilibrated state of the system and should thus not depend on the initial configuration with which the simulation was started. This was routinely checked by starting the simulations from different initial configurations, as well as by using different initial random number seeds. Fig. D.1 illustrates this by showing the evaluation of the total energy during a MC simulation for a 0.5 ML oxygen coverage in a (20×20) Pd(100) simulation cell. The final energy obtained after about $10^7$ MC steps does not depend on the varied initial configurations, nor on the random number seed.

While we can thus assume that the equilibrated state is reached, the initial transient equilibration period should also not enter into the averaging procedure for the thermodynamic properties. As illustrated by Fig. D.2, the initial equilibration period varies with the system temperature (and of course with O coverage). We systematically verified however that it never exceeds $\sim 5\times10^7$ MC steps (at the accuracy level of interest to our study). We therefore always employed a corresponding number of equilibration MC steps, before starting the averaging procedure for the thermodynamic properties.

## D.2 Simulation Cell for O-Pd(100)

The finite size of the simulation cell is another crucial technical factor for MC simulations, known to induce so-called *finite-size effects* [73]. Fortunately, such effects play only a minor role at the accuracy level of interest to our study, which aims more at a semi-quantitative determination of the critical temperature, rather than at a detailed investigation of the nature of the phase transition (critical exponents *etc.*) itself. Already rather small simulation cells are sufficient to determine the critical temperature for the order-disorder transition to within ±25 K. This is illustrated in Fig. D.3 by the variation of the employed order parameter and specific heat for two different O cover-

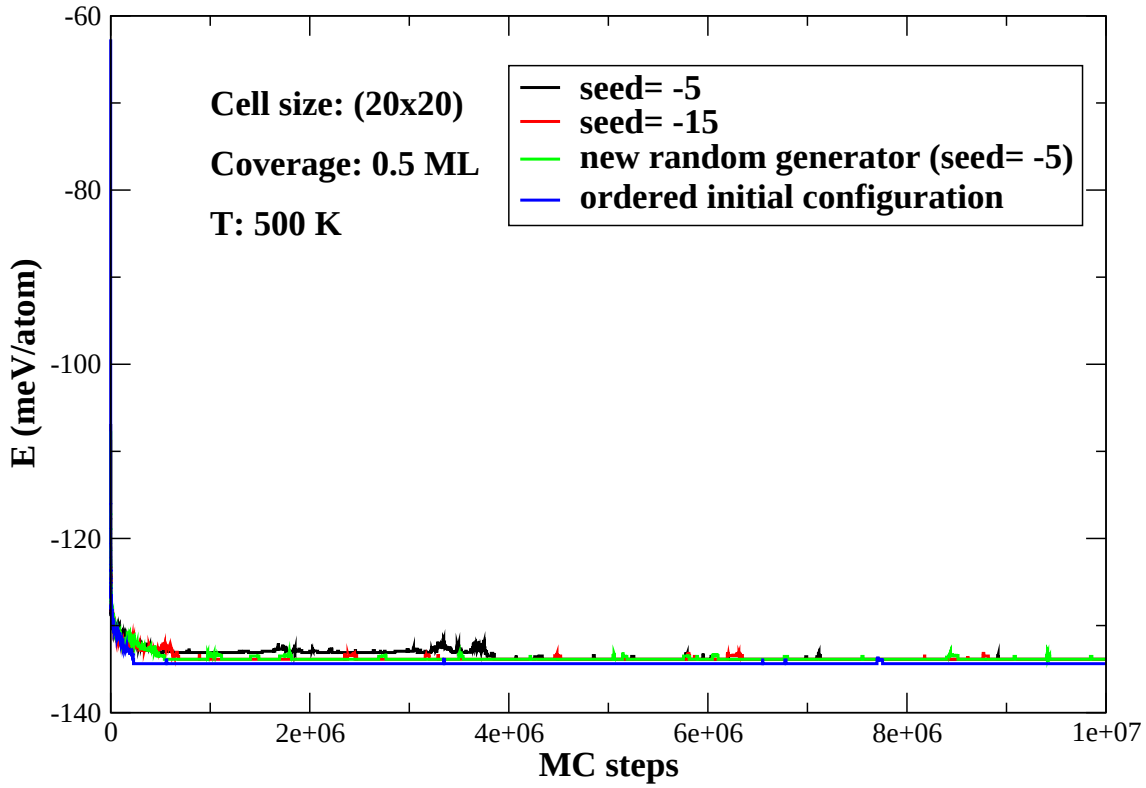


Figure D.1: Illustration of the evaluation of the total energy with Monte Carlo (MC) steps for a 0.5 ML oxygen coverage in the (20×20) simulation cell. The finally obtained value does not depend on the initial random number seed (and starting from a random initial starting configuration) or when starting from an ordered configuration.

ages at Pd(100). With increasing simulation cell size the former approaches the ideal step-function shape and the latter the $\delta$-peak shape. Using the inflection and peak temperature from both, respectively, it is clear that converged critical temperatures to within ±25 K can be obtained from simulation cells exceeding (40×40).

## D.3 Identical $T_c$ from $\Psi$ and $C_V$

Using the optimum (40 × 40) simulation cell, we identify the critical temperatures of the order-disorder transitions at 0.25 ML and 0.5 ML on Pd(100) surface by the order parameters ($\Psi_{p(2\times2)}$ in Eq. 5.23 and $\Psi_{c(2\times2)}$ in Eq. 5.27) and the specific heat. Fig. D.4 clearly shows that at low temperatures the order parameters are 1.0, which means configurations show the $p(2 \times 2)$ and $c(2 \times 2)$ order for coverages at 1/4 ML and 1/2 ML, and the specific heats are both small. When the temperatures are near the critical temperatures ($T_C$), the order parameters drop sharply, and a peak in the specific heat occurs. Increasing the temperature further, both order parameters and

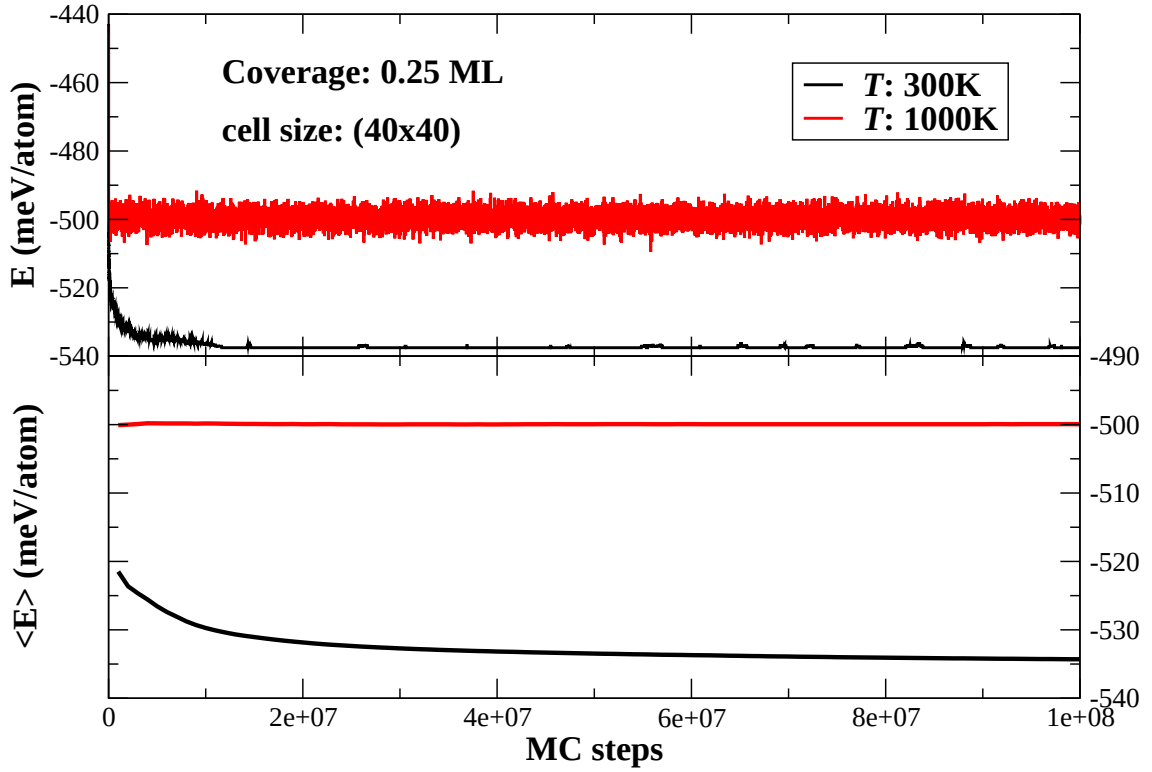


Figure D.2: E vs. MC step (top panel), and $< E >$ vs. MC step (bottom panel) for two different temperatures, 300K and 1000K.

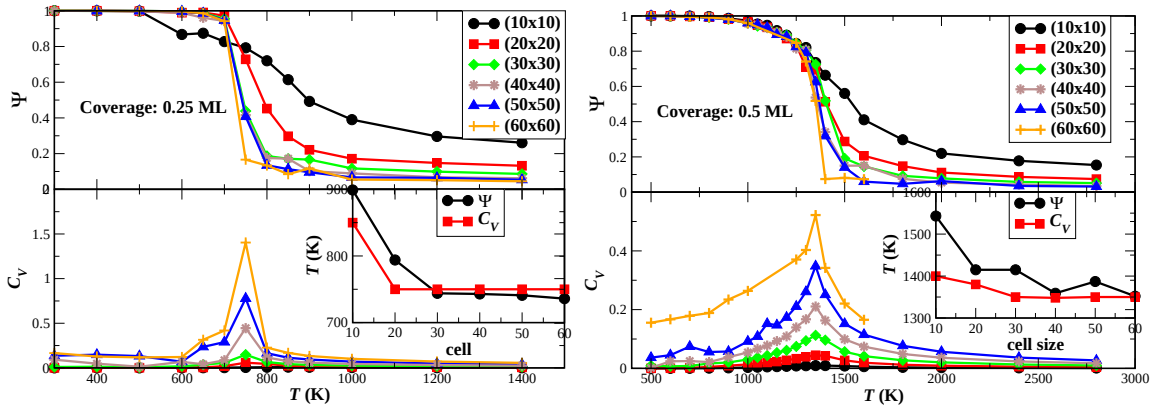


Figure D.3: Finite-size effect for two O coverages at Pd(100), $\theta$=0.25 ML (left panel) and $\theta$=0.5 ML (right panel). The critical temperatures are deduced from the order parameter (top panels) and specify heat (bottom panels). The insert panels are the $T_C$ vs. cell size.

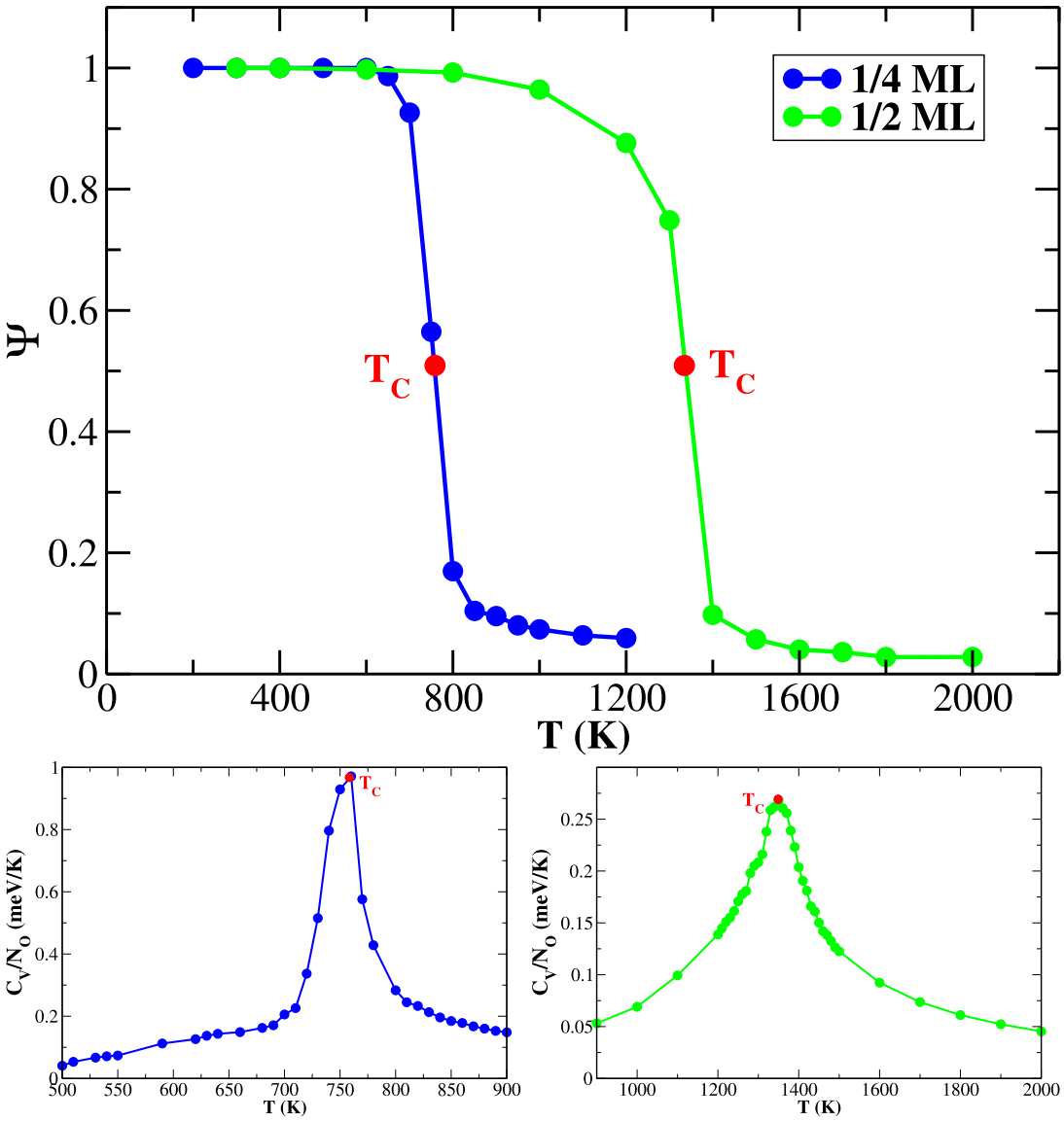


Figure D.4: Critical temperatures determined by order parameters (top panel) and specific heat (bottom panels) in a $(40 \times 40)$ simulation cell. The critical temperatures at 0.25 ML and 0.5 ML determined by the inflection points of the $p(2 \times 2)$ and $c(2 \times 2)$ order parameters, respectively, are identical to the critical temperatures determined from the peak of the specific heats to within 10 K.

specific heats are decreasing to a small value. Taking the inflection points in the order parameter curves and the peaks in the specific heat curves as the critical temperatures, we can say both of methods predict identical critical temperatures to within 10 K.

## D.4 Simulation Cell for Stepped Pd(100)

The MC simulations addressing the influence of the (111) step on the ordering behavior should simulate the limit of an isolated step. Since they still have to be simulated with periodic boundary conditions, a further series of tests needed to establish the minimum terrace width that is required to eliminate any step-step interactions. For this, we employed simulation cells of increasing terrace width ($W\times40$) with $W > 40$, *i.e.* simulation cells that exhibit one (111) step along the $y$-axis, separated by terraces of width $W$ Pd(100) unit-cells. Monitored was the specific heat for each row parallel to the (111) step separately, to identify at which distance from the step the deduced critical temperature becomes indistinguishable from that at the ideal extended Pd(100) surface.

Fig. D.5 shows this test for GCMC simulations corresponding to nominal O coverages of 0.1 and 0.15 ML at low temperatures. For two employed terrace widths we observe a rapid convergence of the critical temperature towards the value of the ideal Pd(100) surface over only 6 terrace row.

At the extended (80×40) simulation cell this behavior is exactly the same as at the (60×40) cell, just with 20 additional Pd(100) terrace rows in between. We correspondingly conclude that a (60×40) cell corresponding to terraces of 60 unit-cell width is fully sufficient to simulate the ordering behavior at "isolated" (111) steps.

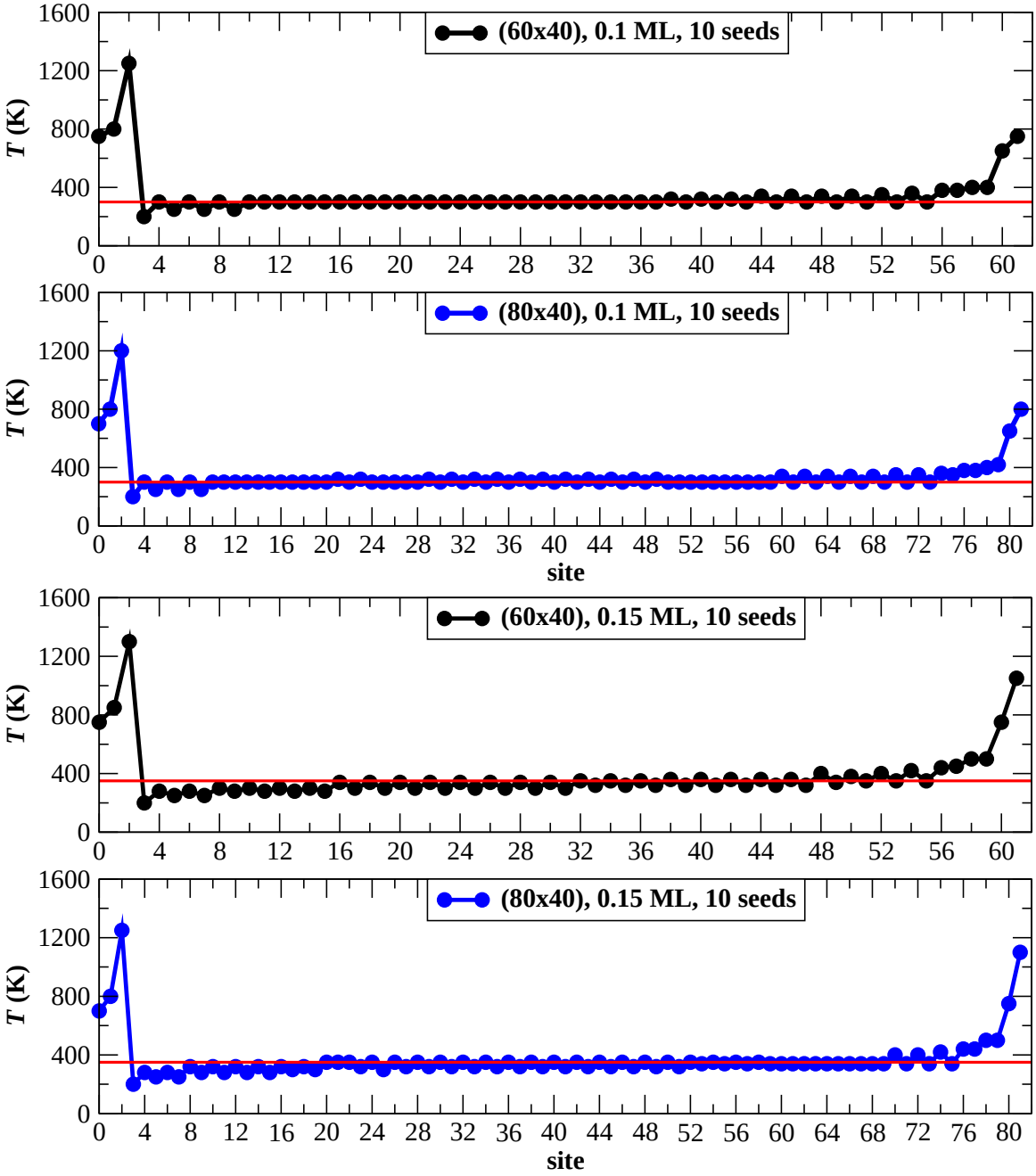


Figure D.5: Cell size tests for two coverages, $\theta$=0.1 ML (top two panels) and $\theta$=0.15 ML (bottom two panels) using two kinds of cells, $(60 \times 40)$ and $(80 \times 40)$. The additional red lines are the critical temperature for the ideal O-Pd(100) surface at the same coverages, respectively. The (111) step site Sh2 is at position 0.

# Appendix E

# Computed Ordered Configurations for O-Pd(100)

Listed are all ordered configurations of O at Pd(100) that were computed by (L)APW+ lo DFT. Shown is a schematic top view indicating the surface unit-cell. The computed DFT average binding energy is given in meV, and the LGH expansion using all cluster figures in the considered pool is stated. Configurations (hol-hol)-1 to (hol-hol)-27 correspond to configurations with O in hollow sites; configurations (br-br)-1 to (br-br)-18 to configurations with O in bridge sites; and configurations (hol-br)-1 to (hol-br)-6 to configurations with O in hollow and bridge sites. Light grey spheres represent Pd atoms, and dark (red) spheres represent O atoms.

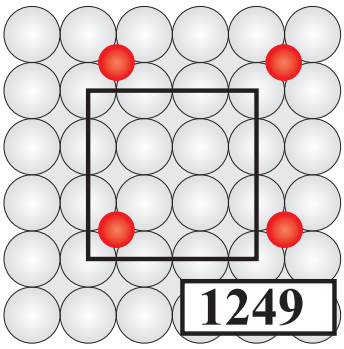


**(hol-hol)-1**

$$E_b^{\text{(hol-hol)-1}} = E^{\text{on-site}}$$

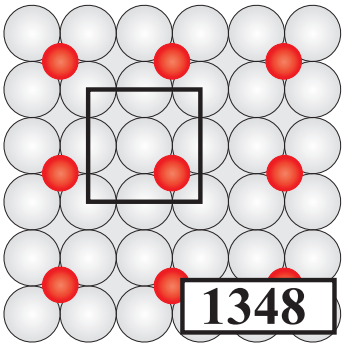


**(hol-hol)-2**

$$E_b^{\text{(hol-hol)-2}} = E^{\text{on-site}} + 2V_{3p} + 2V_{5p}$$

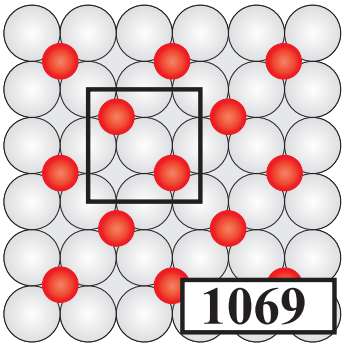


**(hol-hol)-3**

$$E_b^{\text{(hol-hol)-3}} = E^{\text{on-site}} + 2V_{2p} + 2V_{3p} + 2V_{5p} + 4V_{4t} + 2V_{6t} + 8V_{7t} + V_{3q}$$

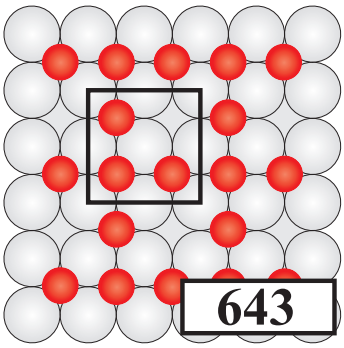


**(hol-hol)-4**

$$E_b^{\text{(hol-hol)-4}} = E^{\text{on-site}} + 4/3V_{1p} + 4/3V_{2p} + 2V_{3p} + 8/3V_{4p} + 2V_{5p} + 4/3V_{1t} + 4/3V_{2t} + 8/3V_{3t} + 8/3V_{4t} + 16/3V_{5t} + 4/3V_{6t} + 16/3V_{7t} + 8/3V_{8t} + 4/3V_{2q} + 2/3V_{3q} + 1/3V_{1qu}$$

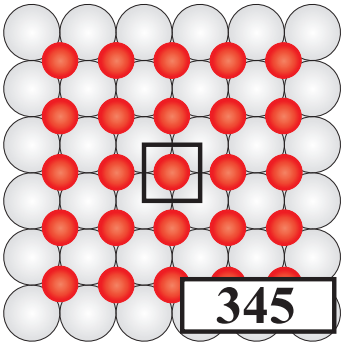


### (hol-hol)-5

$$E_b^{\text{(hol-hol)-5}} = E^{\text{on-site}} + 2V_{1p} + 2V_{2p} + 2V_{3p} + 4V_{4p} + 2V_{5p} + 2V_{1t} + 4V_{2t} + 8V_{3t} + 4V_{4t} + 8V_{5t} + 2V_{6t} + 8V_{7t} + 4V_{8t} + V_{1q} + 4V_{2q} + V_{3q} + V_{1qu}$$

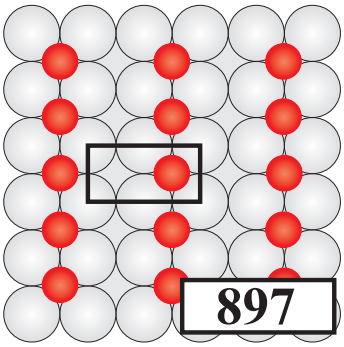


### (hol-hol)-6

$$E_b^{\text{(hol-hol)-6}} = E^{\text{on-site}} + V_{1p} + 2V_{3p} + 2V_{4p} + 2V_{5p} + V_{1t} + 4V_{5t} + 2V_{8t}$$

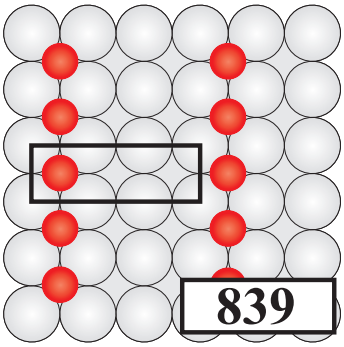


### (hol-hol)-7

$$E_b^{\text{(hol-hol)-7}} = E^{\text{on-site}} + V_{1p} + V_{3p} + V_{1t} + 2V_{8t}$$

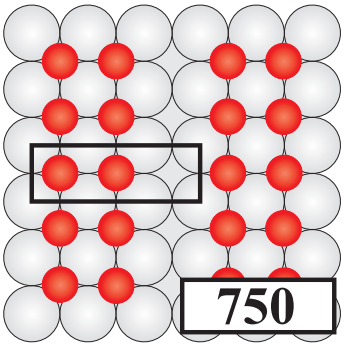


### (hol-hol)-8

$$E_b^{\text{(hol-hol)-8}} = E^{\text{on-site}} + 3/2V_{1p} + V_{2p} + 3/2V_{3p} + 2V_{4p} + V_{5p} + V_{1t} + 3V_{2t} + 2V_{3t} + V_{4t} + 4V_{5t} + 4V_{7t} + 3V_{8t} + 1/2V_{1q} + V_{2q}$$

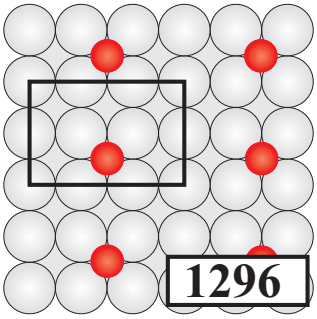


**(hol-hol)-9**

$$E_b^{\text{(hol-hol)-9}} = E^{\text{on-site}} + V_{3p}$$

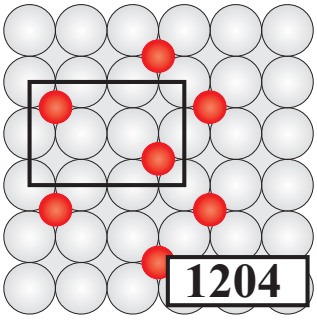


**(hol-hol)-10**

$$E_b^{\text{(hol-hol)-10}} = E^{\text{on-site}} + V_{2p} + V_{3p} + V_{4p} + V_{4t} + 2V_{7t}$$

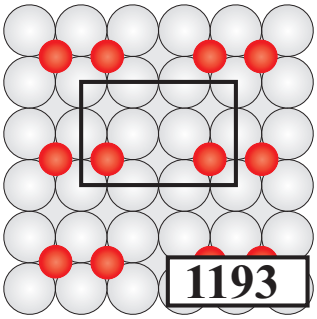


**(hol-hol)-11**

$$E_b^{\text{(hol-hol)-11}} = E^{\text{on-site}} + 1/2V_{1p} + 3/2V_{3p} + V_{4p} + V_{5p} + 2V_{5t} + V_{8t}$$

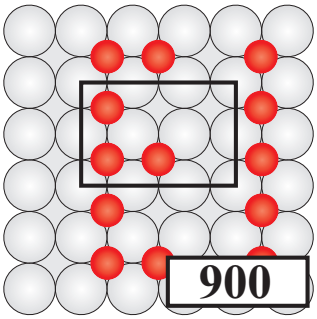


**(hol-hol)-12**

$$E_b^{\text{(hol-hol)-12}} = E^{\text{on-site}} + V_{1p} + 2/3V_{2p} + 4/3V_{3p} + 4/3V_{4p} + 2/3V_{5p} + 2/3V_{1t} + 2/3V_{2t} + 2/3V_{3t} + 2/3V_{4t} + 2V_{5t} + 2V_{7t} + 2V_{8t} + 1/3V_{2q}$$

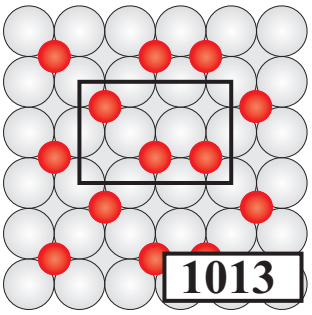


**(hol-hol)-13**

$$E_b^{\text{(hol-hol)-13}} = E^{\text{on-site}} + 1/3V_{1p} + 4/3V_{2p} + 4/3V_{3p} + 2V_{4p} + 2/3V_{5p} + 4/3V_{3t} + 2V_{4t} + 4/3V_{5t} + 2/3V_{6t} + 8/3V_{7t} + 2/3V_{8t} + 1/3V_{3q}$$

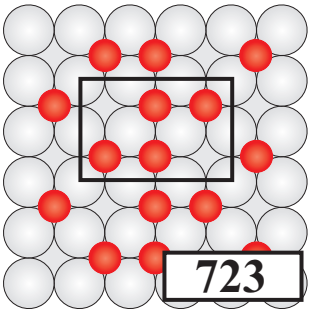


**(hol-hol)-14**

$$E_b^{\text{(hol-hol)-14}} = E^{\text{on-site}} + V_{1p} + 3/2V_{2p} + 3/2V_{3p} + 5/2V_{4p} + V_{5p} + 1/2V_{1t} + V_{2t} + 3V_{3t} + 5/2V_{4t} + 3V_{5t} + V_{6t} + 4V_{7t} + 2V_{8t} + 1/2V_{2q} + 1/2V_{3q}$$

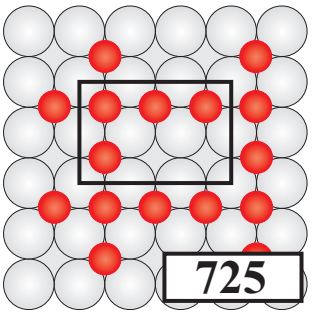


**(hol-hol)-15**

$$E_b^{\text{(hol-hol)-15}} = E^{\text{on-site}} + 5/4V_{1p} + V_{2p} + 7/4V_{3p} + 5/2V_{4p} + 3/2V_{5p} + 5/4V_{1t} + V_{2t} + 2V_{3t} + 3/2V_{4t} + 4V_{5t} + 1/2V_{6t} + 3V_{7t} + 5/2V_{8t} + V_{2q} + 1/4V_{3q} + 1/4V_{1qu}$$

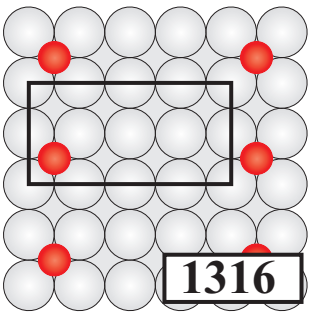


**(hol-hol)-16**

$$E_b^{\text{(hol-hol)-16}} = E^{\text{on-site}} + V_{3p}$$

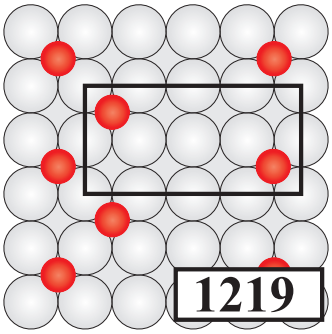


**(hol-hol)-17**

$$E_b^{\text{(hol-hol)-17}} = E^{\text{on-site}} + V_{2p} + V_{3p}$$

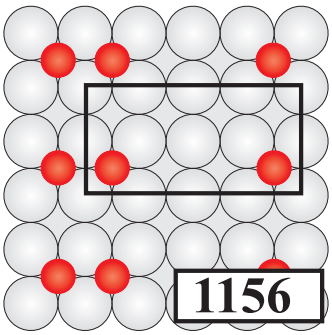


**(hol-hol)-18**

$$E_b^{\text{(hol-hol)-18}} = E^{\text{on-site}} + 1/2V_{1p} + V_{3p} + V_{4p} + 2V_{5t}$$

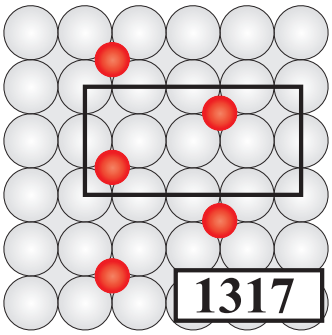


**(hol-hol)-19**

$$E_b^{\text{(hol-hol)-19}} = E^{\text{on-site}} + V_{3p} + 2V_{4p}$$

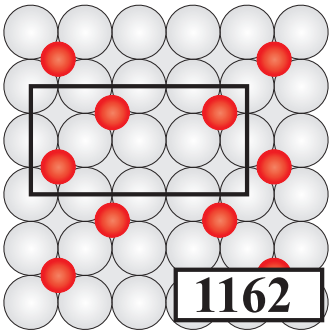


**(hol-hol)-20**

$$E_b^{\text{(hol-hol)-20}} = E^{\text{on-site}} + 4/3V_{2p} + 5/3V_{3p} + 4/3V_{5p} + 2V_{4t} + 2/3V_{6t} + 4V_{7t} + 1/3V_{3q}$$

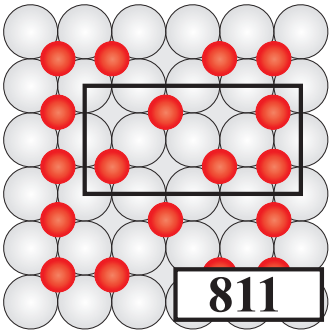


**(hol-hol)-21**

$$E_b^{\text{(hol-hol)-21}} = E^{\text{on-site}} + 4/5V_{1p} + 8/5V_{2p} + 9/5V_{3p} + 8/5V_{4p} + 8/5V_{5p} + 3/5V_{1t} + 4/5V_{2t} + 8/5V_{3t} + 16/5V_{4t} + 12/5V_{5t} + 8/5V_{6t} + 32/5V_{7t} + 6/5V_{8t} + 4V_{2q} + 4V_{3q} + 1/5V_{1qu}$$

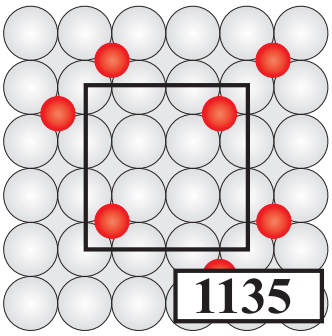


**(hol-hol)-22**

$$E_b^{\text{(hol-hol)-22}} = E^{\text{on-site}} + 1/2V_{2p} + V_{4p} + 1/2V_{5p}$$

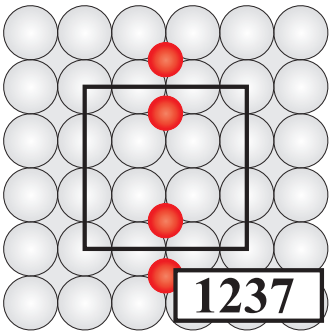


**(hol-hol)-23**

$$E_b^{\text{(hol-hol)-23}} = E^{\text{on-site}} + 1/2V_{1p} + 1/2V_{3p} + V_{8t}$$

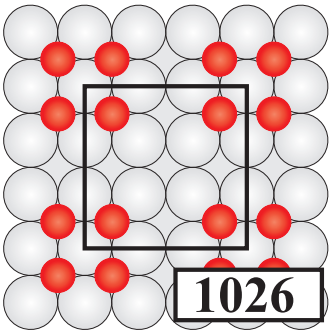


**(hol-hol)-24**

$$E_b^{\text{(hol-hol)-24}} = E^{\text{on-site}} + V_{1p} + 1/2V_{2p} + V_{3p} + V_{4p} + 1/2V_{5p} + V_{2t} + 2V_{5t} + 2V_{7t} + 2V_{8t}$$

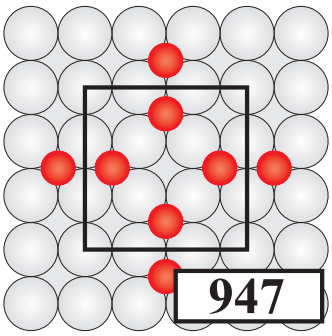


**(hol-hol)-25**

$$E_b^{\text{(hol-hol)-25}} = E^{\text{on-site}} + 1/2V_{1p} + V_{2p} + 1/2V_{3p} + 2V_{4p} + 2/3V_{5p} + 2V_{3t} + V_{4t} + V_{8t} + 1/4V_{3q}$$

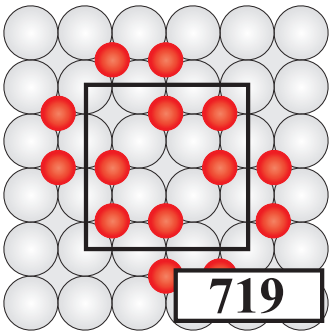


**(hol-hol)-26**

$$E_b^{\text{(hol-hol)-26}} = E^{\text{on-site}} + V_{1p} + 3/2V_{2p} + V_{3p} + 3V_{4p} + 3/2V_{5p} + V_{2t} + 4V_{3t} + 2V_{4t} + 2V_{5t} + V_{6t} + 2V_{7t} + 2V_{8t} + 1/2V_{3q}$$

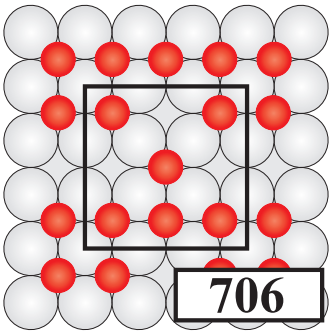


**(hol-hol)-27**

$$E_b^{\text{(hol-hol)-27}} = E^{\text{on-site}} + 7/6V_{1p} + 4/3V_{2p} + 7/6V_{3p} + 8/3V_{4p} + 4/3V_{5p} + 1/2V_{1t} + 4/3V_{2t} + 3V_{3t} + 3/2V_{4t} + 8/3V_{5t} + V_{6t} + 8/3V_{7t} + 7/3V_{8t} + 1/3V_{1q} + 1/2V_{2q} + 1/3V_{3q}$$

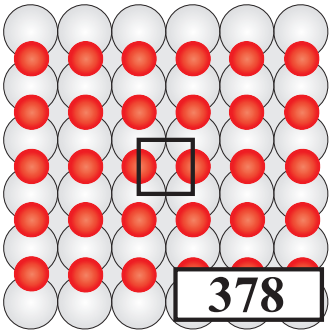


**(br-br)-1**

$$E_b^{(\text{br-br})\text{-}1} = E_{\text{bridge}}^{\text{on-site}} + V_{1p} + V_{1p}' + 2V_{2p} + V_{4p} + V_{4p}' + V_{1t} + V_{1t}' + 4V_{2t} + 4V_{3t} + 4V_{3t}' + 2V_{6t} + 2V_{6t}' + 4V_{7t} + 4V_{7t}' + 2V_{8t}$$

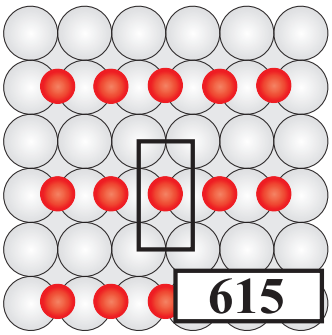


**(br-br)-2**

$$E_b^{(\text{br-br})\text{-}2} = E_{\text{bridge}}^{\text{on-site}} + V_{1p} + V_{4p} + V_{4p}' + V_{1t} + 4V_{7t}'$$

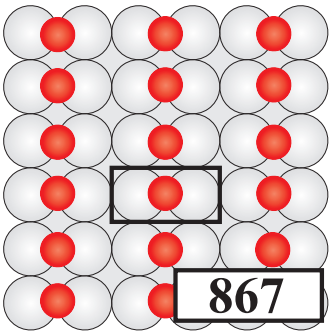


**(br-br)-3**

$$E_b^{(\text{br-br})\text{-}3} = E_{\text{bridge}}^{\text{on-site}} + V_{1p}' + V_{4p} + V_{4p}' + V_{1t}' + 4V_{7t}$$

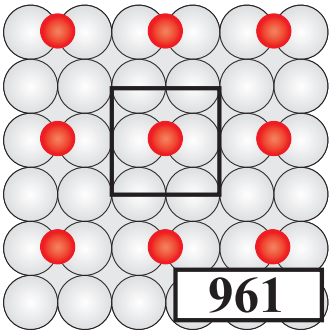


**(br-br)-4**

$$E_b^{(\text{br-br})\text{-}4} = E_{\text{bridge}}^{\text{on-site}} + V_{4p} + V_{4p}'$$

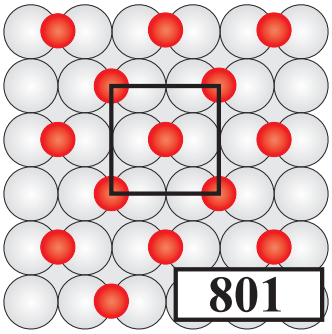


**(br-br)-5**

$$E_b^{\text{(br-br)-5}} = E_{\text{bridge}}^{\text{on-site}} + V_{2p} + V_{4p} + V_{4p}' + 2V_{6t} + 2V_{6t}' + 2V_{8t}$$

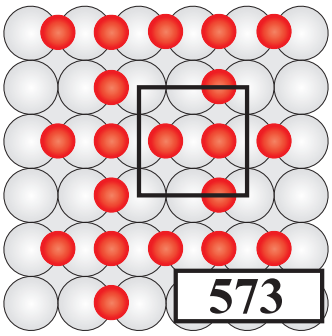


**(br-br)-6**

$$E_b^{\text{(br-br)-6}} = E_{\text{bridge}}^{\text{on-site}} + 2/3V_{1p} + 2/3V_{1p}' + 4/3V_{2p} + V_{4p} + V_{4p}' + 2/3V_{1t} + 2/3V_{1t}' + 4/3V_{2t} + 4/3V_{3t} + 4/3V_{3t}' + 4/3V_{6t} + 4/3V_{6t}' + 8/3V_{7t} + 8/3V_{7t}' + 4/3V_{8t}$$

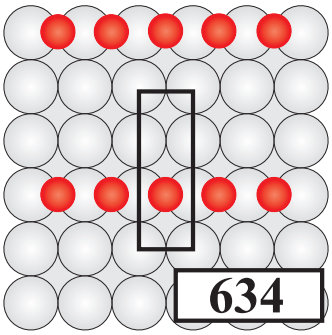


**(br-br)-7**

$$E_b^{\text{(br-br)-7}} = E_{\text{bridge}}^{\text{on-site}} + V_{1p} + V_{4p} + V_{1t}$$

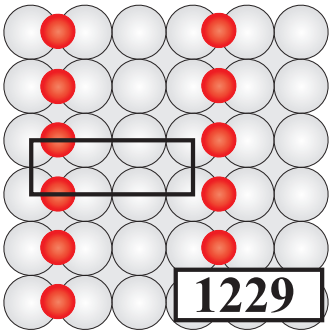


**(br-br)-8**

$$E_b^{\text{(br-br)-8}} = E_{\text{bridge}}^{\text{on-site}} + V_{1p}' + V_{4p}' + V_{1t}'$$

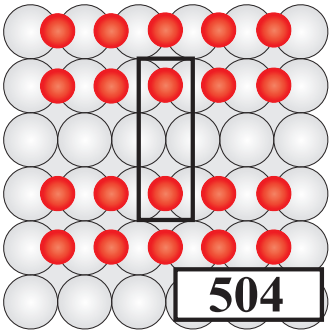


## (br-br)-9

$$E_b^{(br\text{-}br)\text{-}9} = E_{bridge}^{on\text{-}site} + V_{1p} + 1/2V_{1p}' + V_{2p} + V_{4p} + 1/2V_{4p}' + V_{1t} + 2V_{2t} + 2V_{3t}$$

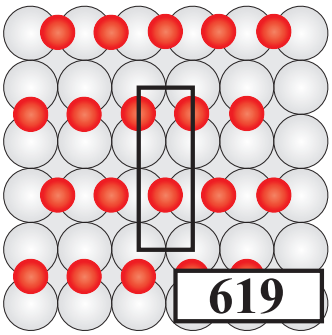


## (br-br)-10

$$E_b^{(br\text{-}br)\text{-}10} = E_{bridge}^{on\text{-}site} + 1/2V_{1p} + 1/2V_{1p}' + 2V_{3p} + 1/2V_{4p} + 1/2V_{4p}' + 2V_{5p} + 1/2V_{1t} + 1/2V_{1t}' + 2V_{4t} + 2V_{4t}' + V_{5t} + V_{5t}'$$

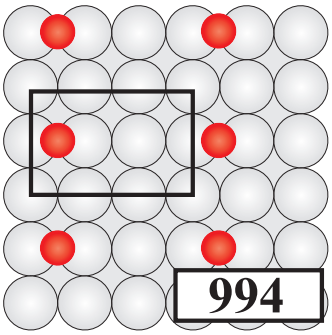


## (br-br)-11

$$E_b^{(br\text{-}br)\text{-}11} = E_{bridge}^{on\text{-}site} + 1/2V_{4p}'$$

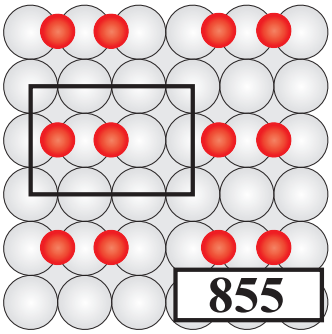


## (br-br)-12

$$E_b^{(br\text{-}br)\text{-}12} = E_{bridge}^{on\text{-}site} + 1/2V_{1p} + 1/2V_{4p} + V_{4p}' + 2V_{7t}'$$

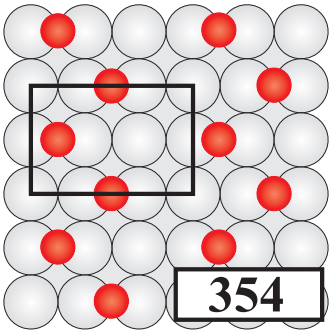


**(br-br)-13**

$$E_b^{(br\text{-}br)\text{-}13} = E_{bridge}^{on\text{-}site} + V_{2p} + V_{4p}' + V_{6t}'$$

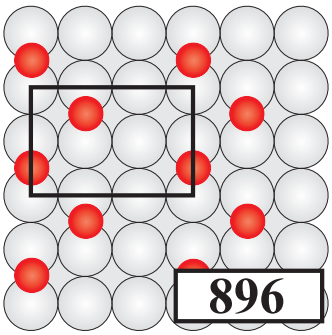


**(br-br)-14**

$$E_b^{(br\text{-}br)\text{-}14} = E_{bridge}^{on\text{-}site} + V_{2p} + V_{4p} + V_{6t}$$

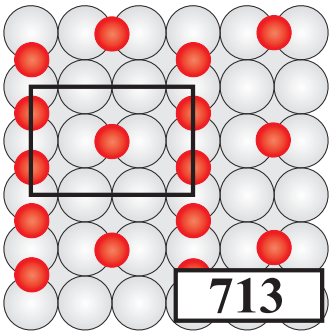


**(br-br)-15**

$$E_b^{(br\text{-}br)\text{-}15} = E_{bridge}^{on\text{-}site} + 2/3V_{1p} + 4/3V_{3p} + 2/3V_{4p} + 1/3V_{4p}' + 4/3V_{5p} + 2/3V_{1t} + 4/3V_{4t} + 2/3V_{5t}$$

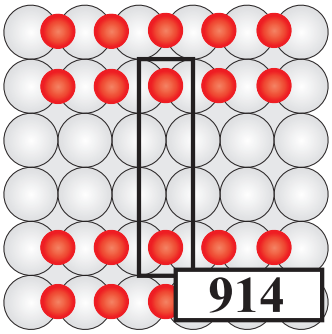


**(br-br)-16**

$$E_b^{(br\text{-}br)\text{-}16} = E_{bridge}^{on\text{-}site} + V_{1p}' + V_{4p}' + V_{1t}'$$

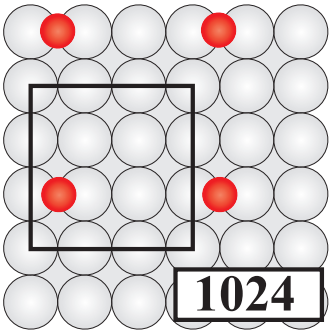


**(br-br)-17**

$$E_b^{\text{(br-br)-17}} = E_{\text{bridge}}^{\text{on-site}}$$

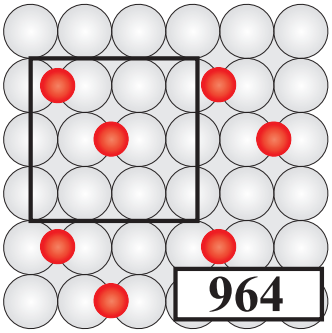


**(br-br)-18**

$$E_b^{\text{(br-br)-18}} = E_{\text{bridge}}^{\text{on-site}} + 1/2 V_{2p}$$

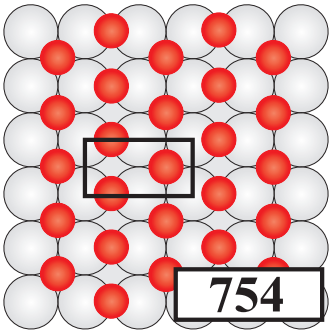


**(hol-br)-1**

$$E_b^{\text{(hol-br)-1}} = E_{\text{bridge}}^{\text{on-site}} + E_{\text{hollow}}^{\text{on-site}} + 4V_{1p} + 4V_{3p} + 2V_{1t} + 2V_{1t}' + 2V_{3t} + 2V_{3t}' + 2V_{4t} + 2V_{4t}'$$

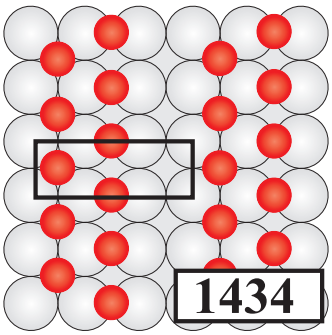


**(hol-br)-2**

$$E_b^{\text{(hol-br)-2}} = E_{\text{bridge}}^{\text{on-site}} + E_{\text{hollow}}^{\text{on-site}} + 2V_{2p} + 4V_{3p}$$

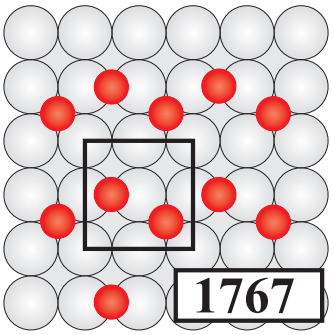


**(hol-br)-3**

$$E_b^{\text{(hol-br)-3}} = E_{\text{bridge}}^{\text{on-site}} + E_{\text{hollow}}^{\text{on-site}} + 2V_{1p} + 2V_{3p} + V_{3t} + V_{3t}'$$

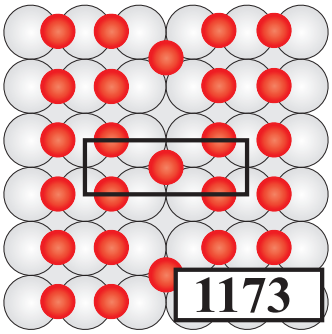


**(hol-br)-4**

$$E_b^{\text{(hol-br)-4}} = 2E_{\text{bridge}}^{\text{on-site}} + E_{\text{hollow}}^{\text{on-site}} + 4V_{1p} + 4V_{3p} + 4V_{4p} + 3V_{1t} + 3V_{1t}' + 3V_{3t}' + 3V_{4t}'$$

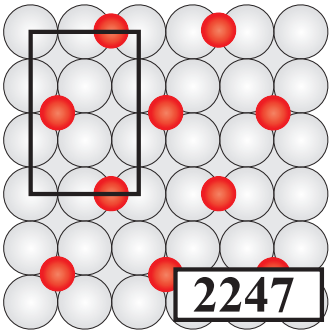


**(hol-br)-5**

$$E_{b}^{\text{(hol-br)-1}} = E_{\text{bridge}}^{\text{on-site}} + E_{\text{hollow}}^{\text{on-site}} + 4V_{3p}$$

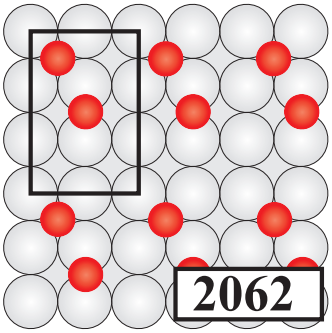


**(hol-br)-6**

$$E_{b}^{\text{(hol-br)-2}} = E_{\text{bridge}}^{\text{on-site}} + E_{\text{hollow}}^{\text{on-site}} + V_{1p} + V_{3p} + V_{4p}$$

# Appendix F

# Computed Ordered Configurations for O-Pd(117)

Listed are all ordered configurations of O at Pd(117) that were computed by (L)APW+ lo DFT. Shown is a schematic top view indicating the surface unit-cell. The computed DFT total binding energy is given in meV, and the LGH expansion using all cluster figures in the considered pool (Fig. 8.1) is stated. Light grey spheres represent Pd atoms, while the Pd step atoms are shown in grey, to better illustrate the step structure in the top view, and dark (red) spheres represent O atoms.

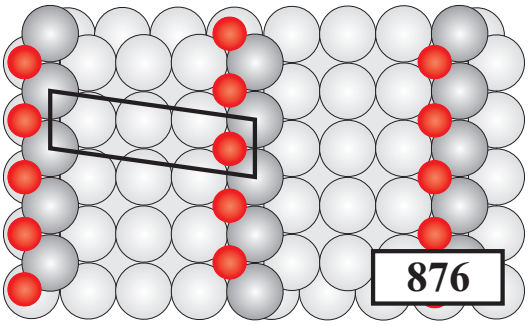


**V7-1**

$$E_b^{\text{V7-1}} = E_{b,\text{Thu}}^{\text{On-site}} + V_{1p}^{11} + V_{3p}^{11} + V_{1t}^{111}$$

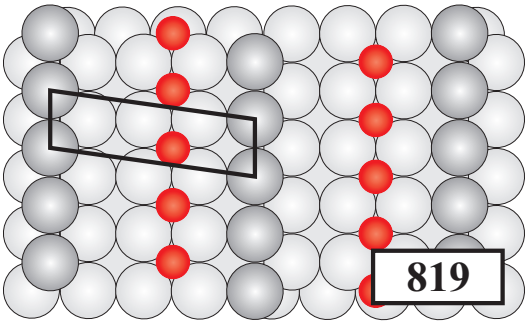


**V7-2**

$$E_b^{\text{V7-2}} = E_{b,\text{Thc}}^{\text{On-site}} + V_{1p}^{22} + V_{3p}^{22} + V_{1t}^{222}$$

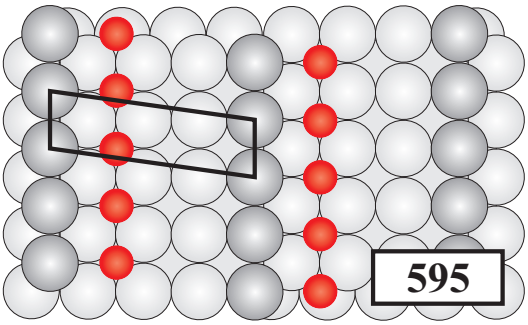


**V7-3**

$$E_b^{\text{V7-3}} = E_{b,\text{Thl}}^{\text{On-site}} + V_{1p}^{33} + V_{3p}^{33} + V_{1t}^{333}$$

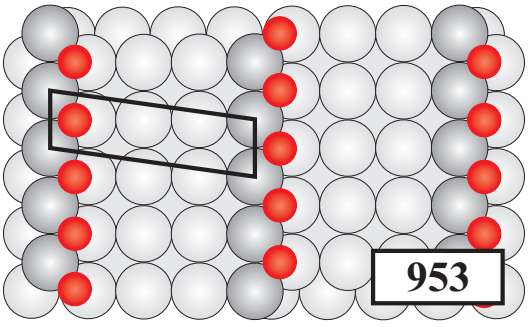


**V7-4**

$$E_b^{\text{V7-4}} = E_{b,\text{Sh2}}^{\text{On-site}} + V_{1p}^{44} + V_{3p}^{44} + V_{1t}^{444}$$

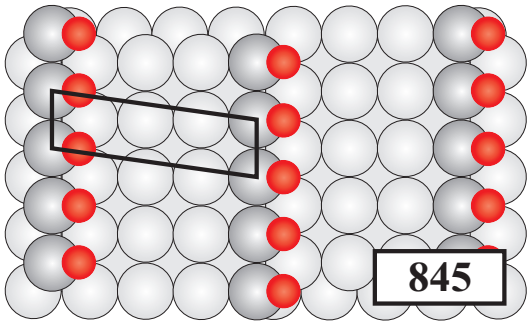


## V7-5

$$E_b^{\text{V7-5}} = E_{b,\text{Sh1}}^{\text{On-site}} + V_{1p}^{55} + V_{3p}^{55} + V_{1t}^{555}$$

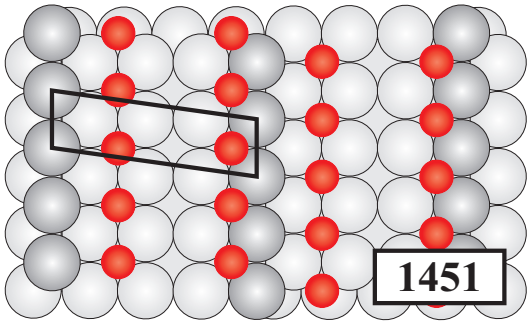


## V7-6

$$E_b^{\text{V7-6}} = E_{b,\text{Thu}}^{\text{On-site}} + E_{b,\text{Thl}}^{\text{On-site}} + V_{1p}^{11} + V_{3p}^{11} + V_{1p}^{33} + V_{3p}^{33} + V_{3p}^{13} + V_{3cp}^{13} + V_{1t}^{111} + V_{1t}^{333}$$

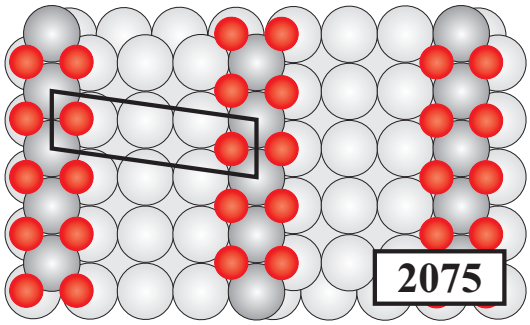


## V7-7

$$E_b^{\text{V7-7}} = E_{b,\text{Thu}}^{\text{On-site}} + E_{b,\text{Sh2}}^{\text{On-site}} + V_{1p}^{11} + V_{3p}^{11} + V_{1p}^{14} + 2V_{2p}^{14} + V_{1p}^{44} + V_{3p}^{44} + V_{1t}^{111} + 2V_{2t}^{114} + 2V_{2t}^{144} + V_{1t}^{444} + 2V_{3t}^{114} + 2V_{3t}^{144}$$

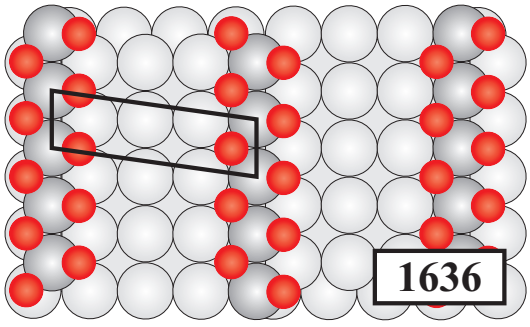


## V7-8

$$E_b^{\text{V7-8}} = E_{b,\text{Thu}}^{\text{On-site}} + E_{b,\text{Sh1}}^{\text{On-site}} + V_{1p}^{11} + V_{3p}^{11} + V_{1p}^{55} + V_{3p}^{55} + 2V_{2p}^{15} + 2V_{3p}^{15} + V_{1t}^{111} + 2V_{2t}^{115} + 2V_{2t}^{155} + 2V_{3t}^{115} + 2V_{3t}^{155} + V_{1t}^{555}$$

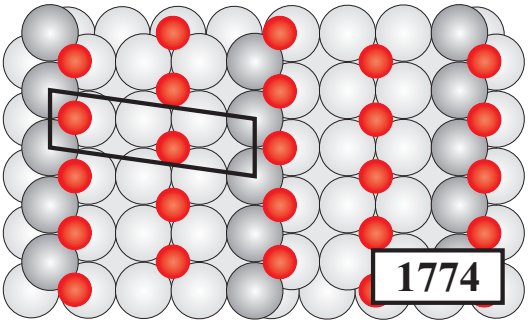


## V7-9

$$E_b^{\text{V7-9}} = E_{b,\text{Thc}}^{\text{On-site}} + E_{b,\text{Sh2}}^{\text{On-site}} + V_{1p}^{22} + V_{3p}^{22} + V_{1p}^{44} + V_{3p}^{44} + V_{3p}^{24} + 2V'^{24}_{3p} + V_{1t}^{222} + V_{1t}^{444}$$

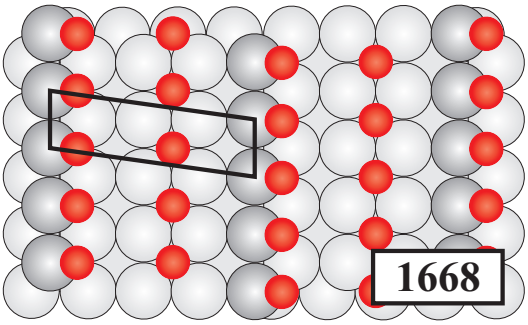


## V7-10

$$E_b^{\text{V7-10}} = E_{b,\text{Thc}}^{\text{On-site}} + E_{b,\text{Sh1}}^{\text{On-site}} + V_{1p}^{22} + V_{3p}^{22} + V_{3p}^{25} + V_{1p}^{55} + V_{3p}^{55} + V_{1t}^{222} + V_{1t}^{555}$$

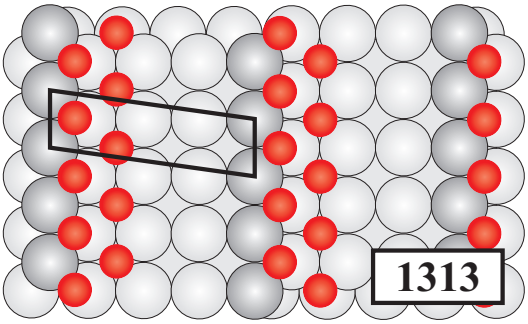


## V7-11

$$E_b^{\text{V7-7}} = E_{b,\text{Thl}}^{\text{On-site}} + E_{b,\text{Sh2}}^{\text{On-site}} + V_{1p}^{33} + V_{3p}^{33} + V_{1p}^{44} + V_{3p}^{44} + 2V_{2p}^{34} + 2V_{3p}^{34} + V_{1t}^{333} + V_{1t}^{444} + V_{2t}^{334} + V_{2t}^{344} + V_{3t}^{334} + V_{3t}^{344}$$

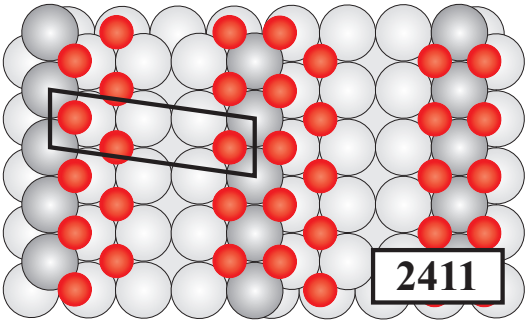


## V7-12

$$E_b^{\text{V7-12}} = E_{b,\text{Thu}}^{\text{On-site}} + E_{b,\text{Thl}}^{\text{On-site}} + E_{b,\text{Sh2}}^{\text{On-site}} + V_{1p}^{11} + V_{3p}^{11} + V_{1p}^{14} + 2V_{2p}^{14} + V_{1p}^{33} + V_{3p}^{33} + V_{3p}^{13} + 2V_{3cp}^{13} + V_{1p}^{44} + V_{3p}^{44} + 2V_{2p}^{34} + 2V_{3p}^{34} + V_{1t}^{111} + V_{1t}^{333} + V_{1t}^{444} + 2V_{2t}^{114} + 2V_{2t}^{144} + 2V_{2t}^{334} + 2V_{2t}^{344} + 2V_{3t}^{114} + 2V_{3t}^{144} + 2V_{3t}^{334} + 2V_{3t}^{344} + 2V_{3t}^{134} + 2V'^{134}_{3t}$$

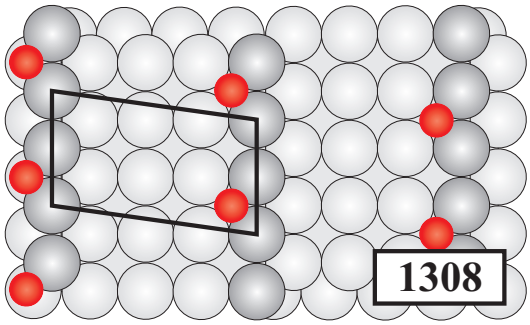


**V7-13**

$$E_b^{\text{V7-13}} = E_{b,\text{Thu}}^{\text{On-site}} + V_{3p}^{11}$$

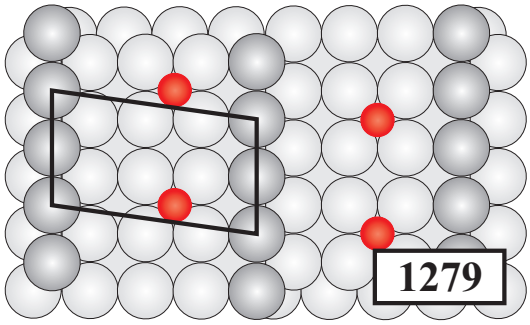


**V7-14**

$$E_b^{\text{V7-14}} = E_{b,\text{Thc}}^{\text{On-site}} + V_{3p}^{22}$$

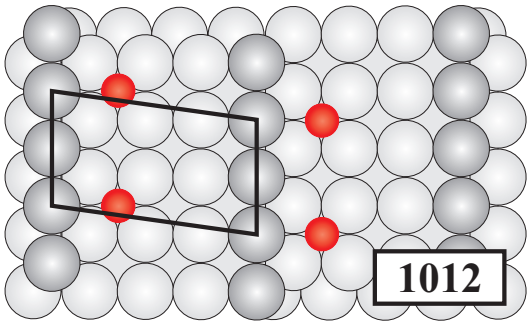


**V7-15**

$$E_b^{\text{V7-15}} = E_{b,\text{Thl}}^{\text{On-site}} + V_{3p}^{33}$$

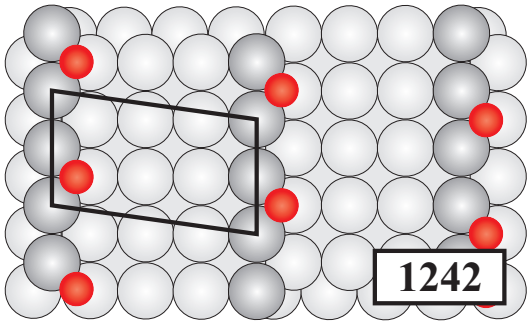


**V7-16**

$$E_b^{\text{V7-16}} = E_{b,\text{Sh2}}^{\text{On-site}} + V_{3p}^{44}$$

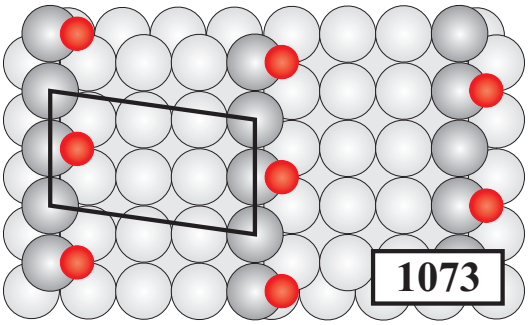


## V7-17

$$E_b^{\text{V7-17}} = E_{b,sh1}^{\text{On-site}} + V_{3p}^{55}$$

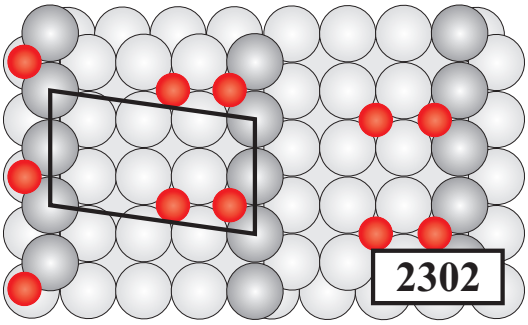


## V7-18

$$E_b^{\text{V7-18}} = E_{b,Thu}^{\text{On-site}} + E_{b,Thc}^{\text{On-site}} + V_{3p}^{11} + V_{3p}^{22} + V_{1p}^{12}$$

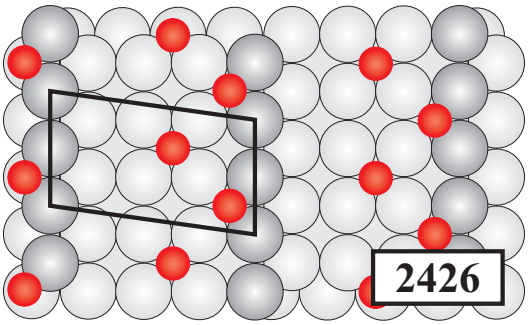


## V7-19

$$E_b^{\text{V7-19}} = E_{b,Thu}^{\text{On-site}} + E_{b,Thc}^{\text{On-site}} + V_{3p}^{11} + V_{3p}^{22} + 2V_{2p}^{12}$$

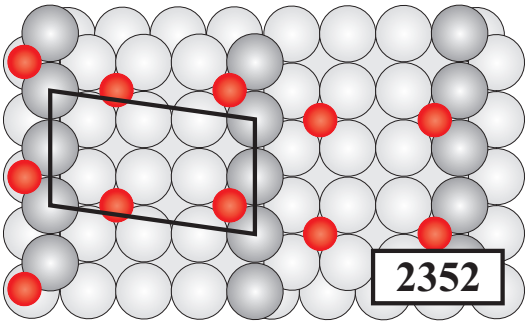


## V7-20

$$E_b^{\text{V7-20}} = E_{b,Thu}^{\text{On-site}} + E_{b,Thl}^{\text{On-site}} + V_{3p}^{11} + V_{3p}^{33} + V_{3p}^{13} + V_{3cp}^{13}$$

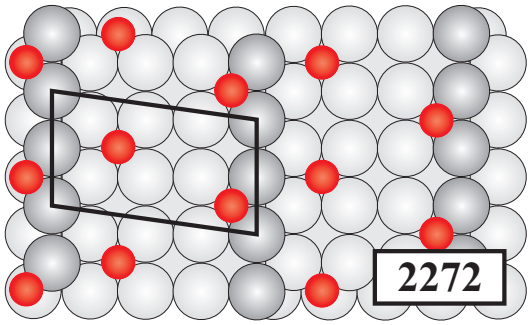


**V7-21**

$$E_b^{\text{V7-21}} = E_{b,\text{Thu}}^{\text{On-site}} + E_{b,\text{Thl}}^{\text{On-site}} + V_{3p}^{11} + V_{3p}^{33} + V_{3cp}^{13}$$

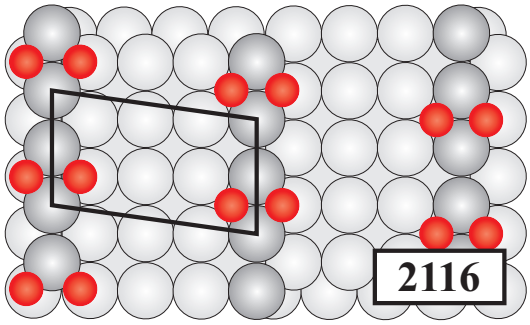


**V7-22**

$$E_b^{\text{V7-22}} = E_{b,\text{Thu}}^{\text{On-site}} + E_{b,\text{Sh2}}^{\text{On-site}} + V_{3p}^{11} + V_{3p}^{44} + V_{1p}^{14}$$

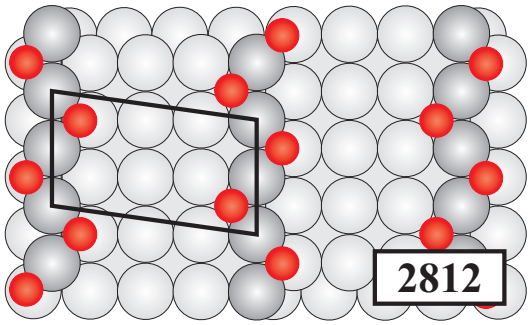


**V7-23**

$$E_b^{\text{V7-23}} = E_{b,\text{Thu}}^{\text{On-site}} + E_{b,\text{Sh2}}^{\text{On-site}} + V_{3p}^{11} + V_{3p}^{44} + 2V_{2p}^{14}$$

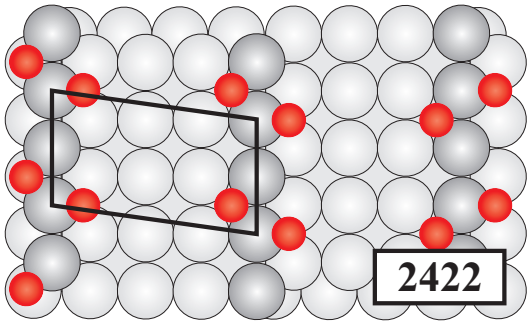


**V7-24**

$$E_b^{\text{V7-24}} = E_{b,\text{Thu}}^{\text{On-site}} + E_{b,\text{Sh1}}^{\text{On-site}} + V_{2p}^{15} + V_{3p}^{11} + V_{3p}^{15} + V_{3p}^{55}$$

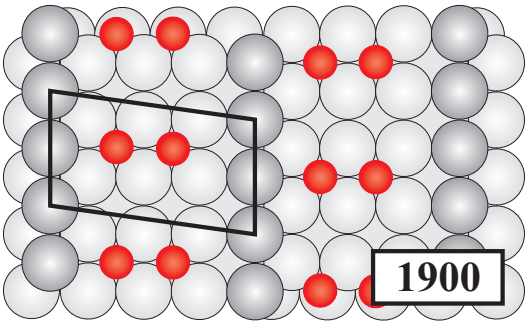


## V7-25

$$E_b^{\text{V7-25}} = E_{b,\text{Thc}}^{\text{On-site}} + E_{b,\text{Thl}}^{\text{On-site}} + V_{1p}^{23} + V_{3p}^{22} + V_{3p}^{33}$$

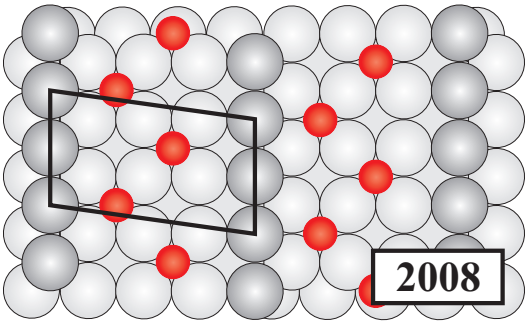


## V7-26

$$E_b^{\text{V7-26}} = E_{b,\text{Thc}}^{\text{On-site}} + E_{b,\text{Thl}}^{\text{On-site}} + 2V_{2p}^{23} + V_{3p}^{22} + V_{3p}^{33}$$

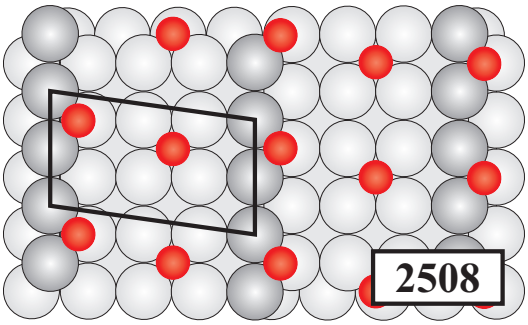


## V7-27

$$E_b^{\text{V7-27}} = E_{b,\text{Thc}}^{\text{On-site}} + E_{b,\text{Sh2}}^{\text{On-site}} + V_{3p}^{22} + V_{3p}^{44} + V_{3p}^{24} + V'^{24}_{3p}$$

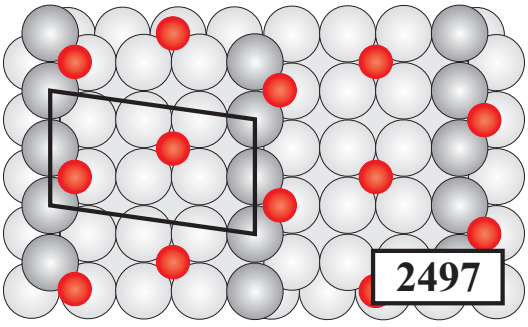


## V7-28

$$E_b^{\text{V7-28}} = E_{b,\text{Thc}}^{\text{On-site}} + E_{b,\text{Sh2}}^{\text{On-site}} + V_{3p}^{22} + V_{3p}^{44} + V'^{24}_{3p}$$

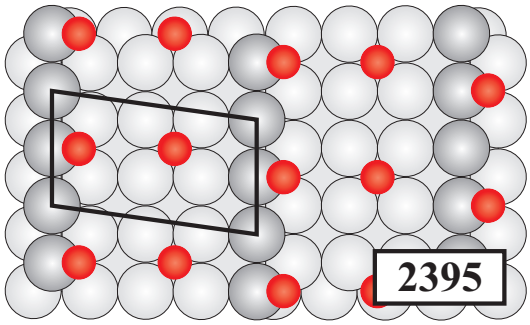


**V7-29**

$$E_b^{\text{V7-29}} = E_{b,\text{Thc}}^{\text{On-site}} + E_{b,\text{Sh1}}^{\text{On-site}} + V_{3p}^{22} + V_{3p}^{25} + V_{3p}^{55}$$

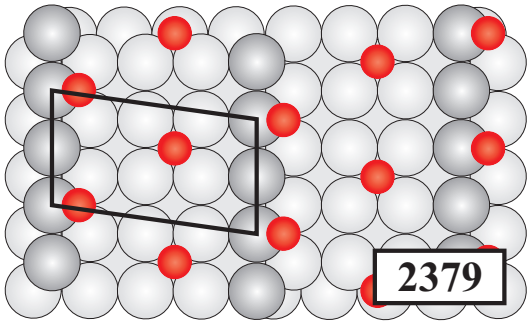


**V7-30**

$$E_b^{\text{V7-30}} = E_{b,\text{Thc}}^{\text{On-site}} + E_{b,\text{Sh1}}^{\text{On-site}} + V_{3p}^{22} + V_{3p}^{55}$$

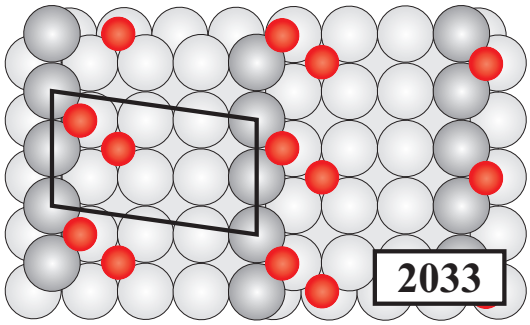


**V7-31**

$$E_b^{\text{V7-31}} = E_{b,\text{Thl}}^{\text{On-site}} + E_{b,\text{Sh2}}^{\text{On-site}} + V_{2p}^{34} + V_{3p}^{33} + V_{3p}^{34} + V_{3p}^{44}$$

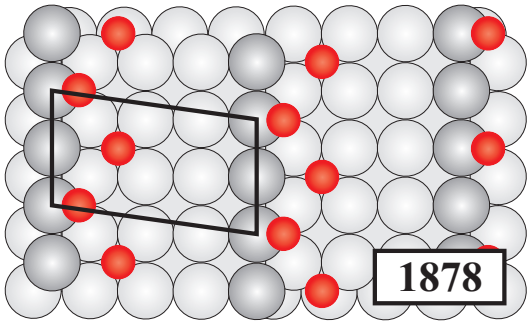


**V7-32**

$$E_b^{\text{V7-32}} = E_{b,\text{Thl}}^{\text{On-site}} + E_{b,\text{Sh1}}^{\text{On-site}} + 2V_{2p}^{35} + V_{3p}^{33} + V_{3p}^{55}$$

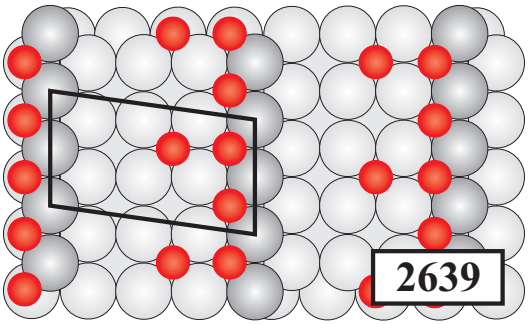


## V7-33

$$E_b^{\text{V7-33}} = 2E_{b,\text{Thu}}^{\text{On-site}} + E_{b,\text{Thc}}^{\text{On-site}} + 2V_{1p}^{11} + 2V_{3p}^{11} + V_{3p}^{22} + V_{1p}^{12} + 2V_{2p}^{12} + 2V_{1t}^{111} + 2V_{2t}^{112} + 2V_{3t}^{112}$$

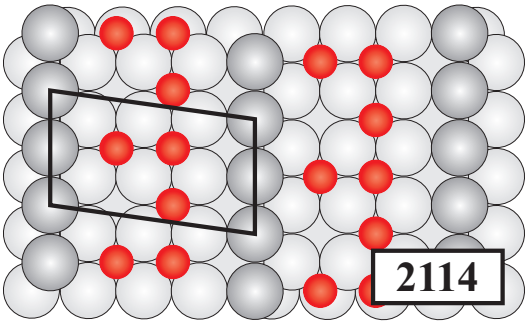


## V7-34

$$E_b^{\text{V7-34}} = 2E_{b,\text{Thc}}^{\text{On-site}} + E_{b,\text{Thl}}^{\text{On-site}} + 2V_{1p}^{22} + 2V_{3p}^{22} + V_{3p}^{33} + V_{1p}^{23} + 2V_{2p}^{23} + 2V_{1t}^{222} + 2V_{2t}^{223} + 2V_{3t}^{223}$$

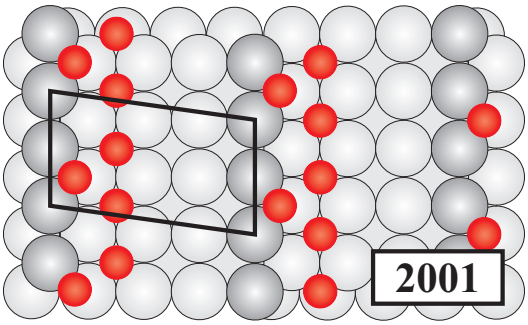


## V7-35

$$E_b^{\text{V7-35}} = 2E_{b,\text{Thl}}^{\text{On-site}} + E_{b,\text{Sh2}}^{\text{On-site}} + 2V_{1p}^{33} + 2V_{2p}^{34} + 2V_{3p}^{33} + 2V_{3p}^{34} + V_{3p}^{44} + 2V_{1t}^{333} + V_{2t}^{334} + 2V_{3t}^{334}$$

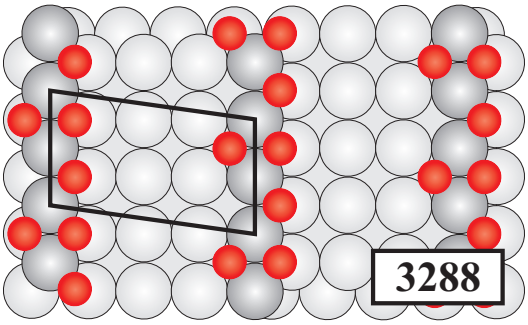


## V7-36

$$E_b^{\text{V7-36}} = 2E_{b,\text{Sh2}}^{\text{On-site}} + E_{b,\text{Thu}}^{\text{On-site}} + 2V_{1p}^{44} + 2V_{3p}^{44} + V_{3p}^{11} + V_{1p}^{14} + 2V_{2p}^{14} + 2V_{1t}^{444} + 2V_{2t}^{144} + 2V_{3t}^{144}$$

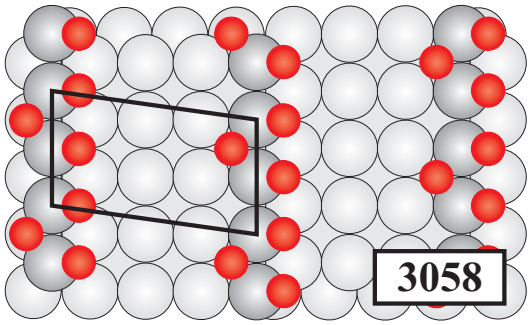


## V7-37

$$E_b^{\text{V7-37}} = 2E_{b,\text{Sh1}}^{\text{On-site}} + E_{b,\text{Thu}}^{\text{On-site}} + 2V_{1p}^{55} + V_{3p}^{11} + 2V_{3p}^{55} + 2V_{2p}^{15} + 2V_{3p}^{15} + 2V_{1t}^{555} + V_{2t}^{155} + 2V_{3t}^{155}$$

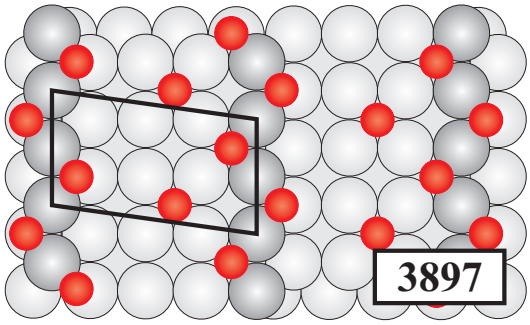


## V7-38

$$E_b^{\text{V7-38}} = E_{b,\text{Thu}}^{\text{On-site}} + E_{b,\text{Thc}}^{\text{On-site}} + E_{b,\text{Sh2}}^{\text{On-site}} + V_{3p}^{11} + V_{3p}^{22} + V_{3p}^{44} + 2V_{2p}^{12} + 2V_{2p}^{14} + V_{3p}^{24} + V'^{24}_{3p}$$

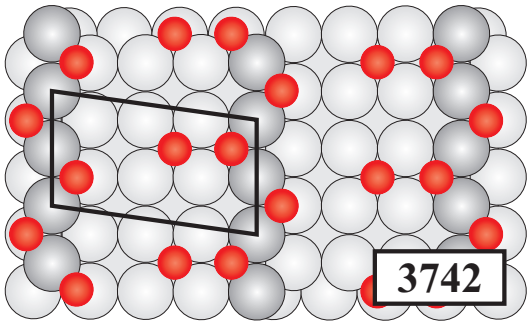


## V7-39

$$E_b^{\text{V7-39}} = E_{b,\text{Thu}}^{\text{On-site}} + E_{b,\text{Thc}}^{\text{On-site}} + E_{b,\text{Sh2}}^{\text{On-site}} + V_{3p}^{11} + V_{3p}^{22} + V_{3p}^{44} + V_{1p}^{12} + 2V_{2p}^{14} + V'^{24}_{3p} + 2V_{3t}^{124}$$

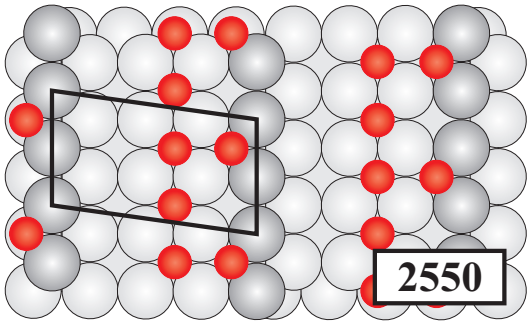


## V7-40

$$E_b^{\text{V7-40}} = E_{b,\text{Thu}}^{\text{On-site}} + 2E_{b,\text{Thc}}^{\text{On-site}} + V_{3p}^{11} + 2V_{1p}^{22} + 2V_{3p}^{22} + V_{1p}^{12} + 2V_{2p}^{12} + 2V_{1t}^{222} + 2V_{2t}^{122} + 2V_{3t}^{122}$$

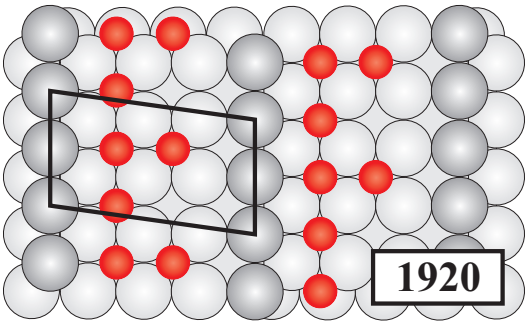


## V7-41

$$E_b^{\text{V7-41}} = E_{b,\text{Thc}}^{\text{On-site}} + 2E_{b,\text{Thl}}^{\text{On-site}} + V_{3p}^{22} + 2V_{1p}^{33} + 2V_{3p}^{33} + V_{1p}^{23} + 2V_{2p}^{23} + 2V_{1t}^{333} + 2V_{2t}^{233} + 2V_{3t}^{233}$$

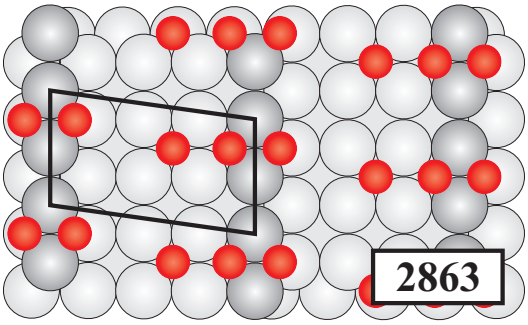


## V7-42

$$E_b^{\text{V7-42}} = E_{b,\text{Thu}}^{\text{On-site}} + E_{b,\text{Thc}}^{\text{On-site}} + E_{b,\text{Sh2}}^{\text{On-site}} + V_{3p}^{11} + V_{3p}^{22} + V_{3p}^{44} + V_{1p}^{12} + V_{1p}^{14} + V_{3p}^{24} + V'^{24}_{3p} + V_{1t}^{124}$$

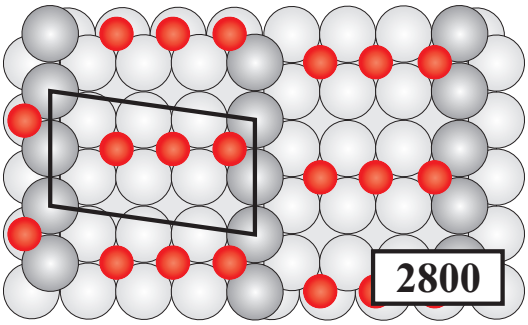


## V7-43

$$E_b^{\text{V7-43}} = E_{b,\text{Thu}}^{\text{On-site}} + E_{b,\text{Thc}}^{\text{On-site}} + E_{b,\text{Thl}}^{\text{On-site}} + V_{3p}^{11} + V_{3p}^{22} + V_{3p}^{33} + V_{1p}^{12} + V_{3p}^{13} + V_{3cp}^{13} + V_{1p}^{23} + V_{1t}^{123}$$

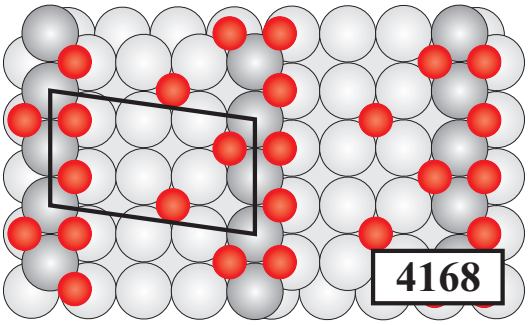


## V7-44

$$E_b^{\text{V7-44}} = E_{b,\text{Thu}}^{\text{On-site}} + E_{b,\text{Thc}}^{\text{On-site}} + 2E_{b,\text{Sh2}}^{\text{On-site}} + V_{3p}^{11} + V_{3p}^{22} + 2V_{1p}^{44} + 2V_{3p}^{44} + V_{1p}^{14} + 2V_{2p}^{12} + 2V_{2p}^{14} + V_{3p}^{24} + 2V'^{24}_{3p} + 2V_{1t}^{444} + 2V_{2t}^{144} + 2V_{3t}^{144} + 2V'^{124}_{3t}$$

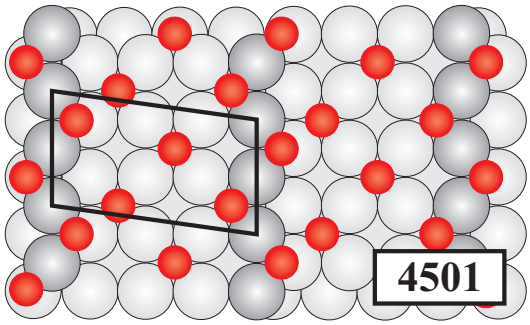


## V7-45

$$E_b^{\text{V7-45}} = E_{b,\text{Thu}}^{\text{On-site}} + E_{b,\text{Thc}}^{\text{On-site}} + E_{b,\text{Thl}}^{\text{On-site}} + E_{b,\text{Sh2}}^{\text{On-site}} + V_{3p}^{11} + V_{3p}^{22} + V_{3p}^{33} + V_{3p}^{44} + 2V_{2p}^{12} + 2V_{2p}^{14} + V_{1p}^{13} + V_{3cp}^{13} + 2V_{2p}^{23} + V_{3p}^{24} + V'^{24}_{3p} + V_{2p}^{34} + V_{3p}^{34} + V'^{134}_{3t}$$

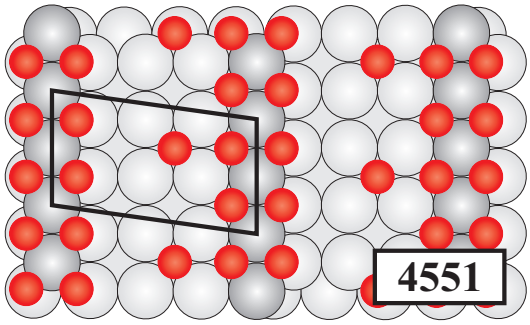


## V7-46

$$E_b^{\text{V7-46}} = 2E_{b,\text{Thu}}^{\text{On-site}} + E_{b,\text{Thc}}^{\text{On-site}} + 2E_{b,\text{Sh2}}^{\text{On-site}} + 2V_{1p}^{11} + 2V_{3p}^{11} + V_{3p}^{22} + 2V_{1p}^{44} + 2V_{3p}^{44} + V_{1p}^{12} + 2V_{2p}^{12} + 2V_{1p}^{14} + 4V_{2p}^{14} + V_{3p}^{24} + 2V'^{24}_{3p} + 2V_{1t}^{111} + 2V_{2t}^{112} + 4V_{2t}^{114} + 4V_{2t}^{144} + 2V_{1t}^{444} + V_{1t}^{124} + 2V_{3t}^{122} + 4V_{3t}^{114} + 4V_{3t}^{144} + 2V_{3t}^{124} + 2V'^{124}_{3t}$$

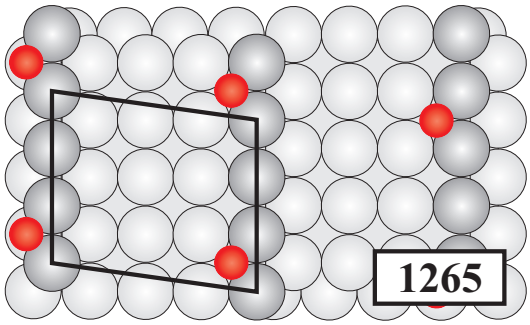


## V7-47

$$E_b^{\text{V7-47}} = E_{b,\text{Thu}}^{\text{On-site}}$$

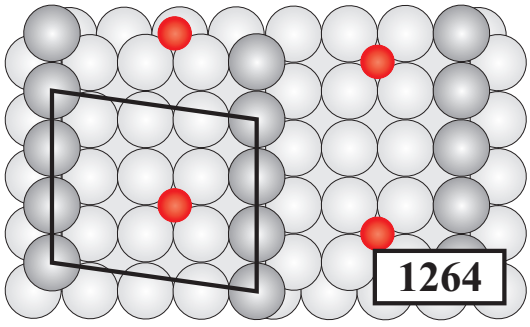


## V7-48

$$E_b^{\text{V7-48}} = E_{b,\text{Thc}}^{\text{On-site}}$$

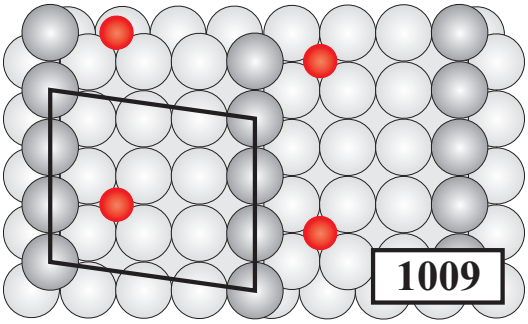


**V7-49**

$$E_b^{\text{V7-49}} = E_{b,\text{Thl}}^{\text{On-site}}$$

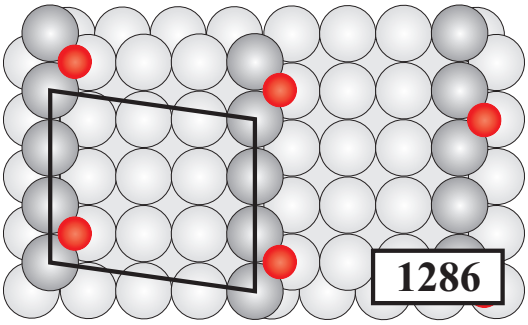


**V7-50**

$$E_b^{\text{V7-50}} = E_{b,\text{Sh2}}^{\text{On-site}}$$

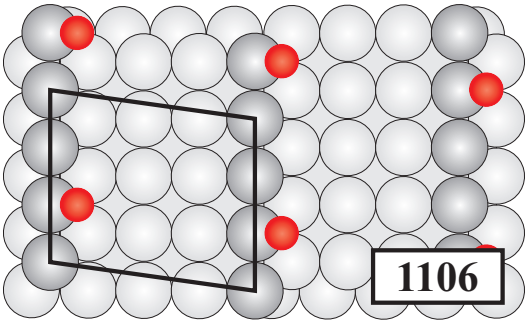


**V7-51**

$$E_b^{\text{V7-51}} = E_{b,\text{Sh1}}^{\text{On-site}}$$

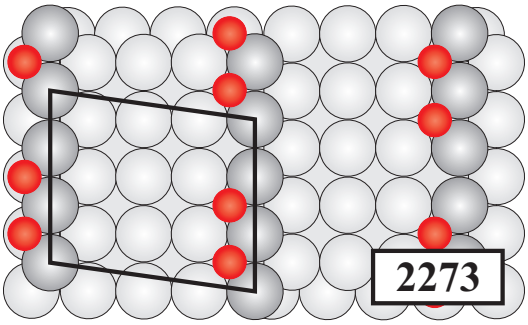


**V7-52**

$$E_b^{\text{V7-52}} = E_{b,\text{Thu}}^{\text{On-site}} + V_{1p}^{11} + V_{3p}^{11}$$

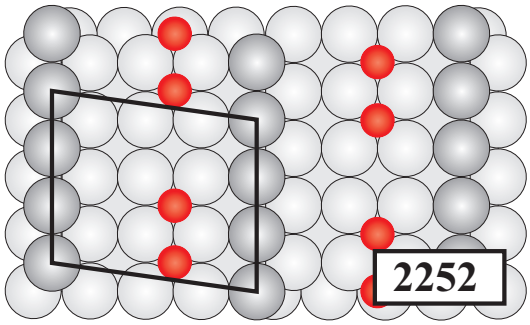


## V7-53

$$E_b^{\text{V7-53}} = E_{b,\text{Thc}}^{\text{On-site}} + V_{1p}^{22} + V_{3p}^{22}$$

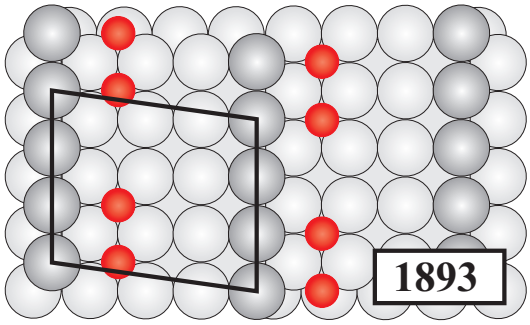


## V7-54

$$E_b^{\text{V7-54}} = E_{b,\text{Thl}}^{\text{On-site}} + V_{1p}^{33} + V_{3p}^{33}$$

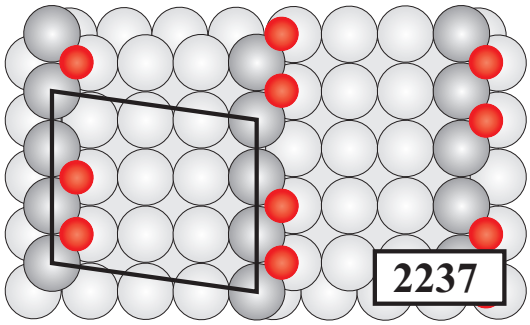


## V7-55

$$E_b^{\text{V7-55}} = E_{b,\text{Sh2}}^{\text{On-site}} + V_{1p}^{44} + V_{3p}^{44}$$

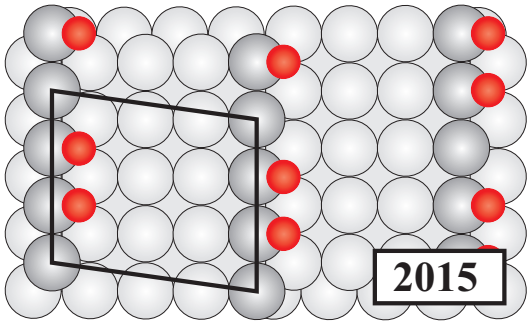


## V7-56

$$E_b^{\text{V7-56}} = E_{b,\text{Sh1}}^{\text{On-site}} + V_{1p}^{55} + V_{3p}^{55}$$

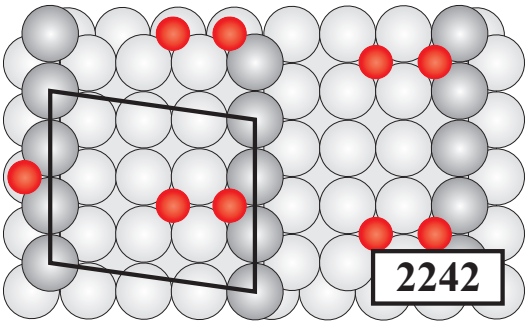


## V7-57

$$E_b^{\text{V7-57}} = E_{b,\text{Thu}}^{\text{On-site}} + E_{b,\text{Thc}}^{\text{On-site}} + V_{1p}^{12}$$

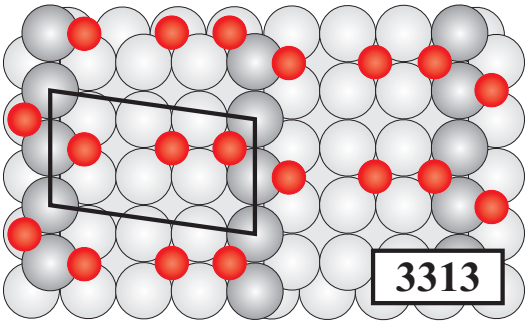


## V7-58

$$E_b^{\text{V7-58}} = E_{b,\text{Thu}}^{\text{On-site}} + E_{b,\text{Thc}}^{\text{On-site}} + E_{b,\text{Sh1}}^{\text{On-site}} + V_{1p}^{12} + V_{2p}^{15} + V_{3p}^{11} + V_{3p}^{15} + V_{3p}^{22} + V_{3p}^{25} + V_{3p}^{55} + V_{3t}^{125}$$

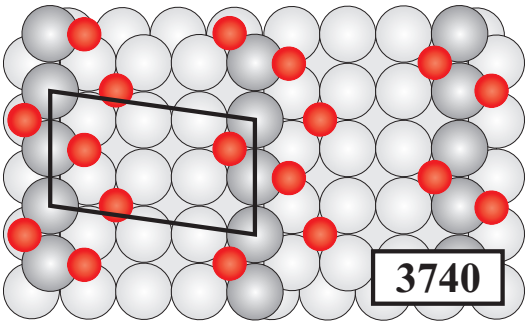


## V7-59

$$E_b^{\text{V7-59}} = E_{b,\text{Thu}}^{\text{On-site}} + E_{b,\text{Thc}}^{\text{On-site}} + E_{b,\text{Sh1}}^{\text{On-site}} + V_{2p}^{15} + V_{3p}^{11} + V_{3cp}^{13} + V_{3p}^{15} + 2V_{2p}^{35} + V_{3p}^{33} + V_{3p}^{55} + V_{3t}^{135}$$

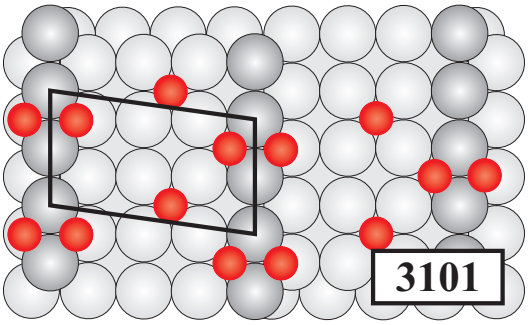


## V7-60

$$E_b^{\text{V7-60}} = E_{b,\text{Thu}}^{\text{On-site}} + E_{b,\text{Thl}}^{\text{On-site}} + E_{b,\text{Sh2}}^{\text{On-site}} + V_{1p}^{14} + 2V_{2p}^{12} + V_{3p}^{11} + V_{3p}^{22} + V'_{3p}{}^{24} + V_{3p}^{44} + 2V'^{124}_{3t}$$

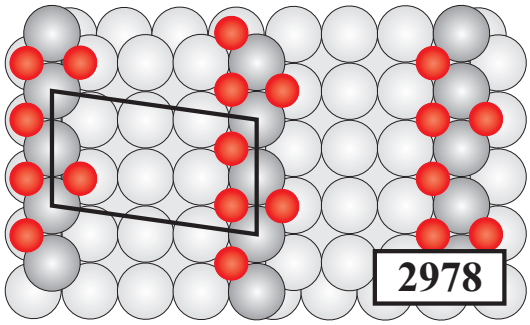


## V7-61

$$E_b^{\text{V7-61}} = 2E_{b,\text{Thu}}^{\text{On-site}} + E_{b,\text{Sh2}}^{\text{On-site}} + 2V_{1p}^{11} + V_{1p}^{14} + 2V_{2p}^{14} + 2V_{3p}^{11} + V_{3p}^{44} + 2V_{1t}^{111} + 2V_{2t}^{114} + 2V_{3t}^{114}$$

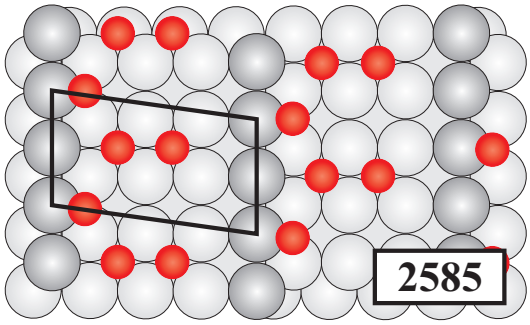


## V7-62

$$E_b^{\text{V7-62}} = E_{b,\text{Thc}}^{\text{On-site}} + E_{b,\text{Thl}}^{\text{On-site}} + E_{b,\text{Sh1}}^{\text{On-site}} + V_{1p}^{23} + V_{3p}^{22} + 2V_{2p}^{35} + V_{3p}^{33} + V_{3p}^{55} + 2V_{3t}^{235}$$

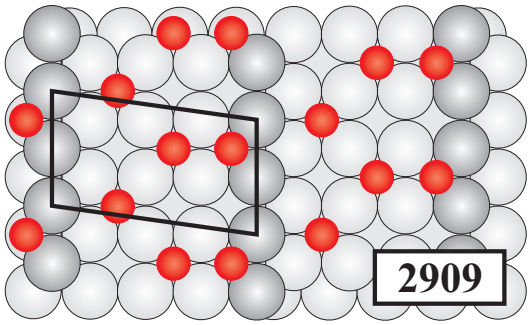


## V7-63

$$E_b^{\text{V7-63}} = E_{b,\text{Thu}}^{\text{On-site}} + E_{b,\text{Thc}}^{\text{On-site}} + E_{b,\text{Thl}}^{\text{On-site}} + V_{1p}^{12} + V_{3p}^{11} + V_{3cp}^{13} + 2V_{2p}^{23} + V_{3p}^{22} + V_{3p}^{33} + 2V_{3t}^{123}$$

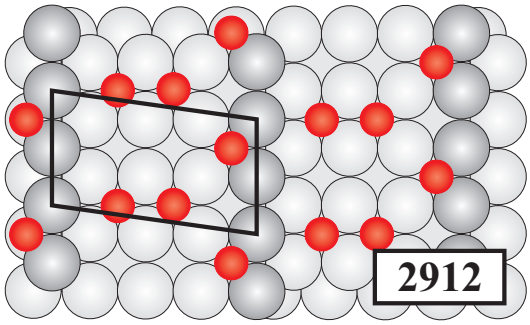


## V7-64

$$E_b^{\text{V7-64}} = E_{b,\text{Thu}}^{\text{On-site}} + E_{b,\text{Thc}}^{\text{On-site}} + E_{b,\text{Thl}}^{\text{On-site}} + 2V_{2p}^{12} + V_{3p}^{11} + V_{3cp}^{13} + V_{1p}^{23} + V_{3p}^{22} + V_{3p}^{33} + 2V_{3t}^{\prime 123}$$

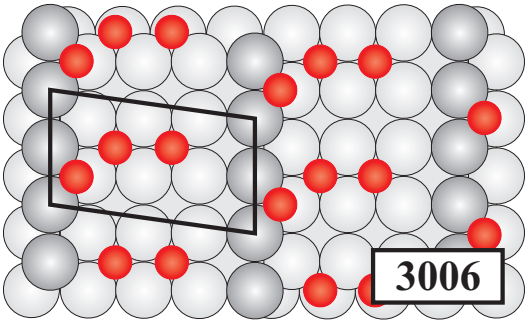


## V7-65

$$E_b^{\text{V7-65}} = E_{b,\text{Thc}}^{\text{On-site}} + E_{b,\text{Thl}}^{\text{On-site}} + E_{b,\text{Sh2}}^{\text{On-site}} + V_{1p}^{23} + V_{3p}^{22} + V'^{24}_{3p} + V_{2p}^{34} + V_{3p}^{33} + V_{3p}^{34} + V_{3p}^{44} + V_{3t}^{234}$$

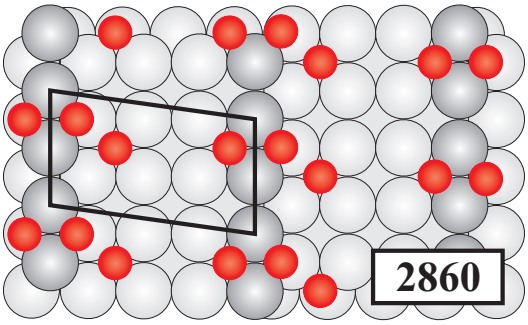


## V7-66

$$E_b^{\text{V7-66}} = E_{b,\text{Thu}}^{\text{On-site}} + E_{b,\text{Thl}}^{\text{On-site}} + E_{b,\text{Sh2}}^{\text{On-site}} + V_{1p}^{14} + V_{3p}^{11} + V_{3p}^{13} + V_{3cp}^{13} + V_{2p}^{34} + V_{3p}^{33} + V_{3p}^{34} + V_{3p}^{44} + V_{3t}^{134}$$

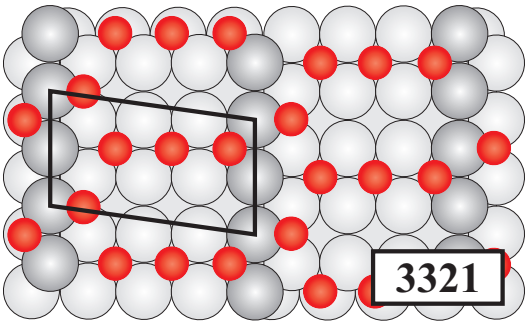


## V7-67

$$E_b^{\text{V7-67}} = E_{b,\text{Thu}}^{\text{On-site}} + E_{b,\text{Thc}}^{\text{On-site}} + E_{b,\text{Thl}}^{\text{On-site}} + E_{b,\text{Sh1}}^{\text{On-site}} + V_{1p}^{12} + V_{2p}^{15} + V_{3p}^{11} + V_{3p}^{13} + V_{3cp}^{13} + V_{3p}^{15} + V_{1p}^{23} + V_{3p}^{22} + 2V_{2p}^{35} + V_{3p}^{33} + V_{3p}^{55} + V_{1t}^{123} + V_{3t}^{125} + V_{3t}^{135} + 2V_{3t}^{235}$$

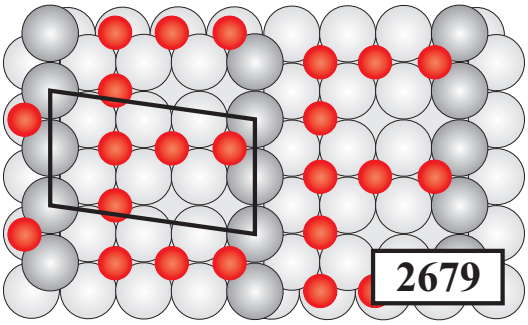


## V7-68

$$E_b^{\text{V7-68}} = E_{b,\text{Thu}}^{\text{On-site}} + E_{b,\text{Thc}}^{\text{On-site}} + 2E_{b,\text{Thl}}^{\text{On-site}} + V_{1p}^{12} + V_{3p}^{11} + V_{3p}^{13} + 2V_{3cp}^{13} + V_{1p}^{23} + 2V_{2p}^{23} + V_{3p}^{22} + 2V_{1p}^{33} + V_{3p}^{33} + V_{1t}^{123} + 2V_{3t}^{123} + 2V_{2t}^{233} + 2V_{3t}^{233} + 2V_{1t}^{333}$$

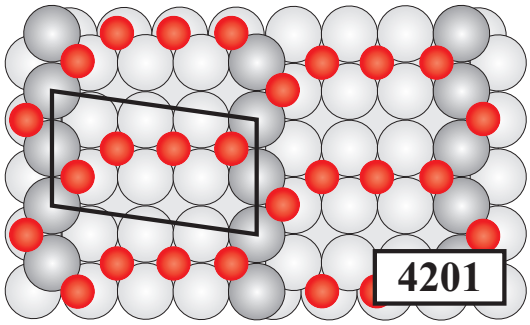


## V7-69

$$E_b^{\text{V7-69}} = E_{b,\text{Thu}}^{\text{On-site}} + E_{b,\text{Thc}}^{\text{On-site}} + E_{b,\text{Thl}}^{\text{On-site}} + E_{b,\text{Sh2}}^{\text{On-site}} + V_{1p}^{12} + 2V_{2p}^{14} + V_{3p}^{11} + V_{3p}^{13} + V_{3cp}^{13} + V_{1p}^{23} + V_{3p}^{22} + V'^{24}_{3p} + V_{2p}^{34} + V_{3p}^{33} + V_{3p}^{34} + V_{3p}^{44} + V_{1t}^{123} + 2V_{3t}^{124} + V_{3t}^{134} + V_{3t}^{234}$$

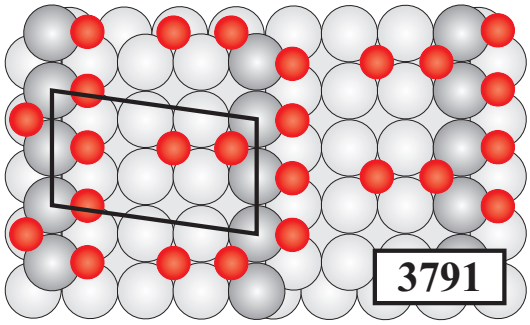


## V7-70

$$E_b^{\text{V7-70}} = E_{b,\text{Thu}}^{\text{On-site}} + E_{b,\text{Thc}}^{\text{On-site}} + 2E_{b,\text{Sh1}}^{\text{On-site}} + V_{1p}^{12} + 2V_{2p}^{15} + V_{3p}^{11} + 2V_{3p}^{15} + V_{3p}^{22} + V_{3p}^{25} + 2V_{1p}^{55} + 2V_{3p}^{55} + V_{2t}^{155} + 2V_{3t}^{155} + 2V_{3t}^{125} + 2V_{1t}^{555}$$

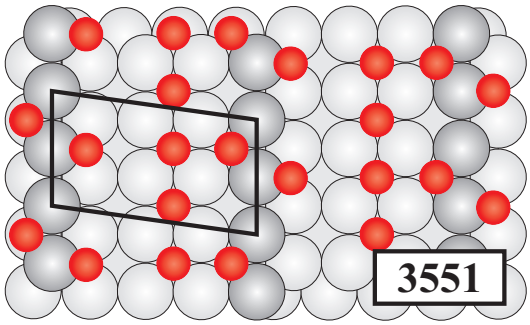


## V7-71

$$E_b^{\text{V7-71}} = E_{b,\text{Thu}}^{\text{On-site}} + 2E_{b,\text{Thc}}^{\text{On-site}} + E_{b,\text{Sh1}}^{\text{On-site}} + V_{1p}^{12} + 2V_{2p}^{12} + V_{2p}^{15} + V_{3p}^{11} + V_{3p}^{15} + 2V_{1p}^{22} + 2V_{3p}^{22} + V_{3p}^{25} + V_{3p}^{55} + 2V_{2t}^{122} + 2V_{3t}^{122} + V_{3t}^{125} + 2V_{1t}^{222}$$

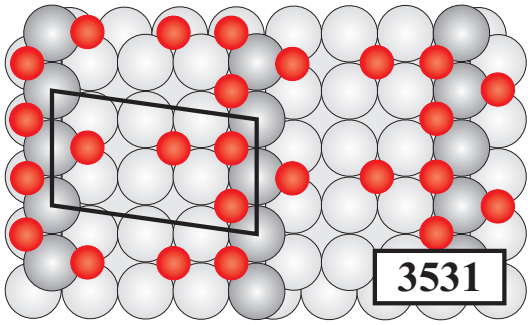


## V7-72

$$E_b^{\text{V7-72}} = 2E_{b,\text{Thu}}^{\text{On-site}} + E_{b,\text{Thc}}^{\text{On-site}} + E_{b,\text{Sh1}}^{\text{On-site}} + 2V_{1p}^{11} + V_{1p}^{12} + 2V_{2p}^{12} + 2V_{2p}^{15} + 2V_{3p}^{11} + 2V_{3p}^{15} + V_{3p}^{22} + V_{3p}^{25} + V_{3p}^{55} + 2V_{1t}^{111} + 2V_{2t}^{112} + V_{2t}^{115} + 2V_{3t}^{112} + 2V_{3t}^{115} + V_{3t}^{125}$$

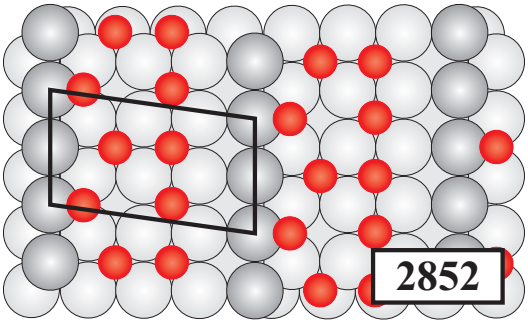


## V7-73

$$E_b^{\text{V7-73}} = 2E_{b,\text{Thc}}^{\text{On-site}} + E_{b,\text{Thl}}^{\text{On-site}} + E_{b,\text{Sh1}}^{\text{On-site}} + 2V_{1p}^{22} + V_{1p}^{23} + 2V_{2p}^{23} + 2V_{3p}^{22} + V_{3p}^{25} + 2V_{3p}^{35} + V_{3p}^{33} + V_{3p}^{55} + 2V_{1t}^{222} + 2V_{2t}^{223} + 2V_{3t}^{223} + 2V_{3t}^{235}$$

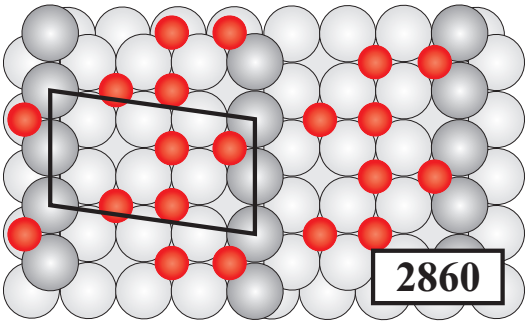


## V7-74

$$E_b^{\text{V7-74}} = E_{b,\text{Thu}}^{\text{On-site}} + 2E_{b,\text{Thc}}^{\text{On-site}} + E_{b,\text{Thl}}^{\text{On-site}} + V_{1p}^{12} + 2V_{2p}^{12} + V_{3p}^{11} + V_{3cp}^{13} + 2V_{1p}^{22} + V_{1p}^{23} + 2V_{2p}^{23} + 2V_{3p}^{22} + 2V_{2t}^{122} + 2V_{3t}^{122} + 2V_{3t}^{123} + 2V'^{123}_{3t} + 2V_{1t}^{222} + 2V_{2t}^{223} + 2V_{3t}^{223}$$

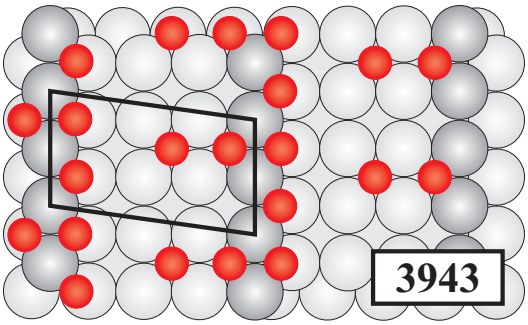


## V7-75

$$E_b^{\text{V7-75}} = E_{b,\text{Thu}}^{\text{On-site}} + E_{b,\text{Thc}}^{\text{On-site}} + 2E_{b,\text{Sh2}}^{\text{On-site}} + V_{1p}^{12} + V_{1p}^{14} + 2V_{2p}^{14} + V_{3p}^{11} + V_{3p}^{22} + V_{3p}^{24} + 2V'^{24}_{3p} + 2V_{1p}^{44} + 2V_{3p}^{44} + V_{1t}^{124} + 2V_{2t}^{144} + 2V_{3t}^{144} + 2V_{3t}^{124} + 2V_{1t}^{444}$$

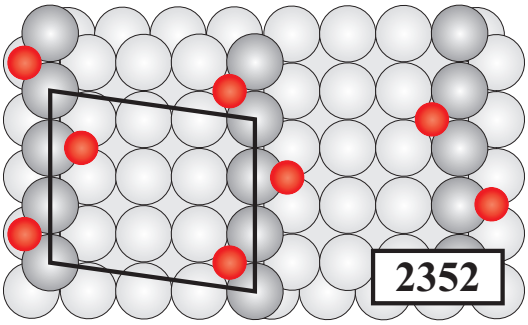


## V7-76

$$E_b^{\text{V7-76}} = E_{b,\text{Thu}}^{\text{On-site}} + E_{b,\text{Sh1}}^{\text{On-site}} + 2V_{3p}^{15}$$

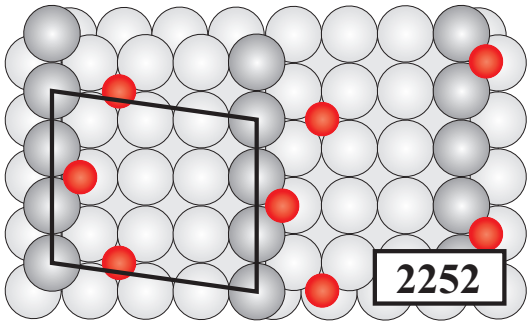


**V7-77**

$$E_b^{\text{V7-77}} = E_{b,\text{Thl}}^{\text{On-site}} + E_{b,\text{Sh2}}^{\text{On-site}} + 2V_{3p}^{34}$$

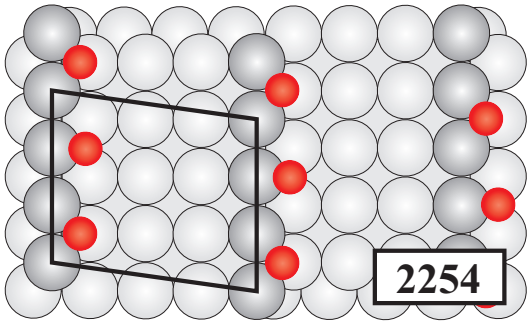


**V7-78**

$$E_b^{\text{V7-78}} = E_{b,\text{Sh1}}^{\text{On-site}} + E_{b,\text{Sh2}}^{\text{On-site}} + 2V_{3p}^{45}$$

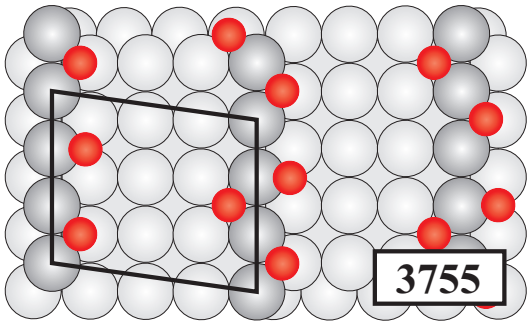


**V7-79**

$$E_b^{\text{V7-79}} = E_{b,\text{Thu}}^{\text{On-site}} + E_{b,\text{Sh1}}^{\text{On-site}} + E_{b,\text{Sh2}}^{\text{On-site}} + V_{2p}^{14} + V_{2p}^{15} + 2V_{3p}^{45} + V_{3t}^{145}$$

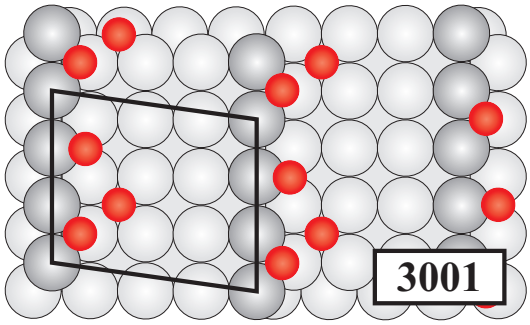


**V7-80**

$$E_b^{\text{V7-80}} = E_{b,\text{Thl}}^{\text{On-site}} + E_{b,\text{Sh1}}^{\text{On-site}} + E_{b,\text{Sh2}}^{\text{On-site}} + V_{2p}^{34} + V_{2p}^{35} + 2V_{3p}^{45} + V_{3t}^{345}$$

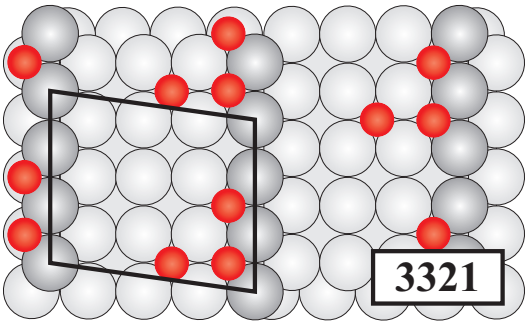


**V7-81**

$$E_b^{\text{V7-81}} = 2E_{b,\text{Thu}}^{\text{On-site}} + E_{b,\text{Thc}}^{\text{On-site}} + V_{1p}^{11} + V_{1p}^{12} + V_{2p}^{12} + V_{3p}^{11} + V_{2t}^{112}$$

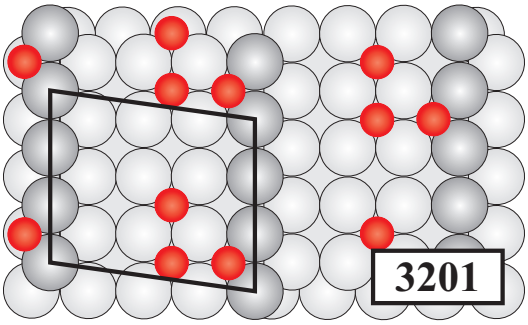


**V7-82**

$$E_b^{\text{V7-82}} = E_{b,\text{Thu}}^{\text{On-site}} + 2E_{b,\text{Thc}}^{\text{On-site}} + V_{1p}^{12} + V_{1p}^{22} + V_{2p}^{12} + V_{3p}^{22} + V_{2t}^{122}$$

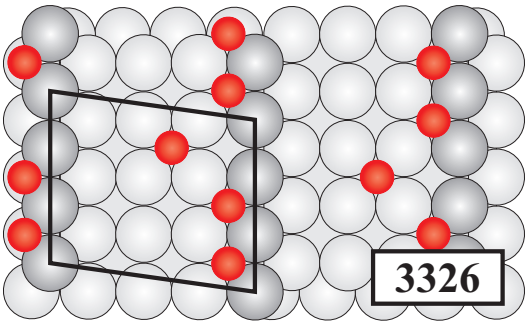


**V7-83**

$$E_b^{\text{V7-83}} = 2E_{b,\text{Thu}}^{\text{On-site}} + E_{b,\text{Thc}}^{\text{On-site}} + V_{1p}^{11} + 2V_{2p}^{12} + V_{3p}^{11} + 2V_{3t}^{112}$$

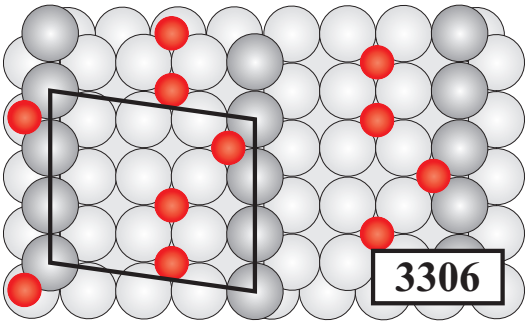


**V7-84**

$$E_b^{\text{V7-84}} = E_{b,\text{Thu}}^{\text{On-site}} + 2E_{b,\text{Thc}}^{\text{On-site}} + V_{1p}^{22} + 2V_{2p}^{12} + V_{3p}^{22} + 2V_{3t}^{122}$$

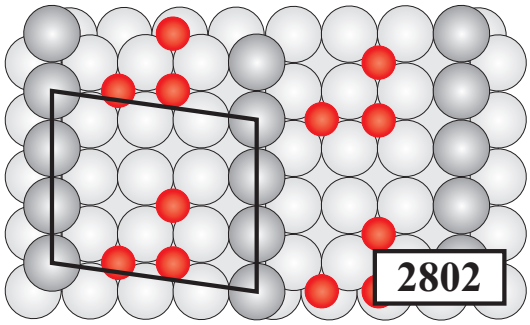


**V7-85**

$$E_b^{\text{V7-85}} = 2E_{b,\text{Thc}}^{\text{On-site}} + E_{b,\text{Thl}}^{\text{On-site}} + V_{1p}^{22} + V_{1p}^{23} + V_{2p}^{23} + V_{3p}^{22} + V_{2t}^{223}$$

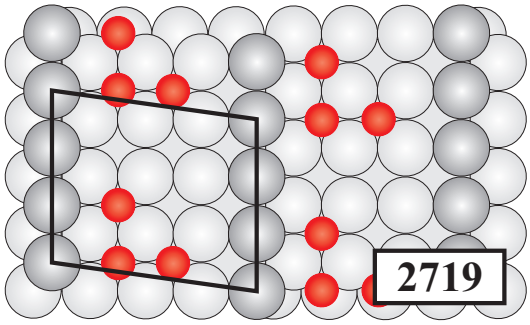


**V7-86**

$$E_b^{\text{V7-86}} = E_{b,\text{Thc}}^{\text{On-site}} + 2E_{b,\text{Thl}}^{\text{On-site}} + V_{1p}^{23} + V_{2p}^{23} + V_{1p}^{33} + V_{3p}^{33} + V_{2t}^{233}$$

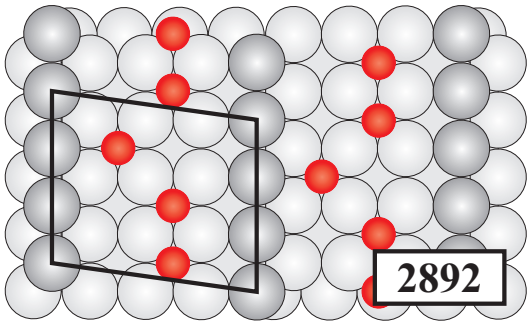


**V7-87**

$$E_b^{\text{V7-87}} = 2E_{b,\text{Thc}}^{\text{On-site}} + E_{b,\text{Thl}}^{\text{On-site}} + V_{1p}^{22} + 2V_{2p}^{23} + V_{3p}^{22} + 2V_{3t}^{223}$$

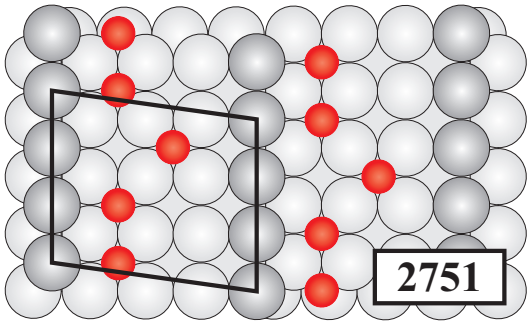


**V7-88**

$$E_b^{\text{V7-88}} = E_{b,\text{Thc}}^{\text{On-site}} + 2E_{b,\text{Thl}}^{\text{On-site}} + 2V_{2p}^{23} + V_{1p}^{33} + V_{3p}^{33} + 2V_{3t}^{233}$$

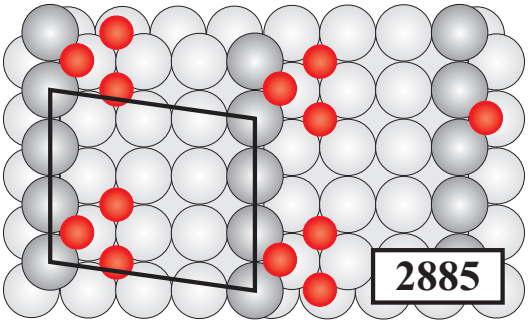


**V7-89**

$$E_b^{\text{V7-89}} = 2E_{b,\text{Thl}}^{\text{On-site}} + E_{b,\text{Sh2}}^{\text{On-site}} + V_{1p}^{33} + 2V_{2p}^{34} + V_{3p}^{33} + V_{2t}^{334}$$

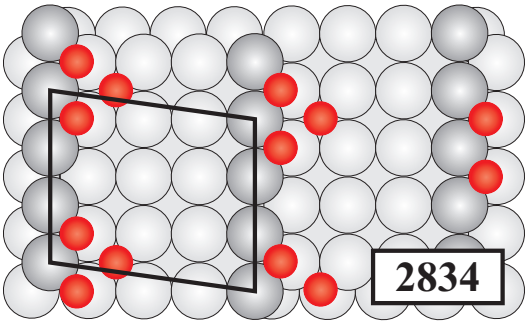


**V7-90**

$$E_b^{\text{V7-90}} = E_{b,\text{Thl}}^{\text{On-site}} + 2E_{b,\text{Sh2}}^{\text{On-site}} + 2V_{2p}^{34} + V_{1p}^{44} + V_{3p}^{44} + V_{2t}^{344}$$

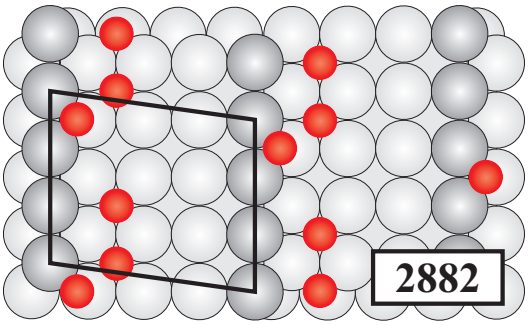


**V7-91**

$$E_b^{\text{V7-91}} = 2E_{b,\text{Thl}}^{\text{On-site}} + E_{b,\text{Sh2}}^{\text{On-site}} + V_{1p}^{33} + V_{2p}^{34} + V_{3p}^{33} + 2V_{3p}^{34} + V_{3t}^{334}$$

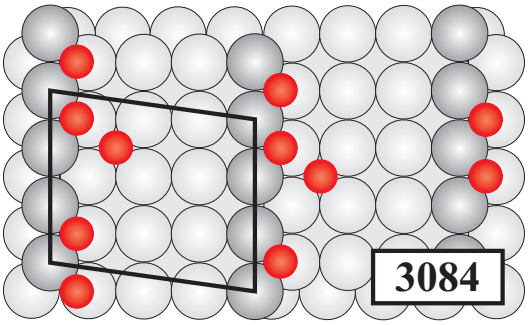


**V7-92**

$$E_b^{\text{V7-92}} = E_{b,\text{Thl}}^{\text{On-site}} + 2E_{b,\text{Sh2}}^{\text{On-site}} + V_{2p}^{34} + 2V_{3p}^{34} + V_{1p}^{44} + V_{3p}^{44} + V_{3t}^{344}$$

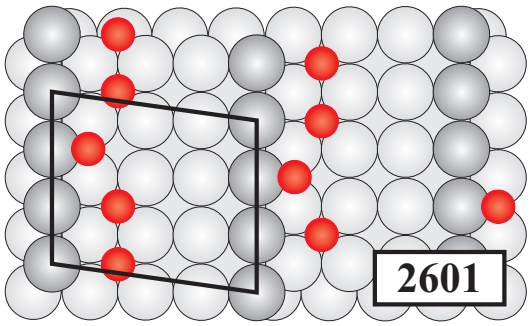


**V7-93**

$$E_b^{\text{V7-93}} = 2E_{b,\text{Thl}}^{\text{On-site}} + E_{b,\text{Sh1}}^{\text{On-site}} + V_{1p}^{33} + 2V_{2p}^{35} + V_{3p}^{33} + 2V_{3t}^{335}$$

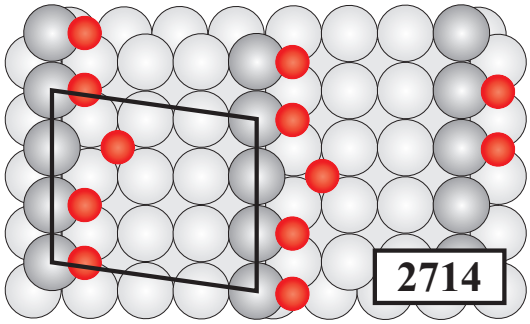


**V7-94**

$$E_b^{\text{V7-94}} = E_{b,\text{Thl}}^{\text{On-site}} + 2E_{b,\text{Sh1}}^{\text{On-site}} + 2V_{2p}^{35} + V_{1p}^{55} + V_{3p}^{55} + 2V_{3t}^{355}$$

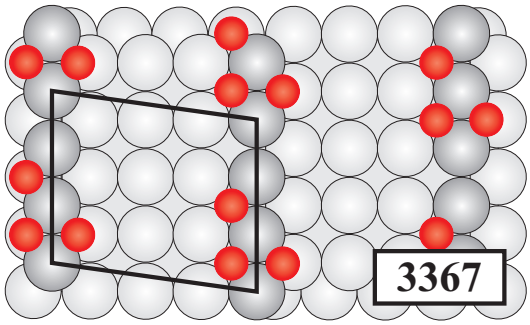


**V7-95**

$$E_b^{\text{V7-95}} = 2E_{b,\text{Thu}}^{\text{On-site}} + E_{b,\text{Sh2}}^{\text{On-site}} + V_{1p}^{11} + V_{1p}^{14} + V_{2p}^{14} + V_{3p}^{11} + V_{3t}^{335}$$

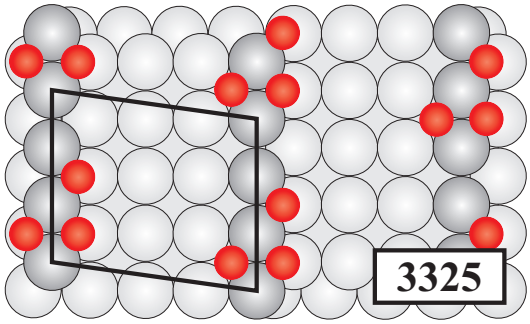


**V7-96**

$$E_b^{\text{V7-96}} = E_{b,\text{Thu}}^{\text{On-site}} + 2E_{b,\text{Sh2}}^{\text{On-site}} + V_{1p}^{14} + V_{2p}^{14} + V_{1p}^{44} + V_{3p}^{44} + V_{2t}^{144}$$

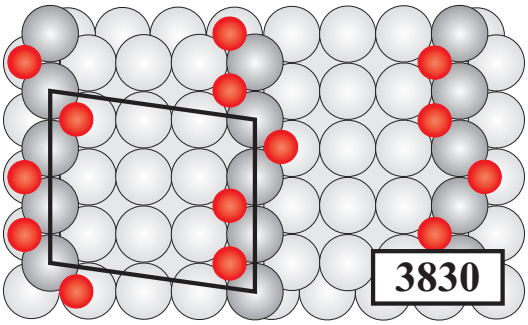


**V7-97**

$$E_b^{\text{V7-96}} = 2E_{b,\text{Thu}}^{\text{On-site}} + E_{b,\text{Sh2}}^{\text{On-site}} + V_{1p}^{11} + 2V_{2p}^{14} + V_{3p}^{11} + 2V_{3t}^{114}$$

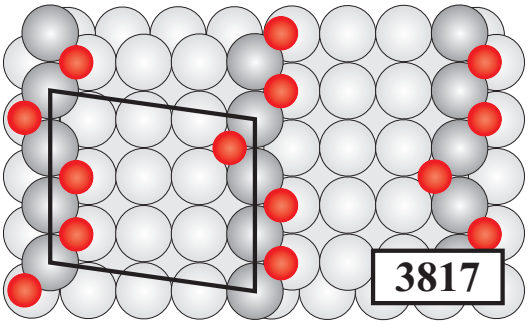


**V7-98**

$$E_b^{\text{V7-98}} = E_{b,\text{Thu}}^{\text{On-site}} + 2E_{b,\text{Sh2}}^{\text{On-site}} + 2V_{2p}^{14} + V_{1p}^{44} + V_{3p}^{44} + 2V_{3t}^{144}$$

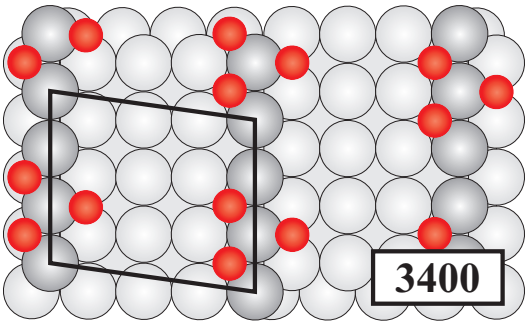


**V7-99**

$$E_b^{\text{V7-99}} = 2E_{b,\text{Thu}}^{\text{On-site}} + E_{b,\text{Sh1}}^{\text{On-site}} + V_{1p}^{11} + 2V_{2p}^{15} + V_{3p}^{11} + V_{2t}^{115}$$

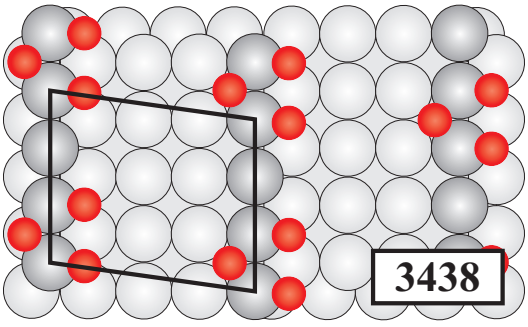


**V7-100**

$$E_b^{\text{V7-100}} = E_{b,\text{Thu}}^{\text{On-site}} + 2E_{b,\text{Sh1}}^{\text{On-site}} + 2V_{2p}^{15} + V_{1p}^{55} + V_{3p}^{55} + V_{2t}^{155}$$

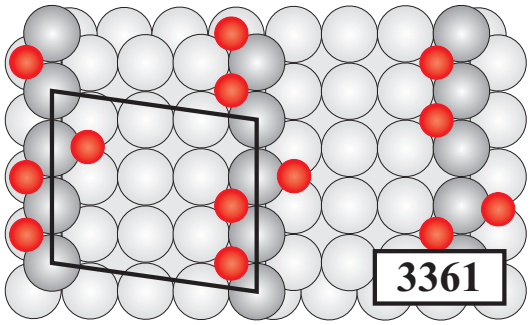


## V7-101

$$E_b^{\text{V7-101}} = 2E_{b,\text{Thu}}^{\text{On-site}} + E_{b,\text{Sh1}}^{\text{On-site}} + V_{1p}^{11} + V_{2p}^{15} + V_{3p}^{11} + 2V_{3p}^{15} + V_{3t}^{115}$$

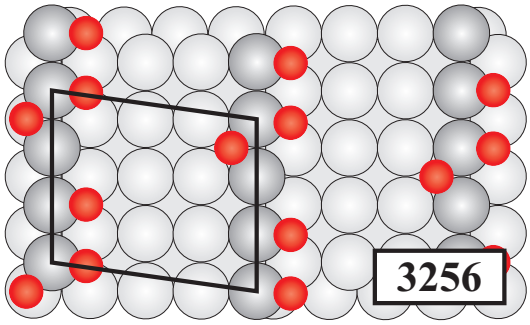


## V7-102

$$E_b^{\text{V7-102}} = E_{b,\text{Thu}}^{\text{On-site}} + 2E_{b,\text{Sh1}}^{\text{On-site}} + V_{2p}^{15} + V_{1p}^{55} + V_{3p}^{55} + 2V_{3p}^{15} + V_{3t}^{155}$$

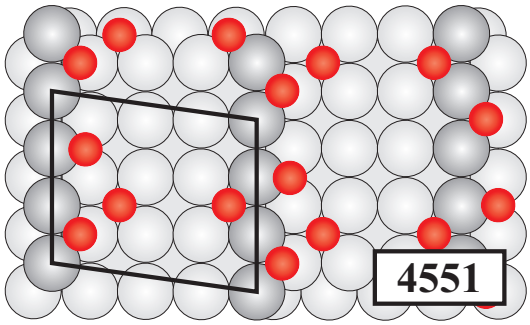


## V7-103

$$E_b^{\text{V7-103}} = E_{b,\text{Thu}}^{\text{On-site}} + E_{b,\text{Thl}}^{\text{On-site}} + E_{b,\text{Sh2}}^{\text{On-site}} + E_{b,\text{Sh1}}^{\text{On-site}} + V_{2p}^{14} + V_{2p}^{15} + V_{3p}^{13} + V_{3cp}^{13} + V_{2p}^{34} + V_{2p}^{35} + 2V_{3p}^{45} + V'^{134}_{3t} + V_{3t}^{135} + V_{3t}^{145} + V_{3t}^{345}$$

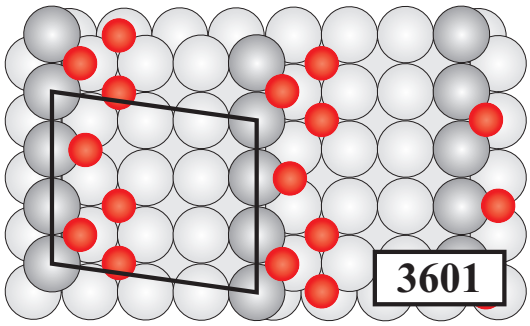


## V7-104

$$E_b^{\text{V7-104}} = 2E_{b,\text{Thl}}^{\text{On-site}} + E_{b,\text{Sh2}}^{\text{On-site}} + E_{b,\text{Sh1}}^{\text{On-site}} + V_{1p}^{33} + 2V_{2p}^{34} + 2V_{2p}^{35} + V_{3p}^{33} + 2V_{3p}^{45} + V_{2t}^{334} + 2V_{3t}^{335} + 2V_{3t}^{345}$$

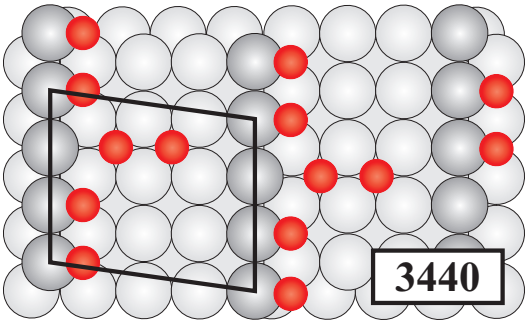


**V7-105**

$$E_b^{\text{V7-105}} = E_{b,\text{Thc}}^{\text{On-site}} + E_{b,\text{Thl}}^{\text{On-site}} + 2E_{b,\text{Sh1}}^{\text{On-site}} + V_{1p}^{23} + 2V_{2p}^{35} + V_{1p}^{55} + V_{3p}^{55} + 2V_{3t}^{235} + 2V_{3t}^{355}$$

# Bibliography


[1] W. Kohn, *Rev. Mod. Phys.* **71**, 1253 (1998)

[2] R. M. Dreizler and E. K. U. Gross, *Density Functional Theory*, Springer, Berlin (1990)

[3] C. Møller and M. S. Plesset, *Phys. Rev.* **46**, 618 (1934)

[4] A. R. Leach, *Molecular Modeling Principles and Applications*, 2nd ed., Henry Ling Ltd., London (2001)

[5] B. O. Roos and P. R. Taylor, *Chem. Phys.* **48**, 157 (1980)

[6] R. J. Bartlett, *J. Chem. Phys.* **93**, 1697 (1989)

[7] R. G. Parr and W. Yang, *Density-Functional Theory of Atoms and Molecules*, Oxford University Press, New York (1989)

[8] P. Hohenberg and W. Kohn, *Phys. Rev. B* **136**, 864 (1964)

[9] W. Kohn and L. J. Sham, *Phys. Rev. A* **140**, 1133 (1965)

[10] E. Wigner and F. Seitz, *Phys. Rev.* **46**, 509 (1034)

[11] D. M. Ceperley and B. J. Alder, *Phys. Rev. Lett.* **45**, 566 (1980)

[12] M. Gell-Mann and K. A. Brueckner, *Phys. Rev.* **106**, 364 (1957)

[13] W. J. Carr and A. A. Maradudin, *Phys. Rev.* **133**, A371 (1964)

[14] P. Nozières and D. Pines, *Phys. Rev.* **111**, 442 (1958)

[15] W. J. Carr, *Phys. Rev.* **122**, 1437 (1961)

[16] S. J. Vosko, L. Wilk, and M. Nusair, *Can. J. Phys.* **58**, 1200 (1980)

[17] J. P. Perdew and Y. Wang, *Phys. Rev. B* **45**, 13244 (1992)

[18] J. P. Perdew, K. Burke, and M. Ernzerhof, *Phys. Rev. Lett.* **77**, 3865 (1996)

[19] C. Lee, W. T. Yang, and R. G. Parr *Phys. Rev. B* **37**, 785 (1988)

[20] C. Kittel, *Introduction to Solid State Physics*, 6th ed., Wiley, New York (1986)

[21] M. D. Segall, P. L. D. Lindan, M. J. Probert, C. J. Pickard, P. J. Hasnip, S. J. Clark, and M. C. Payne *J. Phys.: Cond. Mat.* **14** 2717 (2002)

[22] J. C. Slater, *Phys. Rev.* **51**, 846 (1937)

[23] O. K. Anderson, *Phys. Rev. B* **12**, 3060 (1975)

[24] D. J. Singh and L. Nordström, *Planewaves, Pseudopotentials and the LAPW Method,* 2nd ed., Springer, New York (2006)

[25] D. D. Koelling and G. O. Arbman, *J. Phys. F: Metal Phys.* **5**, 2041 (1975)

[26] E. Sjöstedt, L. Nordström, and D. J. Singh, *Solid State Comm.* **114**, 15 (2000)

[27] G. K. H. Madsen, P. Blaha, K. Schwarz, E. Sjöstedt, and L. Nordström, *Phys. Rev. B* **64**, 195134 (2001)

[28] O. Jepsen and O. K. Andersen, *Solid State Comm.* **9**, 1763 (1977)

[29] J. Rath and A. F. Freeman, *Phys. Rev. B* **11**, 2109 (1975)

[30] D. J. Chadi and M. L. Cohen, *Phys. Rev. B* **8**, 5747 (1973)

[31] H. J. Monkhorst and J. D. Pack, *Phys. Rev. B* **13**, 5188 (1976)

[32] H. J. Monkhorst and J. D. Pack, *Phys. Rev. B* **16**, 1748 (1977)

[33] P. Blaha, K. Schwarz, G. K. H. Madsen, D. Kvasnicka, and J. Luitz, **WIEN2k**, *An Augmented Plane Wave + Local Orbitals Program for Calculaing Crystal Properties*, (Karlheinz Schwarz, Techn. Universität Wien, Austria), 2001, ISBN 3-9501031-1-2.

[34] D. Singh, H. Krakauer, and C. -S. Wang, *Phys. Rev. B* **34**, 8391 (1986)

[35] L. K. Dash and M. J. Gillan, *Surf. Sci.* **549**, 217 (2004)

[36] J. L. F. Da Silva, K. Schroeder, and S. Blügel, *Phys. Rev. B* **69**, 245411 (2004)

[37] A. Zangwill, *Physics at Surfaces*, Cambridge University Press, USA (2001)

[38] P. J. Feibelman, *Phys. Rev. B* **60**, 11118 (1999)

[39] R. Stumpf and M. Scheffler, *Phys. Rev. B* **53**, 4958 (1996)

[40] C. Herring, Phys. Rev. **82**, 87 (1951)

[41] J. Rogal, K. Reuter, and M. Scheffler, *Phys. Rev. B* **69**, 075421 (2004)

[42] W. R. Tyson and W. A. Miller, *Surf. Sci.* **62**, 267 (1977)

[43] J. Rogal, *Ph. D. Thesis*, FU, Berlin (2006).

[44] R. Smoluchowski, *Phys. Rev.* **60**, 661 (1941)

[45] M. W. Finnis and V. Heine, *J. Phys. F: Metal Phys.* **4**, L37 (1974)

[46] J. E. Dennis, D. M. Gay, and R. E. Welsch, *ACM Trans. Math. Software* **7**, 348 (1981)

[47] C. G. Broyden, J. E. Dennis, and J. J. Moré, *J. Inst. Maths. Appl.* **12**, 223 (1973)

[48] L. Vitos, H. L. Skriver, and J. Kollár, *Surf. Sci.* **425**, 212 (1999)

[49] F. Raouafi, C. Barreteau, M. C. Desjonquères, and D. Spanjaard, *Surf. Sci.* **505**, 183 (2002)

[50] W. F. Egelhoff, *Surf. Sci. Rep.* **6**, 253 (1987)

[51] S. Lizzit, A. Baraldi, A. Groso, K. Reuter, M. V. Ganduglia-Pirovano, C. Stampfl, M. Scheffler, M. Stichler, C. Keller, W. Wurth, and D. Menzel *Phys. Rev. B* **63**, 205419 (2001)

[52] A. Baraldi, S. Lizzit, and G. Paolucci, *Surf. Sci.* **457**, L354 (2000)

[53] M. V. Ganduglia-Pirovano, V. Natoli, M. H. Cohen, J. Kudrnovský, and I. Turek, *Phys. Rev. B* **12**, 8892 (1996)

[54] C. Stampfl, M. V. Ganduglia-Pirovano, K. Reuter, and M. Scheffler, *Surf. Sci.* **500**, 368 (2002)

[55] K. Reuter and M. Scheffler, *Phys. Rev. B* **65**, 035406 (2001)

[56] W.X. Li, C. Stampfl, and M. Scheffler, Phys. Rev. Lett. **90**, 256102 (2003)

[57] K. Reuter and M. Scheffler, *Phys. Rev. B* **68**, 045407 (2003)

[58] K. Reuter and M. Scheffler, *Appl. Phys. A* **78**, 793 (2004)

[59] D. R. Stull and H. Prophet, *JANAF Thermochemical Tables*, 2nd ed. (U.S. National Bureau of Standards, Washington, DC, 1971)

[60] J. Rogal and K. Reuter, *Ab Initio Atomistic Thermodynamics for Surfaces: A Primer.* In: Experiment, Modeling and Simulation of Gas-Surface Interactions for Reactive Flows in Hypersonic Flights. Educational Notes RTO-EN-AVT-142, Neuilly-sur-Seine (2007), 2-12-18, ISBN 978-92-837-0057-9

[61] M. E. J. Newman and G. T. Barkema, *Monte Carlo Methods in Statistical Physics*, Oxford Clarendon Press, USA (2001)

[62] D. Frenkel and B. Smit, *Understanding Molecular Simulation from Algorithms to Applications*, Academic Press, USA (2002)

[63] L. D. Landau and E. M. Lifshitz, *Statistical Mechanics*, 3rd ed. Butterworth-Heinemann, Oxford (1999)

[64] N. Metropolis, A. W. Rosenbluth, M. N. Rosenbluth, A. H. Teller, and E. Teller, *J. Chem. Phys.* **21**, 1087 (1953)

[65] J. M. Sanchez, F. Ducastelle, and D. Gratias, *Physica* **128A**, 334 (1984)

[66] C. Stampfl, H. J. Kreuzer, S. H. Payne, H. Pfnür, and M. Scheffler, *Phys. Rev. Lett.* **83**, 2993 (1999)

[67] K. Reuter, C. Stampfl, and M. Scheffler, *Ab Initio Atomistic Thermodynamics and Statistical Mechanics of Surface Properties and Functions.* In: Handbook of Materials Modeling, Vol. 1. (Ed.) Sidney Yip. Springer Berlin Heidelberg (2005), 149-194. ISBN 1-4020-3287-0

[68] W. H. Press, B. P. Flannery, S. A. Teukolsky, and W. T. Vetterling, *Numerical Recipes in Fortran*, 2nd ed., Cambridge University Press, Cambridge (1992)

[69] C. R. L. Fuentes, *Ph. D. thesis*, TU Hamburg-Harburg (2005)

[70] J. Glosli and M. Plischke, *Can. J. Phys.* **61**, 1515 (1983)

[71] P. Piercy, K. DeBell, and H. Pfnür, *Phys. Rev. B* **45**, 1869 (1992)

[72] J. S. Walker and M. Schick, *Phys. Rev. B* **20**, 2088 (1979)

[73] D. P. Landau, *Phys. Rev. B* **27**, 5604 (1983)

[74] H. Pfnür and P. Piercy, *Phys. Rev. B* **40**, 2515 (1989)

[75] Leo P Kadanoff, *Statistical Physics: Statics, Dynamics and Renormalization*, World Scientific, Singapore (2000)

[76] R. I. Masel, *Principles of Adsorption and Reaction on Solid Surfaces*, Wiley, New York (1996)

[77] D. De Fontaine, In: *Statics and Dynamics of Alloy Phase Transformations*, (Eds.) P.E.A. Turchy and A. Gonis, NATO ASI Series, Plenum Press, New York (1994)

[78] A. Zunger, *First Principles Statistical Mechanics of Semiconductor Alloys and Intermetallic Compounds*. In: Statics and Dynamics of Alloy Phase Transformations, (Eds.) P.E.A. Turchy and A. Gonis, NATO ASI Series, Plenum Press, New York (1994)

[79] F. H. Ree and D. A. Chestnut, *Phys. Rev. Lett.* **18**, 5 (1967)

[80] K. Binder and D. P. Landau, *Phys. Rev. B* **21**, 1941 (1980)

[81] W. Kinzel and M. Schick, *Phys. Rev. B* **24**, 324 (1981)

[82] R. G. Caflisch and A. N. Berker, *Phys. Rev. B* **29**, 1279 (1984)

[83] J. Amar, K. Kaski, and J. D. Gunton, *Phys. Rev. B* **29**, 1462 (1984)

[84] P. Bak, P. Kleban, W. N. Unertl, J. Ochab, G. Akinci, N. C. Bartelt, and T. L. Einstein, *Phys. Rev. Lett.* **54**, 1539 (1985)

[85] N. C. Bartelt, L. D. Roelofs, and T. L. Einstein, *Surf. Sci.* **221**, L750 (1989)

[86] D. J. Liu and J. W. Evans, *Surf. Sci.* **563**, 13 (2004)

[87] S. -L. Chang and P. A. Thiel, *Phys. Rev. Lett.* **59**, 296 (1987); J. Chem. Phys. **88**, 2071 (1988)

[88] T. W. Orent and S. D. Bader, *Surf. Sci.* **115**, 323 (1982)

[89] S. -L. Chang, P. A. Thiel, and J. W. Evans, *Surf. Sci.* **205**, 117 (1988)

[90] G. Zheng and E. I. Altman, *Surf. Sci.* **504**, 253 (2002)

[91] M. Todorova, E. Lundgren, V. Blum, A. Mikkelsen, S. Gray, J. Gustafson, M. Borg, J. Rogal, K. Reuter, J. N. Andersen, and M. Scheffler, *Surf. Sci.* **541**, 101 (2003)

[92] G. Ertl and J. Koch, *Z. Phys. Chem.* **69**, 323 (1970)

[93] E. M. Stuve, R. J. Madix, and C. R. Brundle, *Surf. Sci.* **46**, 155 (1984)

[94] An alternative formulation equally found in the literature would be to let all sums run independently over the lattice sites, necessarily implying a multiple counting of site contributions. Pair interactions would then *e.g.* be double counted, which needs to be taken into account, when comparing interaction values quoted within this formulation to values quoted within the single-counting formulation employed here.

[95] T. L. Einstein and J. R. Schrieffer, *Phys. Rev. B* **7**, 3629 (1973); T. L. Einstein. In: *Handbook of Surface Science*, Vol. **1**, (Ed.) W.N. Unertl, Elsevier, Amsterdam (1996)

[96] A. Kiejna, G. Kresse, J. Rogal, A. De Sarkar, K. Reuter, and M. Scheffler, *Phys. Rev. B* **73**, 035404 (2006)

[97] J. Shao, *J. Amer. Statist. Assoc.* **88**, 486 (1993)

[98] P. Zhang, *Ann. Statist.* **21**, 299 (1993)

[99] A. van de Walle and G. Ceder, *J. Phase Equilib.* **23**, 348 (2002)

[100] M. Borg, C. Stampfl, A. Mikkelsen, J. Gustafson, E. Lundgren, M. Scheffler, and J. N. Andersen, *ChemPhysChem* **6**, 1923 (2005)

[101] G.W. Simmons, Y. -N. Wang, J. Marcos, and K. Klier, *J. Phys. Chem.* **95**, 4522 (1991)

[102] Q. -M. Hu, K. Reuter, and M. Scheffler, *Phys. Rev. Lett.* **98**, 176103 (2007)

[103] Q. -M. Hu, K. Reuter, and M. Scheffler, *Phys. Rev. Lett.* **99**, 169903 (2007)

[104] K. Reuter, *Nanometer and Sub-Nanometer Thin Oxide Films at Surfaces of Late Transition Metals*. In: Nanocatalysis: Principles, Methods, Case Studies. (Eds.) U. Heiz and U. Landman. Springer, Berlin (2006)

[105] M. C. Payne, M. P. Teter, D. C. Allan, T. A. Arias, and J. D. Joannopoulos, *Rev. Mod. Physics* **64**, 1045 (1992)

[106] A. Groß, *Theoretical Surface Science*, Springer, Berlin (2003)

[107] *Handbook of Heterogeneous Catalysis*. (Eds.) G. Ertl, H. Knözinger, and J. Weitkamp. Wiley, New York (1997)

[108] M. V. Ganduglia-Pirovano and M. Scheffler, *Phys. Rev. B* **59**, 15533 (1999)

[109] K. Reuter, M. V. Ganduglia-Pirovano, C. Stampfl, and M. Scheffler, *Phys. Rev. B* **65**, 165403 (2002)

[110] L. A. Curtiss, K. Raghavachari, G. W. Trucks, and J. A. Pople, *J. Chem. Phys.* **94**, 7221 (1991)

[111] M. Todorova, K. Reuter, and M. Scheffler, *J. Phys. Chem. B* **108**, 14477 (2004)

[112] W. X. Li, C. Stampfl, and M. Scheffler, *Phys. Rev. B* **65**, 075407 (2002)

[113] J. L. F. Da Silva, C. Stampfl, and M. Scheffler, *Surf. Sci.* **600**, 703 (2005)

[114] M. Methfessel, D. Hennig, and M. Scheffler, *Phys. Rev. B* **46**, 4816 (1992)

[115] R. Smoluchowski, *Phys. Rev.* **60**, 661 (1941)

[116] see *e.g.* L. Pauling, *The Nature of the Chemical Bond*, 3rd. ed., Cornell University Press, Ithaca, NY (1960)

[117] J. L. F. Da Silva, K. Schroeder, and S. Bluegel, *Phys. Rev. B* **70**, 245432 (2004)

[118] Y. Tian, K. -W. Lin, and F. Jona, *J. Vac. Sci. Technol. A* **17**, 1635 (2000)

[119] Y. Y. Sun, H. Xu, Y. P. Feng, A. C. H. Huan, and A. T. S. Wee, *Phys. Rev. Lett.* **93**, 136102 (2004)

[120] I. Makkonen, P. Salo, M. Alatalo, and T. S. Rahman, *Phys. Rev. B* **67**, 165415 (2003)

[121] S. K. Kwon, Z. Nabi, K. Kadas, L. Vitos, J. Kollar, B. Johansson, and R. Ahuja, *Phys. Rev. B* **72**, 235423 (2005)

[122] J. P. Perdew and Y. Wang, *Phys. Rev. B* **45**, 13244 (1992)

[123] L. Vitos, A. V. Ruban, H. L. Skriver, and J. Kollar, *Surf. Sci.* **411**, 186 (1998)

[124] J. Zabloudil, R. Hammerling, L. Szunyogh, and P. Weinberger, *Phys. Rev. B* **73**, 115410 (2006)

[125] F. Raouafi, C. Barreteau, M. C. Desjonquères, and D. Spanjaard, *Surf. Sci.* **505**, 183 (2002)

[126] J. Frohn, M. Giesen, M. Poensgen, J. F. Wolf, and H. Ibach, *Phys. Rev. Lett.* **67**, 3543 (1991)

[127] Y. Y. Sun, H. Xu, J. C. Zheng, J. Y. Zhou, Y. P. Feng, and A. T. S. Wee, *Surf. Sci.* **548**, 309 (2004)

[128] The consistency between the number published in [43] and our numbers were conferred for several ordered adlayers, so that we correspondingly use the value for the $(\sqrt{5} \times \sqrt{5})R27^0$ binding energy published in [43] to construct the phase diagram.

[129] R. B.Anderson, K. C. Stein, J. J. Feenan, and L. J. E. Hofer, *Ind. Eng. Chem.* **53**, 809 (1961)

[130] G. Ertl, H. Knözinger, and J. Weitkamp, *Environmental Catalysis*, Wiley, New York (1999)

[131] C. J. Zhang and P. Hu, *J. Chem. Phys.* **116**, 322 (2002)

[132] J. Han, D. Y. Zemlyanov, and F. H. Ribeiro, *Catal. Today* **117**, 506 (2006)

[133] X. Zhang, C. S. -M. Lee, D. M. P. Mingos, and D. O Hayward *Appl. Catal. A: Gen.* **240**, 183 (2003)

[134] M. Lyubovsky, L. L. Smith, M. Castaldi, H. Karim, B. Nentwick, S. Etemad, R. LaPierre, and W. C. Pfefferle, *Catal. Today* **83**, 71 (2003)

[135] J. Rogal, K. Reuter, and M. Scheffler, *Phys. Rev. Lett.* **98**, 046101 (2007); *Phys. Rev. B* **75**, 205433 (2007)

[136] G. Zhu, J. Han, D.Y. Zemlyanov, and F.H. Ribeiro, *J. Am. Chem. Soc.* **126**, 9896 (2004)

[137] R. Westerström, J. Gustafson, A. Resta, A. Mikkelsen, J. N. Andersen, E. Lundgren, N. Seriani, F. Mittendorfer, M. Schmid, J. Klikovits, P. Varga, M. D. Ackermann, J. W. M. Frenken, N. Kasper, and A. Stierle, *Phys. Rev. B* **76**, 155410 (2007)

[138] *Handbook of Chemistry and Physics*, **76**$^{\text{th}}$ edition, 12-18, CRC press, (1995-1996)

[139] M. Todorova, *Ph. D. Thesis*, TU, Berlin (2004)

[140] F. Birch, *J. Appl. Phys.* **9**, 279 (1938)

[141] F. D. Murnaghan, *Proc. Nat. Acad. Sci.* **30**, 244 (1944)

[142] C. -L. Fu and K. -M. Ho, *Phys. Rev. B* **28**, 5480 (1983)

[143] J. C. Boettger, *Phys. Rev. B* **49**, 16798 (1994)

[144] J. Neugebauer and M. Scheffler, *Phys. Rev. B* **46**, 16067 (1992)

[145] L. Bengtsson, *Phys. Rev. B* **59**, 12301 (1999)

# Acknowledgments

Lots of people have helped me in countless ways enroute to the final stage of my doctoral studies. I would like to thank Karsten Reuter for giving me the chance to study at the famous Fritz-Haber-Institute. As my supervisor, he helped me out with all kinds of difficulties, and introduced me not only to first-principles statistical mechanics, but also to the scientific spirit.

Special thanks are due to my colleague Jutta Rogal for helping me get my project started, and surviving as a non-German speaker in Germany. I would furthermore like to acknowledge fruitful discussions on the lattice-gas Hamiltonian with Volker Blum and John Kitchin, and lots of fun with Qingmiao Hu, Xinzheng Li, Erik McNellis, Andrea Sanfilippo, Li Sheng and other people in our group. I also thank the International Max-Planck Research School for funding me for two years, and for offering nice courses and discussions.

It is my great luck to be married to Yuanyuan Shen. She has given me essential support in the course of my Ph.D. work by providing wonderful living and studying conditions at home. Despite a lack of understanding of my work, she bravely acted as my only audience when I rehearsed my talks. I am sorry that I spent so much time in front my computer, instead of with you. I LOVE you. Additionally, I would like to thank my parents for their endless support.

At last, I would like to thank Berlin's nice environment for keeping me healthy, and giving me lots of energy to work.

# Curriculum Vitae

## Personal Data

| | | | |
|---|---|---|---|
| Name: | Yongsheng Zhang | Sex: | Male |
| Nationality: | Chinese | Marital Status: | Married |
| Place of Birth: | Shandong - P.R˜China | Data of Birth: | Sep. 01, 1976 |

## Education

2003-2008 - Fritz-Haber-Institut, Abt. Theorie Department, Max-Planck-Gesellschaft, Germany, PhD

2000-2003 - Institute of Solid State Physics, Chinese Academy of Sciences, P.R˜China, M.S

1996-2000 - Qufu Normal University, P.R˜China, B.S.

# Publications

1. *Density-functional theory investigation of oxygen adsorption at Pd(11N) vicinal surfaces (N=3,5,7): Influence of neighboring steps*,
   **Yongsheng Zhang**, Jutta Rogal and Karsten Reuter,
   Phys. Rev. B **74**, 125414, (2006).

2. *On the accuracy of first-principles lateral interactions: Oxygen at Pd (100)*,
   **Yongsheng Zhang**, Volker Blum and Karsten Reuter,
   Phys. Rev. B **75**, 235406, (2007)

3. *First-principles statistical mechanics approach to step decoration at surfaces*,
   **Yongsheng Zhang** and Karsten Reuter,
   submitted to Phys. Rev. Lett. (2008)